Photodissociation Dynamics and UV Spectroscopy of Ozone

Patrick O'Keeffe

Doctor of Philosophy

University of Edinburgh

1999

Declaration

I hereby declare that this thesis has been composed by myself and, except where due acknowledgement is given, the work described in it is my own and was carried out at the University of Edinburgh.

Patrick O'Keeffe

17/02/00
Date

He, too, has been changed in his turn,

Transformed utterly:

A terrible beauty is born

W. B. Yeats.

Acknowledgements

After three years in Edinburgh there are a number of people I would like to thank. Firstly, my supervisor, Prof. Robert Donovan whose enthusiasm, interest and direction in all research matters has made my Ph.D. a fruitful experience both academically and personally. I must also mention and thank Dr. Kenneth Lawley for many useful discussions and helpful instructions which have taught me a great deal. I am especially indebted to Dr. Trevor Ridley for his many hours of patient help both in the laboratory and during our many discussions. It is no exaggeration to that that without his help this thesis would not now be finished.

Thanks also to all of the other people in the laser group (you know who you are!), past or present, who have made my stay here very enjoyable. I would also like to say a big cheers to my flat-mates, the two Roberts, who have been my partners in thesis pain for the last few months and have allowed me to stay three years as their flat-mate before finally getting rid of me. A special thanks to my mum and siblings who have tolerated many forgotten birthdays, overly long absences etc. during the last few years and still gave me their support throughout my Ph.D.

Finally, but certainly not least thanks to Isabella for keeping me sane for the last few months and providing me with a needed relaxing break prior to finishing this thesis.

Abstract

The UV absorption and photodissociation dynamics of ozone have been extensively studied by spectroscopic analysis of both the atomic and diatomic photofragments. Central to the study is the UV absorption which consists of the extremely intense Hartley band (200 - 310 nm) and the less intense structured tail to lower energy called the Huggins bands (310 - 360 nm). The dissociation channels along with their thermodynamic thresholds for the dissociation of vibrationally relaxed ground state ozone are as follows:

(A)	O_3	+	$h\nu$	$\rightarrow$	$O(^3P_J)$	+	$O_2\ (X\ ^3\Sigma_g^-)$	(1178 nm)
(B)				$\rightarrow$	$O(^3P_J)$	+	$O_2\ (a\ ^1\Delta_g)$	(612 nm)
(C)				$\rightarrow$	$O(^3P_J)$	+	$O_2\ (b\ ^1\Sigma_g^+)$	(463 nm)
(D)				$\rightarrow$	$O(^1D)$	+	$O_2\ (X\ ^3\Sigma_g^-)$	(411 nm)
(E)				$\rightarrow$	$O(^1D)$	+	$O_2\ (a\ ^1\Delta_g)$	(310 nm)

The contribution of the spin-forbidden channels to Huggins band photodissociation was quantified using Resonance Enhanced Multiphoton Ionisation (REMPI) detection of the O ($^3P_0$) fragments combined with a delayed pulsed field extraction technique. The translational and angular properties of the photofragments were measured as part of this technique. The observed trimodal velocity distribution of the O ($^3P_0$) fragments was suggested to be a result of the different amounts of internal energy taken from the dissociation event by the diatomic co-fragments of channels (A), (B) and (C). However, a bimodal vibrational distribution of one of the channels could not be excluded at this stage as the slowest velocity peak of the O ($^3P_0$) fragments may be due

to formation of high vibrational levels of the diatomic fragments of channels (A) or (B).

REMPI spectroscopy was used to detect the diatomic photofragments in a rotationally and vibrationally selective manner. In these experiments ozone was photolysed with tunable UV radiation and the fragments were state selectively ionised using (2 + 1) REMPI *via* the O_2 ($d\ 3s\sigma_g\ ^1\Pi_g$) state using a second probe laser. This Rydberg state was found to be heavily perturbed by nearby a valence state, yet it was possible to identify O_2 ($b\ ^1\Sigma_g^+$, $v = 0$) fragments produced *via* spin-forbidden dissociation from a singlet state of ozone excited by absorption in the Huggins band region. Measurement of the kinetic energy of these fragments was used to confirm that they are produced *via* channel (C) and not a multiphoton process in ozone. This represents the first experimental evidence for the operation of the spin-forbidden channel (C) in this region.

The vibrational structure of the Hartley and Huggins bands has been re-assigned. These vibrational assignments are related to the relevant literature *ab initio* Potential Energy Surfaces (PESs) of the excited states of ozone and the electronic assignments of the two systems are inferred.

Velocity and angular measurements of ozone photofragments at a number of photolysis wavelengths revealed a strong mode specificity of the dissociation processes. A model of the photodissociation dynamics is presented which is consistent with these results and is also linked with the vibrational re-assignment of the Huggins bands. Further intricacies of the dissociation process are revealed by examination of the different velocity distributions of the O ($^3P_{2,1,0}$) multiplets. The end result is an overall model of the complex dissociation dynamics of ozone incorporating all of the experimental results.

Further experiments were performed involving rotationally selective pumping of the O_2 ($b \leftarrow X$) transition as the first step in an optical-optical double resonance technique used to investigate the perturbations of the O_2 ($d\ 3s\sigma_g\ ^1\Pi_g$) Rydberg state. The resulting individual J states of the O_2 ($b\ ^1\Sigma_g^+$) molecule

were detected *via* a (2 + 1) REMPI process which ionised these states through the resonance enhancements of the most perturbed vibrational levels of the d state. The results of these experiments are used to assign the perturbed REMPI spectra and are discussed with respect to the most recent analysis of these perturbations.

Contents

List of Tables

List of Figures

Chapter 1

Introduction

"Among the many interesting bodies which the researches of modern chemists have brought to light, few are more remarkable than the substance to which the name ozone has been given."

So begins an article written in 1856 by a Professor Thomas Andrews of Queens, Belfast [1]. During the course of this thesis it will be seen that this statement is still true today nearly 150 years later. Since the above pioneering days of research into ozone an extraordinary amount of effort has been expended in the attempt to understand this apparently simple molecule and its interactions with external stimuli such as the reaction with other atmospheric molecules and the absorption of the sun's radiation. The latter is the subject of spectroscopic studies of ozone and, in particular, this thesis.

1.1 Atmospheric Absorption of Radiation

The depth of penetration of radiation of a particular wavelength into the earth's atmosphere is dictated by how efficiently the constituent gases of the atmosphere absorb that radiation. As can be seen from Figure 1.1 the

major constituents of the atmosphere, O_2 and N_2, absorb most of the very energetic and dangerous radiation below 200 nm. The ozone molecule absorbs very strongly in the 200 - 310 nm region of the electromagnetic spectrum which is on the edge of the visible region but lower in energy than the absorption regions of O_2 and N_2. It is thus solely responsible for the filtering out of this energy band of solar radiation which is of high enough energy to cause damage to organic material. A vibrational analysis of the absorption structure of both the Hartley band (200 - 310 nm) and the Huggins bands (310 - 360 nm) which forms much of this important region of the absorption of ozone is presented in Chapter 7 of this thesis.

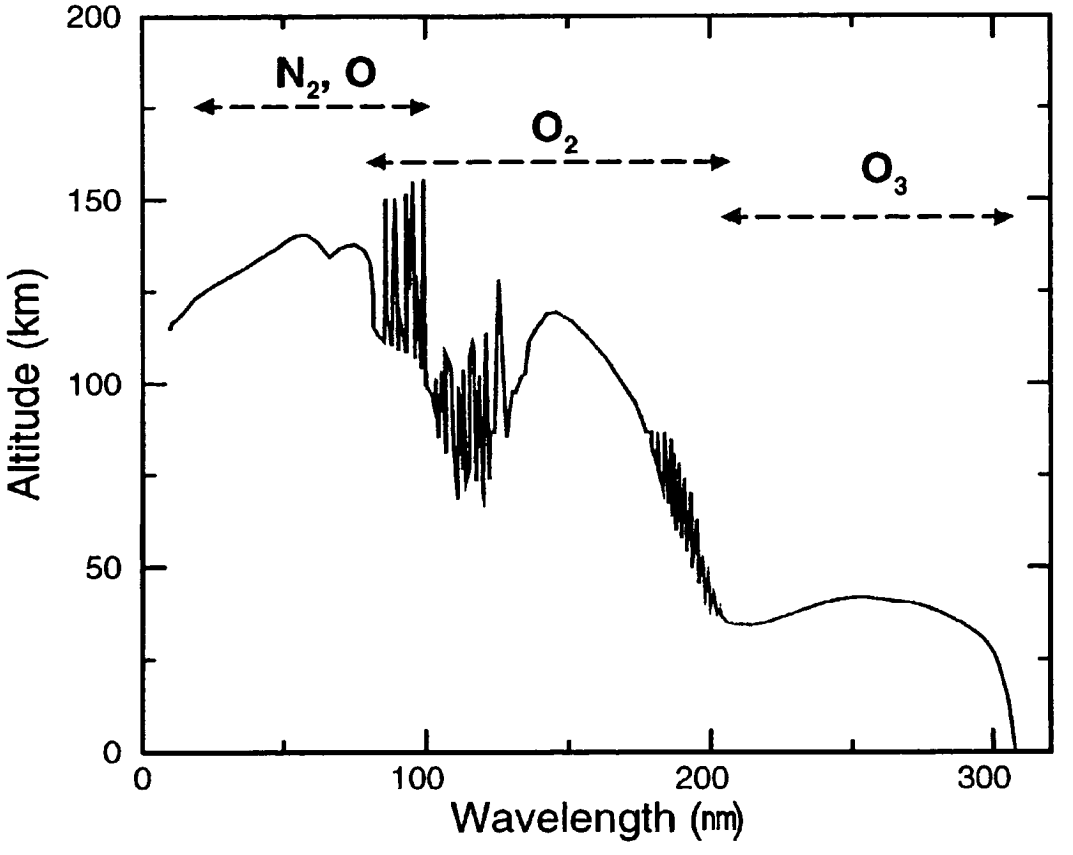

Figure 1.1.: The atmospheric altitude of maximum absorption of light as a function of the wavelength (after Watanabe, ref [2]). Also, shown are the atmospheric constituents principally responsible for absorption in each region.

In spite of the important role which the ozone molecule plays in the earth's atmosphere, it only constitutes a tiny percentage of the atmosphere. As an indication of this it has been calculated that if all of the ozone in the earth's atmosphere was compressed to the pressure at the earth's surface it would only form a layer 3 mm thick. This tiny amount of ozone plays such an important part in the atmosphere due to the auto-catalytic cycle which it undergoes called the *Chapman cycle* [3]:

$$O_2 + h\nu(\lambda \leq 242nm) \rightarrow O + O \quad (1.1)$$

$$O + O_2 + M \rightarrow O_3 + M \quad (1.2)$$

$$O_3 + h\nu \rightarrow O + O_2 \quad (1.3)$$

$$O + O_3 \rightarrow 2O_2 \quad (1.4)$$

Most of the ozone is located in the stratosphere, between 20 - 40 km, and hence this protective band of ozone molecules has been called the *ozone layer.* Due to the small concentration of ozone even small changes in the atmosphere's chemistry can greatly affect the ozone layer.

It was the work of Molina and Rowland [4] that revealed just how delicate the balance of atmospheric chemistry is with respect to human influence. They discovered that ChloroFluoroCarbons (CFCs) leaked into the atmosphere from human sources can lead to destruction of atmospheric ozone *via* the following mechanism shown for CF_2Cl_2:

$$\begin{aligned} CF_2Cl_2 + h\nu &\rightarrow CF_2Cl + Cl \\ Cl + O_3 &\rightarrow ClO + O_2 \\ ClO + O &\rightarrow Cl + O_2 \\ net \quad O + O_3 &\rightarrow 2O_2 \end{aligned} \quad (1.5)$$

This mechanism along with number of similar cycles involving other halogen containing compounds was shown to be responsible for the so called 'hole

in the ozone layer'. This was a term coined to describe the seasonal declines in the concentration of ozone in particular over the poles. The reduction in the concentration, and in extreme cases complete depletion, increases the quantity of radiation of the wavelength 200 - 310 nm reaching the earth's surface. Excessive exposure to this type of light has been associated with damage of the skin and eyes as well as human skin cancer.

Therefore, an understanding of the photochemistry of all molecules involved has been found to be crucial for the overall understanding of the earth's atmosphere. The study of ozone photochemistry provides essential information for the modelling of atmospheric processes, particularly the production of excited state products of both the diatomic and atomic fragments of ozone photolysis have a number of subsequent effects in the atmosphere. It is the identification of the type of excitation of the products, whether it be electronic, vibrational, rotational or translational, and explaining how these products are formed which is the main subject of this thesis.

1.2 The Present Study

The photolysis of ozone indicated in equation 1.3 which was presented as part of the Chapman cycle is an oversimplification. A more complete representation of the photolysis also includes a step involving the formation of an excited state of the ozone molecule due to a rearrangement of the electronic structure following photon absorption. This excited state then dissociates rapidly to form products in a range of states. Measuring the nascent fragment state distribution provides information which can yield a fundamental understanding of the dissociation process as well as being useful in terms of atmospheric chemistry.

The experimental work performed for this thesis uses two main techniques to identify the fragments. The common initial step is to photolyse ozone

with a pulsed laser and then detect the fragments formed in the photolysis process using a second laser. This laser can be tuned to detect the fragments in an electronically, vibrationally and rotationally selective manner which is characterised by the spectroscopy of the fragments. The second technique involves the manipulation of the ions, formed by ionising the fragments, using electrical fields in such a way that the translational and angular properties of the neutral fragments can be measured. How these techniques are implemented in the laboratory is outlined in Chapter 4.

The information gathered from these experiments can then be used to understand the dissociation dynamics of the ozone molecule as the wavelength of photolysis radiation is varied. The main aim of this thesis is therefore to provide an analysis of the products of UV photolysis of ozone and to use the results of these experiments to understand the fundamental spectroscopy and dynamics of ozone. To this end the first results chapter (Chapter 5) of this thesis describes the analysis of the translational and angular properties of the $O(^3P_0)$ fragments produced from Huggins band photolysis while Chapter 6 concentrates on the identification of the vibrational and rotational states of one of the electronically excited diatomic fragments produced by photolysis in this region. Further results from the detection of both atomic and diatomic fragments from photolysis of ozone at a number of wavelengths within the Huggins bands are presented in Chapter 8 along with a discussion of the dissociation dynamics which could produce these fragments.

The final chapter entails a closer look at the spectroscopic detection system used for detecting the diatomic fragments. The perturbations observed in the presented spectra are related to the structure of the intermediate Rydberg state of O_2 used in the detection method.

References

[1] T. Andrews. *Phil. Trans. Roy. Soc.* **6** (1856) 1.

[2] K. Watanabe. *J. Chem. Phys.* **21** (1953) 1651.

[3] S. Chapman. *Mem. Roy. Meteorol. Soc.* **3** (1930) 103.

[4] M. J. Molina and F. S. Rowland. *Nature* **249** (1974) 810.

Chapter 2

Background Principles

The principle subject of this thesis is the chemistry and physics of a molecule as it dissociates to form fragments following the absorption of a photon. In the case of a triatomic such a so-called 'half-reaction' can be generally represented by equation 2.1:

$$ABC + h\nu \rightarrow ABC^* \rightarrow AB(E_{elec}, E_{vib}, E_{rot}, E_{trans}) + C(E_{elec}, E_{trans}) \tag{2.1}$$

Concealed within this equation is a wealth of information which can be probed by a number of techniques. In the following sections each aspect of this process will be discussed followed by a brief review of the various methods used for measuring each of the quantities associated with the process. The spectroscopy and photodissociation of ozone is then taken as a case study in the following chapter and the research performed to date is reviewed.

2.1 Absorption of a Photon

When light interacts with a molecule some of the electromagnetic energy

of the light can be absorbed and converted into internal (i.e. electronic, vibrational or rotational) energy to form an excited quantum state of the the molecule. In the case of electric dipole mediated transitions, it is the perturbation of the electric dipole of the molecule by the presence of the electric field which induces the transition. This perturbation can be described by $\hat{h}(t)$ of equation 2.2.

$$\hat{h}(t) \; = \; -\hat{\mu} \cdot E_0 \, cos \, (\omega t) \tag{2.2}$$

where $\hat{\mu}$ is the electric dipole moment operator, E_0 is the electric field vector of the light and ω is the frequency of the radiation.

This interaction can be treated by first-order perturbation theory beginning with the time-dependent Schrödinger equation to derive an equation of the general form [1]:

$$\sigma(\omega) \; \propto \; \omega_{fi} \delta(\omega_{fi} \, - \, \omega) \, |\langle F_f | \hat{\mu} \cdot E_0 | F_i \rangle|^2 \tag{2.3}$$

where $\sigma(\omega)$ is the absorption cross-section between the initial state $|F_i\rangle$ and the final state $|F_f\rangle$, ω_{fi} is the energy difference between $|F_i\rangle$ and $|F_f\rangle$ (i.e. E_i - E_f) and $\delta(\omega)$ is the Dirac delta function which is zero unless $\omega_{fi} = \omega$. This condition of a matching of the energy of the photon with the energy difference between the states involved is the resonance condition of absorption. To find the total absorption cross-section the partial cross-sections due to all initial and final states must be summed.

The principal assumption of first order perturbation theory is that the perturbation is weak which holds for all of the experiments described in this thesis which involves the dissociation of molecules by coherent light of a laser. Further assumptions used in the derivation of equation 2.3 are infinitely long light pulses and monochromatic light. If these conditions were imposed with no loss of the initially prepared state, $|F_f\rangle$, the absorption spectrum would consist of lines with positions and widths solely defined by the molecular energies E_i

and E_f. However, in reality it is impossible to achieve such conditions and the lines are broadened by the frequency width of the laser light, thermal motion of the molecules and loss of the excited state by emission or predissociation. The broadening effects of predissociation can be so large that rotational and in some cases even vibrational structure can be lost due to the large linewidths of the individual transitions.

The aspects of photodissociation and predissociation will be discussed in the next section. However, first it is necessary to consider the rules which govern which excited states are accessed by the absorbed photon. In the case of non-linear polyatomic molecules many of the quantum numbers used in deriving the selection rules for atomic and diatomic systems are no longer good quantum numbers. The one surviving quantum number is the total spin angular momentum, S, and the resultant selection rule:

$$\Delta S = 0 \tag{2.4}$$

applies to polyatomic systems as well as to both atomic and diatomic systems. In other words, singlet-singlet ($S = 0 \rightarrow S = 0$) transitions and triplet-triplet ($S = 1 \rightarrow S = 1$) transitions are allowed whereas any change of the spin multiplicity will result in a much weaker transition.

To determine whether a transition between two states is allowed for an electric dipole transition it is necessary to consider the operation of the electric dipole operator shown in equation 2.2. The absorption cross-section varies with the square of the transition dipole moment, μ_{fi}:

$$\mu_{fi} = |\langle F_f|\mu_e|F_i\rangle| \tag{2.5}$$

where μ_e is the component of the transition dipole moment in the direction of the electric field vector. If we ignore the vibration and rotation wavefunctions for the present a selection rule for the transition between electronic states can be determined by examining the symmetry of the electronic

$\Gamma(F_f)$	Transition Moment Alignment	Selection rule
A_1	z	allowed
A_2	-	forbidden
B_1	x	allowed
B_2	y	allowed

Table 2.1.: Electronic selection rules for one-photon transitions in a C_{2v} molecule with a totally symmetric lower state.

wavefunctions. The symmetry requirement for a non-zero transition dipole moment, $\mu_{fi} \neq 0$, is that [2]:

$$\Gamma(F_f) \otimes \Gamma(\mu) \otimes \Gamma(F_i) = A \tag{2.6}$$

where Γ is the symmetry determining function and A represents the totally symmetric representation of the point group. The symmetry of each electronic configuration of the molecule can be determined from the singly occupied molecular orbitals which for the ground state is usually (as in the case of O_3) totally symmetric. Also, the transition moment can be aligned along any axis of the molecule and can therefore be broken into Cartesian co-ordinates so that equation 2.6 reduces to :

$$\begin{aligned} & \Gamma(F_f) \otimes \Gamma(T_x) = A \\ \textit{and/or} \quad & \Gamma(F_f) \otimes \Gamma(T_y) = A \\ \textit{and/or} \quad & \Gamma(F_f) \otimes \Gamma(T_z) = A \end{aligned} \tag{2.7}$$

where $T_{x,y,z}$ are translations along each of the Cartesian axes. Therefore, where the Cartesian axes of ozone are defined as in Figure 2.1 it can be shown using the C_{2v} point group that the selection rules for a one-photon transition shown in Table 2.1 hold.

Inclusion of the vibrational wavefunctions in the consideration of the

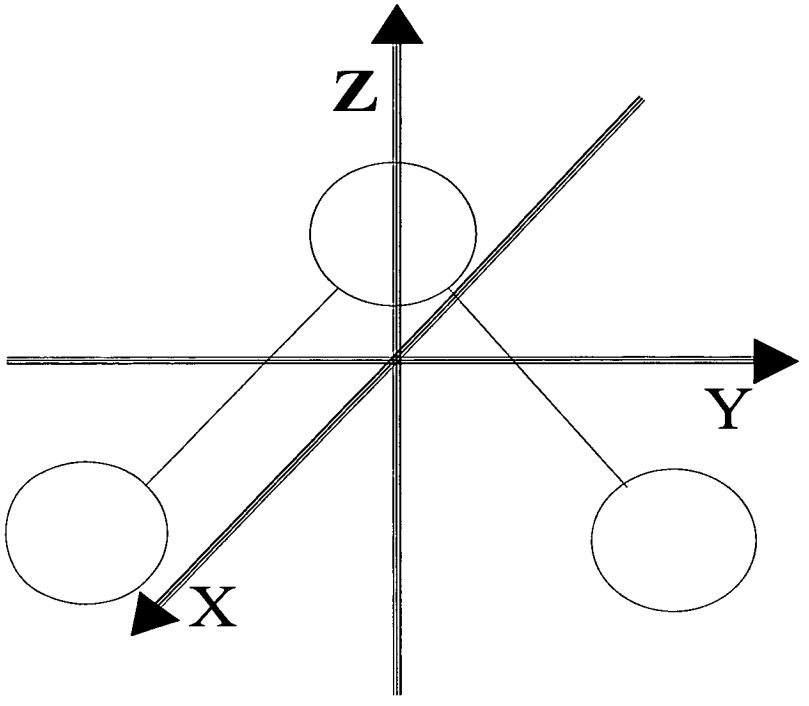

Figure 2.1.: The definition of Cartesian axes of O_3 used in deriving the selection rules shown in Table 2.1.

selection rules results in further complications but can be dealt with in a similar way by examining the symmetry of each vibration. Other selection rules may arise due to the limitation on the electron movements. For example, if two electronic states differ by the occupation of two or more orbitals then the transition intensity between these states will be low and the transition is said to be orbitally forbidden.

2.2 Decay of the Excited States

Having considered how an excited state of a polyatomic molecule can be accessed by the absorption of a photon the question 'What happens to the excited state?' must now be addressed. The excited state can be lost

in numerous ways including the absorption of further photons to ionise the molecule forming the basis of the Resonance Enhanced Multi-Photon Ionisation (REMPI) technique or the emission of a photon and relaxation to a lower energy electronic state, a process which is the essence of Laser Induced Fluorescence (LIF) detection systems. Prior to these processes the molecule can rearrange the energy absorbed from the photon by internal conversion of vibrational and electronic energy to facilitate crossing to another electronic state of the same spin-multiplicity. The excited state may also undergo inter-system crossing which involves a change in the total electron spin angular momentum to allow a change to another electronic state of different spin multiplicity.

The most important loss process in terms of this study however is the dissociation of the molecule to neutral fragments. This process can occur in a number of ways and even the same initially prepared state can dissociate *via* a number of different channels with different probabilities as will be seen in the case of O_3.

2.2.1 Direct Dissociation

This type of dissociation involves excitation to a repulsive electronic state or excitation to a bound state but with enough internal energy to promote the molecule above the dissociation threshold of that state. In these cases the molecule dissociates very rapidly (typically on a femtosecond timescale) to give the neutral fragments. The absorption spectra of such systems are usually featureless due to the nature of the bound-free transition as illustrated schematically in Figure 2.2.

The continuum wavefunction of the upper state exhibits a build up of probability at the classical turning point and as a result the shape of the ground state wavefunction is 'reflected' in the absorption spectrum. This 'Reflection Principle' [1] leads to a broad bell shaped continuum absorption for a one-dimensional repulsive state. However, in the case of multi-dimensional

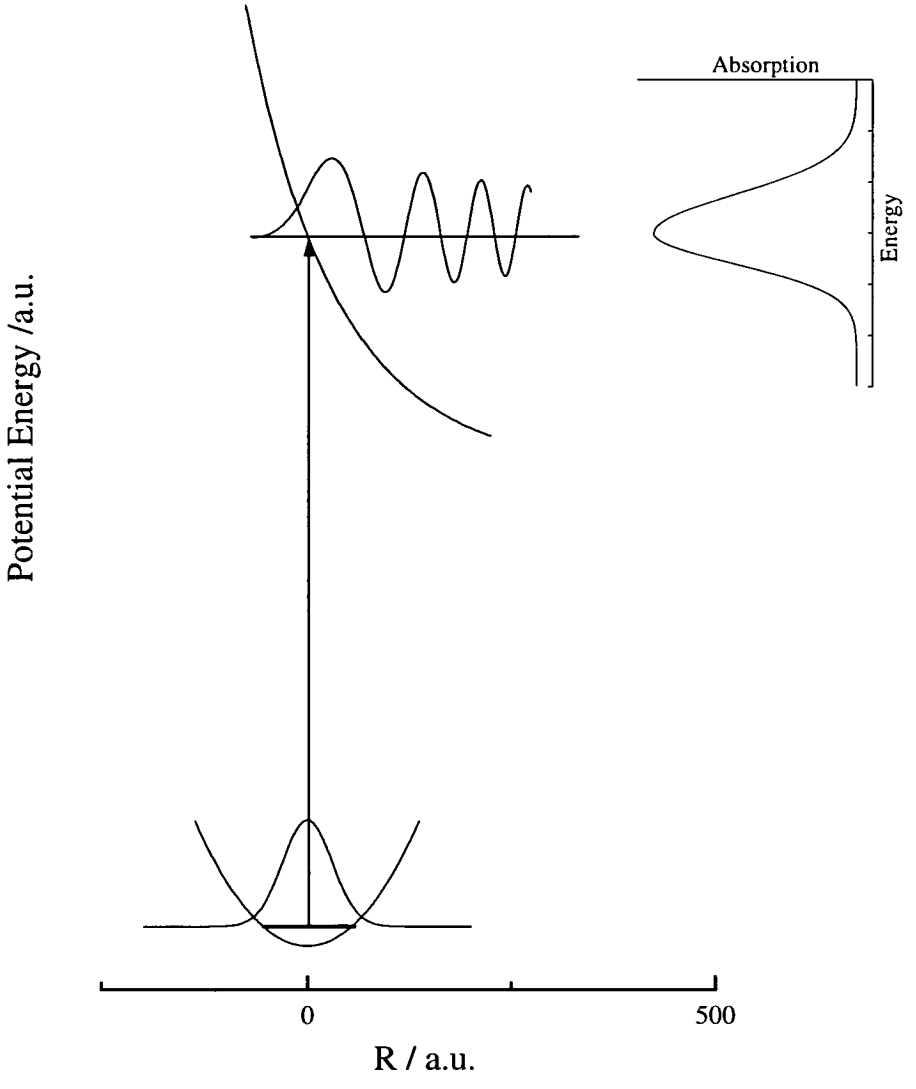

Figure 2.2.: A schematic illustration of the absorption process involving a bound lower state and repulsive upper state. The overlap of the bound wavefunction with the continuum wavefunction gives rise to a featureless continuum absorption.

Potential Energy Surfaces (PESs), where it is possible to have repulsive co-ordinates co-existing with bound co-ordinates of the same surface, some structure in the absorption may be observed. Therefore, combining an analysis of this structure due to the bound regions of the PES with an analysis of the neutral photofragments can yield a great deal of information about the excited state topology as well as the dissociation dynamics of this state.

2.2.2 Predissociation/Indirect Dissociation

Predissociation often plays an important role in the photodissociation of bound states. When a bound excited state is accessed the molecule can be promoted into discrete quantum (rotational/ vibrational) states with a new electronic arrangement. If such states were not subject to loss processes the absorption spectrum as a function of frequency would be controlled only by the energy difference between the discrete lower level state and the discrete upper states and would therefore be a series of very sharp lines. However, in certain situations the discrete upper levels can dissociate by coupling to a dissociative continuum and the lifetime of the upper state is controlled by the strength of this coupling. This mechanism, called 'predissociation' results in a lifetime broadening of the absorption features. If the broadening of the spectral lines is dominated by this mechanism then the Full Width Half Maximum (FWHM) of the absorption feature can be used as a measure of the lifetime of the excited state. The FWHM of the lines is related to the lifetime by the following equation:

$$\kappa = \frac{1}{2\pi c\tau} \tag{2.8}$$

where κ (cm^{-1}) is the FWHM of the Lorentzian component of the lines and τ is the time in which $1/e$ of the molecules in the excited state are predissociated. However, if the predissociation rate is large, individual rotational features may be broadened to such an extent that they are not resolved from the adjacent features and hence the information about the excited state may be lost.

Herzberg classified three types of predissociation under the headings electronic, vibrational and rotational predissociation which are referred to as Herzberg types I, II and III predissociation respectively [3]. The most common of these is the electronic predissociation which involves a coupling between a discrete level of the initially excited electronic state with the dissociative con-

tinuum of a different electronic state. This type of predissociation is illustrated in Figure 2.3 and is labelled by arrow (1). Herzberg II predissociation on the other hand involves a coupling between a discrete vibrational level of the excited state with a continuum on a different region of the same electronic state. An example of this type of predissociation is illustrated by the arrow labelled (2) in Figure 2.3. The initially excited level can access the continuum region either by tunnelling through the potential barrier or, in the case of polyatomics, by internal vibrational relaxation where energy is transfered from other vibrational modes to allow the molecule to overcome the barrier in the dissociative mode.

The final type of predissociation, Herzberg type III, is not very common and involves high rotational levels of a stable vibrational level which couple to a dissociative continuum. This type of predissociation is not illustrated in Figure 2.3. Each of these predissociation types has the effect of decreasing the lifetime of the upper state and causes broadening of the discrete levels of the excited state. Specific examples of the first two types will be revealed in the investigation of the photodissociation dynamics of ozone later in the text.

2.3 Internal Energy, Translational and Angular Properties of Photofragments

2.3.1 Internal Energy Distributions

Considering again the absorption of a photon by a triatomic molecule as shown in equation 2.1, it is useful to examine how the energy of the photon is partitioned both within the excited state and subsequently in the products of dissociation. Most of the energy of the photon is required to break a bond, D_0, in the molecule, however, the fate of the excess energy can be described

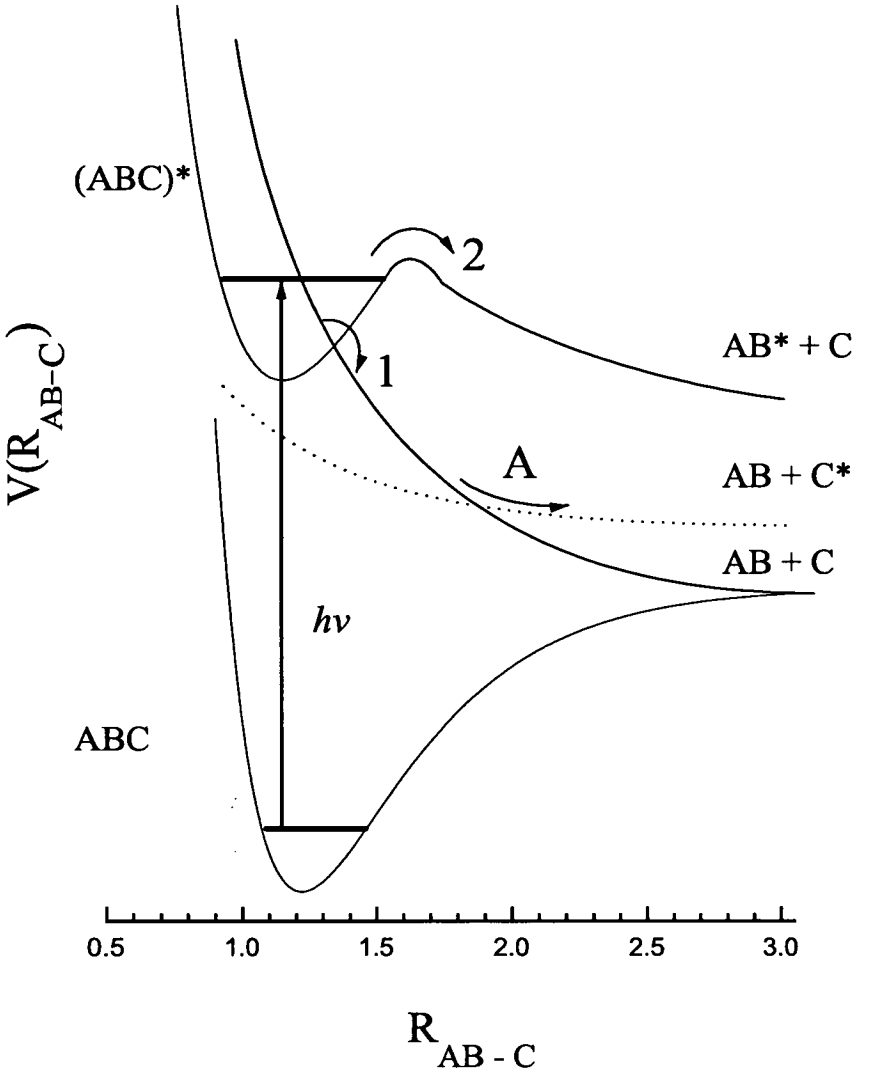

Figure 2.3.: An illustration of the different types of predissociation. The arrow labelled 1 shows electronic predissociation (Herzberg type I) while arrow 2 illustrates vibrational predissociation (Herzberg type II). Arrow *A* shows the effect of possible 'secondary' crossing of the predissociative state on the product state distributions.

in the following way:

$$E_{excess} = h\nu - D_0 = E_{trans} + E_{int} \qquad (a)(2.9)$$

$$where \quad E_{trans} = E_{trans}(AB) + E_{trans}(C) \qquad (b)$$

$$and \quad E_{int} = E_{elec}(AB) + E_{vib}(AB) + E_{rot}(AB) + E_{elec}(C) \qquad (c)$$

The electronic states in which the products are ejected from the molecule can help ascertain whether the initially prepared electronic excited state has

coupled with the dissociative continuum of another state as different electronic states often correlate with different products. As an example of this, it is possible to imagine the situation where the two types of predissociation, 1 and 2, illustrated in Figure 2.3 may occur simultaneously. If the rates of the two predissociation processes are similar, both processes will occur and hence by measuring the relative amounts of AB and AB* the rates of the two processes can be observed. It may even be feasible that a secondary process illustrated by the dotted potential and arrow A may occur giving rise to a third channel where an electronically excited atom C* is produced. However, it is quite difficult to distinguish such a secondary process from the primary ones simply by measuring the quantities of the electronically excited states.

In the example given above the molecule dissociates to give an atom and also a diatomic fragment which may be produced in a range of vibrationally and rotationally excited states. These states can be denoted for simplicity by the quantum numbers v and J respectively, i.e. AB(v, J). The states in which the diatomic fragment is produced can be influenced by a number of factors such as the vibrational and rotational state of the discrete level from which the parent molecule dissociates, the geometry of the dissociating molecule and the general topology of the dissociative surface. Each of these factors will affect the product distribution in different ways and hence the rotational and vibrational distribution of the diatomic photofragments can provide a sort of history of the dynamics of the molecule in the fragment channels.

2.3.2 Translational Energy Distribution of the Fragments

Equation 2.9 (a) describes how the energy of the absorbed photon is distributed by the molecule as it dissociates. The two observables on the right hand side of this equation are E_{trans} and E_{int}. In most cases determining the internal energy distribution of the fragments by spectroscopic means is extremely difficult due to the necessity of having an in depth knowledge of

the electronic structure of the fragments and to avoid overlap between the dissociation wavelengths and the probe wavelengths used for the detection of the fragment. However, if the translational energy of the fragments (in particular the atomic fragment) can be determined the internal energy of all of the co-fragments can be calculated. Assuming that the parent molecule is close to its zero point energy then equation 2.9 (a) can be rearranged using in addition the conservation of momentum to eliminate the velocity of the diatomic fragment to give [4]:

$$E_{int}(AB) = (h\nu - D_0(AB-C)) - \frac{m_C v_C^2}{2}(1+\frac{m_C}{m_{AB}}) \qquad (2.10)$$

where m_C and m_{AB} are the masses of the atomic and diatomic fragments respectively and v_C is the velocity given to the atomic fragment by the dissociation event. Therefore, it is clear that if the v_C can be measured then the internal energy distribution of the diatomic co-fragment can be readily extracted. So for example in the dissociation processes depicted in Figure 2.3 a great deal of information about both channels involving this fragment could be obtained using this technique. The limitations of this method, however, is in the practicable experimental resolution attainable. It is usually not possible to gain the rotational resolution using such an experiment as it is by spectroscopic detection of the diatomic fragment.

2.3.3 Angular Distributions and Vector Correlations of Photofragments

Not only do fragments recoil from the dissociation event with a certain translational energy, they also recoil in a particular direction giving a vector property to the recoiling fragment, $\vec{v}$. This vector can be measured with respect to the electric field vector, $\vec{E}$, of the linearly polarised light which is fixed in the laboratory frame and thus a lab frame velocity distribution of the fragments

can be determined.

To see how absorbing molecules are aligned with respect to $\vec{E}$, the interaction of the electromagnetic light with a molecule must again be examined. In section 2.3 it was seen that the treatment of first order perturbation theory showed that absorption depends on the projection of $\vec{E}$ on to $\vec{\mu_{fi}}$ as follows:

$$\begin{aligned} \sigma(\omega) &\propto |\vec{\mu_{fi}} \cdot \vec{E}|^2 \\ &\propto \mu_{fi}^2 E^2 cos^2\gamma \end{aligned} \tag{2.11}$$

where γ is the angle between $\vec{\mu_{fi}}$ and $\vec{E}$. So the alignment of the transition dipole moment with $\vec{E}$ is a $\cos^2$ distribution.

The lab frame fragment recoil vector distribution needs, however, to be related to this centre of mass frame angular distribution of the transition dipole moment and therefore the relationship between $\vec{E}$ and $\vec{v}$ can be stated. This is achieved by averaging the square of the projection of $\vec{E}$ onto $\vec{\mu_{fi}}$ and incorporating an anisotropy parameter, β, for the relationship between $\vec{\mu_{fi}}$ and $\vec{v}$ to give the well known equation first reported by Zare [5]:

$$P(v,\theta) = \frac{f(v)}{4\pi v^2}[1 + \beta(v)P_2(cos\theta)] \tag{2.12}$$

where $f(v)$ is the photofragment speed distribution, θ is the angle between $\vec{E}$ and $\vec{v}$ and P_2 is the second Legendre polynomial ($P_2(x) = \frac{1}{2}(3x^2 - 1)$). $\beta(v)$ is the speed dependent anisotropy parameter which describes the distribution of $\vec{v}$ with respect to $\vec{\mu_{fi}}$ which is a function of the angle, χ, between these two vectors.

Before proceeding with the discussion of the angular properties of polyatomic molecule dissociation it is useful to first describe the anisotropy of fragments formed from the photolysis of a diatomic molecule because of the simplifications involved. For pure transitions in a diatomic molecule followed by rapid dissociation, the β parameter attains limiting values of + 2 and - 1 which correspond to $\cos^2$ and $\sin^2$ distributions respectively. The first case

arises from a parallel transition, so called because $\vec{\mu_{fi}}$ is aligned along the internuclear axis of the diatomic, i.e. $\gamma = 0$. The axial recoil approximation dictates that the fragments recoil along the breaking bond and hence $\vec{v}$ is aligned with $\vec{\mu_{fi}}$. This type of transition occurs when the projection of the total angular momentum onto the internuclear axis does not change on going from the initial to the final state, $\Delta\Omega = 0$. Conversely, a perpendicular transition is one where the $\vec{\mu_{fi}}$ is perpendicular to the internuclear axis, for $\Delta\Omega = \pm 1$.

In reality most transitions do not adhere to these limiting cases due to the following points:

(i) The molecule may rotate in the time scale of dissociation and so the anisotropy of the the dissociation process is reduced as the alignment of $\vec{v}$ by $\vec{E}$ is lost. The reduction of anisotropy by this mechanism can be modelled using the classically derived relationship [6]:

$$\beta_{eff} = \beta\left[\frac{1 + \omega^2\tau^2}{1 + 4\omega^2\tau^2}\right] \tag{2.13}$$

where β is the anisotropy due to the $\vec{E}$ - $\vec{\mu_{fi}}$ correlation, ω is the frequency of rotation of the parent molecule and τ is the lifetime of the dissociative state. β_{eff} is then the *effective* anisotropy which is reduced from the 'true' value by rotation. This classical expression was found to approximate very well to the fully quantal approach which revealed that the classical expression only breaks down in the limit of low rotational angular momentum [7].

(ii) If the axial recoil approximation breaks down, i.e. if $\vec{v}$ is not parallel to the internuclear axis then equation 2.12 is not valid. Such a situation may occur when rotation of the parent molecule is large in comparison to the speed of recoil of the fragments formed.

(iii) The transition may not be pure perpendicular or parallel in nature due to the mixing of the upper state with other states in the region to gain transition intensity and hence the most probable value of the angle, χ, between $\vec{\mu_{fi}}$ and $\vec{v}$ is neither 0 ° nor 90 °. This gives rise to an intermediate value of β.

However, if the first two points can be excluded, then the observed value of β can be used as a measure of this mixing [8].

The situation of photodissociation of a bent triatomic is complicated by the less rigorous relationship between $\vec{v}$ and $\vec{E}$ [9] as indicated in the example shown in Figure 2.4. This illustrates the relationship between $\vec{E}$, $\vec{\mu_{fi}}$ and $\vec{v}$ for a b_2 transition. Excluding other reductions of the anisotropy mentioned above the anisotropy parameter can be related to the angle of the triatomic as it dissociates by the equation:

$$\beta = 2P_2\left(cos(90 - \frac{\alpha}{2})\right) \tag{2.14}$$

Therefore, for an instantaneous dissociation involving an unmixed electronic transition where the recoil vector is directed along the breaking bond, the β parameter can be used to investigate the geometry of the molecule as it dissociates. However, a number of the mentioned mechanisms for the reduction of the anisotropy may be operating simultaneously and hence more than one of the above analyses may be required.

Due to the rotation of fragments resulting from the photodissociation of polyatomics further vector correlations must be considered which do not arise for diatomic dissociation. Among these the $\vec{E}$ - $\vec{\mu_{fi}}$ - J and $\vec{v}$ - J correlations were described in detail by Houston [10]. The first of these correlations is quite similar to the $\vec{E}$ - $\vec{\mu_{fi}}$ - $\vec{v}$ correlation described above and in the case of dissociation of a bent triatomic molecule arises due to alignment of the rotational angular momentum vector, J, of the diatomic fragment with respect to $\vec{E}$. As this vector correlation relates a lab frame vector to a centre of mass frame vector transformation the anisotropy of the process can be affected by all of the points outlined above. However, in the case of a pure parallel transition in a triatomic dissociation where all losses of the anisotropy are negligible the J vector is aligned preferentially in the perpendicular plane to the $\vec{E}$ of the dissociating light.

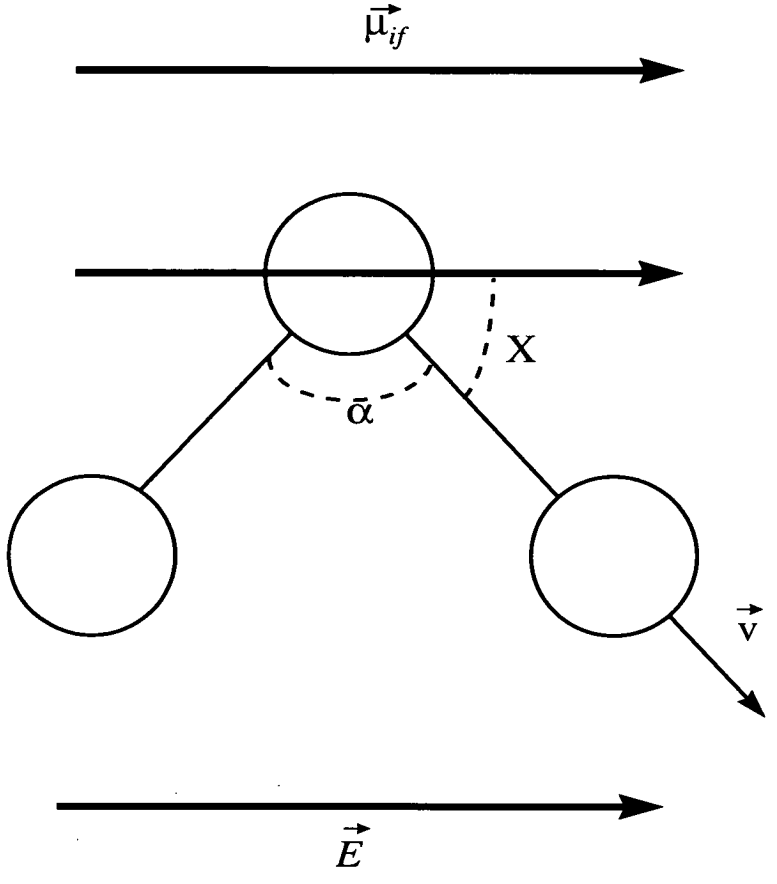

Figure 2.4.: The alignment of the transition moment for a one-photon transition of b_2 symmetry.

The $\vec{v}$ - J correlation is slightly different as it is completely independent of the lab frame and therefore cannot be 'washed out' due to rotation. This correlation is trivial in the case of triatomic dissociation as $\vec{v}$ is always perpendicular to J. The effect of this correlation was observed by Suits *et al.* [11] in their detection of the O_2 ($a\ ^1\Delta_g$) fragments from O_3 photolysis.

2.4 Measurements of Photofragment Properties

The experimental investigation of photodissociation dynamics has blossomed in recent years mainly due to the advent of pulsed lasers and molecular beam systems. As a result there are a wide range of methods available to probe each property of the fragments and parent molecule discussed in the previous sections and hence in this work it is only possible to describe the principles of the experimental techniques used in gathering the results for this thesis. Other methods may be mentioned briefly for the purpose of comparison but will not be discussed in depth.

2.4.1 State Selective Detection of Photofragments

As stated previously the fragments formed by photodissociation of a polyatomic molecule may be produced in a range of electronic, vibrational and rotational quantum states and therefore it is necessary to be able to selectively detect these fragments in order to gain information about the dynamics of the process. This can be achieved using REMPI which allows individual quantum states to be probed due to the wavelength specific resonantly enhanced ionisation of these states. A typical scheme of such a method involves the simultaneous absorption of two photons from a light pulse to access a high lying electronic state of the fragment followed by one more photon to reach the ion state in what is commonly abbreviated to a (2 + 1) REMPI process. The ions can then be manipulated by electric fields and detected in a mass specific manner which will be described in chapter 4.

The state selectivity arises because each quantum state will only absorb when a resonance occurs between the energy difference between the nascent state of the fragment and a high lying excited state with the energy of the

input photons. Thus, as the frequency of the laser light is tuned different quantum states will be ionised and hence detected. Of course, another laser is required to select the dissociation (pump) frequency for the parent molecule, the energy of which should be different from that of the probe process. A schematic figure illustrating each of these points is shown in Figure 2.5.

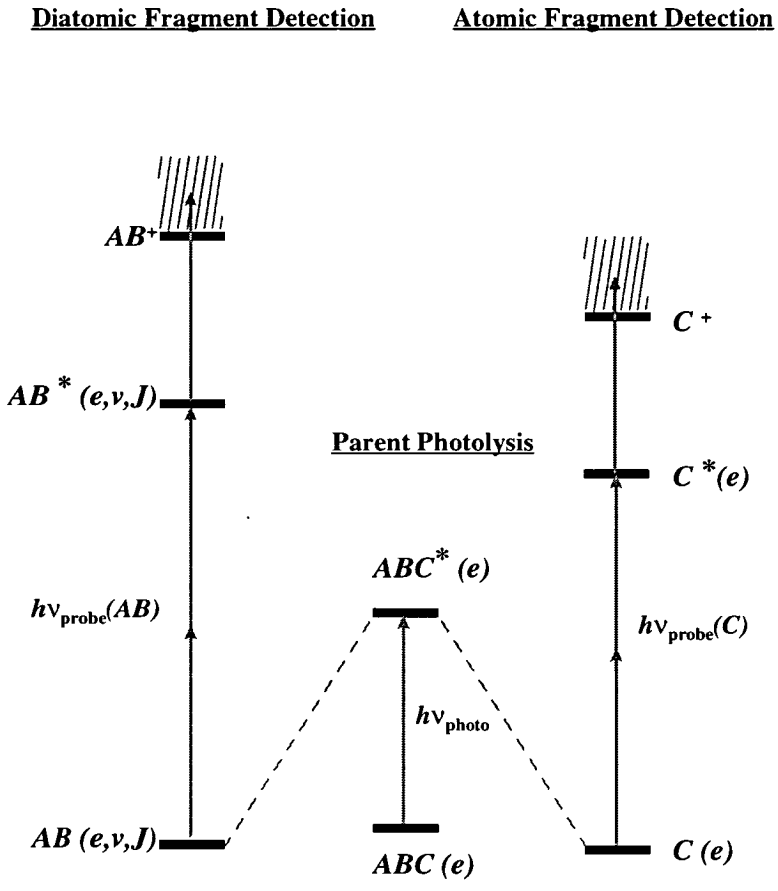

Figure 2.5.: An illustration of the pump and REMPI probe techniques used to investigate the fragment state distributions from triatomic photodissociation.

In theory it should be possible to scan the probe laser over all of the energies required to detect all quantum states of both products. There are, however, a number of practical problem with this method of extracting nascent quantum state distributions:

(i) If the dissociating photon energy is largely in excess of the dissociation energy of the molecule the energy of the quantum states of the fragments may range over as much as 2 - 3 eV which would involve scanning the probe laser in a 150 nm range using visible light for a two-photon transition to a common upper state. This type of experiment is often impractical as the parent molecule may absorb also in this region and cause very complicated spectra. An example of this problem is seen later in the thesis.

(ii) Also, due to the selection rules of multiphoton transitions the nascent fragments may be in different electronic states which will have allowed transition to a number of different upper states. As a result of the large number of resonances caused the REMPI spectra can be very dense making a full analysis very difficult.

(iii) The upper state energy region usually accessed in REMPI techniques often has a number of states in the same energy region. The resulting mixing of the resonant state with possible 'dark' states in the same energy region causes perturbations of the spectra which add to the task of analysing the spectra.

In spite of all of these limitations and difficulties it is still possible to identify features in the REMPI spectra due to the various quantum states of the fragments. Much of Chapter 6 deals with describing the analysis of these spectra to identify the diatomic product states produced in the UV photodissocitaion of ozone.

One extremely useful method associated with the REMPI detection of fragments is the ability to record PHotoFragment EXcitation (PHOFEX) spectra of the parent molecule. Once a suitable probe frequency is selected so that the identity of the detected fragment is known, the dissociation (pump) laser can then be scanned to monitor the quantum yield of that fragment as a function of the dissociation frequency. If the fragment produced is the sole

atomic or diatomic fragment produced in the photodissociation process, the PHOFEX spectrum produced should correspond to the absorption spectrum of the molecule. This is due to the fact that as a resonance in the parent molecule is encountered the quantum yield of the fragmentation process increases proportionately. In this process care must be taken that excited parent molecules are not lost to other processes such as a multiphoton absorption by the parent or a short radiative lifetime. The first of these can be minimised by using low pump laser powers and the second is negligible in the case of rapidly dissociating molecules where this technique is commonly used.

In reality, of course, more than one quantum state of the atomic and diatomic fragment is produced and hence only the absorption features which give rise to that fragment will be observed in the PHOFEX spectrum. The obvious choice of fragment for this method is the atomic fragment as no vibrational or rotational states can be produced and hence a limited number of quantum states are accessed depending only on the energy spacing of the states of the atom involved. The absorption can thus be broken down into the components which produce a particular electronic state of the atomic fragment upon dissociation. This can also be useful for gaining information about the product channels of dissociation.

If the absorption spectrum is reproduced well by detecting the dominant fragment using this PHOFEX technique it may be a very useful method to record a low temperature absorption spectrum of the parent. As the PHOFEX technique is used to analyse rotationally cold parent molecules due to their expansion in a molecular beam (described in detail in Chapter 4), the PHOFEX spectra produced remove a great deal of the spectral congestion of higher temperature absorption data. The resulting spectra may be easier to interpret than the rotationally congested higher temperature absorptions.

2.4.2 Measurements of Translational and Angular Properties of the Fragments

The advantages of knowing the translational and angular distributions of fragments has been demonstrated in the previous section and as a result a wide range of experimental techniques have been developed to measure these quantities. The method used in this thesis involves the REMPI state selective technique described above, combined with a delayed pulsed field extraction technique and Time-of-Flight (TOF) analysis.

In TOF mass spectrometry the ions created by the pump and probe laser pulses are extracted from the molecular beam/ light interaction region as soon as they are formed by a dc electric field. The ions then separate in the field free TOF region solely due to the difference in their masses so that ions of different masses can be selectively detected. The delayed pulsed field extraction technique on the other hand allows the ions to recoil under the velocities imparted to them by the dissociation event prior to extraction. In this way an ion packet of macroscopic proportions can be produced. When the pulsed electric field is then applied the ions experience an acceleration which is related to their position within the extraction region. This process is illustrated schematically in Figure 2.6 for a process with a single recoil velocity.

As is clear from this schematic, the ions closest to the repeller electrode, which has a high positive voltage, spend longer in the extraction field and thus acquire a higher velocity than those far that from this electrode. The result is an extended TOF profile. The ions which arrive at the detector first correspond to those which initially recoiled away from the detector while the later peak is due to those ions which initially recoiled towards the detector. The forces experienced by the ions in the extraction region can be modelled by the simple equations of motion and electrostatics and thus the time of arrival can be related to the position of those ions in the extraction region when

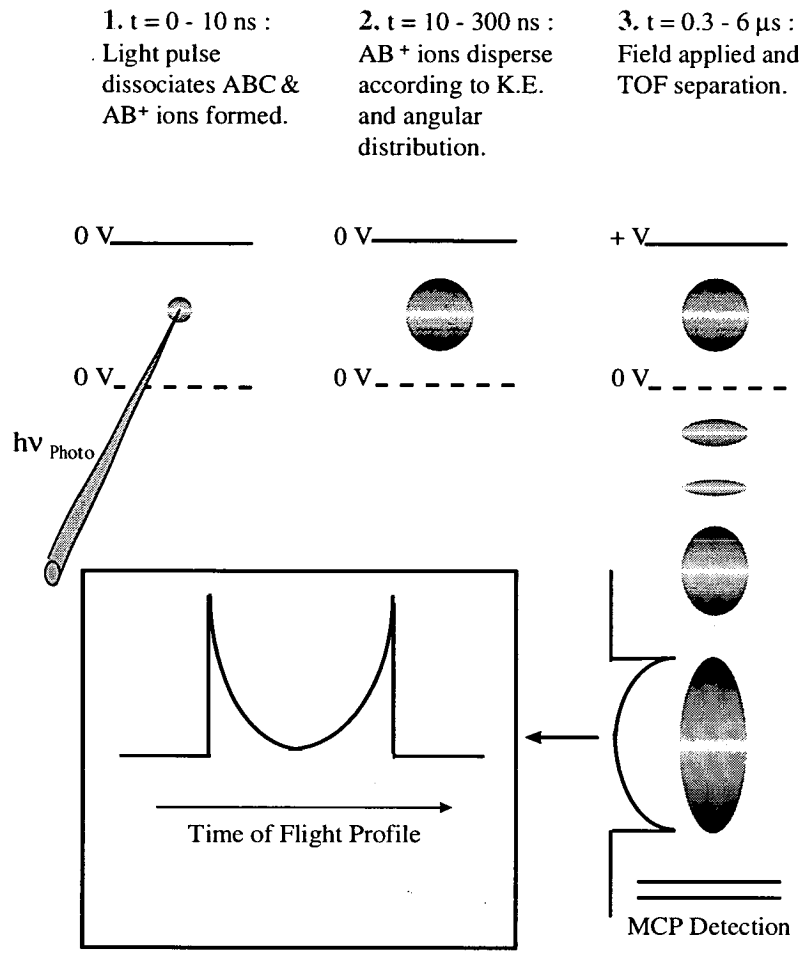

Figure 2.6.: A schematic illustration of how the photofragments separate due to their translational and angular properties during the delayed pulsed field extraction technique. This is related to the Time-of-Flight profile in the final section.

the electric field is applied and thus to the recoil velocity of these fragments along the direction of the time of flight axis. The velocity profile can be studied as a function of dissociation laser polarisation, yielding information about the alignment of $\vec{\mu_{fi}}$ relative to $\vec{E}$. Mons and Dimicoli [12] were the first to report this technique during their work on NO_2. However, since then many groups have employed this technique [13, 14, 15, 16, 17] to investigate the photodissociation dynamics of a range of molecules.

The main drawback of this process is that it involves the projection of

a three-dimensional ion packet onto a one-dimensional TOF axis. The result is that only the velocity component of the ions along the direction of the TOF axis can be measured. The angular information of the ion packet is thus convoluted with the velocities of the fragments. Ideally, it would be useful to separate these two properties so that they could be measured individually and in fact, this can be achieved by a method called core-extraction [15, 17] where only the ions recoiling along the TOF axis are detected. The effect of this method can be visualised by examination of the schematic shown in Figure 2.7.

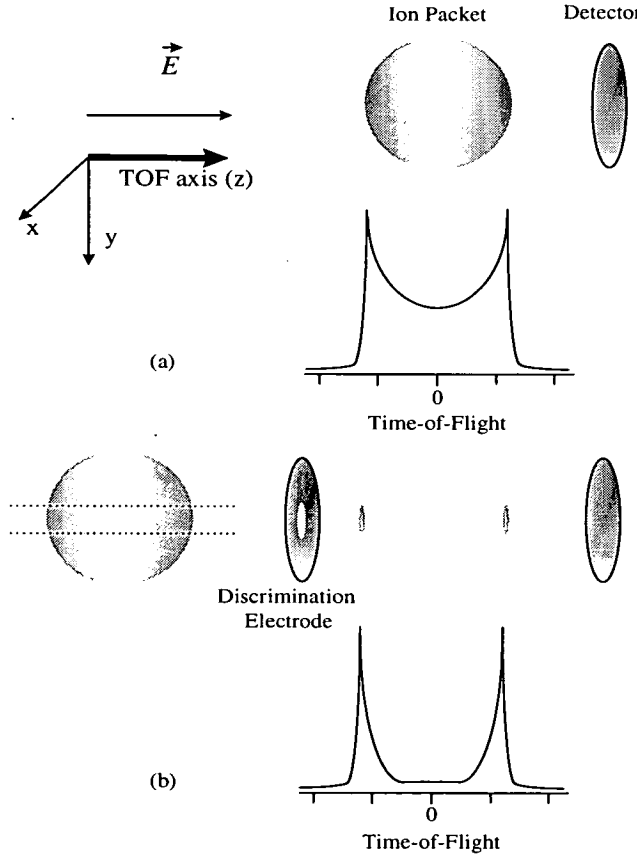

Figure 2.7.: A comparison of the TOF profile of the full ion packet with that of the core-extracted ion packet.

Part (a) of this figure illustrates the detection of a fragment ion packet produced by a parallel transition in the parent molecule such that the fragments recoil in a $\cos^2$ distribution about $\vec{E}$ and hence about the TOF axis, z. If no core-extraction is applied all fragments are detected and hence both the speed distribution and the $\cos^2$ angular distribution are projected onto the TOF axis. In part (b) the effect of the discrimination electrode is illustrated where it can be seen that any fragments with a significant velocity component orthogonal to the TOF axis (significant v_{xy}) are not detected. As the fragments which are detected are again projected onto the TOF axis only the v_z component of the fragments is measured in the TOF profile. However, since the v_{xy} component of these core-extracted fragments is small, $v_z \approx v$ and so the speed distribution of the fragments is measured.

How this process is achieved in practice will be addressed in the following chapter which describes the experimental apparatus used. The main advantage of this technique is that the angular information is deconvoluted from the speed distribution and thus when the TOF equations for the core-extracted profiles are solved the lab frame velocity of the fragments is yielded. This can then be related to the centre of mass frame using the $\vec{E}$ - $\vec{\mu_{fi}}$ - $\vec{v}$ correlation.

However, the angular information is also quite useful and therefore it is desirable to be able to measure this also. In the case of one-photon dissociation the angular information is described by equation 2.12 and so the anisotropy of the ion packet can be reconstructed by recording two core-extracted profiles which sample the complete ion packet in two different ways so that the $\cos^2$ or $\sin^2$ distribution can be calculated. This can be achieved by changing the geometry of the linearly polarised dissociating light from being parallel with the TOF axis to a perpendicular geometry. When the resulting ion packet is core-extracted the intensities of the early and late peaks (see Figure 2.7) represent the quantity of fragments recoiling parallel to $\vec{E}$ and perpendicular to $\vec{E}$ respectively and so the angular anisotropy of the process can be reconstructed

using the formula of Syage [17]:

$$\beta = \frac{I_0 - I_{90}}{\frac{1}{2}I_0 + I_{90}} \tag{2.15}$$

where I_0 is the intensity of peaks in the parallel $\vec{E}$ geometry and I_{90} is the intensity in the perpendicular $\vec{E}$ geometry.

Measurement of the photofragment angular distributions from photodissociation which is no longer accurately described by equation 2.12 requires a more sophisticated technique to measure the distribution. In order to describe the types of effects which can be observed it is useful to describe some techniques which were not used in the course of the research for this thesis. The advantage of these *'2 - D'* techniques over the *'1 - D'* method used here is that both angular and translational properties of the dissociation process can be measured in a single experiment. An early example of this type of experiment is called ion imaging [18] which utilises a position sensitive detector and space focusing condition of the extraction ion optics. This technique is illustrated schematically in Figure 2.8 which shows how the three dimensional ion packet is focussed onto the two dimensional detector surface. The resulting two-dimensional image can then be converted back to the three dimensional 3-D fragment distribution using an inverse Abel transformation and the relation between the position and detected ion on the detector can be used to work out the velocity of the photofragments.

Recent advances of this general technique have involved a velocity mapping [19] procedure which uses the ion optics to expand the image and removes the blurring effect of the ion optic grids. Most recently, an ion-counting method [20] has been reported for image analysis to increase the image resolution and hence the velocity resolution of these techniques. The overall ion-imaging/velocity methods are mentioned to enable an illustrative comparison later in the thesis of this technique with the one-dimensional technique used to record the results of this thesis.

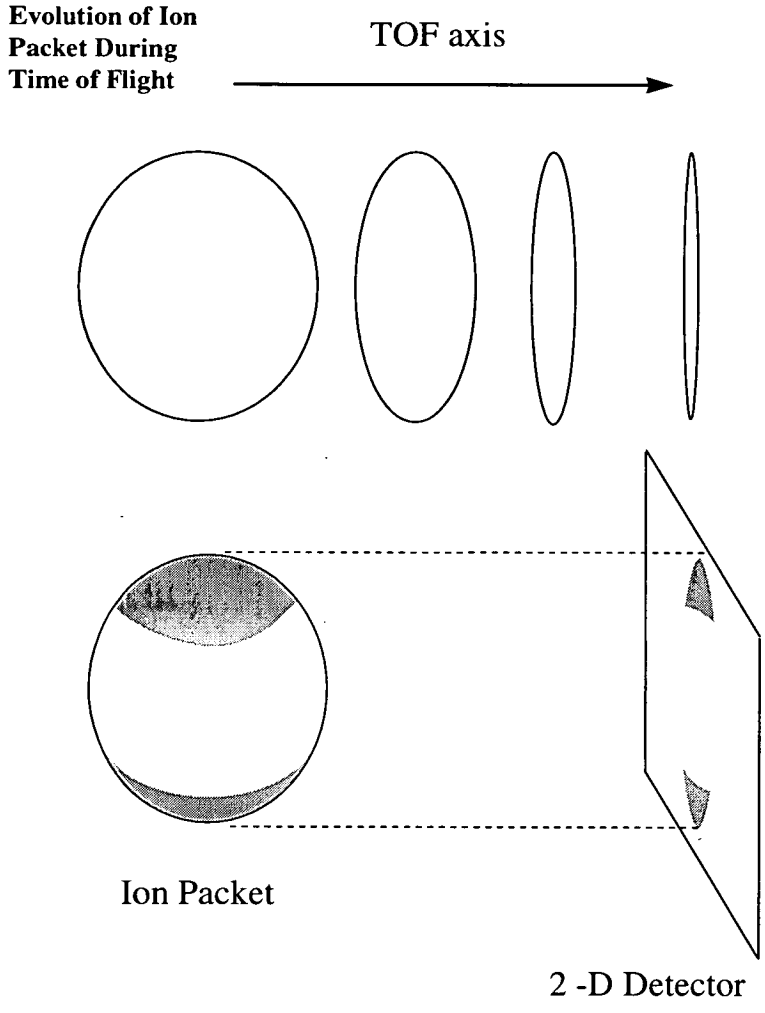

Figure 2.8.: A schematic illustration of how the three-dimensional ion packet is focussed onto a two-dimensional position sensitive detector during the ion-imaging technique.

References

[1] R. Schinke. *Photodissociation Dynamics, Cambridge monographs on atomic molecular and chemical physics*, (Cambridge University Press, U. K., 1993).

[2] J. M. Hollas. *Modern Spectroscopy*, (John Wiley and Sons, 1988).

[3] G. Herzberg. *Molecular Spectra and Molecular Structure III, Spectra of Polyatomic Molecules*, (Van Nostrand, New York, 1967).

[4] A. Orr-Ewing. *Second Summer School on Trends in Molecular Physics: Presentation Notes* (1998).

[5] R. N. Zare. *Mol. Photochem.* **4** (1974) 1.

[6] C. Jonah. *J. Chem. Phys.* **55** (1971) 1915.

[7] E. R. Wouters. *PhD Thesis, Amsterdam.* (1996).

[8] B. Buijsse, W. J. van der Zande, A. T. J. B. Eppink, D. H. Parker, B. R. Lewis and S. T. Gibson, *J. Chem. Phys.* **108** (1998) 7229.

[9] G. E. Busch and K. R. Wilson. *J. Chem. Phys.* **56** (1972) 3638.

[10] P. L. Houston. *J. Phys. Chem.* **91** (1987) 5388.

[11] A. G. Suits, R. L. Miller, L. S. Bontuyan and P. L. Houston. *J. Chem. Soc. Faraday Trans.* **89** (1993) 1443.

[12] M. Mons and I. Dimicoli. *Chem. Phys. Lett.* **131** (1986) 298.

[13] R. Ogorzalek Loo, H. -P. Haerri, G. E. Hall and P. L. Houston. *J. Chem. Phys.* **90** (1989) 4222.

[14] T. Kinugawa, T. Sato, T. Arikawa, Y. Matsumi and M. Kawasaki. *J. Chem. Phys.* **93** (1990) 3289.

[15] H. J. Hwang, J. Griffiths and M. A. El-Sayed. *Int. J. Mass Spec. and Ion Proc.* **131** (1994) 265.

[16] J. Cao, Y. Wang and C. X. W. Qian. *J. Chem. Phys* **103** (1995) 9653.

[17] J. A. Syage. *J. Chem. Phys.* **105** (1996) 1007.

[18] D. W. Chandler and P. L. Houston. *J. Chem. Phys.* **87** (1987) 1445.

[19] A. T. J. B. Eppink and D. H. Parker. *Rev. Sci. Instum.* **68** (1997) 3477.

[20] B. -Y. Chang, R. C. Hoetzein, J. A. Mueller, J. D. Geiser and P. L. Houston. *Rev. Sci. Instum.* **69** (1998) 1665.

Chapter 3

Review of the Spectroscopy & Dissociation Dynamics of Ozone

As noted in the first chapter it is the UV absorption and subsequent dissociation dynamics of ozone which has captured the most attention due to its importance in the absorption of harmful UV solar radiation. However, to fully appreciate the electronic structure of ozone in this energy region it is first necessary to examine briefly both the ground state electronic structure and the low energy excited states.

3.1 Ozone Ground Electronic State and Low Energy Excited States

Ozone belongs to the C_{2v} point group in its equilibrium ground state geometry which involves a bond angle of 116.8° and bond lengths of 1.278 Å [1]. It is unusual in that it is a spin-paired biradical, i.e. its ground state configuration cannot be represented by a single configuration. The constituent ground state electronic configurations are shown below and the molecular or-

bital representation of the Highest Occupied Molecular Orbitals (HOMOs) and Lowest Unoccupied Molecular Orbitals (LUMOs) are shown schematically in Figure 3.1 [2].

$$\begin{aligned} &\textit{leading configuration } (81\%) \\ &\qquad core + \quad (5a_1)^2(3b_2)^2(1b_1)^2(6a_1)^2(4b_2)^2(1a_2)^2(2b_1)^0 \\ &\textit{Next largest contribution } (8\%) \\ &\qquad core + \quad (5a_1)^2(3b_2)^2(1b_1)^2(6a_1)^2(4b_2)^2(1a_2)^0(2b_1)^2 \end{aligned} \tag{3.1}$$

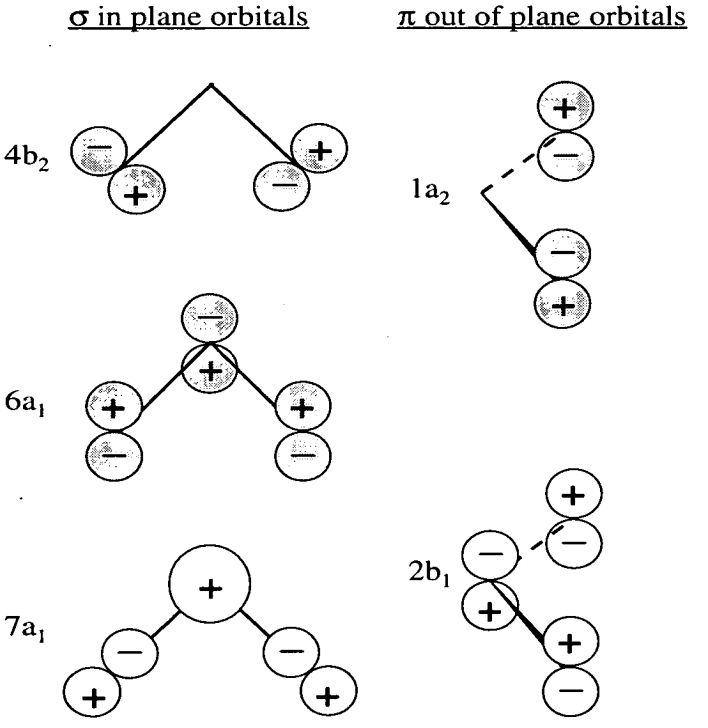

Figure 3.1.: The Highest Occupied Molecular Orbitals (HOMOs) are shown with grey shading while the Lowest Unoccupied Molecular Orbitals (LUMOs) are the remaining orbitals illustrated.

The biradical nature of ground state ozone leads to the existence of a number of low lying electronically excited states which involve transitions into the $2b_1$ orbital which can be seen to be a π^* orbital from Figure 3.1. A further

consequence of the biradical form of the ozone ground state is that theoretical studies of transition strengths become notoriously difficult due to the necessity of including the major ground state configurations in all calculations [3].

Another complicating factor in the description of transitions to excited states of ozone is that the asymmetric stretch destroys the C_{2v} symmetry and so it is often necessary to discuss the orbitals and excited states in terms of a C_S geometry description. To facilitate converting between C_{2v} and C_S notation a correlation diagram is shown in Figure 3.2. Also shown on this diagram are the approximate vertical transition energies and the thermodynamic energies of the dissociation channels involved.

This diagram also serves as a useful summary of the excited states of ozone involved in its absorption spectrum from the near infrared (IR) to the UV region including the Wulf, Chappuis, Huggins and Hartley band systems. The discussion of the UV absorption and dynamics is reserved for its own section as these are the principal subjects of research for this thesis.

However, it is also useful to include a very brief discussion of the lower energy absorption systems to provide the background information for the central study. Absorptions to the three low lying triplet meta-stable states of ozone between 600 - 1100 nm are traditionally grouped together to form the band system known as the Wulf bands. Originally, the very weak discrete absorption structure, which is 9 orders of magnitude less intense than the Hartley bands were thought to be due to a progression of $^1A_2$ (0,ν_2', 1) $\leftarrow$ $X\,^1A_1$ (0,0,0) cold bands and $^1A_2$ (0,ν_2', 1) $\leftarrow$ $X\,^1A_1$ (0,0,1) hot bands [5]. However, the rotationally resolved absorption spectra and rotational analysis by Minaev and Årgen [6] and Bouvier *et al.* [7] showed that the major component of these bands was in fact due to the $^3A_2 \leftarrow X\,^1A_1$ and $^3B_1 \leftarrow X\,^1A_1$ with the possibility of the $^3B_2 \leftarrow X\,^1A_1$ transition contributing to some of the higher energy bands in the region.

The Chappuis band system between 400 - 650 nm consists of what appears to be an irregular vibrational progression superimposed on a continuum

absorption feature [8]. The largest contribution to this band system involves the absorption into the bound $1\ ^1B_1$ state which correlates with the excited $O(^1D) + O_2\ (a\ ^1\Delta_g)$ products. It is clear from Figure 3.2 that the transition energies involved in the Chappuis bands are not sufficient to allow this state to dissociate *via* this channel and therefore it might be expected that this system would exhibit long excited state lifetimes and possibly spontaneous emission. The fact that no spontaneous emission has been observed following Chappuis band excitation can be explained by considering interactions of the initially excited state with the energetically close lying $1\ ^1A_2$ state.

Unlike the $1\ ^1B_1$ surface, the $1\ ^1A_2$ state is not bound and correlates with the ground state products. Also, the $1\ ^1A_2 \leftarrow X\ ^1A_1$ transition is symmetry forbidden (see Table 2.1 of the previous chapter) but can become vibronically allowed *via* coupling with the ν_3, asymmetric stretch of the $1\ ^1B_1$ state. Therefore, the direct absorption onto the repulsive $1\ ^1A_2$ surface results in the dissociation within one vibrational period and provides a continuum background absorption to the Chappuis bands. This still does not explain why the molecules excited to the $1\ ^1B_1$ state are short-lived. To provide the reasoning for this experimental observation it is necessary to consider what happens to these two states when they are distorted from C_{2v} to C_S geometry. The correlation diagram shown in Figure 3.2 shows that the reduction of symmetry of the systems results in both of these states having $^1A''$ symmetry in the lower symmetry designation. An avoided crossing occurs between these two state in C_S symmetry while the states are allowed to cross in C_{2v} symmetry, and so a conical intersection is formed with the crossing occurring at a bond angle of 120° and at a range of bond lengths [9, 10]. As a result the bound vibrational levels initially excited on the $^1B_1$ surface 'leak' through the conical intersection on to the lower surface and hence dissociate to the observed ground state fragments [9, 10].

While this general picture provides a good explanation of the overall absorption structure in this region, the details of the $1\ ^1B_1 \leftarrow X\ ^1A_1$ vibrational

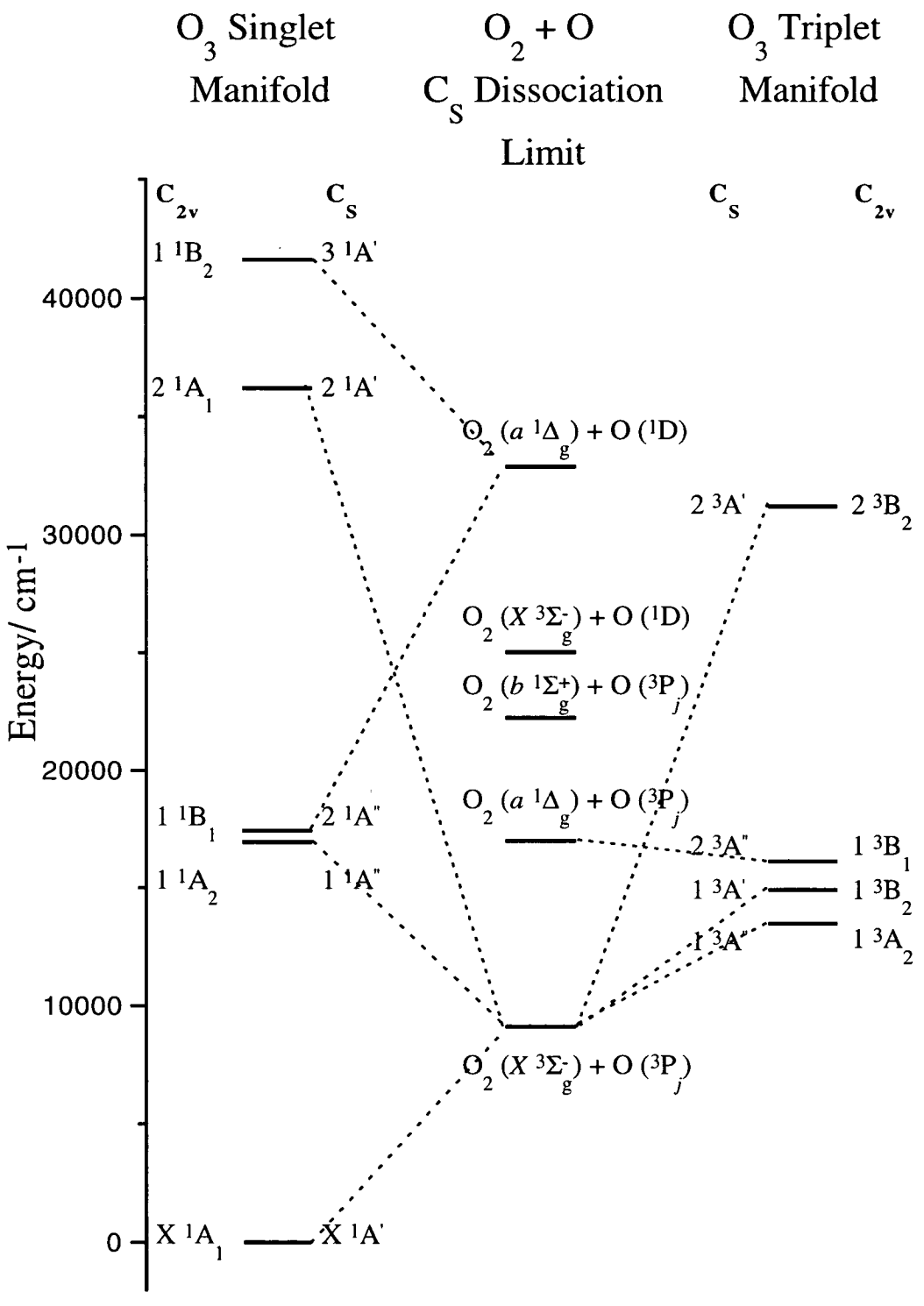

Figure 3.2.: The calculated vertical transition energies of the lowest singlet and triplet states are shown where the energies were taken from ref [4]. Also shown are the C_{2v} and C_S notations for all of the states as well as the C_S dissociation limit to which each of them correlates in the adiabatic representation of the states. It should be noted that the $2\ ^1A_1$ ($2\ ^1A'$ state correlates with the $O(^1D)$ + O_2 ($a\ ^1\Delta_g$) limit in the diabatic view but due to a strongly avoided crossing with a repulsive state of the same symmetry the adiabatic correlation of this state is as shown.

assignment is still a subject of dispute. In fact, Anderson and Mauersberger [8] note that none of the five vibrational assignment which have been proposed by various sources appear to satisfy all of the experimental observations. Also, due to the overlap of the Wulf and Chappuis absorption systems, Braunstein and Pack [9] noted that it was necessary to include some contribution of the excited states involved in the Wulf bands to the absorption to provide the complete description of the Chappuis absorption.

3.2 The Ultra-Violet Absorption and Excited States

The ultra-violet absorption of ozone ranges over the 200 - 360 nm energy region and consists of the two absorption systems: the Hartley and Huggins bands. In this energy region a number of dissociation channels become accessible (see Figure 3.2) hence complicating the dissociation dynamics significantly and therefore it is convenient to separate the discussion of the initial absorption processes from the subsequent dissociation dynamics for greater clarity.

3.2.1 The Huggins Bands

The Huggins bands are observed in the spectral region 310 - 360 nm which is on the red side of the Hartley band system. These absorption systems are illustrated from the experimental measurements of Molina and Molina at 226 K [11] in Figure 3.3 (a) and (b). The low absorption region between the end of the Huggins bands at 360 nm and the beginning of the Chappuis bands at $\sim$ 400 nm provide what is effectively a 'window' in the ozone absorption which will prove useful in the REMPI detection of the diatomic fragments from the UV photolysis of ozone as will be demonstrated later in the thesis.

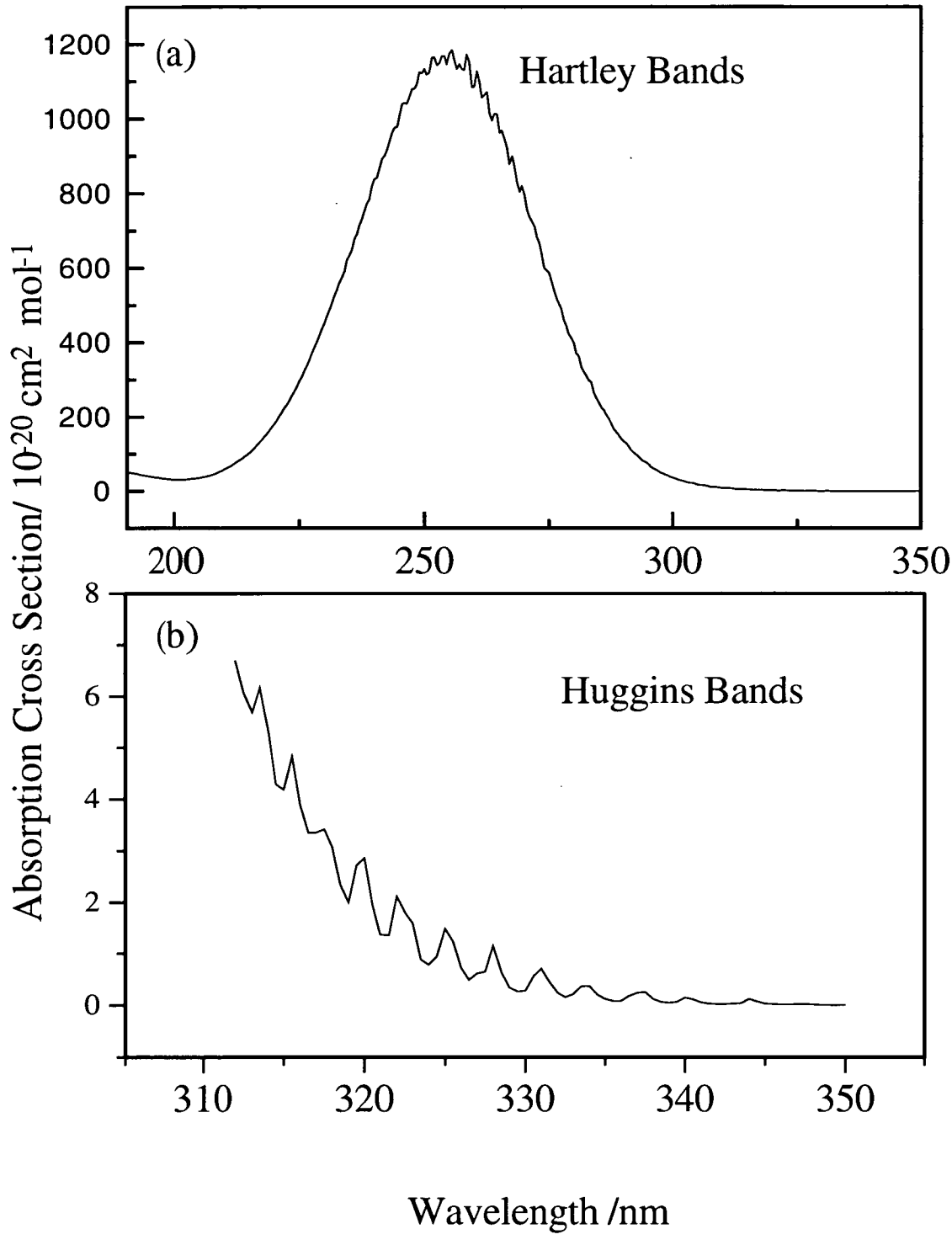

Figure 3.3.: The absorption spectrum of O_3 in the UV region is represented using the 226 K absorption data of Molina and Molina [11]. Section (a) shows the Hartley band system while section (b) shows an enlarged Huggins band system so that the vibrational structure can be clearly seen.

The Huggins band absorption exhibits a strong temperature dependence as noted by Malicet *et al.* [12] who also noted that the whole structure of the bands appears to be shifted by approximately 0.05 nm to higher energy upon change of temperature from 298 K to 218 K.

In spite of the large amount of research in this area there is still controversy over the assignment of the vibrational structure observed in this band and the electronic transition involved. In particular the main source of debate is whether the Huggins band is just a continuation of the same transition responsible for the Hartley band weakened by the poor Franck-Condon factors involved or whether the low intensity observed is due to a transition to a 'forbidden' electronic state. In the former case, ab initio calculations predict the most likely upper state to be the 1 $^1B_2$ state [3, 13] and in the latter case, to be the 2 $^1A_1$ state where the 2 $^1A_1 \leftarrow$ X $^1A_1$ transition [14, 15] is orbitally forbidden due to a double electron movement but can become weakly allowed when vibronically mediated mixing with the strongly allowed $^1B_2$ state *via* the ν_3 asymmetric stretching mode is taken into account. To fully appreciate the complexity of the problem it is best to discuss the development of each view individually.

Early vibrational assignments [16, 17] of the Huggins band structure assumed that there was no activity in the asymmetric stretching mode, ν_3, in the excited state and assigned the structure to progressions in the remaining two vibrational modes ν_1, the symmetric stretching mode and ν_2, the bending motion. This type of vibrational assignment is shown in Table 3.1 and is labelled as 'Assignment No. 1'.

However, following an analysis of the observed hot-band structure of the Huggins bands which suggested that the hot-bands originated from the 001 vibrational level of the ground state ozone [18], a re-assignment was made involving activity of the ν_3 mode in the excited state. Katayama's [19] assignment which was made on this basis was also the result the of the analysis of a cooled Huggins band absorption spectrum and isotope shift data. This

$^{16}O_3$ Cold Band Positions /cm^{-1}	Assignment No. 1 ref [17]	Assignment No. 2 ref [19]	Assignment No. 3 ref [20]	Assignment No. 4 ref [4]
(27122)	—	000	001	—
27818	—	110	011	—
28465	000	200	101	000
28803	010	210	111	010
29082	100	300	201	000[a]
29146	020	201	003	001
29412	110	310	211	030
29660	200	400	301	200 (001[a])
29724	120	301	103	021

Table 3.1.: A summary of the vibrational assignments of the Huggins band system which have been reported in the literature and are discussed in the text. [a] Indicates that the features marked are due to the second state of the double electronic state assignment of Banichevich *et al.* [4].

assignment is labelled as 'Assignment No. 2' in Table 3.1. This assignment differed from previous assignments in the observation of two previously unreported bands at wavelengths greater than 351.4 nm and hence resulted in the re-assignment of the origin to an unobserved feature at 368.8 nm.

Using this assignment Sinha *et al.* [21] undertook a rotational contour analysis of the (501) and (600) bands as given by Katayama's assignment. The rotationally structured spectra were achieved using LIF from ozone in a supersonic beam expansion (estimated T_{rot} = 3K). The analysis was performed using an asymmetric rotor contour program with a prolate rotor basis. To correct for the non-Boltzmann distribution of the rotational states in the supersonic beam a two temperature fit was used. The simulations showed that the (501) and (600) bands are of the same rotational type - this is important as transitions to these states involved both odd and even changes in ν_3. Using symmetry arguments the authors were able to show that this observation is consistent with an upper excited state with a double well along the q_3 axis

indicating that the excited state is of C_S symmetry. It is on these grounds that the authors concluded that the $^1B_2$ is the correct excited state for the Huggins band. Other information obtained by this rotational analysis were estimations of the predissociative lifetime of approximately 3.6 ps and of the limits of the bond angle of ozone in the excited state involved in the Huggins band: $70° \leq \theta \leq 106°$. In support of the above experimental data there is also theoretical evidence for the transition to locally bound regions on the $^1B_2$ surface in the vicinity of the Franck-Condon region being responsible for the Huggins Band. In fact LeQuere and Leforestier [22] have been able to simulate the Huggins band using a 3D quantum calculation involving a $^1B_2$ potential energy surface. The results led the authors to conclude that the simulation is of good enough quality to confirm that the Huggins band arises from the $^1B_2 \leftarrow X^1A_1$ transition.

The other possible explanation for the Huggins band is the forbidden electronic transition $2\,^1A_1 \leftarrow X^1A_1$. This theory is supported by the molecular orbital calculations of Thunemann *et al.* [14]. Based on the above electronic assignment of the upper state of the Huggins bands, Joens has recently proposed a re-assignment of the vibrational structure in the Huggins band which is labelled as 'Assignment No. 3' in Table 3.1. The basis of this re-assignment is the enforcement of the $\Delta\nu_3$ = odd selection rule deduced from symmetry considerations. The number of stretching quanta ν_s, are kept constant when compared with the assignment of Katayama (i.e. $\nu_1 + \nu_3 = \nu_s$) [19]. The new assignments still fit the isotope shift data obtained by Katayama. The arguments made in favour of this assignment include that the absence of the (0, 0, 0) $\leftarrow$ (0, 0, 0) band is now easily explained while it is predicted to occur at 368.8 nm by Katayama who claims that it is not observed due to a low absorption cross section. In Joens' assignment [20] this transition becomes forbidden due to the enforcement of the $\Delta\nu_3$ = odd selection rule. The hot bands of the system can also be accounted for by this new assignment. The observations of Sinha *et al.* [21] now have a much simpler explanation - the

transitions they examined were the (501) and (600) bands in Katayama's assignment but in Joens assignment these bands are (3,0,3) and (5,0,1). Since both of these transitions correspond to odd values of $\Delta\nu_3$ the rotational type is expected to be the same.

Finally, an alternative assignment was suggested by Banichevich *et al.* [4] following their molecular orbital calculations on the excited states of ozone in a range of C_S symmetries. Based on these *ab initio* calculations they suggest that the origin of the Huggins bands is at 351.4 nm as originally assumed. They assigned the lower energy features observed by Katayama to high vibrational levels of the Chappuis system. This work also suggests that two excited states participate in the absorption. The more intense features are assigned to the strongly allowed $^1B_2 \leftarrow X^1A_1$ transition which is labelled as the $2\ ^1A' \leftarrow X^1A'$ transition in C_S symmetry and the weaker features are assigned to the less intense $^1A_1 \leftarrow X^1A_1$ transition which is labelled as the $1\ ^1A' \leftarrow X^1A'$ transition in C_S symmetry.

3.2.2 The Hartley Bands

The Hartley band absorption system which covers the 200 - 310 nm range shown in Figure 3.3 (a) appears to be a broad continuum with weak superimposed structure.

Unlike the Huggins bands the electronic assignment of this system is well established as the $^1B_2 \leftarrow X^1A_1$ transition. Due to the central role which this system plays in the absorption of UV radiation from the sun as described in Chapter 1 the Hartley band system has been extensively studied by both theoreticians and experimentalists. In particular the irregularly spaced diffuse peaks on top of the Hartley bands which have energy spacings ranging from 150 - 300 cm^{-1} have provided a very popular source of investigation. Accurately measured absorption spectra (including the data illustrated in Figure 3.3) at a range of temperatures have provided a solid basis of these investigations.

Two distinct approaches to this type of study can be taken which are dictated by the time-dependent view or time-independent formalism of the problem. The first of these approaches involves the assignment of the diffuse structure to transitions between the (000) level of the X^1A_1 state and bound vibrations on the $^1B_2$ surface. This type of analysis is interpreted with reference to the model of Pack [23] where a bound motion in one (or more) coordinates can co-exist with unbound coordinates and give rise to diffuse structure. This model will be discussed in more detail later in the text. The first to adopt this approach was Joens [24] who used the absorption data of Freeman *et al.* [25] to assign all of the observed structure to harmonic progression in the ν_1 and ν_2 coordinates where ν_3 is the dissociative coordinate. Parisse *et al.* [26] extended this assignment using higher resolution $^{16}O_3$ and $^{18}O_3$ absorption spectra. They also performed an isotope shift analysis on all of the bands in this region in an attempt to confirm the absolute numbering of the vibrational assignment of Joens. Using this method they identified the origin of the $^{16}O_3$ Hartley band system to be at an energy of 33570 cm^{-1} above the zero point energy of the ground state ozone.

The alternative method of analysis of the absorption spectrum is to use the time-dependent approach to relate the absorption cross-section to the Fourier integral of the dipole-dipole autocorrelation function. This relationship is shown in equation 3.2 [27, 28]:

$$\frac{\sigma(\omega)}{\omega} \propto \int_{-\infty}^{\infty} e^{i(\omega + \frac{E_0}{\hbar})t} \langle \Phi(0) | \Phi(t) \rangle dt \tag{3.2}$$

where E_0 is the initial level in the ground state $|\Phi(0)\rangle = \mu|\psi_0\rangle$ ($|\psi_0\rangle$ is the nuclear eigenstate of the ground state) and $|\Phi(t)\rangle$ is the time-evolution of the wavepacket on the excited state surface. In simple terms, the auto-correlation function is the measure of the overlap of the dissociating wavepacket with the coordinates of the initially prepared wavepacket as a function of time. This dynamical information about the dissociating molecule can be extracted from the experimental absorption data by simply performing an inverse Fourier

integral of the absorption. From a theoretical point of view it has proved easier to calculate these auto-correlation functions by propagating the initial wavepacket on the *ab initio* PES of the excited state [29, 30] than to calculate the 3-dimensional bound states on the same surface [31]. Hence this approach has been more widely adopted in recent years.

Johnson and Kinsey [32] calculated the auto-correlation function from the absorption data of Freeman [25] and found recurrences of the wavepacket at 19, 41, 68, 99 and 128 fs. They also proposed unstable periodic orbits of the wavepacket on the excited state surface which could account for all but the shortest of these recurrences. A more difficult task is to perform the reverse calculation, i.e. starting with a PES and calculating the auto-correlation function by propagating the initially excited wavepacket, the shape of which can be calculated from the ground state PES. This auto-correlation function should then match the experimental auto-correlation function of Johnson and Kinsey [32] and hence the experimental absorption spectrum. Two recent calculations of this sort are those performed by Leforestier *et al.* [29] using the $^1B_2$ surface of Yamashita and Morokuma (YM) [33] and the calculations of Balakrishnan and Billing [30] with the PESs of both YM and Sheppard and Walker (SW) [34]. Both calculations on the YM surface yielded recurrences which were too intense and oscillations in the calculated absorption spectrum which were much larger than in the experimental spectrum. However, the calculation on the SW surface provided a better match to the experimental data. A number of points were yet to be explained such as the experimental recurrence at 19 fs was not reproduced in any of the calculations. Also a detailed comparison of the energy of the calculated features with those from experiment was not made in any of the calculations.

3.3 The UV Photodissociation Dynamics of Ozone

As can be seen from the correlation diagram in Figure 3.2 a number of photodissociation channels are accessible following the UV dissociation of ozone. The six lowest channels are shown below along with their thermodynamic thresholds below which they cannot be accessed from the (000) level of the ground state :

(A)	O_3	+	$h\nu$	$\rightarrow$	$O(^3P_j)$	+	$O_2\ (X\,^3\Sigma_g^-)$	(1178 nm)
(B)				$\rightarrow$	$O(^3P_j)$	+	$O_2\ (a\,^1\Delta_g)$	(612 nm)
(C)				$\rightarrow$	$O(^3P_j)$	+	$O_2\ (b\,^1\Sigma_g^+)$	(463 nm)
(D)				$\rightarrow$	$O(^1D)$	+	$O_2\ (X\,^3\Sigma_g^-)$	(411 nm)
(E)				$\rightarrow$	$O(^1D)$	+	$O_2\ (a\,^1\Delta_g)$	(310 nm)
(F)				$\rightarrow$	$O(^1D)$	+	$O_2\ (b\,^1\Sigma_g^+)$	(267 nm)

As the absorbing excited states in the UV energy range are dominated by singlet surfaces and the dissociation on such surfaces are governed by spin conservation rules which dictate that such surfaces can only correlate with products of the same spin (i.e. channels (A), (E) and (F)) it would be expected that these would be the principal dissociation paths.

3.3.1 Dissociation Processes of Ozone Following Huggins Bands Absorption

Considering first the Huggins bands (310 - 360 nm), it is clear that the only accessible spin-allowed fragmentation process is *via* channel (A) for the dissociation of molecules within this energy region. Therefore it was originally assumed that channel (A) was the dominant product channel following Huggins band absorption. However, early experiments revealed a 'tail' of $O(^1D)$

quantum yield, $\Phi(O(^1D))$, below the energetic threshold to channel (E) at 310 nm. It was recognised that the source of $O(^1D)$ at these wavelengths may come from photolysis of vibrationally excited ground state O_3 which would have the effect of lowering the threshold of channel (E). In fact, early calculations on the quantity of this source of $O(^1D)$ by Trolier and Weisenfeld [35] led these authors to conclude that the observed $\Phi(O(^1D))$ in the region > 310 nm could be accounted for entirely by this source. More recently Takahashi *et al.* [36] have recorded a jet-cooled PHOFEX spectrum of the $O(^1D)$ fragments as a function of photolysis wavelength in this region. Their results exhibit sharp changes in the gradient of the $O(^1D)$ yield both at the channel (E) threshold for photolysis of (000) ground state O_3 at 310 ± 0.2 nm and a second gradient change at 320.7 ± 0.2 nm. From the energies of the ground state vibrational modes they assigned this second gradient change to be due to the threshold for photolysis of the small percentage population in the (001) vibrational level of the ground state *via* channel (E). Hence they concluded that the principal contribution to the $O(^1D)$ yield from vibrationally mediated dissociation is due to the increased absorption cross-section of the ν_3'' level of ozone at these energies. This is confirmation of the work of Zittel and Little [37] who measured a two order of magnitude increase in the production of $O(^1D)$ following 314.5 nm photolysis of ozone without and with IR excitation of the ν_3 band of ozone respectively.

Takahashi *et al.* [36] also observed discrete structure in their $O(^1D)$ PHOFEX spectra superimposed on the continuum yield due to the photolysis of vibrationally excited ozone. Measurement of the Doppler profiles of the $O(^1D)$ products revealed two contributions to the $O(^1D)$ yield, one of which has a markedly higher translational distribution that the other. The higher translational energy products was unarguably assigned to the production of $O(^1D)$ fragments *via* the spin-forbidden dissociation channel (D) while the slower fragments are clearly due to the vibrationally mediated dissociation *via* channel (E). This conclusion was supported by the TOF analysis of $O(^1D)$

fragments performed by Denzer *et al.* [38] who observed similar trends.

Accurately quantifying the $O(^1D)$ yield as a function of dissociation wavelength, irrespective of its source, has been an extremely popular subject of research in recent years. This is due to the central role which the $O(^1D)$ atom plays in the chemistry of the troposphere which will be discussed in more detail in the following section. $\Phi(O(^1D))$ is the ratio of the number of $O(^1D)$ atoms produced per number of photons absorbed. It is most often presented as a function of wavelength and temperature and the absolute values have been contested by a number of groups. This controversey is largely fuelled by the inaccuracies in the recommendations of NASA/JPL [39] published as recently as 1997 which is the source most used in atmospheric modelling and hence plays as important role in ozone research. These data suggest that $\Phi(O(^1D))$ drops very rapidly below the 310 nm threshold to channel (E), plateaus in the region of vibrationally mediated photolysis (310 - 320 nm) and then tends towards zero at lower energies. This neglect of the spin-forbidden contribution to $\Phi(O(^1D))$ which has already been discussed is contradicted by a large number of recent investigations which will be briefly outlined here.

A large range of techniques has been used to quantify $\Phi(O(^1D))$ in the Huggins band and the lowest energy region of the Hartley band (300 - 335 nm). Among these is the measurement of both the $O(^1D)$ and $O(^3P_j)$ PHOFEX spectra, recorded using LIF detection of the relevant fragments, followed by scaling the sum of these spectra to the absolute absorption cross-section of ozone in this region. This method, used by Takahashi *et al.* [40], can be used to determine the contribution of these two fragments to the total dissociation process and hence the absolute quantum yields of the two fragments. The method used by Ball *et al.* [41] involved the REMPI detection of the $O(^1D)$ fragments as a function of wavelength which can be used to calculate the relative quantum yield of $O(^1D)$. These relative yields are then placed on an absolute scale by comparison with other work using absolute methods at specific wavelengths. Less direct methods which have relied on the subsequent

reaction of the $O(^1D)$ fragment with H_2O to produce the easily detectable OH radical have also been used [42, 43]. All of these techniques have resulted in the same general conclusion that the $O(^1D)$ quantum yield persists with an absolute value of ~ 0.1 out to a photolysis wavelength of at least 330 nm. This $\Phi(O(^1D))$ 'tail' is assigned to the spin-forbidden dissociation *via* channel (D).

Ball *et al.* [44, 45] also measured a long wavelength tail in the quantum yield of O_2 ($a\ ^1\Delta_g$) to wavelengths as high as 325 nm which could not be attributed to the spin-allowed channel (E) for the same reasons mentioned above for the $\Phi(O(^1D))$ 'tail'. The production of these fragments was assigned to spin-forbidden dissociation *via* channel (B). This conclusion was later confirmed by the same group [38] using TOF measurements to monitor the kinetic energies of the O_2 ($a\ ^1\Delta_g$) fragments . In these experiments they detected the O_2 ($a\ ^1\Delta_g$, v = 0) fragments by a (2 + 1) REMPI process *via* the v = 2 level of the pertubed $d\ 3s\sigma(^1\Pi_g)$ Rydberg state. The velocities of the O_2 ($a\ ^1\Delta_g$, v = 0) fragments are then estimated from the effect of the different velocities of the fragments on the TOF profiles. Using this method they observed a high velocity component of the O_2 ($a\ ^1\Delta_g$) fragments which they assigned to spin-forbidden dissociation *via* channel (B) and also a low velocity component due to the spin-allowed photolysis of 'hot' ground state ozone *via* channel (E).

The lack of certainty about the upper electronic state involved in the Huggins band as well as the incompletely explained participation of the spin-forbidden channels in the dissociation combine to make an intriguing problem to describe the overall absorption and dissociation dynamics of ozone in this region. However, due to the lack of further knowledge of the processes involved no satisfactory explanation has been provided to date.

3.3.2 Dissociation Processes of Ozone Following Hartley band Absorption

As the photolysis wavelength is tuned above the threshold to channel (E) at 310 nm the dissociation becomes apparently simpler due to the dominance of direct dissociation *via* channel (E) on the $^1B_2$ surface. Fairchild *et al.* [46] measured the translational and angular distribution of the oxygen atoms following 274 nm photolysis and found a branching ratio of channel (A):channel (E) of 0.1:0.9 and a parallel transition for both channels (consistent with a $^1B_2$ upper surface). Sparks *et al.* [47] measured a similar branching ratio when measuring the translational energy of the O_2 fragments following 266 nm photodissociation. Thelen *et al.* [48] performed this second experiment at greater resolution and at a number of different photolysis wavelengths and were able to report the vibrational distributions of the O_2 ($a\ ^1\Delta_g$) fragments. A very interesting result from these experiments involved the ratio of v = 1/v = 0 of the O_2 ($a\ ^1\Delta_g$) fragments produced. It was shown that this ratio could change markedly for photolysis wavelengths within a very small region. For example, the v = 1/v = 0 ratio was found to have a value of 0.71 for 283.0 nm photolysis versus 0.3 at 283.7 nm. This effect was suggested to be due either to the vibronic structure of the excited ozone molecule or to the interference effect caused by the part of the wavepacket that moves directly into the exit channel and that which remains trapped in the initially excited region of the surface. State-selective detection of the fragments was used by Valentini *et al.* [49] at a number of widely spaced wavelengths within the Hartley band region and hence did not observe the large fluctuation of the v = 1/v = 0 ratio reported by Thelen *et al.* [48]. However, their use of Coherent Anti-stokes Raman Spectroscopy (CARS) allowed rotational resolution of the fragments. The reported rotational distributions were consistent with a simple impulsive model of dissociation.

The general trends of photodissociation within the Hartley band can be rationalised by the consideration of the potential energy curves of the electronic states suggested to be involved in the dissociation. As was stated previously, it is generally accepted that the Hartley band is due to a transition from the

ground state of ozone onto the repulsive limb of the 1^1B_2 surface. Direct dissociation on this surface to the $O(^1D)$ + O_2 ($a\ ^1\Delta_g$) fragments is the dominant process. Direct dissociation pathways of this sort can often be modeled by the impulsive model of dissociation which simulates an instantaneous force between the diatomic and atomic fragments leading to internal and translation distribution of fragments which can be calculated from geometric and energetic considerations alone. A more complex model would be required to reproduce the results of Thelen *et al.*. The dissociation of 10 % of the molecules by channel (A) is due to a surface crossing from the initially excited 1^1B_2 surface to a repulsive R $^1A_1$ state which correlates with these products (both of these states are A' in C_S symmetry).

This minor channel has been rigorously researched with most attention focused on measurement of the internal energy distributions of the O_2 ($X\,^3\Sigma_g^-$) fragments either by measurement of the $O(^3P_j)$ velocity distribution [50, 51] or direct methods of probing the O_2 ($X\,^3\Sigma_g^-$) fragments in a state selective manner [52]. Miller *et al.* [50] reported a bimodal vibrational distribution of the O_2 ($X\,^3\Sigma_g^-$) fragments using ion imaging of the $O(^3P_j)$ atoms following photolysis at 226 nm. They observed a broad peak in this vibrational distribution at v = 14 and a sharper peak at v = 27 with confirmation that these states were produced by probing the O_2 ($X\,^3\Sigma_g^-$, v) fragments using LIF. A number of groups investigated this bimodal nature of the O_2 ($X\,^3\Sigma_g^-$) vibrational distribution due to the suggestion that reaction 3.3 could account for the 'ozone deficit'.

$$O_2(X, v \geq 26) + O_2(X, v = 0) \rightarrow O_3 + O \qquad (3.3)$$

This 'ozone deficit' was a lower predicted concentration of O_3 by atmospheric models than observed in the atmosphere and it was thought that the above reaction could participate in the auto-catalytic production mechanism of O_3. This mechanism was later shown to be unfeasible by calculation of the reaction rate of this reaction which showed that vibrational quenching of 'hot'

O_2 molecules dominated. A further related mechanism was also suggested for this ozone deficit problem which involved the following series of reactions:

$$\begin{aligned} O_3 + h\nu &\rightarrow O_2(X, v = high) + O(^3P_j) \quad (a) \\ O_2(X, v = high) + h\nu &\rightarrow 2O(^3P_j) \quad (b) \\ 3\{O(^3P_j) + O_2 + M &\rightarrow O_3 + M\} \quad (c) \end{aligned} \tag{3.4}$$

However, this mechanism was also shown to contribute too small an amount of O_3, again due to the dominance of vibrational quenching of the O_2 ($X\,^3\Sigma_g^-$, v) fragments over the photolysis step shown in reaction 3.4 (b).

From a more fundamental viewpoint however the bimodal vibrational distribution of the diatomic fragments *via* channel (A) is quite interesting. Further experiments on the wavelength dependence of this bimodal nature showed that the vibrational distribution of the O_2 ($X\,^3\Sigma_g^-$) fragments produced by photolysis at 226 and 230 nm both exhibit strong bimodality but as the photolysis wavelength is increased to 240 and 266 nm a smooth single distribution was observed. This behaviour was rationalised by the suggestion that the repulsive R A' surface crosses the initially excited $1\,^1B_2$ surface in two distinct regions one of which is energetically too high to be accessed by the lower energy photons (240 and 266 nm).

Finally, the spin-allowed channel (F) becomes accessible at energies higher than 267 nm and has indeed been observed in experiments involving photolysis of ozone in this energy region. Taherian and Slanger [53] showed that the O_2 ($b\,^1\Sigma_g^+$) fragment is produced following photolysis at 157 nm and Turnipseed *et al.* [54] and later Stranges *et al.* [55] also observed this channel in their bulb experiments using 193 and 222 nm photolysis wavelengths. Therefore, it appears that channel (F) also contributes to high energy photolysis within the Hartley bands.

3.4 Implications of Dynamical Studies of Photodissociation for Atmospheric Chemistry

Near the beginning of an article of R.P. Wayne [56], the author states that:

> *" ..... there is much to be learned of atmospheric relevance from the results of laboratory experiments whose primary aim was to study ever more intimate details of the photodissociation process."*

To illustrate this point the discussion of the relevance of the $O(^1D)$ quantum yield from the Huggins band photolysis has been left until this stage. In spite of the low absorption cross-section of ozone in this wavelength region the relative importance of absorption at tropospheric altitudes (0 - 20 km) becomes central due to the increase of the relative solar radiation of these wavelengths at this altitude. By the time the suns radiation reaches the troposphere almost all of the radiation below 300 nm has been absorbed by the ozone layer in the stratosphere (20 - 40 km) whereas much of the radiation above this wavelength penetrates to this altitude due to the lower absorption cross-section of ozone in this region. Therefore, the dominant mechanism for the production of the reactive $O(^1D)$ atom is due to the photolysis of ozone by 300 - 360 nm radiation. Above 360 nm the cross-section of ozone goes almost to zero and therefore does not contribute to this process.

The $O(^1D)$ atom drives the photochemical processes of the troposphere due to its reaction with H_2O to form the OH radical. The OH radical then acts as a scavenger for many of the atmospheres pollutants such as hydrocarbons.

By extending the production of $O(^1D)$ due to spin-forbidden dissociation of ozone many subsequent effects on the photochemistry of the troposphere result. Talukdar *et al.* [57] attempted to quantify the effect of including spin-forbidden dissociation to produce $O(^1D)$ on the $O(^1D)$ production rates in the

troposphere. The method used was to calculate the first order rate coefficients for $O(^1D)$ production from photolysis of ozone (called J values) which depend on the solar irradience, altitude , temperature, ozone concentration and solar zenith angles. It was found that by including the spin-forbidden production of $O(^1D)$ as well as the $O(^1D)$ production from photolysis of vibrationally excited ground state molecules the total J value increased by as much as 100 %. And so it appears that the measurement of a small spin-forbidden channel which is a type of dissociation which is traditionally assumed to be negligible can have profound consequences for the understanding of the atmosphere.

References

[1] G. Herzberg. *Molecular Spectra and Molecular Structure III, Spectra of Polyatomic Molecules*, (Van Nostrand, New York, 1967).

[2] N. J. Mason, J. M. Gingell, J. A. Davies, H. Zhao, I. C. Walker and M. R. F. Siggel. *J. Phys. B: At. Mol. Opt. Phys.* **29** (1996) 3075.

[3] P. J. Hay and T. H. Dunning, Jr. *J. Chem. Phys.* **67** (1977) 2290.

[4] A. Banichevich, S. D. Peyerimhoff and F. Grein. *Chem. Phys.* **178** (1993) 155.

[5] S. M. Anderson, J. Morton and K. Mauersberger *J. Chem. Phys.* **93** (1990) 3826.

[6] B. Minaev and H. Årgen. *Chem. Phys. Lett.* **217** (1994) 531.

[7] A. J. Bouvier, R. Bacis, B. Bussery, S. Churassy, D. Inard, M. Nota, J. Brion, J. Malicet and S. M. Anderson. *Chem. Phys. Lett.* **255** (1996) 263.

[8] S. M. Anderson and K. Mauersberger *J. Geophys. Res.* **100** (1995) 3033.

[9] M. Braunstein and R. T. Pack. *J. Chem. Phys.* **96** (1992) 6378.

[10] A. Banichevich, S. D. Peyerimhoff, J. A. Beswick and O. Atabek. *J. Chem. Phys.* **96** (1992) 6580.

[11] L. T. Molina and M. J. Molina, *J. Geophys. Res.* **91** (1986) 14501.

[12] J. Malicet, D. Daumont, J. Charbonnier, C. Parisse, A. Chakir and J. Brion. *J. Atmos. Chem.* **21** (1995) 263.

[13] P. J. Hay, R. T. Pack, R. B. Walker and E. J. Heller. *J. Phys. Chem.* **86** (1982) 862.

[14] K. H. Thunemann, S. D. Peyerimhoff and R. J. Buenker. *J. Mol. Spec.* **70** (1978) 432.

[15] A. Banichevich and S. D. Peyerimhoff. *Chem. Phys.* **173** (1993) 93.

[16] A. Jakowlewa and V. Kondratjew, *Phys. Z. Sowjetunion* **9** (1936) 106.

[17] J. W. Simons, R. J. Paur, H. A. Webster III and E. J. Blair, *J. Chem. Phys.* **59** (1973) 1203.

[18] J. C. D. Brand, K. J. Cross and A. R. Hoy, *Can. J. Phys.* **56** (1978) 327.

[19] D. H. Katayama. *J. Chem. Phys.* **71** (1979) 815.

[20] J. A. Joens. *J. Chem. Phys.* **101** (1994) 5431.

[21] A. Sinha, D. Imre, J. H. Goble, Jr., and J. L. Kinsey *J. Chem. Phys.* **84** (1986) 6108.

[22] F. Lequere and C. Leforestier. *Chem. Phys. Lett.* **189** (1992) 537.

[23] R. T. Pack. *J. Chem. Phys.* **65** (1976) 4765.

[24] J. A. Joens. *J. Chem. Phys.* **100** (1994) 3407.

[25] D. E. Freeman, K. Yoshino, J. R. Esmond and W. H. Parkinson. *Planet. Space Sci.* **32** (1984) 239.

[26] C. Parisse, J. Brion and J. Malicet. *Chem. Phys. Lett.* **248** (1996) 31.

[27] E. J. Heller. *J. Chem. Phys.* **68** (1978) 3891.

[28] E. J. Heller. *Acc. Chem. Res.* **14** (1981) 368.

[29] C. Leforestier, F. LeQuere, K. Yamashita and K. Morokuma. *J. Chem. Phys.* **101** (1994) 3806.

[30] N. Balakrishnan and G. D. Billing. *J. Chem. Phys.* **101** (1994) 2968.

[31] O. Atabek, M. T. Bourgeois and M. Bacon. *J. Chem. Phys.* **84** (1986) 6699.

[32] B. R. Johnson, and J. L. Kinsey. *J. Chem. Phys.* **91** (1989) 7638.

[33] K. Yamashita and K. Morokuma. *Faraday Discuss. Chem. Soc.* **91** (1991) 47.

[34] M. G. Sheppard and R. B. Walker. *J. Chem. Phys.* **78** (1983) 7191.

[35] M. Trolier and J. R. Wiesenfeld. *J. Geophys. Res.* **93** (1988) 7119.

[36] K. Takahashi, M. Kishigami, N. Taniguchi, Y. Matsumi, and M. Kawasaki, *J. Chem. Phys.* **106** (1997) 6390.

[37] P. F. Zittel and D. D. Little. *J. Chem. Phys.* **72** (1980) 5900.

[38] W. Denzer, G. Hancock, J. Pinot de Moira and P. L. Tyley, *Chem. Phys.* **231** (1998) 109.

[39] W. B. DeMore, S. P. Sander, D. M. Golden, R. F. Hampson, M. J. Kurylo, C. J. Howard, A. R. Ravishankara, C. E. Kolb and M. J. Molina. *Chemical Kinetics and Photochemical Data for use in Stratospheric Modelling, Evaluation No. 12* JPL. Publication 97-4 (1997).

[40] K. Takahashi, N. Taniguchi, Y. Matsumi, M. Kawasaki and M. N. R. Ashfold. *J. Chem. Phys.* **108** (1998) 7161.

[41] S. M. Ball, G. Hancock, S. E. Martin and J. C. Pinot de Moira. *Chem. Phys. Lett.* **264** (1997) 531.

[42] W. Armerding, F. J. Comes and B. Schülke *J. Phys. Chem.* **99** (1995) 3137.

[43] E. Silvente, R. C. Richter, M. Zheng, E. S. Saltzmann and A. J. Hynes. *Chem. Phys. Lett.* **264** (1997) 309.

[44] S. M. Ball and G. Hancock. *Geophys. Res. Lett.* **22** (1995) 1213.

[45] S. M. Ball, G. Hancock and F. Winterbottom. *Faraday Discuss.* **100** (1995) 215.

[46] C. E. Fairchild, E. J. Stone and G. M. Lawrence. *J. Chem. Phys.* **69** (1978) 3632.

[47] R. K. Sparks, L. R. Carlson, K. Shobatake, M. L. Kowalczyk and Y. T. Lee. *J. Chem. Phys.* **72** (1980) 1401.

[48] M. -A. Thelen, T. Gejo, J. A. Harrison and J. R. Huber. *J. Chem. Phys.* **103** (1995) 7946.

[49] J. J. Valentini, D. P. Gerrity, D. L. Philips, J. C. Nieh and K. D. Tabor. *J. Chem. Phys.* **86** (1987) 6745.

[50] R. L. Miller, A. G. Suits, P. L. Houston, R. Toumi, J. A. Mack and A. M. Wodtke. *Science* **265** (1994) 1831.

[51] R. J. Wilson, J. A. Mueller and P. L. Houston. *J. Phys. Chem. A* **101** (1997) 7593.

[52] K. M. Hickson, P. Sharkey, I. W. M. Smith, A. C. Symonds, R. P. Tuckett and G. N. Ward. *J. Chem. Soc., Faraday Trans.* **94** (1998) 533.

[53] M. R. Taherian and T. G. Slanger. *J. Chem. Phys.* **83** (1985) 6246.

[54] A. A. Turnipseed, G. L. Vaghjiani, T. Gierczak, J. E. Thompson and A. R. Ravishankara. *J. Chem. Phys.* **95** (1991) 3244.

[55] D. Stranges, X. Xang, J. D. Chesko and A. G. Suits. *J. Chem. Phys.* **102** (1995) 6067.

[56] R. P. Wayne. *J. Geophys. Res.* **98** (1993) 13119.

[57] R. K. Talukdar, M. K. Gilles, F. Batin-Leclerc, A. R. Ravishankara J. - M. Fracheboud, J. J. Orlando and G. S. Tyndall. *Geophys. Res. Lett.* **24** (1997) 1091.

Chapter 4

Experimental Details and Data Analysis

4.1 Introduction

Although the same experimental equipment was used for most of the results presented in this thesis, two distinct types of experiments were performed and these required different experimental arrangements. The first of these involved recording one-colour and two-colour REMPI and PHOFEX spectra which have been described in the previous chapter. The experimental set-up for these types of experiments, referred to as the mass spectrometer mode for the rest of the thesis, is shown schematically in Figure 4.1. In this mode, the outputs of either one or two independently tunable dye lasers pumped by the output of a XeCl excimer laser produced ions which were detected and mass analysed by a linear Time-of-Flight Mass Spectrometer (TOF-MS), the resultant signal being processed by a boxcar and recorded on a personal computer. The individual components of this set-up are described in the following sections. The second operating mode, subsequently referred to as the translational spectrometer mode, involved the implementation of the delayed pulsed field extraction technique described schematically in Chapter 2. This

technique involved the use of all of the equipment mentioned above but also utilised a delay between the laser pulse and the voltage applied to the ion optics of the extraction region to measure the velocities of fragments formed in a dissociation process. Much of this chapter is devoted to the description of this technique as it was developed for use on the experimental equipment described above during the course of the experimental work of this thesis. The analysis of the subsequent results to extract the velocity and angular properties of photofragments outlined in Chapter 2 are also described.

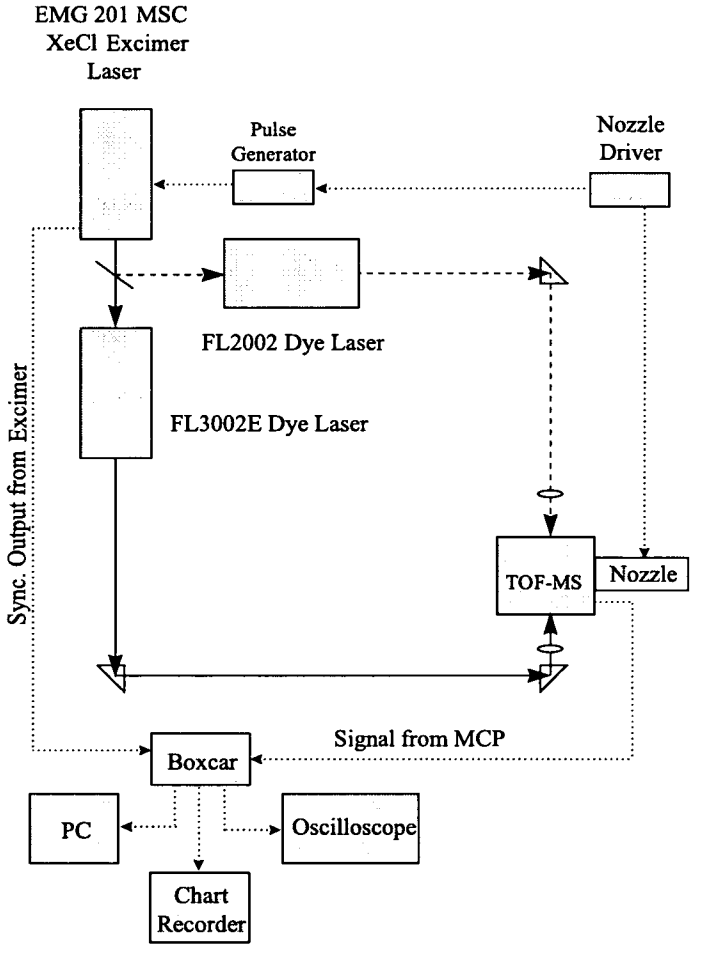

Figure 4.1.: The schematic diagram illustrating the experimental set-up used for REMPI and PHOFEX experiments.

The schematic shown in Figure 4.1 illustrates a general set-up of the equipment used in a two-colour laser photolysis-laser probe technique. Before discussing how the different arrangements can be utilised it is first necessary to describe the individual components.

4.2 The Laser System

4.2.1 The Excimer Laser

In all of the experiments involving the photolysis of ozone the laser radiation was generated using dye lasers pumped by an excimer laser. The Lambda Physik EMG 201 MSC excimer laser [1] was operated with a XeCl active medium and generated a laser beam of 308 nm light with a pulse length of $\sim$ 25 ns and a maximum output of 400 mJ/pulse. The mechanism of operation consists of the discharge of a high voltage across the cavity, containing a gas mixture of xenon, hydrogen chloride and neon, resulting in the formation of a $XeCl^*$ exciplex by collisions of the excited Xe atoms formed in the discharge with the gas mixture. The $XeCl^*$ then radiates to the ground state XeCl followed by immediate dissociation of the very weakly bound complex. The population inversion forming the basis of the lasing action is achieved due to the relatively long radiative lifetime of the exciplex versus the short dissociation lifetime of the ground state complex.

4.2.2 The Dye Lasers

The excimer laser beam can be used to pump a single dye laser or can be split into two components by a beam splitter to pump two dye lasers as illustrated in Figure 4.1. A Lambda Physik FL3002E [2] and a Lambda Physik FL2002 were employed which utilise highly fluorescent organic dyes which have

a high absorption cross-section at the 308 nm pump light [2]. The population inversion is provided by the slightly different equilibrium geometries of the S_0 and S_1 states of these dye molecules. The molecules in the S_1 state produced by the optical pumping of the excimer beam must vibrationally relax to their equilibrium geometries before the emission of a photon producing S_0 molecules which are far from their equilibrium geometries and hence also undergo vibrational relaxation. As the rate of vibrational relaxation is faster than the emission rate a population inversion between these two state is induced and the lasing action can take place.

The advantage of these systems is that the dye molecules radiate over a range of energies from which the lasing wavelength can be varied using a diffraction grating for selection of a narrow spectral region of the emitted light for amplification. The centre of lasing range of the dye system can be varied by the selection of suitable dye molecules which have different energy separations of their S_0 and S_1 states. Therefore, tunable radiation over a large portion of the spectrum can be produced by using a number of different dye molecules. This is illustrated in Table 4.1 which contains the fundamental lasing wavelength ranges of the dyes used in the course of this thesis. The manufacturer conversion efficiencies are also shown in this table. However, in practice the efficiencies attained were slightly lower than these giving fundamental outputs of 30 - 50 mJ/pulse at peak pump powers.

4.2.3 Frequency Doubling

It may be noted from this table that the wavelength region below 335 nm cannot be accessed by the fundamental output of any of the dyes. Due to the nature of the lasing process described above it is not possible to have a dye which can lase any closer in energy to the pump wavelength. Therefore, to increase the accessible range of wavelengths it is necessary to use the non-linear optical effects of certain crystalline materials which can double the energy of

Dye	Range / nm	Peak / nm	% Efficiency
DCM	632-690	658	12
Rhodamine 101	614-672	623	12
Rhodamine B	588-644	600	12
Rhodamine 6G	569-608	581	16
Coumarin 153	522-600	540	15
Coumarin 307	479-553	500	16
Coumarin 47	440-484	456	18
QUI	360-400	390	11
DMQ	345-365	360	9
PTP	335-345	343	8

Table 4.1.: Wavelength ranges, wavelength of peak efficiency and % efficiency of the dyes used in the course of this work.

the radiation of the fundamental output of the dye lasers. Suitable materials for this purpose are beta-barium borate (BBO) and Potassium Dihydrogen Phosphate (KDP) which are used in the Lambda Physik FL37-1 (BBO I) and FL30 crystals respectively. These crystals can double incident radiation between 440 and 630 nm (BBO I) and 540 and 690 nm (FL30). This allows the range of accessible wavelengths to be extended down to 220 nm.

Although the finer details of non-linear optics [3] are far from the central subject of this thesis some important points must be made at this stage on the effect of these second harmonic generating crystals on the laser beam. Briefly, when an electric field, E passes through a material a charge polarisation, P, is induced due to the interaction of the light field with the bound charges of the medium. If this medium has a relatively high second order polarisation susceptibility, $\chi^{(2)}$, second harmonic generation (SHG) of the incident light can be achieved, the power of which is proportional to the square of the incident field. The peak efficiency of this process depends on the optical thickness of the material which is different for different wavelengths of incident light. Therefore to optimise the SHG efficiency the crystal must be tilted to different

angles to give the optimum optical thickness for each wavelength. This can be achieved by synchronising the tilt angle of the crystal with the grating angle within the dye laser and is controlled by the electronics of the laser. The maximum efficiency of this process does not exceed 20% and hence the frequency doubled outputs of < 10 mJ/pulse are achieved. The remaining part of the beam passes through largely unaffected and must be separated from the frequency doubled part either by use of a UG5 filter which is opaque to visible radiation and transmits UV radiation above 250 nm or a Pellin Broca prism system (Lambda Physik FL35) which makes use of the dependence of the refractivity of light on its wavelength to deflect the fundamental from the second harmonic beam path.

A further important point is the effect that these crystals have on the polarisation of the output light. The input radiation from the fundamental of the dye laser is linearly polarised in the vertical plane and in the present experiments collinear with the axis of the TOF system. However, the SHG crystal rotates the polarisation of the output light by 90° and this point becomes very important later when discussing the photofragment velocity measurements.

4.3 The Molecular Beam

A molecular beam [4] consists of a sample gas expanded from a high pressure (P_0) chamber into a low pressure (P_b) ambient background chamber *via* a small hole called a nozzle. A very high pressure gradient is achieved by pumping down the chamber into which the beam is expanded to achieve background pressures of $\sim 1 \times 10^{-6}$ Torr and using the relatively large backing pressure of the sample gas of 700 Torr giving a very large P_0/P_b of 7×10^8. Under such conditions, as the gas expands into the vacuum, it cools rapidly and very high velocities of the sample molecules are achieved. The cooling of the molecules is achieved by the collisions which transfer energy from the internal

modes to translational energy. These collisions occur close to the nozzle at the beginning of the expansion but as the gas expand they move into a collision-free environment where the temperature of the molecules stabilise. As rotational cooling requires less collisions than vibrational cooling the molecules reach a lower rotational temperature than vibrational temperature.

In the experiments performed during the course of this thesis the molecular beam was pulsed in order to achieve the low background pressure quoted above. A commercial pulsed valve (General Valve Series 9) was used which consisted of an electronically driven solenoid with a Teflon tip pulsed against a nozzle diameter of 250 μm. The solenoid, and hence the nozzle opening time and repetition rate, was controlled by a General Valve Iota One pulse driver. The sample gas, consisting of a mixture of 5 % ozone seeded in helium, was introduced into the nozzle system using an all glass backing line at a total backing pressure of 700 Torr. Little decomposition of the sample gas at the metal surfaces of nozzle system was observed and a rotational temperature of 10 - 30 K was achieved in this way.

The advantages of using a molecular beam for studying molecules are numerous. The principal one of these is that the rotational cooling reduces the number of populated internal states of the molecules greatly and hence reduces the number of possible transitions which a molecule can undergo. This simplifies the resulting rotationally resolved spectra and makes them easier to analyse. Also the molecules are studied in a region of the beam where they are free from interaction with other molecules and hence the effects of the carefully introduced light perturbation can be investigated free from other complicating external factors. In terms of the fragment velocity measurements, the investigation of the parent molecules in a highly collimated beam travelling orthogonal to both the laser input axis and the one-dimensional detection axis is essential due to the resulting negligible contribution of the parent molecule velocity to the fragment velocity in the direction of detection.

4.4 General Features of the Time-of-Flight System

The operational modes of the TOF system will be discussed in the following section. However, at this point the general features will be outlined. The starting point of the TOF system consisted of an ionisation and extraction chamber in which the molecules were photolysed and the photofragments ionised and subsequently accelerated by an electric field. The ions then passed through a field free TOF tube at the end of which they were accelerated through a large potential drop and detected by a MicroChannel Plate (MCP) detector.

The ionisation chamber consisted of a small cube of dimension 70 x 70 x 70 mm through the opposing windowed faces of which the outputs of the two counter propagating lasers passed. The remaining four faces are shown schematically in Figure 4.2 and it can be seen that the laser beams travel orthogonally to both the molecular beam and the TOF axis. The major advantage of using such a small chamber was that very short focal length lenses (6 cm) could be used to achieve high power densities in the focal regions of the laser beams. Also the external lenses could be controlled freely with XYZ translators to give the best possible overlap of the two lasers and the molecular beam.

As the nozzle requires an opening time of approximately 250 μs to produce an efficient molecular beam a delay between the triggering of the nozzle and the laser system must be incorporated to achieve temporal overlap. This was attained by ultimately triggering both sources by the nozzle driver but including a Farnell (PG102) pulse generator before the triggering of the laser to produce the required delay and hence to overlap the two in time.

A schematic of the flight path of the ions through the three regions of the TOF system is illustrated in Figure 4.2. This diagram shows the change in the

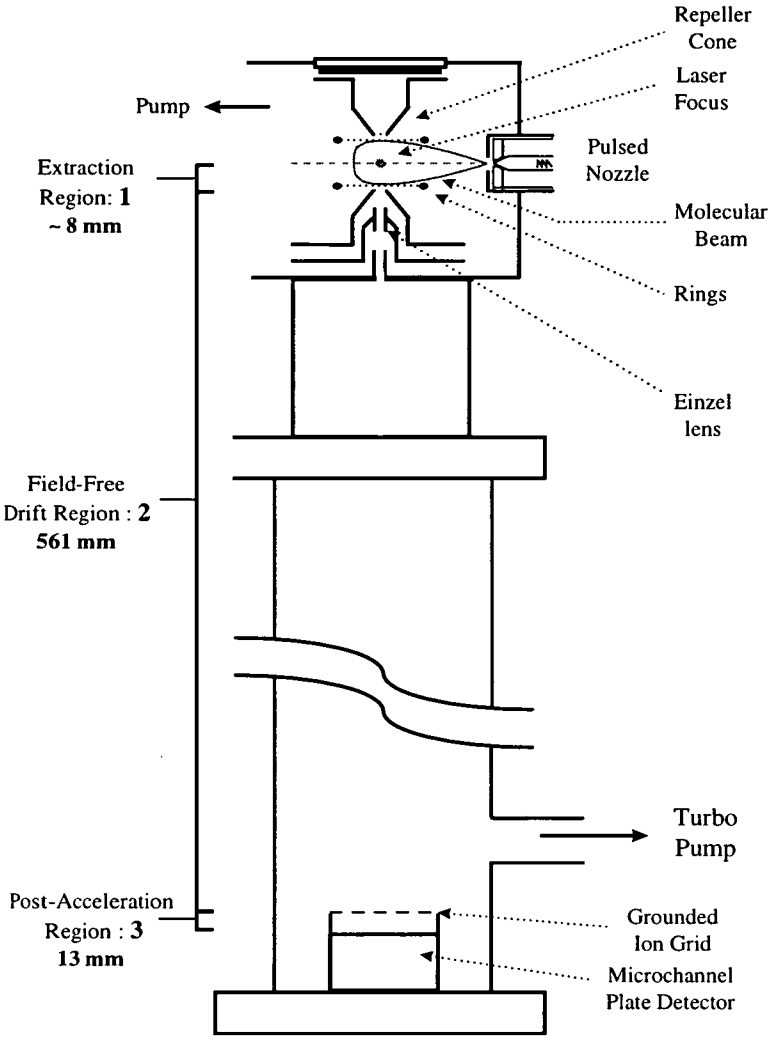

Figure 4.2.: A schematic diagram of the TOF system employed for the experiments of this thesis.

electric field experienced by the ions as they pass through the TOF system. The ions produced by the light interaction with the molecules were accelerated into the field free TOF tube due to a uniform electric field gradient produced by a voltage difference applied across the repeller cone, rings and extraction cone (region 1). The purpose of the rings in the extraction chamber was to provide a uniform field which would otherwise be deformed by the conical shapes of the electrodes. The ions were accelerated through a 2 mm hole in the lower grounded cone into a second region of flight which consisted of field-

free separation of the ions in the TOF tube. An Einzel lens was situated at the beginning of TOF tube. When a voltage was applied to this lens the ions were collimated so that maximum detection efficiency at the detector could be achieved. Finally, a grounded grid 13 mm in front of the MCP, was encountered followed by a large potential drop of $\sim$ 2.4 kV before the ions were detected. A further stepped potential drop was applied across the two micro channel plates so that the signal was amplified at each stage due to the high energy ions/electrons causing a cascade of electrons on collision with the MCP which were designed for this purpose. The resulting electron current was analysed and recorded in different ways depending on the experiment.

4.5 The Mass Spectrometer Mode of Operation

4.5.1 The Time of Flight Equations

The mass spectrometer mode was used when the simple selection of the ion mass was required for probing the spectroscopy of the fragments such as when recording REMPI and PHOFEX spectra. The triggering of the constituent pieces of equipment in this mode is illustrated in Figure 4.1. The most important factor is that the voltages on the extraction optics of the ionisation chamber of the TOF system were applied in a dc manner.

When the extraction optics were operated in this manner, all ions experience the same acceleration force due to the uniform field gradient, E_1, in the extraction region. Effects due to fragment velocities and relative positions of the ions are ignored resulting in the following equations for the time, T_1, T_2 and T_3 spent in each region:

$$T_1 = (2m)^{\frac{1}{2}}(\frac{l_1}{qE_1})^{\frac{1}{2}} \tag{4.1}$$

$$T_2 = (m)^{\frac{1}{2}} l_2 (\frac{1}{2qE_1 l_1})^{\frac{1}{2}} \tag{4.2}$$

$$T_3 = (2m)^{\frac{1}{2}} (qE_3)^{-1} \left[(qE_1 l_1 + qE_3 l_3)^{\frac{1}{2}} - (qE_1 l_1)^{\frac{1}{2}}\right] \tag{4.3}$$

where m is the mass of the ion, q is the unit charge, l_1, l_2 and l_3 are the lengths of the flight paths in each region of the TOF system and E_1 and E_3 are the field gradients in regions 1 and 3. The effect of the field gradient on the ions as they move through these three regions of the TOF are illustrated in Figure 4.3 where the acceleration voltage experienced by the ions is graphed against the time of flight.

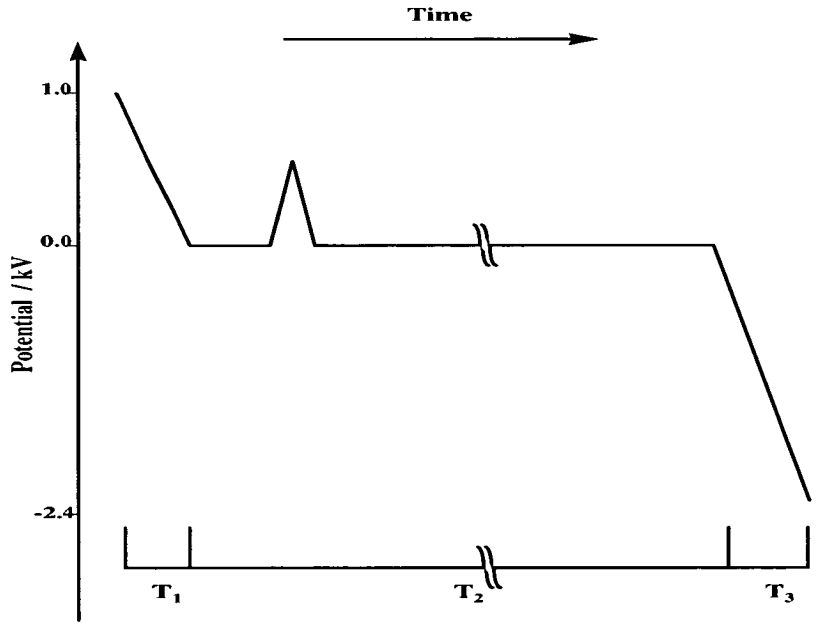

Figure 4.3.: A schematic illustration of the flight path of ions in the mass spectrometer mode. The voltage potentials experienced by the ions are plotted against Time-of-Flight where T_1 T_2 and T_3 are the times spent in regions 1, 2 and 3 of Figure 4.2

The important point to be noted from these equations is that T_1, T_2 and T_3 all vary with the square root of the mass of the ion. Therefore, when all other parameters are kept constant the ions separate during their flight

path solely due to their masses thus fulfilling the basic premise of linear mass spectrometry. A further point to be noted is that the recorded TOF spectra are offset relative to the true time of flight due to the triggering of the oscilloscope not corresponding exactly with the laser pulse. However, this problem can be easily overcome by reducing the three equations above to the following equation:

$$T = A(m)^{\frac{1}{2}} - \Delta T \tag{4.4}$$

where all of the constants of equations 4.1, 4.2 and 4.3 are gathered into a single unknown, A. This equation can be used to calibrate the entire TOF once the time of arrival of two different ions of known mass are identified and substituted into equation 4.4 which can hence be solved to yield A and ΔT.

It should also be noted that the Einzel lens represented as a small 'bump' at the beginning of the field free region in Figure 4.3, had the effect of collimating the ion packet to ensure that all the ions were detected at the MCPs. The effect on the time of flight can be ignored for the purposes of the above calibration procedure.

Signal Processing

The method used for signal processing of the TOF system when operated in this mode utilised a Stanford Research Systems (SRS) SR250 gated integrator and boxcar averager. The gated integrator is adjustable from a few ns to 100 ms relative to the external trigger. The trigger source used for the boxcar was the synchronous electronic output of the excimer laser which gave a voltage output ~ 2.2 μs before the light pulse. This gave rise to the need to calibrate the TOF spectrum as indicated above. The width of the gate was also adjustable and so a specific mass peak in the TOF spectrum could be selected and integrated as the laser light was scanned to produce a spectrum of the intensity of the mass peak versus the wavelength of the laser. The integration was performed by a fast gated integrator which normalised the output over the

gate width and averaged this output over a variable number of shots, typically 10 or 30, to achieve the required S/N ratio for the resultant spectrum.

The change of signal intensity with laser wavelength was simultaneously recorded on chart paper and personal computer (PC) and monitored on an oscilloscope (LeCroy 9344C 500MHz) . The SRS SR250 was interfaced to the PC with an SR265 computer interface and the data were manipulated using software of the same name.

4.6 The Translational Spectrometer Mode of Operation

4.6.1 Additional Equipment and Timing Changes Required

The essential new component required for the operation of the spectrometer in the translational mode was the hardware required to pulse a high voltage onto the extraction ion optics with a very fast rise-time of < 20 ns. The Behlke GHTS60 high voltage push-pull switch fulfils these requirements and was triggered externally with a voltage of > 2 V. The incorporation of this high voltage switcher with the triggering of the other integral parts of the system for the translational spectrometer mode is shown in Figure 4.4.

A new timing technique was required to circumvent difficulties caused by a large electronic jitter between the synchronous voltage and light outputs of the excimer laser. A fast rise-time photodiode was used for this purpose as indicated in the schematic. The advantage of the photodiode is that the electronic jitter is reduced to $\pm$ 2 - 3 ns and hence, when the TOF profile was averaged over many shots, little resolution was lost.

The analogous flight path to that shown for the mass spectrometer mode in Figure 4.3 is illustrated for the translational mode in Figure 4.5. It should

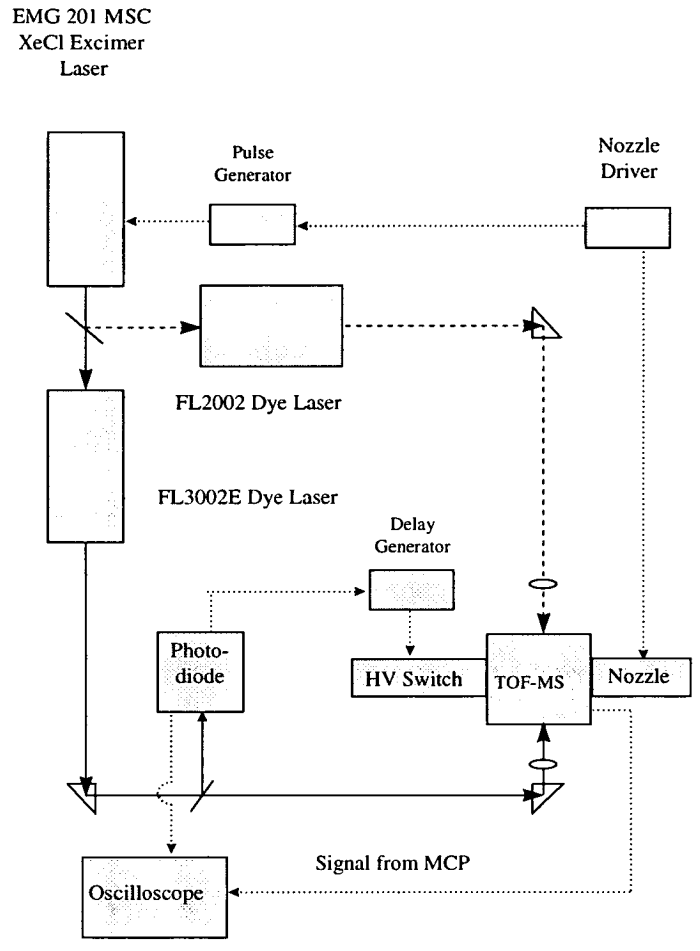

Figure 4.4.: The schematic diagram illustrating the experimental set-up used for REMPI and PHOFEX experiments.

be noted that the Einzel lens used in the mass spectrometer mode is no longer used in this mode as this has the effect of deforming the ion packet during the flight path.

4.6.2 The Time of Flight Equations

The inclusion of the time delay between the laser pulse and the extraction voltages created a complication of the TOF equations which has to be modelled. A look at Figure 2.6 of the Chapter 2 illustrates that, in the trans-

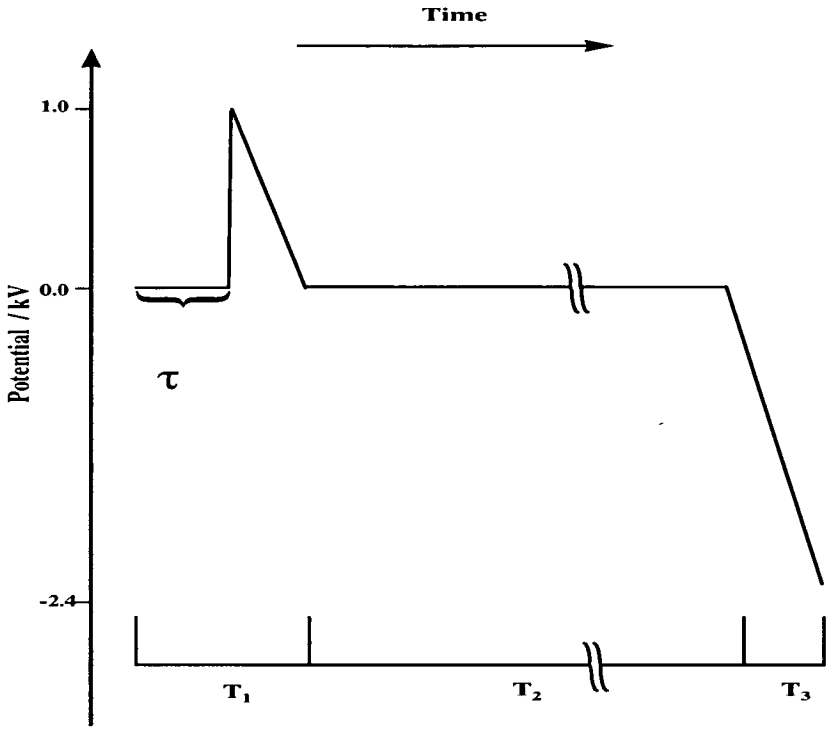

Figure 4.5.: The flight path diagram for the translational spectrometer mode equivalent to that shown in Figure 4.3 for the mass spectrometer mode. τ is the time delay between the light pulse and the voltage pulse applied to the extraction ion optics.

lational mode, the TOF is not simply proportional to the mass of the fragment ions but is also related to the velocity given to them by the photodissociation event.

To reconsider the TOF equations it is necessary to examine the effect which ions moving towards and away from the detector have on the TOF, see Figure 4.6. The fragments which recoil away from the detector spent a longer time in the acceleration field and gain an extra amount of kinetic energy, $qE_1v_z\tau$, where $v_z\tau$ is the extra distance which the ions have to travel in the field. Conversely, ions which recoil towards the detector spend less time in the field and must have this amount of kinetic energy subtracted from the total amount of kinetic energy which is gained. Therefore, the fragments have a kinetic energy (K_1) when they reach the grounded electrode at the beginning of the field free time of flight section determined by equation 4.5.

$$K_1 = qE_1 l_1 \pm qE_1 v_z \tau + \frac{1}{2} m v_z^2 \tag{4.5}$$

where v_z is the velocity component of the fragments along the TOF axis and τ is the time delay between light and electrode voltage pulses. The sign of $qE_1 v_z \tau$ is determined by whether the fragments are recoiling away from (+) or towards (-) the detector.

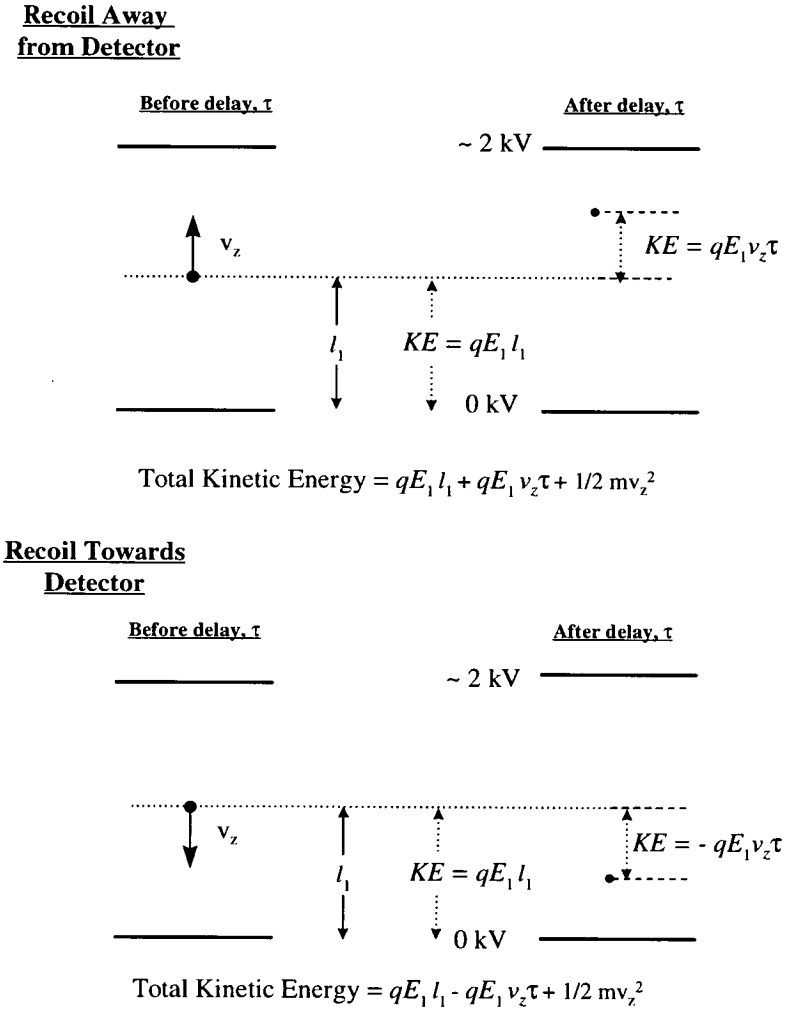

Figure 4.6.: An illustration of the kinetic energy accessed by ions which are allowed to recoil away from and towards a detector during a time delay, τ, prior to switching on a field gradient, E_1. See text for details.

Including this in the TOF equations results in the following equations for the three stages of the flight path:

$$T_1 = (2m)^{\frac{1}{2}}(qE_1)^{-1}(K_1^{\frac{1}{2}} \pm \frac{1}{2}mv_z^2) + \tau \tag{4.6}$$

$$T_2 = (m)^{\frac{1}{2}}\, l_2\, (\frac{1}{2K_1})^{\frac{1}{2}} \tag{4.7}$$

$$T_3 = (2m)^{\frac{1}{2}}\,(qE_3)^{-1}\left[(K_1 + qE_3l_3)^{\frac{1}{2}} - (K_1)^{\frac{1}{2}}\right] \tag{4.8}$$

where the sign in equation 4.6 is linked to that in equation 4.5. It can be seen that when $\tau = 0$ and the effect of v_z was assumed to be negligible these equations reduce to equations 4.1, 4.2 and 4.3. The $\pm\, qE_1v_z\tau$ term contained within the K_1 variable accounts for the broadening and eventual splitting of each mass peak due to the velocity given to those fragments following dissociation, v_z.

4.6.3 Signal Processing and Detection

Unlike the signal processing for the mass spectrometer mode the laser wavelengths were kept constant when recording a TOF profile which means that the boxcar integration step is unnecessary. Therefore, the signal from the MCPs was directly channelled to the oscilloscope which has a shot averaging capability to increase the S/N ratio of the profiles. This is a crucial aspect as the laser powers used in these experiments had to be kept quite low to avoid the creation of a plasma of ions which recoil under the effects of coulombic repulsion and would result in the loss of the velocity information of the photodissociation event. In a typical experiment each shot only produced a small number of ions and therefore the spectra had to be averaged over a large number of shots (300 - 5000) to generate the total profile. The profiles were recorded as a function of intensity versus TOF and transferred from the oscilloscope to a floppy drive in ASCII format for further processing.

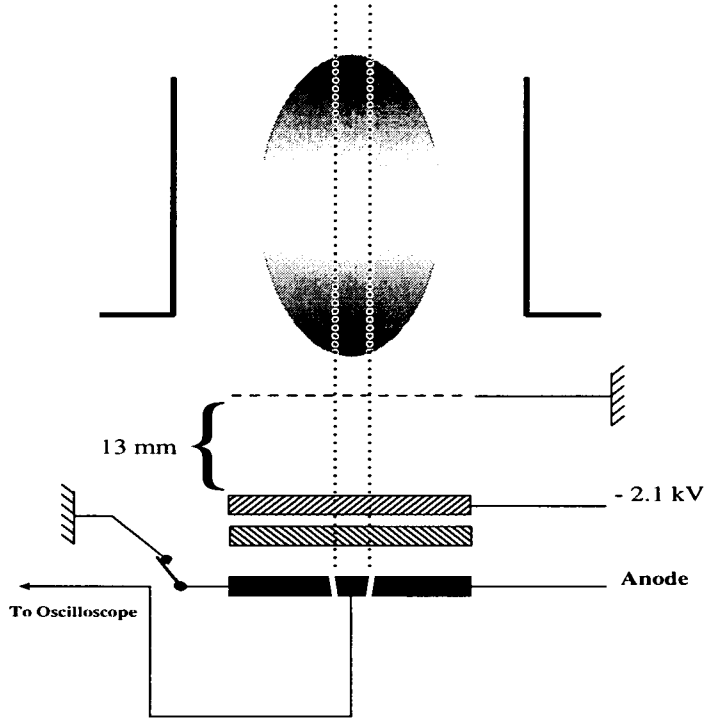

Figure 4.7.: A schematic illustration of how the core-extraction of the ion packet was achieved.

Another modification of the signal detection arose from the fact that only the v_z velocity component of the fragments can be calculated from the TOF and therefore it was convenient to modify the experiment so that only these fragments were detected. This was achieved by modifying the detector to create a position sensitive detection system which could select ions which had their initial recoil velocities along the TOF axis, z, i.e. only the central part of the spherical ion packet was detected. To achieve this aim the anode lying behind the MCPs was segmented as illustrated in Figure 4.7 such that ions impinging on the central 8.5 mm diameter part of the anode could be selectively detected and the signal from the rest of the ion packet discarded. The central part of the anode was insulated from the outer ring and connected in parallel so that the ion signal could be channelled either just from the inner

part or from both sections of the anode to give the total signal. To ensure that the centre of the ion packet coincided with the centre of the anode a set of orthogonal deflection plates were placed in the TOF tube to guide the ion packet. The entire process of detecting only the central part of the ion packet is referred to as core-extraction.

4.6.4 Calibration of the Instrument for use as a Translational Spectrometer

The requirement of calibration arises from the number of unknown parameters in the TOF equations 4.6, 4.7 and 4.8 [5]. While l_2 (= 561 mm), l_3 (= 13 mm) and τ could all be measured with sufficient accuracy, the values of E_1, the field gradient in the extraction region, E_3, the field gradient in the final acceleration stage and l_1, the distance from the laser focal point to the entrance of the field free TOF, could only be approximately determined for each experiment. Of course the desired parameter, v_z, which had to be calculated is intrinsically not known in such an experiment, however, a dissociation process could be selected where this parameter is well characterised and thus could be used in a calibration procedure to determine the unknown parameters to be used in further experiments. The dissociation of O_2 at 225.65 nm was a suitable process for this requirement and it also had the advantage that the wavelength of the dissociation laser selectively ionised the $O(^3P_2)$ fragments formed *via* a (2 + 1) REMPI scheme [6]. As the dissociation of a diatomic results in two atomic species which could only have electronic internal energy and translational energy, the translational energy could be calculated from a simple energy balance equation:

$$E_t = nh\nu + E_{int}(parent) - D_0(O-O) - E_{elec} \qquad (4.9)$$

where E_t is the translational energy of the atomic fragment, n is the

number of photons absorbed, $h\nu$ is the energy of the dissociating photon, $E_{int}(parent)$ is the internal energy of the parent O_2 molecule prior to dissociation, $D_0(O-O)$ is the dissociation energy of the O_2 bond and E_{elec} is the electronic energy of the fragments. The values of $h\nu$, $D_0(O-O)$ and E_{so} were known from the laser wavelength, thermodynamic studies of the bond dissociation energy and atomic spectroscopy respectively. Also, it was assumed that the $E_{int}(parent)$ was negligible as all experiments were carried out in a molecular beam where the range of internal energy states of the parent was minimised by the jet-cooling effect. Therefore the E_t and hence v_z of the atomic fragments could be accurately determined.

An additional advantage of choosing this system was that two processes occur involving the absorption of either one or two photons by the O_2 molecule prior to dissociation as illustrated by the REMPI schematics shown in Figure 4.8. Therefore two well defined velocity distributions of the $O(^3P_2)$ fragments were observed for which the velocity of the fragments could be calculated using equation 4.9. These velocities were determined as $v_z = 1523$ ms^{-1} for $n = 1$ and $v_z = 4856$ ms^{-1} for $n = 2$, providing essentially a double calibration method.

By aligning the electric field vector of the dissociating light, E_{photo}, parallel to the TOF axis the principal velocity component of the $O(^3P_2)$ fragments could be directed along the TOF axis as the absorption process is dominated by a parallel transition in O_2 [6]. A further experimental variable was the time delay between the laser pulse and the extraction voltage, τ. The TOF spectra of the O^+ ions recorded following photolysis of O_2 at 225.65 nm as a function of τ are shown in Figure 4.9. It should be noted that these profiles are only partially core-extracted to allow sufficient intensity of the high velocity component of the profiles recorded for large values of τ.

The two inner peaks in each of the profiles corresponds to the recoiling $O(^3P_2)$ fragments formed by the one-photon photolysis of O_2, process 1 shown in Figure 4.8, while the outer peaks are due to the two-photon process, process

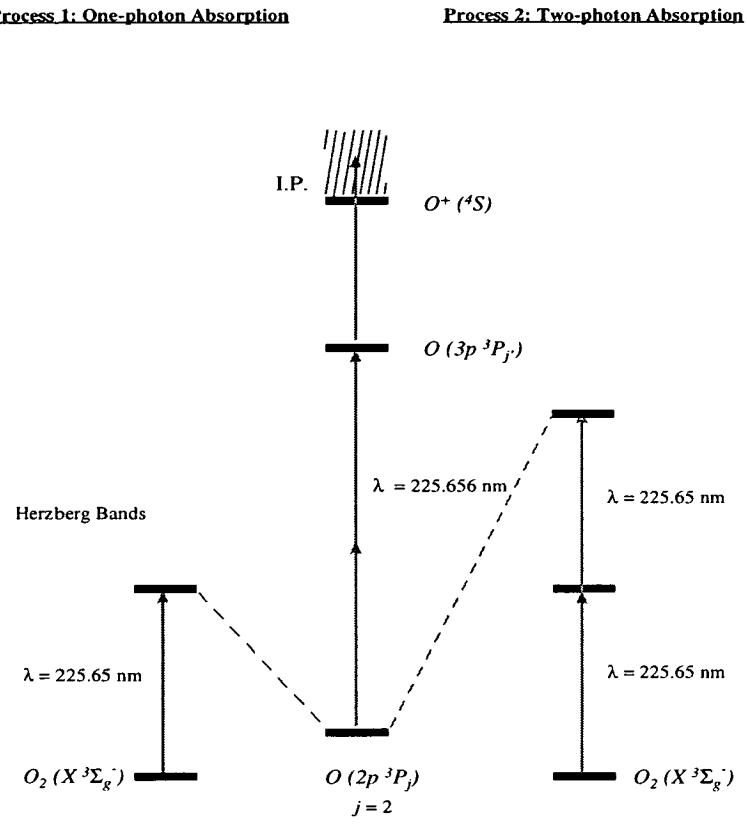

Figure 4.8.: REMPI processes involved in the calibration experiment using the photolysis of O_2 and REMPI detection of the $O(^3P_2)$ fragments.

2. The early arrival peaks correspond to fragments which initially recoiled away from the detector and have a +ve sign in equations 4.5 and 4.6 and hence are designated by the symbol, T_+, while the late arrival times are designated T_-. These values were taken from the profiles of Figure 4.9 for a range of values of τ.

To reduce the number of free parameters in the fitting process the value of E_3 was estimated from the voltage applied to the electrodes in the final stage of the flight path of the ions. This is justified by the fact that the final part of the time of flight, T_3, constitutes < 2 % of the total flight time and hence a small error due to the estimation of E_3 will result in a negligible error in the calculation of the total flight time, T. In fact, to make the fitting procedure

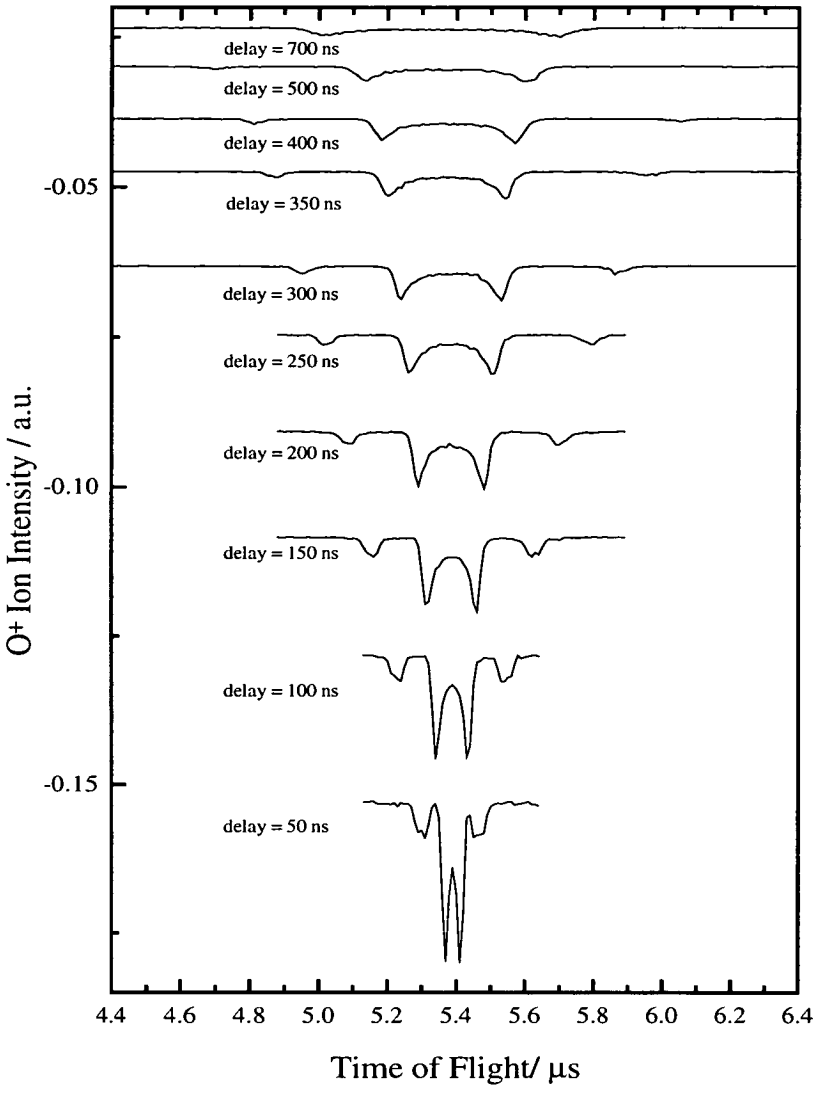

Figure 4.9.: The Time-of-Flight profiles of O^+ ions formed *via* processes 1 and 2 of Figure 4.8 shown as a function of time delay, τ.

more efficient it was sufficient to estimate T_3 and subtract this from the total flight time before fitting to the more simple two stage equation.

Therefore, only two free variables remain: E_1 which remained constant for all experiments as the voltages on the extraction electrodes were kept constant, and l_1 which depends on the laser focus position within the extraction region which changed with each laser realignment. However, provided E_1 could be determined accurately, l_1 could be calculated in subsequent experiments using a method described in the following section.

To determine these parameters the graphs of T_+ vs τ and T_- vs τ were

fitted by a least squares method to the two stage TOF equations 4.6 and 4.7. This process alone did not prove satisfactory for finding a unique fit to the data. The reason for this is most likely to be due to the extreme sensitivity of the fitting procedure to the value of l_1. To aid the fitting procedure it was necessary to also fit the time separation of the early and late peaks, T_- - T_+, as a function of τ. The equation used for this purpose is shown below and was derived in a similar way to equations 4.6 and 4.7 but instead of considering the kinetic energy of the fragments, the acceleration, a_1, experienced by the ions as a function of position within the extraction region was used.

$$T_- - T_+ = \frac{v_z}{l_1}\left(\frac{l_2}{\sqrt{2a_1l_1}} - \frac{\sqrt{2a_1l_1}}{a_1}\right) \tag{4.10}$$

where $a_1 = qE_1/m$ was the acceleration experienced by the ion in the extraction region. The optimum procedure was found to keep l_1 constant and to fit E_1 using equations 4.6, 4.7 and 4.10. The fitted values of E_1 using these three equations can then be plotted against the value used for l_1 as shown in Figure 4.10 for the two-photon calibration data. An accurate value of E_1 = 126000 V m^{-1} was found in this way. The accuracy of this final value of E_1 was validated by a method described in the following section.

It should be noted that a slight asymmetry of the peak separations observed as the time delay increases was not predicted by equations 4.6 and 4.7 and is most likely to be due to non-uniformities of the field in the extraction region. Interestingly this asymmetry of the TOF profile was observed by another group using a similar method [5] but with very different extraction optics.

4.7 Calculation of the Translation Energy from TOF Profiles

Although the velocity data could conceivably have been extracted using

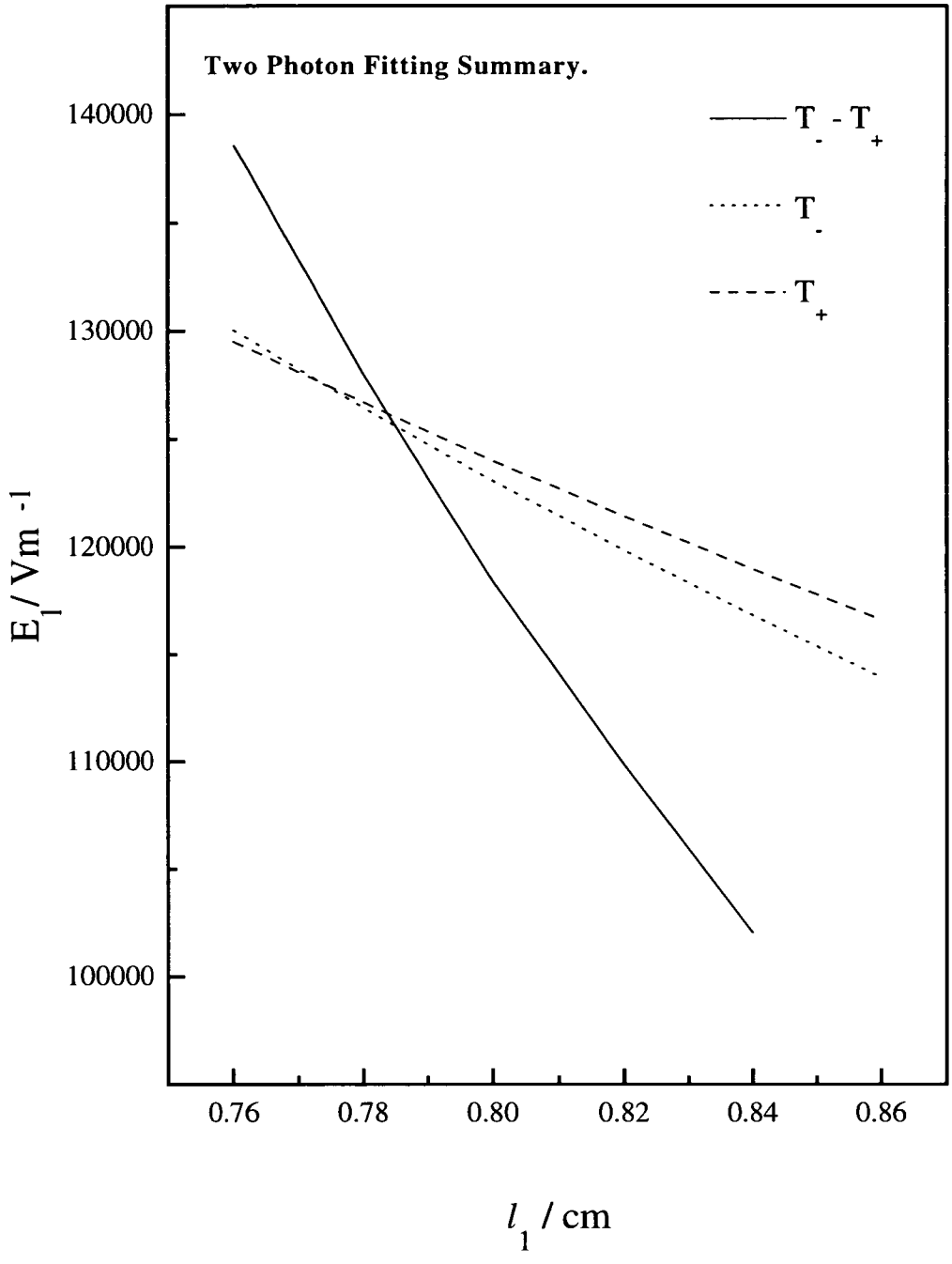

Figure 4.10.: The results of the fitting procedures for the two-photon peaks in Figure 4.9. See text for details.

the fitting procedure outlined in the previous section it was found to be more computationally efficient to calculate v_z in a slightly different manner. Equation 4.11 which shows an expression for the early and late arrival times peaks due to ions accelerated through a two stage time of flight was derived in a similar way to equation 4.10.

$$T_{+/-} = \frac{1}{a_1}\left(-v_z + \sqrt{v_z^2 + 2a_1(l_1 \pm v_z\tau)}\right) + \frac{l_2}{\sqrt{v_z^2 + 2a_1(l_1 \pm v_z\tau)}} + \tau \tag{4.11}$$

This equation is equivalent to equations 4.6 and 4.7 used in the fitting procedure of the calibration method. But before solving this equation it is necessary to know the value of l_1 which depends on the experimental conditions. This parameter could be calculated first by using the zero delay TOF where the two stage TOF equation 4.11 reduces to

$$T_1 + T_2 = \frac{1}{a_1}\sqrt{2a_1l_1} + \frac{l_2}{\sqrt{2a_1l_1}} \tag{4.12}$$

under conditions where $v_z^2 << 2a_1l_1$ which is valid for the system here. Due to the large value of a_1, the v_z^2 parameter could be ignored. The resulting equation could be solved for l_1.

The full two stage TOF equation, 4.11, was then solved using a FORTRAN77 program which has been written in this group [7]. This program could be used to convert an entire TOF flight spectrum to the v_z components of the fragments provided the arrival time for zero delay was known.

This method was used to validate the calibration procedure described in the previous section by solving the TOF equation above for the 300 ns delay TOF profile shown in Figure 4.11. The calculated profile can be seen to correspond very well with to the known velocity release values of these processes with an estimated error of < 5 %.

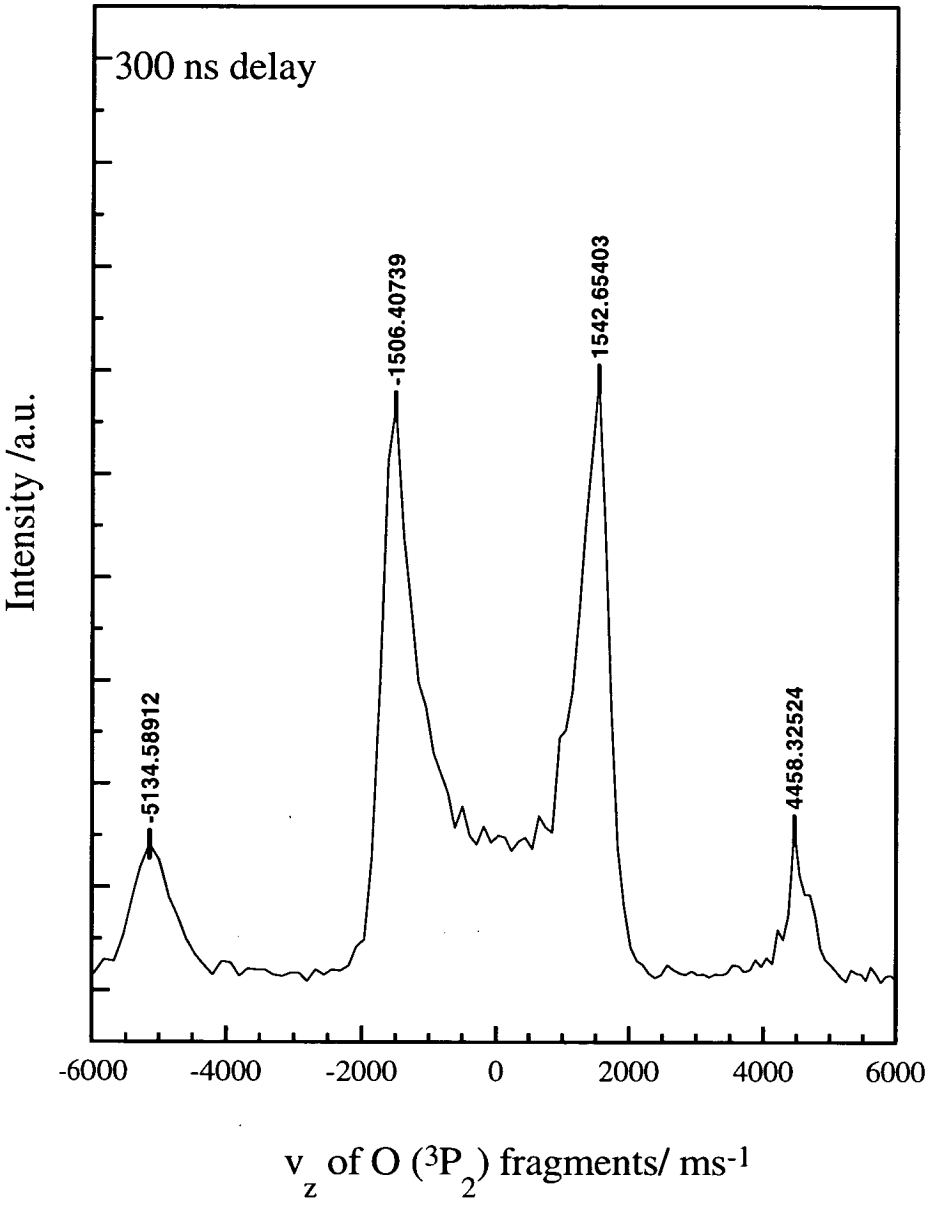

Figure 4.11.: The calculated velocity release of fragments from the 300 ns delay Time-of-Flight profile of Figure 4.9. The peak velocities compare well with the theoretical values of 1523 ms^{-1} and 4856 ms^{-1} for the one and two-photon processes respectively.

4.8 Angular Distributions of the Photofragments

The O_2 photolysis at 225.65 nm has also been examined by other groups using the velocity mapping technique described briefly in the previous chapter to investigate the angular properties of the $O(^3P_2)$ fragments formed [6]. Hence, this process also provided an ideal way to examine the capabilities of the experimental equipment used here for measuring such properties of photofragments. Unlike the velocity mapping experiments the one-dimensional translational method used here requires at least two experiments to determine the photofragment angular distribution. It was necessary to measure the TOF profiles when the electric field vector of the photolysis light, E_{photo} was both parallel and perpendicular to the TOF axis, z, where the measured intensities are $I_{0°}$ and $I_{90°}$ respectively. The anisotropy parameter, β, was then calculated using equation 2.15 given in Chapter 2 [5, 8].

In this case it was essential to perform core-extraction of the ion packet to separate the angular and translational components of the photodissociation process. The effect of core-extraction is reflected in the much sharper peaks due to the fragments recoiling towards and away from the detector. Also, the resulting low intensity due to the discrimination against most of the ion packet means that the peaks due to process 2, the two-photon fragmentation process, were no longer intense enough to be analysed. The profiles for the $O(^3P_2)$ fragments are shown in Figure 4.12 for a 200 ns delay along with the β parameters calculated for this process.

The large difference between the TOF times of these fragments compared with those shown for the same delay in the calibration data in Figure 4.9 is due to the change of the laser position within the extraction region and hence the change in the value of l_1. The β parameter measured using this method does match the values observed by Buisse *et al.* [6] as indicated in the detailed

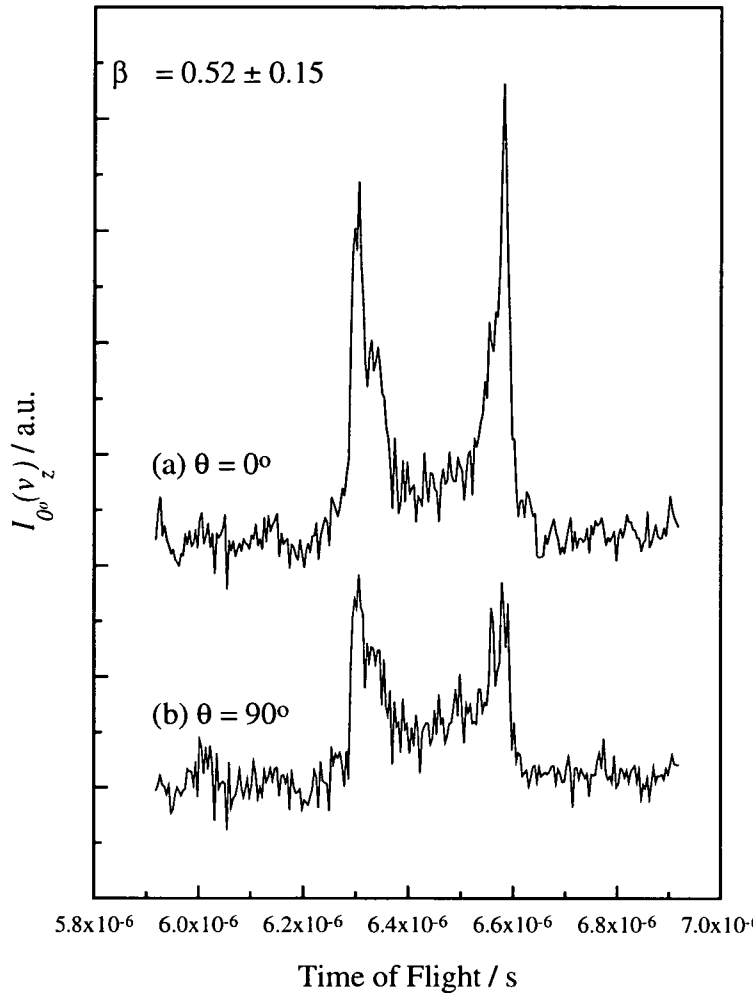

Figure 4.12.: The core-extracted TOF profiles recorded following the photolysis of O_2 with one photon with a wavelength of 225.65 nm and detecting the $O(^3P_2)$ fragments. Profile (a) is the core-extracted profile where the electric field vector of the dissociating light, $\vec{E}$, is parallel to the TOF axis while profile (b) is due to the laser polarisation geometry where $\vec{E}$ is perpendicular to the TOF axis.

comparison shown in Table 4.2. The large errors quoted in the β parameter are due to the difficulty in measuring the intensity of the peaks.

A more accurate method was to vary the angle of E_{photo} relative to z and to plot this angle against the intensities observed in the TOF profile as illustrated in Figure 4.13. A least squares fit of the resulting plot produces a smaller error in the quoted value of β and a closer agreement with the work of Buisse *et al.*. A double Fresnel rhomb was used to vary the angle of the linearly polarised light to any desired angle. The angle of E_{photo} was checked using a second polariser. Similar measurements were also made for the $O(^3P_1)$

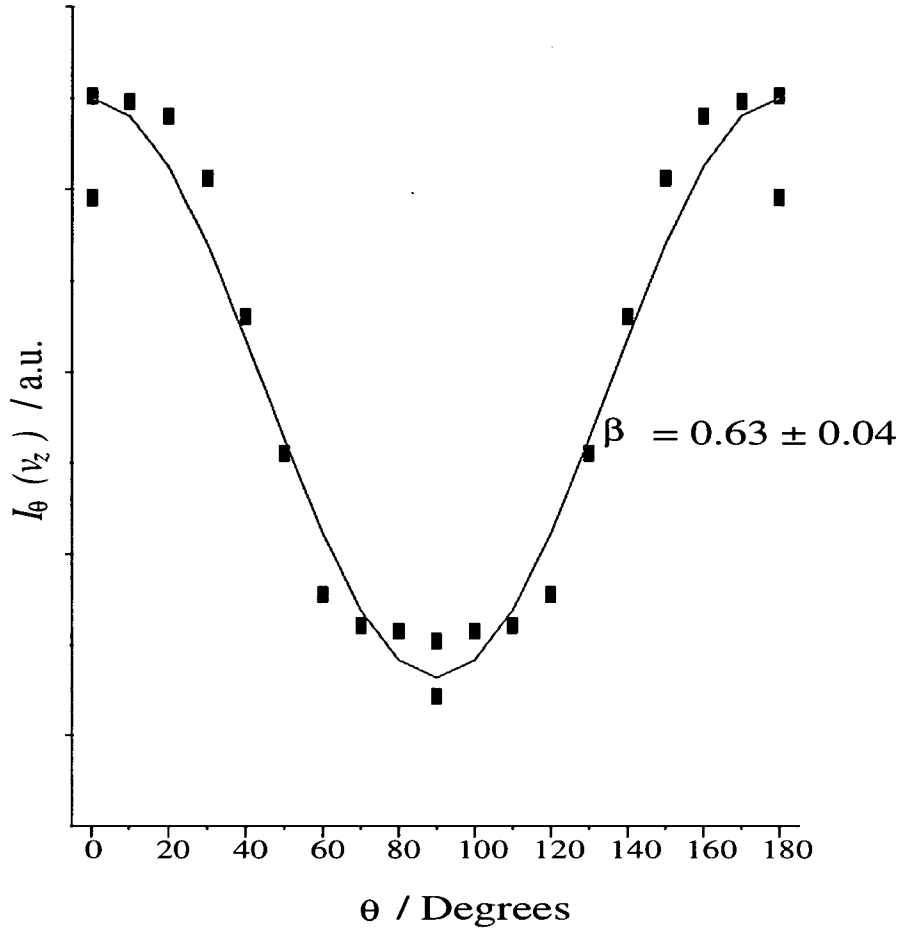

Figure 4.13.: Plot of intensity of the early and late one-photon (process 1 of Figure 4.8) peaks of the core-extracted profiles, I_θ versus the angle which the linearly polarised photolysis light makes with the TOF axis, θ.

$O(^3P_j)$	Wavelength /cm^{-1}	Measured β Parameter Ref [6]	$I_{0°}$ and $I_{90°}$	θ vs I_θ
$j = 2$	225.65	0.64 ± 0.08	0.52 ± 0.15	0.63 ± 0.04
$j = 1$	226.15	0.61 ± 0.09	0.58 ± 0.15	—

Table 4.2.: A comparison of the measured β parameters for $O(^3P_j)$ fragments produced in the photolysis of O_2 at 225.65 and 226.15 nm respectively.

fragments and also compared with the literature values in Table 4.2.

These experiments reveal that the methods used in this thesis can accurately measure the angular distribution of photofragments produced in one-photon photolysis processes.

References

[1] *Lambda Physik EMG201 - 204 Instruction Manual* (1985) Gottingen.

[2] *Lambda Physik FL3001/2 Instruction Manual* (1986) Gottingen.

[3] G. C. Balwin, *An Introduction to Non-Linear Optics* (1969) Plenum Press, New York.

[4] G. Scholes, *Atomic and Molecular Beam Methods, Vol. 1* (1988) Oxford University Press.

[5] H. J. Hwang, J. Griffiths and M. A. El-Sayed. *Int. J. Mass Spec. and Ion Proc.* **131** (1994) 265.

[6] B. Buijsse, W. J. van der Zande, A. T. J. B. Eppink, D. H. Parker, B. R. Lewis and S. T. Gibson, *J. Chem. Phys.* **108** (1998) 7229.

[7] Fortran77 program written by K.P. Lawley.

[8] J. A. Syage. *J. Chem. Phys.* **105** (1996) 1007.

Chapter 5

Kinetic Energy Analysis of the O ($^3P_0$) Photofragments

5.1 Introduction

The photodissociation dynamics of ozone were reviewed briefly in Chapter 3 where it was observed that the accessible UV dissociation channels of ozone are channels (A) to (E) shown below. The thermodynamic threshold of each channel is also indicated.

(A)	O_3	+	$h\nu$	$\rightarrow$	$O(^3P_j)$	+	O_2 $(X\,^3\Sigma_g^-)$	(1178 nm)
(B)				$\rightarrow$	$O(^3P_j)$	+	O_2 $(a\,^1\Delta_g)$	(612 nm)
(C)				$\rightarrow$	$O(^3P_j)$	+	O_2 $(b\,^1\Sigma_g^+)$	(463 nm)
(D)				$\rightarrow$	$O(^1D)$	+	O_2 $(X\,^3\Sigma_g^-)$	(411 nm)
(E)				$\rightarrow$	$O(^1D)$	+	O_2 $(a\,^1\Delta_g)$	(310 nm)

The detection of the $O(^1D)$ [1, 2, 3, 4, 5, 6, 7] and O_2 $(a\,^1\Delta_g)$ [4, 8, 9] fragments has been used to characterise the dissociation of ozone in the Huggins band region (> 310 nm) *via* channels (B), (D) and (E). The only other fragments which have been detected following the photolysis of ozone in this region are the $O(^3P_2)$ fragments. Takahashi *et al.* [3, 10] reported the

vacuum ultraviolet Laser Induced Fluorescence (VUV LIF) detection of the O($^3P_2$) fragment *via* the $3s\ ^3S_0 \leftarrow 2p\ ^3P_2$ resonance line at 130.22 nm. The intensity of the emitted light was recorded as a function of the photolysis laser wavelength to yield a PHOFEX spectrum of the O($^3P_2$) fragments. The spectra recorded in this manner were reported for sample temperatures of 298 and 227 K [3]. Both of these spectra exhibited structure similar to that in the absorption spectrum of ozone. They used the wavelength dependent yield of these O($^3P_2$) fragments in their determination of the Φ (O(^1D)) for the Huggins bands region. However, due to the relatively large linewidth (0.6 cm^{-1}) of the VUV probe laser used in this study it was not possible to extract resolved velocity information from the Doppler profiles of the resonance line. Nonetheless, it was noted that the O($^3P_2$) fragments were produced in translational hot states.

In this chapter high resolution velocity data and angular information of the O($^3P_0$) fragments produced at a specific wavelength within the Huggins bands is presented.

5.2 PHOFEX Spectrum of O($^3P_0$)

The equipment was operated in the mass spectrometer mode with a two laser set-up when recording these spectra. Spectrum 5.1 shows the PHOFEX spectrum of the O($^3P_0$) fragments recorded *via* the O ($3s\ ^3P_j \leftarrow\leftarrow 2p\ ^3P_0$) (2 + 1) REMPI transition at 226.23 nm. This will be discussed in detail in Chapter 7. It can be seen that the peaks in this spectrum reproduce those in the absorption spectrum shown in the upper trace of Figure 5.1. The three arrows indicate the wavelength at which TOF profiles were recorded, two correspond to peak band maxima and the third to an off-resonance wavelength. The vibrational assignment of the discrete features observed in the PHOFEX spectrum are not included as this is discussed in depth in Chapter 7 of this

thesis.

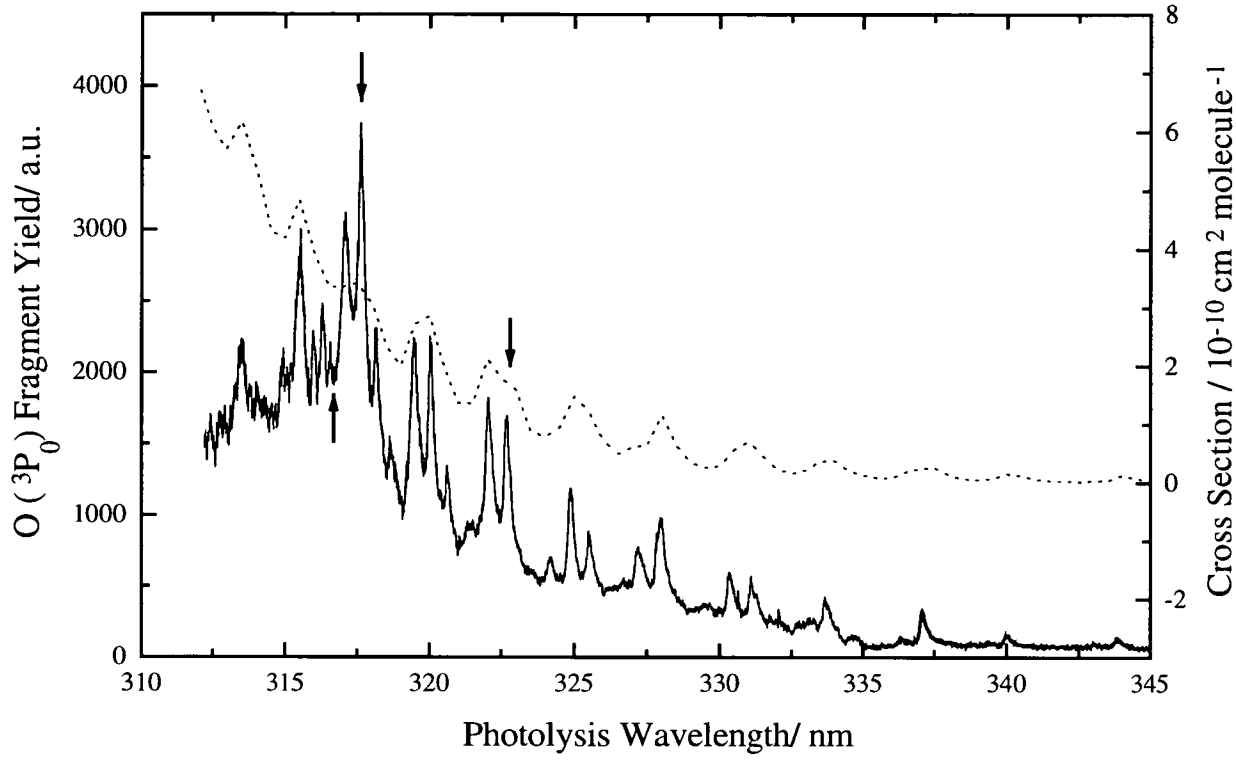

Figure 5.1.: The full line is the PHOFEX spectrum of the Huggins band recorded by detecting the O($^3P_0$) fragments *via* the O ($3s\ ^3P_j \leftarrow\leftarrow 2p\ ^3P_0$) (2 + 1) REMPI transition following photolysis of ozone between 312 and 345 nm. The dotted line is the 226 K absorption data of Molina [11].

5.3 Velocity Release Profiles

The velocity release profiles shown in Figures 5.2 (b) and (c) are the core-sampled profiles of the O($^3P_0$) fragments recoiling from O_3 photolysed at 322.64 nm, which corresponds to an intense band in the PHOFEX spectrum and is arrowed in Figure 5.1. The profiles were recorded by summing over 3000 laser shots with a 200 ns delay between the laser pulse and the high voltage extraction pulse. Both profiles were recorded with the polarisation of the

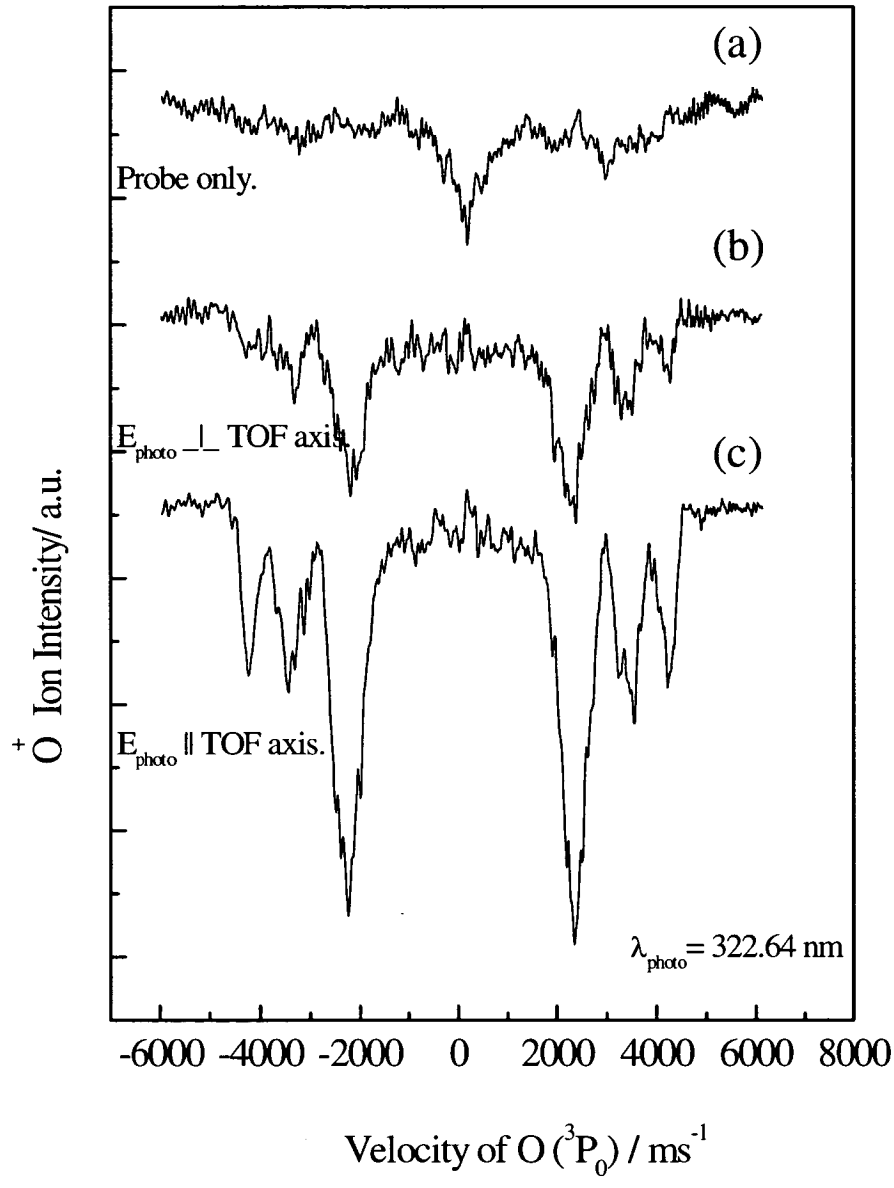

Figure 5.2.: The core-extracted velocity profiles of the O($^3P_0$) fragments produced by the 322.62 nm photolysis. The signal due to the probe laser alone is shown in (a) and is due to production of O($^3P_0$) fragments by probe laser photolysis. This background has already been subtracted from the profiles shown in (b) and (c) which are the profiles recorded by photolysing at 322.64 nm with the polarisation of the photolysis laser perpendicular and parallel to the TOF axis, respectively.

probe perpendicular to the TOF axis, hence the $O(^3P_0)$ fragments resulting from photolysis of O_3 at the probe photon wavelength of 226.23 nm recoil predominantly perpendicular to the detection axis and therefore appear with a velocity release ~ 0 ms^{-1}. The signal due to these $O(^3P_0)$ fragments, which is shown in Figure 5.2 was recorded by averaging the signal of the probe laser only and comprises $< 15\%$ of the total signal. This was achieved by careful adjustment of the spatial overlap of the lasers and the relative powers of the pump (~ 1 mJ) and the probe (< 0.2 mJ) laser powers. This signal was then subtracted from the raw profiles resulting in those shown in Figures 5.2 (b) and (c). The resulting TOF profiles were calibrated and converted to velocity distribution by the procedure outlined in the previous chapter.

The profiles recorded with the polarisation of the photolysis laser both perpendicular and parallel to the TOF axis show trimodal velocity distributions of $O(^3P_0)$ fragments with velocity peaks corresponding to 2380 ms^{-1} (FWHM 600 ms^{-1}), 3430 ms^{-1} (FWHM = 500 ms^{-1}) and 4225 ms^{-1} (FWHM = 370 ms^{-1}).

5.4 Internal Energy of O_2 Co-fragments

5.4.1 Calculation of Internal Energy Distribution of Co-fragments

Based on the core-sampling approximation, the velocity release profiles of the $O(^3P_0)$ fragments can be converted to an internal energy distribution of the O_2 co-fragments using a procedure described by Syage [12]. The velocity profiles shown in Figure 5.2 only involve fragments which recoil either at 0° or 90° with respect to E_{photo}. To calculate an internal energy distribution of the co-fragments it is necessary to know the velocity distribution of the fragments averaged over all of the possible recoil angles. This information can

be extracted from the core-sampled profiles by first calculating the anisotropy parameter which characterises the angular distribution of the fragments for the one-photon photolysis process using equation 2.15 of Chapter 2. The angle averaged velocity distribution, $P(v)$, can then be calculated using the following relationship [12]:

$$P(v) \quad \propto \quad \frac{v_z^2 \, I_0(v_z)}{1 \, + \, \beta(v_z)} \tag{5.1}$$

where v_z is the velocity along the direction of the TOF axis ($v \approx v_z$ in the core-sampling limit), $I_0(v_z)$ is the intensity of the TOF profile when the $E_{photo} \parallel z$ and $\beta(v_z)$ is the speed dependent anisotropy parameter. Therefore, once the anisotropy of the process is known the angle averaged speed distribution can be calculated from a single profile.

Finally, the angle averaged translational energy distribution can be calculated from $P(v)$ using the proportionality shown in equation 5.2 [12].

$$P(E_t) \quad \propto \quad \frac{P(v)}{v} \tag{5.2}$$

where $P(E_t)$ is the intensity distribution of the translational energy of the fragments. The internal energy of the co-fragment can then be calculated using the conservation of energy and momentum which result in equation 5.3.

$$\begin{aligned} E_{int} &= E_{avl} - E_{trans} \\ where \quad E_{avl} &= h\nu - D_0(O_2 \cdots O) \\ and \quad E_{trans} &= \tfrac{3}{4} m_o v_o^2 \end{aligned} \tag{5.3}$$

In this equation E_{avl} is the energy left for internal and translational excitation of the photofragments when the dissociation energy of ozone is subtracted from the the energy of the photon. The total translational energy, E_{trans} of the fragments can be calculated once the velocity of one of the frag-

ments is known using the rules of conservation of momentum.

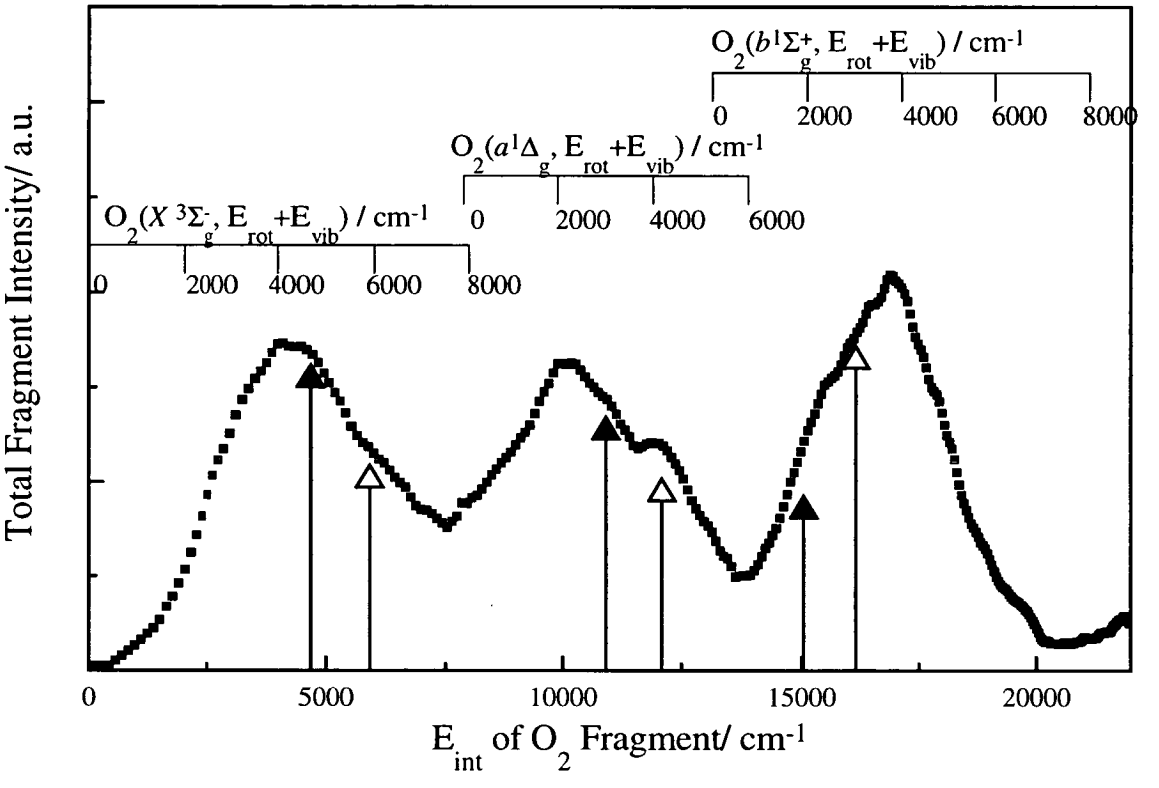

Figure 5.3.: The internal energy distribution of O_2 co-fragments of the $O(^3P_0)$ fragments detected from 322.64 nm photolysis of ozone. The ladders show the excess energies above the zero point energies of the three lowest lying excited states of O_2. The closed and open arrows are the most probable rotational energies of the v = 0 and 1 respectively for each of the three states calculated using a modified impulsive model of dissociation.

The resulting internal energy distribution of the O_2 fragments formed by the same photolysis events as $O(^3P_0)$, shown in Figure 5.3, appears to show three peaks corresponding with vibrational/rotational distributions in O_2 ($X\,^3\Sigma_g^-$), O_2 ($a\,^1\Delta_g$) and O_2 ($b\,^1\Sigma_g^+$).

5.4.2 The Identity of the O_2 Co-fragments

Although the most likely explanation for the trimodal velocity distribution of the $O(^3P_0)$ fragments is that the production of these fragment occurs

via the dissociation leading to channels (A), (B) and (C), the possibility of a bimodal vibrational distribution in either the O_2 ($X\ ^3\Sigma_g^-$) or the O_2 ($a\ ^1\Delta_g$) fragment must be considered. It is known that a bimodal vibrational distribution in O_2 ($X\ ^3\Sigma_g^-$) fragments is produced following 226 nm photolysis of O_3 [12, 13]. However, as the photolysis wavelength is increased to 266 nm, this bimodal distribution is lost [14].

The only method by which vibrational distributions of the molecular fragments can be determined with absolute certainty is by state specific detection of each vibrational level of each molecular state. O_2 ($X\ ^3\Sigma_g^-$) fragments have not been detected in this fashion as nascent products of Huggins band photolysis. However, the first peak in the internal energy distribution of Figure 5.3, centred at 4000 cm^{-1}, must be due to dissociation to ground state O_2 as it is below the term energy of the first excited state, O_2 ($a\ ^1\Delta_g$). Also, Denzer *et al.* [4] have reported the detection of O_2 ($a\ ^1\Delta_g$) fragments in unassigned rotational levels following photolysis in the 320 - 322 nm region and have shown by kinetic energy analysis of these fragments that spin-forbidden photolysis *via* channel (D) is partly responsible for production of these fragments. Using similar techniques, they have also reported the spin-forbidden production of O_2 ($a\ ^1\Delta_g$, v = 1, J = 28) fragments by photolysis of O_3 at 327.93 nm. Therefore, it seems that rotationally excited O_2 ($a\ ^1\Delta_g$, v = 0 and 1) fragments are produced by photolysis in the Huggins bands and account for the second peak in Figure 5.3, centred at 10000 cm^{-1}.

The high internal energy peak shown in Figure 5.3 is most likely to be due to the O_2 ($b\ ^1\Sigma_g^+$) co-fragment. By examining the ladder indicating the amount of energy in excess of the rotationless level of the v = 0 state of the three electronic co-fragments, it is clear that if the final peak is the result of channel (C) then the O_2 ($b\ ^1\Sigma_g^+$) is formed with a peak in its internal energy of $\sim$ 4000 cm^{-1}. By comparison with the previously detected rotational states of the diatomic fragments formed *via* channel (B) [4] it seems likely that this energy is channeled into higher rotational states of the equivalent vibrational levels

of O_2 ($b\ ^1\Sigma_g^+$). To test this hypothesis an impulsive model of the dissociation processes was implemented in an attempt to estimate the rotational energy of the diatomics fragments formed in this way. The results of this model are outlined in the following section.

5.5 The Impulsive Model of Dissociation

The detection of O_2 fragments in low vibrational levels but with large rotational excitation suggests that a simple impulsive model for dissociation may reproduce the experimental distributions [15, 16]. The assumptions required for this model are that the dissociation takes place on a very steeply repulsive potential and that the recoil vector lies along the dissociating bond. A particularly straightforward implementation of this model, described by Levene and Valentini [16], can be used to predict the most probable value in the rotational energy distribution of each vibrational level of the molecular, $\langle E_{rot}\rangle_{O_2}$, using the formula:

$$\langle E_{rot}\rangle_{O_2} = \frac{\langle E_{avl}\rangle \sin^2\theta}{4 - \cos^2\theta} \tag{5.4}$$

where $\langle E_{avl}\rangle = \langle E_{trans}\rangle + \langle E_{rot}\rangle$ and θ is the bond angle of the molecule in the dissociating state, which is assumed to be the same as that of the ground state in the present calculation. The single value of $\langle E_{rot}\rangle_{O_2}$ resulting from the use of this formula is the rotational energy of the diatomic produced from a hypothetical non-rotating, non-vibrating parent triatomic. However, in reality the dissociating O_3 is a rotating vibrator and hence the final distribution of diatom angular momentum contains contributions from these sources [16]. The result is a distribution of J levels around that predicted by equation 5.4. The effect of differing amounts of vibration of the dissociating parent molecule on the O_2 rotational distributions will be discussed later in the text.

Equation 5.4 dictates that 21% of $\langle E_{avl}\rangle$ goes into diatomic rotation and

so the $\langle E_{rot} \rangle_{O_2}$ of O_2 ($X\,^3\Sigma_g^-$, v = 0, 1), O_2 ($a\,^1\Delta_g$, v = 0, 1) and O_2 ($b\,^1\Sigma_g^+$, v = 0, 1) were calculated and are illustrated in increasing energy by the arrows in Figure 5.3. The qualitative matching of the results of this model with those of the experiment support the assignment of the three peaks made previously. However, there are small but real deviations of the experimental results from this impulsive model which predicts slightly more rotational energy in the O_2 ($X\,^3\Sigma_g^-$) and O_2 ($a\,^1\Delta_g$) states, but less in the O_2 ($b\,^1\Sigma_g^+$), than observed. This suggests that at least two significantly different dissociation paths exist. Deviations from the impulsive model of the dissociation may arise either from breakdown of the impulsive model assumptions or possibly due to different dissociating geometries of the molecule in the different photofragment channels.

5.6 The Nature of the Dissociation Processes

In this section a number of different experimental results are presented and related to the dissociation dynamics of ozone. This is, however, only a preliminary discussion with limited conclusions as a more complete list of results are presented in Chapter 7 and many more details about the dissociation dynamics in this region are uncovered.

5.6.1 Anisotropy of the Photofragments

A useful aspect of detecting the $O(^3P_0)$ fragments is that the total angular momentum of this state is zero, $J = 0$, and therefore no E - μ - J vector correlation can occur and therefore the probe laser causes no preferential detection of any alignment of these fragments. Thus the anisotropy observed in the ion packet is a result of the dissociation process alone. The calculated $\beta(v)$ parameters are shown in table 5.1 where the larger error for the faster fragments is due to the difficulty in measuring the $I_{90}(v)$ due to the lower intensity for the $E_{photo} \perp z$ profile shown in Figure 5.2.

Although the anisotropy parameter was calculated during the process

peak ± FWHM Velocity / ms $^{-1}$	$\beta(v)$	% of Total $O(^3P_0)$ signal	Assigned Channel
2380 ± 600	0.6 ± 0.1	34	$O(^3P_0) + O_2\ (b\ ^1\Sigma_g^+)$
3430 ± 500	0.6 ± 0.3	35	$O(^3P_0) + O_2\ (a\ ^1\Delta_g)$
4225 ± 370	0.6 ± 0.3	31	$O(^3P_0) + O_2\ (X\ ^3\Sigma_g^-)$

Table 5.1.: Observed $\beta(v)$ parameters for the three velocity ranges of the peaks observed in the velocity release profiles of $O(^3P_0)$ fragments produced by the photolysis at 322.64 nm which are shown in Figure 5.2. The channel assignments and percentage contribution of each peak to the over all $O(^3P_0)$ signal at this wavelength are also shown.

of converting the TOF profiles of the $O(^3P_0)$ fragments to internal energy of the O_2 co-fragments no discussion of the value of the parameter was made at this time. The value of the β parameter is affected by the transition type of the photolysis step, lifetime of the dissociating state and geometry of the dissociating state. Separating the different contributions of these effects to the β parameter is quite difficult and a discussion of this is made here.

As discussed in the review of ozone spectroscopy in Chapter 3 there is still controversy as to whether the electronic transition responsible for the Huggins bands is to the 2 $^1A_1$ state or to the 1 $^1B_2$ state (responsible for the more intense Hartley band). The $\beta(v)$ should provide some information about the orientation of the transition moment and therefore which of these excitation processes is more likely. For a $^1A_1$ electronic transition the transition moment is parallel to the C_2 axis whereas for a $^1B_2$ transition the transition moment is perpendicular to the C_2 axis and in the plane of the molecule. Therefore, the limiting value of $\beta(v)$ for excitation to a vibronic level of $^1A_1$ symmetry followed by instantaneous dissociation in the ground state geometry with the fragments recoiling along the direction of the bond being broken is -0.18 which compares with a value of 1.18 obtained from a similar calculation for a vibronic level of $^1B_2$ symmetry. The observed value can differ from these limiting values as a result of processes which make the distribution more isotropic, i.e. which

make $\beta(v) \rightarrow 0$. For example, the rotation of the parent molecule may couple directly with the recoil vectors of the fragments or the dissociating molecule may rotate while dissociating, a process which depends on the life times of the excited state. However, there is also the possibility of a geometry change in the excited state which can make the angular distribution either more or less anisotropic. The experimental value is an intermediate between the two limiting values and so does not conclusively identify the symmetry of the excited state. Nevertheless, it is possible to conclude that to reproduce the experimental results, the geometry of the state involved in a pure $^1A_1$ transition would be required to change from the ground state bond angle of 116.8° to < 90°. Since such a geometry change is unlikely it is concluded that the transition almost certainly has $^1B_2$ symmetry. This of course does not necessarily mean that the transition terminates on a state with $^1B_2$, it could equally well excite a $^1A_1$ with odd quanta of a b_2 vibration.

5.6.2 On- and Off-Resonance Dissociation of Ozone

The raw TOF profiles in Figure 5.4 illustrate the comparison between photolysis of O_3 in discrete vibronic bands and in the continuum between them. The profiles in Figures 5.4 (b) and (c) were recorded with photolysis wavelengths of 316.64 nm (off-resonance) and 317.64 nm (resonant), respectively, as indicated by arrows in Figure 5.1. The polarisation of the probe laser is again perpendicular to the TOF axis in both cases and the arrival times of the fragments produced by the probe laser alone are shown for comparison in Figure 5.4 (a). The lower resolution of these profiles compared to those in Figure 5.2 is due to the fact that only partial core-sampling conditions are operative in this experiment and therefore direct extraction of the speed distribution or angular information is not possible. However, this has the advantage that more of the ion packet is detected and therefore there is a much larger signal allowing comparison with the weaker off-resonance signal.

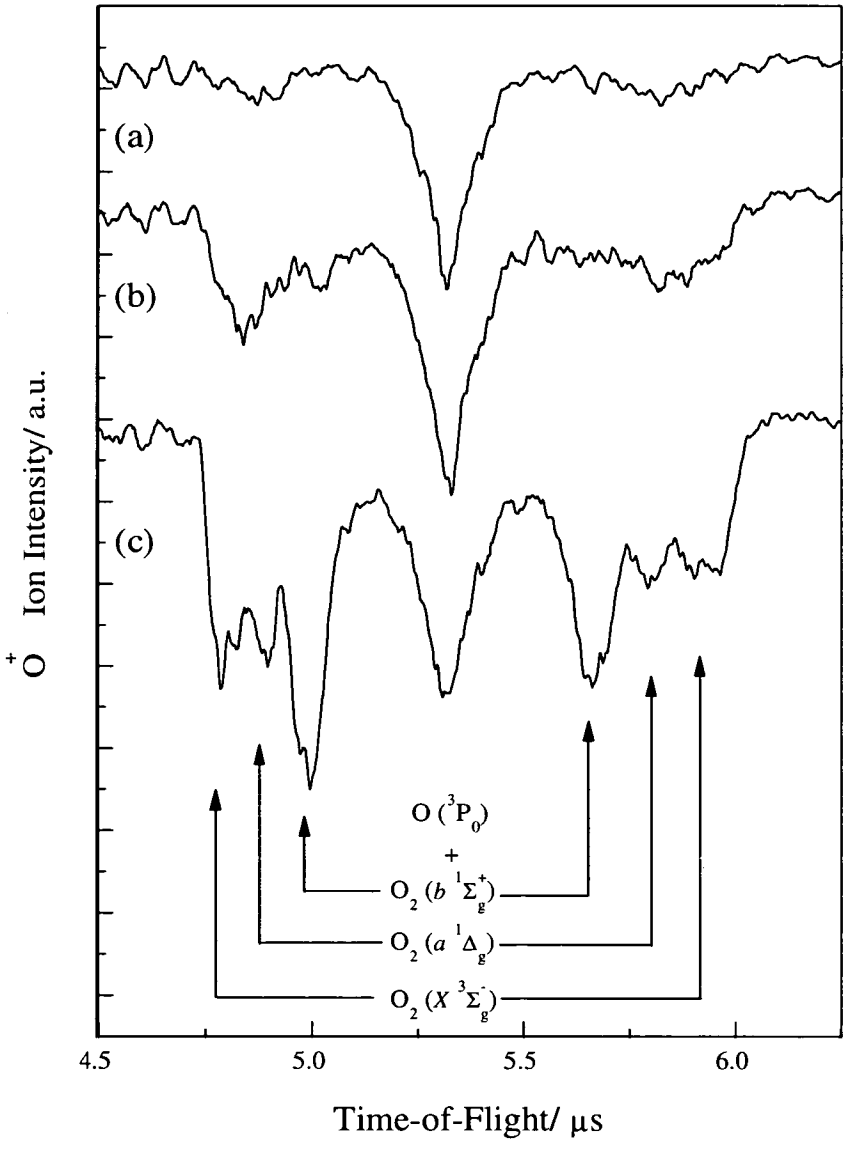

Figure 5.4.: The partially core-extracted TOF profiles of O($^3P_0$) fragments produced from the photolysis of O_3 at various wavelengths in the Huggins bands. Profile (a) is the probe signal only which has not been subtracted from the other profiles while profiles (b) and (c) are the TOF profiles produced following photolysis of ozone at 316.64 nm (off-resonance) and 317.64 nm (on-resonance) respectively.

The main point illustrated in Figure 5.4, is that while the peak assigned to the production of $O(^3P_0)$ in coincidence with O_2 ($b\,^1\Sigma_g^+$) is the most intense when the photolysis wavelength is resonant with a discrete vibronic band , this channel is barely detectable for off-resonance (continuum) dissociation.

5.6.3 Schematic Potential Energy Curve Description of Dissociation

The $O(^1D)$ + O_2 ($X\,^3\Sigma_g^-$) and $O(^3P_j)$ + O_2 ($a\,^1\Delta_g$) products are believed to be formed predominantly as a result of the crossing of the singlet exit channel, which produces $O(^3P_j)$ + O_2 ($X\,^3\Sigma_g^-$), by repulsive triplet states correlating with these products [3]. If a similar crossing in the same exit channel were also responsible for the observation of $O(^3P_j)$ + O_2 ($b\,^1\Sigma_g^+$), the ratios of X:a:b observed when the photolysis photon is resonant with a discrete absorption band should be very similar to those when it is off resonance. Therefore it seems that dissociation *via* the spin-forbidden channel (C) is associated predominantly with the bound levels of the excited state and that the predissociation process responsible for this channel involves a direct crossing of the initially excited singlet state of O_3 by a repulsive state correlating with the $O(^3P_0)$ + O_2 ($b\,^1\Sigma_g^+$) products. Thus, the O_2 ($X\,^3\Sigma_g^-$) and O_2 ($a\,^1\Delta_g$) fragments appear to be produced via a different dissociation process than the O_2 ($b\,^1\Sigma_g^+$) fragments, the differing dynamics of these processes may account for the observed deviations from the impulsive model predictions indicated above.

5.7 Conclusions

The delayed pulsed field extraction technique has been used to measure the velocity profile of the $O(^3P_0)$ fragments formed from photolysis of O_3 at 322.64 nm. The angular distribution of these fragments has also been measured by manipulating the ion packet using the linear polarisation of the

photolysis laser and core-extraction. Using the information gained, the O_2 co-fragment internal energy distribution was constructed. The first two peaks of this trimodal distribution were rigorously assigned to the formation of O_2 ($X\ ^3\Sigma_g^-$) and O_2 ($a\ ^1\Delta_g$) fragments in low vibrational but high rotational states. The highest energy peak was assigned to the production of $O(^3P_0)$ fragments in coincidence with O_2 ($b\ ^1\Sigma_g^+$) diatomic fragments in similar internal energy states. This conclusion was supported by a simple impulsive model calculation on the expected amount of rotational energy with each vibrational levels of the diatomic fragments.

Finally, the on and off resonance $O(^3P_0)$ TOF profiles revealed that O_2 ($b\ ^1\Sigma_g^+$) fragments are only produced following absorption into the structured part of the Huggins bands. It is proposed that the same initial predissociation process produces both the O_2 ($X\ ^3\Sigma_g^-$) and O_2 ($a\ ^1\Delta_g$) fragments where the O_2 ($a\ ^1\Delta_g$) channel is accessed by a crossing in the exit channel of the O_2 ($X\ ^3\Sigma_g^-$) + $O(^3P_j)$ channel. The different behaviour of the O_2 ($b\ ^1\Sigma_g^+$) fragments indicates that this channel is accessed by a separate mechanism.

References

[1] K. Takahashi, M. Kishigami, Y. Matsumi, M. Kawasaki and A. J. Orr-Ewing. *J. Chem. Phys.* **105** (1996) 5290.

[2] K. Takahashi, M. Kishigami, N. Taniguchi, Y. Matsumi, and M. Kawasaki, *J. Chem. Phys.* **106** (1997) 6390.

[3] K. Takahashi, N. Taniguchi, Y. Matsumi, M. Kawasaki and M. N. R. Ashfold, *J. Chem. Phys.* **108** (1998) 7161.

[4] W. Denzer, G. Hancock, J. Pinot de Moira and P. L. Tyley, *Chem. Phys.* **231** (1998) 109.

[5] S. M. Ball, G. Hancock, S. E. Martin and J. C. Pinot de Moira. *Chem. Phys. Lett.* **264** (1997) 531.

[6] W. Armerding, F. J. Comes and B. Schülke *J. Phys. Chem.* **99** (1995) 3137.

[7] E. Silvente, R. C. Richter, M. Zheng, E. S. Saltzmann and A. J. Hynes. *Chem. Phys. Lett.* **264** (1997) 309.

[8] S. M. Ball and G. Hancock. *Geophys. Res. Lett.* **22** (1995) 1213.

[9] S. M. Ball, G. Hancock and F. Winterbottom. *Faraday Discuss.* **100** (1995) 215.

[10] K. Takahashi, Y. Matsumi and M. Kawasaki. *J. Phys. Chem.* **100** (1996) 4084.

[11] L. T. Molina and M. J. Molina, *J. Geophys. Res.* **91** (1986) 14501.

[12] J. A. Syage. *J. Chem. Phys.* **105** (1996) 1007.

[13] R. L. Miller, A. G. Suits, P. L. Houston, R. Toumi, J. A. Mack and A. M. Wodtke. *Science* **265** (1994) 1831.

[14] R. J. Wilson, J. A. Mueller and P. L. Houston. *J. Phys. Chem. A* **101** (1997) 7593.

[15] G. E. Busch and K. R. Wilson. *J. Chem. Phys.* **56** (1972) 3626.

[16] H. B. Levene and J. J. Valentini. *J. Chem. Phys.* **87** (1987) 2594.

Chapter 6

REMPI Detection of O_2 ($a\ ^1\Delta_g$) and O_2 ($b\ ^1\Sigma_g^+$) Fragments

6.1 Introduction

The aim of this chapter is to investigate the state selective detection of the diatomic fragments from Hartley and Huggins band photodissociation of ozone. In the previous chapter a trimodal velocity distribution of the $O(^3P_0)$ fragment which was detected following Huggins band photolysis was assigned to the formation of these fragments in co-incidence with O_2 ($X\ ^3\Sigma_g^-$), O_2 ($a\ ^1\Delta_g$) and O_2 ($b\ ^1\Sigma_g^+$) fragments in low vibrational and high rotational states. However, as noted, only the O_2 ($a\ ^1\Delta_g$) state has been detected by state selective REMPI following the Huggins band photolysis.

This chapter complements the information gained from the previous chapter by reporting the REMPI detection of O_2 ($b\ ^1\Sigma_g^+$) fragments as nascent products from Huggins band photolysis. Multi-photon absorption prior to dissociation to form O_2 ($b\ ^1\Sigma_g^+$) fragments is ruled out by power-dependence measurements and kinetic energy studies of the O_2 ($b\ ^1\Sigma_g^+$) fragments formed.

6.2 The Resonant State for O_2 Photofragment Detection

6.2.1 The One-Laser O_2^+ REMPI Spectrum of the Huggins Band Region of Ozone

A glance at the one-laser REMPI spectrum of ozone shown in Figure 6.1 for wavelengths between 335 - 345 nm recorded by detecting the O_2^+ ion in the mass spectrometer mode reveals a very complicated and highly structured spectrum. This spectrum can be compared with the PHOFEX spectrum of the $O(^3P_0)$ fragments produced in this region shown in the lower trace of Figure 6.1. In the previous chapter it was shown to correspond quite closely to the absorption spectrum. It should be noted that the features observed in the O_2^+ REMPI spectrum are power broadened due to the high power of the one-colour experiment and the tightly focused laser light. However, it is still possible to see that the structured nature of this spectrum is not due solely to the absorption bands in ozone which account for the large features, but also due to the overlap of the ozone absorption with rotational/vibrational resonances in the REMPI detection of the O_2 photofragments.

From the first Ionisation Potential (IP) of the O_2 ($X\ ^3\Sigma_g^-$) molecule (97348 cm^{-1} [1]) the wavelength for three photon ionisation of various states of the O_2 can be calculated and are presented in Table 6.1.

It is clear from this table that if a three-photon REMPI scheme is assumed then if O_2 ($X\ ^3\Sigma_g^-$) fragments are being detected at the wavelengths indicated in Figure 6.1 these fragments must have considerable internal excitation. In fact, the lowest vibrational levels of these fragments which can be detected in this region is the v = 6 whereas it may be possible to detect the v = 0 levels of both the O_2 ($a\ ^1\Delta_g$) and O_2 ($b\ ^1\Sigma_g^+$) fragments. In light of the conclusion of the previous chapter which suggested that the O_2 fragments

O_2 ($X\ ^3\Sigma_g^-$) / nm	O_2 ($a\ ^1\Delta_g$) / nm	O_2 ($b\ ^1\Sigma_g^+$) / nm
v = 9, 356.4	v = 4, 358.5	v = 1, 362.2
v = 8, 350.6	v = 3, 352.6	v = 0, 356.1
v = 7, 345.1	v = 2, 346.7	
v = 6, 339.5	v = 1, 341.0	
v = 5, 334.1	v = 0, 335.4	

Table 6.1.: The three-photon ionisation thresholds of various rotationless vibrational levels of the O_2 ($X\ ^3\Sigma_g^-$), O_2 ($a\ ^1\Delta_g$) and O_2 ($b\ ^1\Sigma_g^+$) states calculated using the IP of O_2 [1] and vibrational constants reported by Slanger and Crosby [2].

produced from Huggins band photolysis are formed in low vibrational levels it appears most likely that the O_2 ($a\ ^1\Delta_g$) and O_2 ($b\ ^1\Sigma_g^+$) fragments are being detected in the O_2^+ spectrum in Figure 6.1.

The only candidates for the resonant states in such a detection system are the $d\ 3s\sigma_g\ ^1\Pi_g$ and $C\ 3s\sigma_g\ ^3\Pi_g$ Rydberg states. As these states occur at approximately 65500 cm^{-1} above the ground state they could provide a resonant enhancement at the two-photon stage resulting in a (2 + 1) REMPI process.

The characterisation of the spectroscopic features of these states has received a great deal of attention. The first four vibrational levels of these states which span the energy region 65500 - 73000 cm^{-1} above the ground state are the most relevant for this work. The d and C states are the first members of the singlet and triplet Rydberg series respectively converging on the O_2^+ ($^2\Pi_g$) ground state of the ion. The experimental studies of these states have concentrated on (2 + 1) REMPI techniques both from the O_2 ($X\ ^3\Sigma_g^-$) [3, 4, 5, 6, 7] and O_2 ($a\ ^1\Delta_g$) [8, 7] states. These studies have shown that while v = 0 of the d state is essentially unperturbed, v = 1 is weakly perturbed due to interaction with a valence state. However, the v = 2 and 3 levels of this state are strongly coupled to a bound valence state resulting

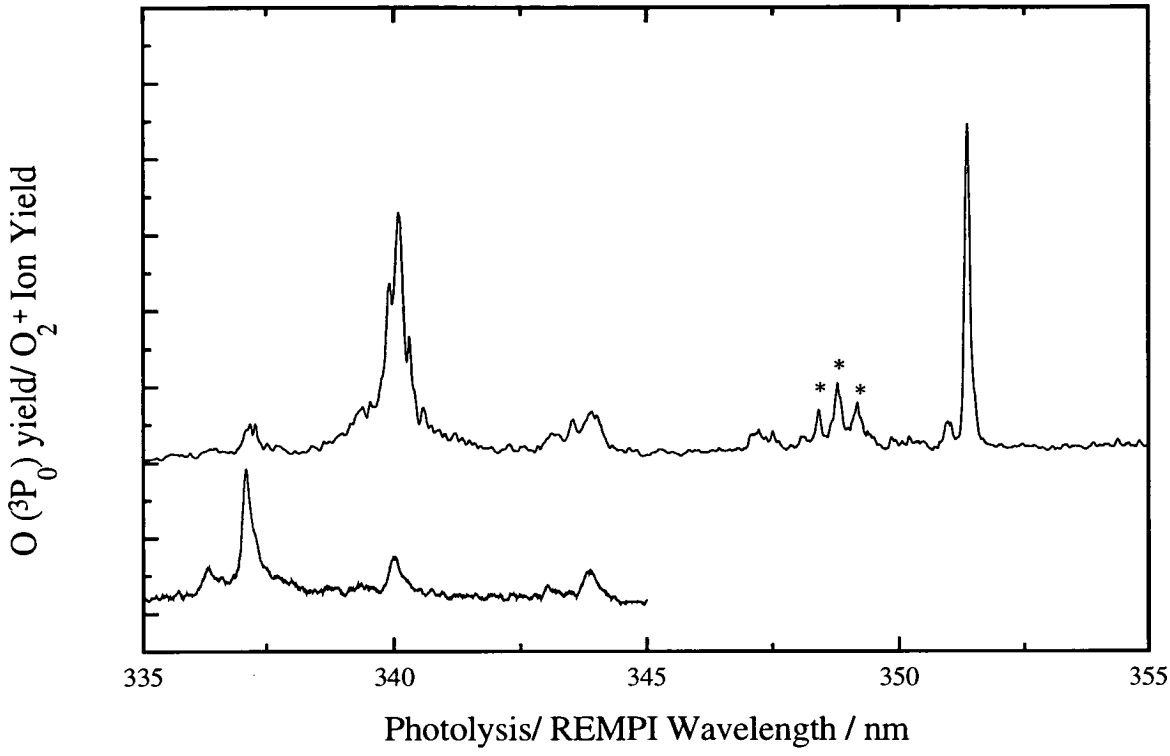

Figure 6.1.: The upper trace is the one-laser O_2^+ REMPI spectrum of ozone. The lower spectrum is the $O(^3P_0)$ PHOFEX spectrum in the same region which was shown in the previous chapter to be similar to the absorption spectrum. The features marked with asterisks are due to (3 + 1) REMPI transitions from O_2 ($X\ ^3\Sigma_g^-$).

in very irregular rotational structure. These interactions will be described in more detail in Chapter 8 of this thesis where the v = 2 and 3 levels of the *d* state are experimentally probed in a rotationally selective manner. This is achieved by populating single rotational lines of the O_2 ($b\ ^1\Sigma_g^+$) state by direct optical pumping from the ground state and then ionising these single J levels by (2 + 1) REMPI *via* the v = 2 and 3 levels of the *d* state. However, in this chapter the *d* state will simply be used to detect the nascent products of ozone photolysis.

6.3 Detection of the O_2 ($a\ ^1\Delta_g$) Photofragments from Hartley Band Photolysis

Investigating the O_2 ($a\ ^1\Delta_g$) fragments produced by the photolysis of ozone in the Hartley bands has a number of advantages. First, the absorption cross-section in the Hartley band region is up to 10^3 times greater than that in the Huggins bands. Also, the O_2 ($a\ ^1\Delta_g$) photofragment channel constitutes $\sim$ 90% of the fragment quantum yield at these wavelengths [9, 10]. These points combine to imply that the Hartley band photolysis of ozone is a very efficient means of producing O_2 ($a\ ^1\Delta_g$) fragments. Secondly, the rotational distributions of these fragments have been measured by experiments involving CARS spectroscopy [11] which provides a means of a better understanding of the rotational structure of the resultant O_2 REMPI spectra *via* the perturbed levels of the d state.

Finally, the wavelengths required to access certain vibrational levels of the d state from the O_2 ($a\ ^1\Delta_g$) fragments *via* the REMPI process described above correspond well with the Huggins band wavelength region shown in Figure 6.1. Due to the very large yield of O_2 ($a\ ^1\Delta_g$) fragments the probe laser can be defocussed slightly giving a lower power so that the one-colour features due to this laser are suppressed while the two-colour features are still observable. In this way the enhanced features in Figure 6.1 can be compared with the O_2 ($a\ ^1\Delta_g$) REMPI spectra to help determine whether they are due to O_2 ($a\ ^1\Delta_g$) fragments.

6.3.1 The (0,1) $d \leftarrow\leftarrow a$ Transition

A spectrum resulting from the photolysis of ozone at 275 nm with a slightly defocussed probe laser scanned between 348 and 352 nm is shown in

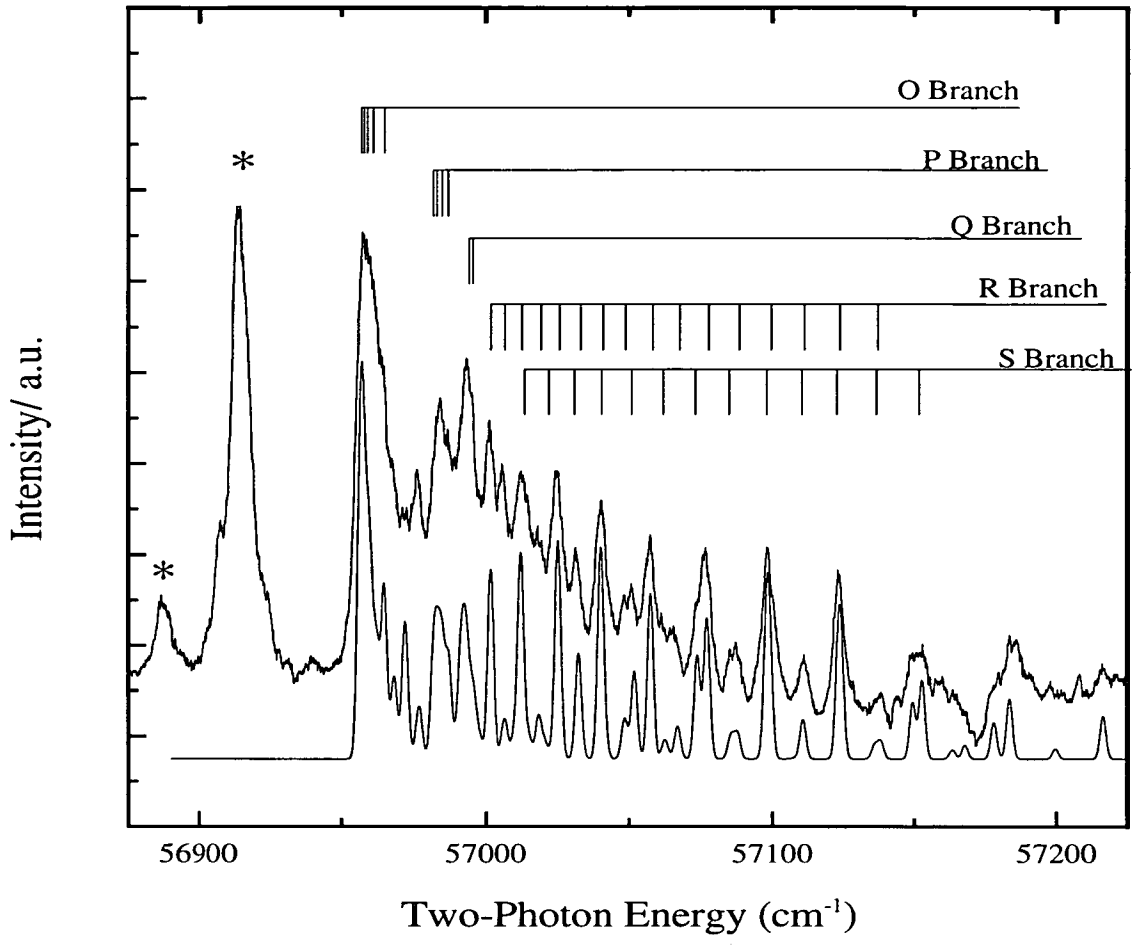

Figure 6.2.: The (0,1) band of the $d\ 3s\sigma_g\ ^1\Pi_g \leftarrow\leftarrow O_2\ (a\ ^1\Delta_g)$ $(2' + 1)$ REMPI transition recorded by photolysis of O_3 at 275 nm and scanning the REMPI transition above with a slightly defocussed probe laser. The simulation was calculated using the reported B_v values of the two states, two photon Hönl-London factors and a Boltzmann temperature of 600 K to represent the rotationally hot O_2 ($a\ ^1\Delta_g$) fragments [12]. Starred bands are solely due to the probe laser.

Figure 6.2. This spectrum is due to the $(2' + 1)$ REMPI detection [1] of the O_2 ($a\ ^1\Delta_g$, v = 1) fragments *via* the v = 0 level of the d state. As discussed in the previous section this vibrational level of the d state is unaffected by the interactions with the perturbing valence states and hence exhibits an unperturbed regular rotational manifold, Therefore this transition can be simulated using two-photon line strength formulae and the known rotational constants of the lower ($B_v(a^1\Delta_g$, v = 1) = 1.400 cm^{-1}) [2] and upper ($B_v(d^1\Pi_g$, v = 0) = 1.68 cm^{-1}) [5] states.

[1]The convention adopted for labelling of the REMPI processes identifies the photolysis photon as having no '

The simulation was performed using a simple Boltzmann distribution at 600 K [12]. As this is not the true rotational distribution of the $O_2(a^1\Delta_g$, v = 1) fragments produced from photolysis of ozone in the Hartley band the intensities of the simulation are only approximate. However, the line positions of the individual rotational transitions match those of the experimental spectrum very well. The reduced intensities of the odd J levels were simulated by multiplying the population of the odd J levels by 0.2. This reduced intensity of the odd J levels is an artifact of the selective depletion of these levels by a crossing in the asymptotic region with a state correlating with the ground state products [11]. Due to nuclear spin statistics, the ground state $O_2(X^3\Sigma_g^-)$ can have only odd J levels. This exerts a symmetry selection rule on crossings in the asymptotic region resulting in the depletion of only odd J levels of the $O_2(a^1\Delta_g)$ state.

There are, however, two starred features to lower energy of the simulated band which are not part of this vibrational transition and are due to the probe laser only.

6.3.2 REMPI Spectra of the $O_2(a^1\Delta_g)$ Fragment *via* the d, v = 2 State

The spectrum in figure 6.3 (a) was recorded by photolysing O_3 at 254 nm, exciting the (2,2) band of the $d \leftarrow\leftarrow O_2(a^1\Delta_g)$ transition with the probe laser and ionising with a further pump photon, i.e. a (2′ + 1) process. The most obvious observation is that only a limited number of J states of the $O_2(a^1\Delta_g)$ photofragment are observed.

Observations made using CARS spectroscopy, show that the rotational distribution peaks sharply at high J, with ΔJ FWHM = 12, for the $O_2(a^1\Delta_g$, v = 2) photofragment [11]. However, even with this limited number of J levels it has not proved possible to simulate the spectrum shown in figure 6.3 (a) and

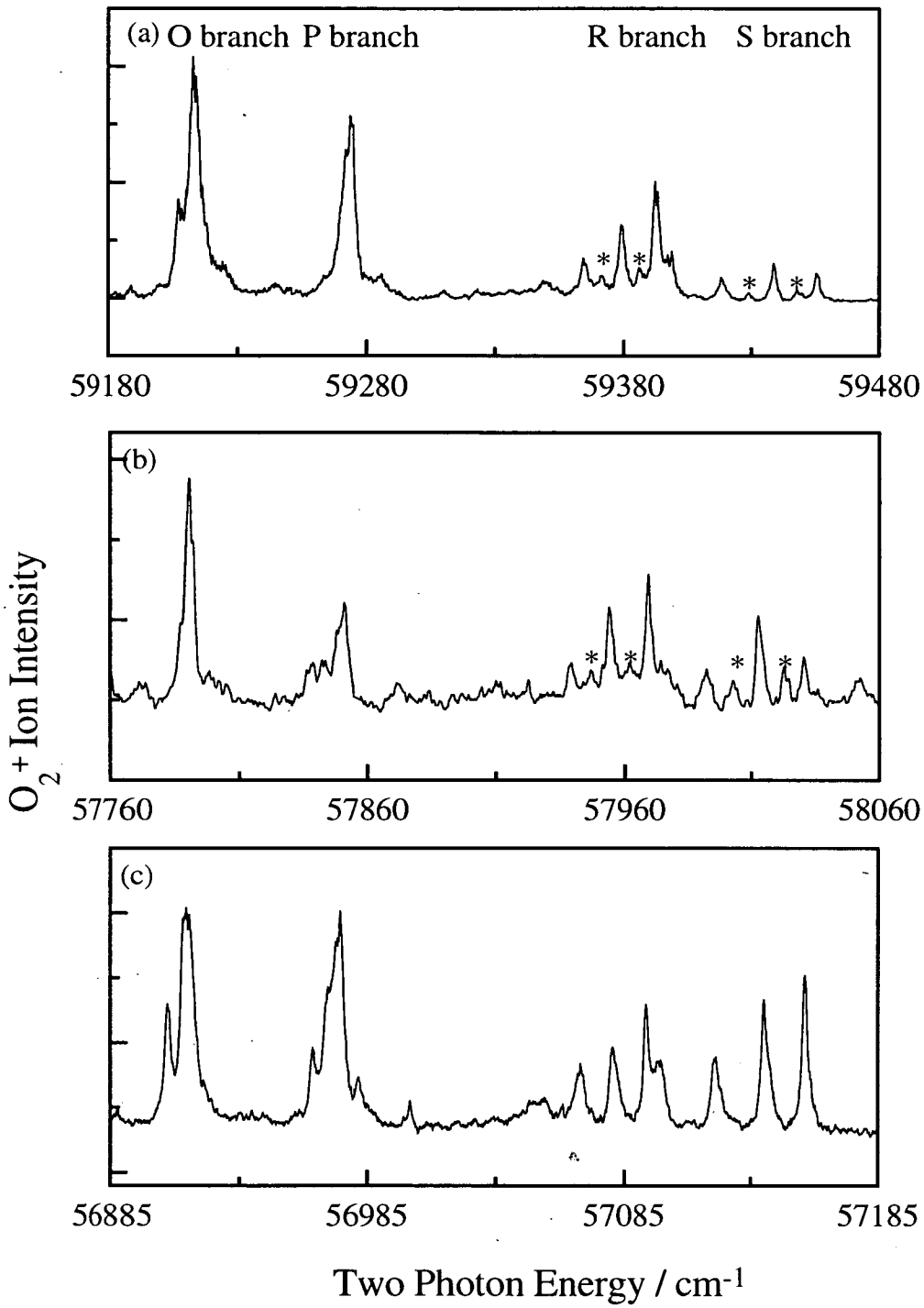

Figure 6.3.: (2 + 1) REMPI spectra of the diatomic fragments produced from photolysis of O_3. Spectra (a) and (b) are the (2,2) and (2,3) bands of the $d\ 3s\sigma_g\ ^1\Pi_g \leftarrow\leftarrow O_2\ (a\ ^1\Delta_g)$ transition recorded by probing the fragments by a $(2' + 1)$ (with some contribution from a $(2' + 1')$) process following O_3 photolysis at 254 nm. Spectrum (c) is recorded following 340 nm photolysis of O_3. This spectrum is the (2,0) band of the $d\ 3s\sigma_g\ ^1\Pi_g \leftarrow\leftarrow O_2\ (b\ ^1\Sigma_g^+)$ produced *via* a combination of $((1 + 1') + 1)$ and $((1 + 1') + 1')$ processes. The features marked with asterisks are due to transitions from depleted odd levels of the O_2 ($a\ ^1\Delta_g$) fragment [11].

it is clear that the upper state is too heavily perturbed to allow analysis of the nascent J distribution following Hartley band photolysis. This is further confirmed by the observation of the same J lines in the (2,3) band of the same electronic transition when photolysing at the same wavelength, see figure 6.3 (b), even though it is known that the nascent J distributions of the v = 2 and 3 levels of the $O_2(a^1\Delta_g)$ state are different [11]. It is concluded that the observation of limited J lines in transitions to the v = 2 level of the d state is the result of strong interactions. However, this limited rotational contour can be considered a 'fingerprint' of transitions to this level of the d state and we will make use of this in the following section. The other interesting point to note is the apparent intensity alternation between transitions from odd and even-J levels of the $O_2(a^1\Delta_g)$ state which is evident in this spectrum, see figure 6.3 (a) and (b). A reduction in intensity of the odd-J levels (indicated by asterisks) has been shown to be a result of the selective depletion of those levels by a curve crossing in O_3 as discussed in the previous section [11].

Having established that the $d\ 3s\sigma_g\ ^1\Pi_g$ Rydberg state can be used to detect $O_2(a^1\Delta_g)$ following photolysis of O_3 in the Hartley band we have used this same upper state to investigate photolysis in the Huggins bands, as described below.

6.4 Detection of O_2 ($b\ ^1\Sigma_g^+$) Photofragments from Huggins Band Photolysis

A problem encountered when attempting to photolyse ozone in the Huggins band region and detect diatomic fragments *via* (2 + 1) REMPI processes are the effects caused by enhancements of some of the REMPI features due to energy overlap with ozone absorption features in this region. To circumvent this problem it is possible to make use of the 'window' in ozone absorption between $\sim$ 355 - 400 nm where the absorption cross-section of ozone is close

to zero. However, as the energy of the transitions to be examined do not lie in this region a different REMPI scheme to that adopted in the previous section must be used. The process used involves ((1 + 1′) + 1) REMPI schemes, i.e. the photolysis laser provides one photon for the REMPI transition which is of a higher energy than the 355 - 400 nm range so that the probe laser can be scanned within this region.

6.4.1 Detection of O_2 ($b\ ^1\Sigma_g^+$, v = 0) Photofragments *via* v = 2 of the *d* State

The experimental approach used was to position the photolysis laser on each of the peaks in the Huggins band region between 335 and 352 nm and to scan the second laser within the window to ozone absorption, 355 - 369 nm. The spectrum observed following photolysis at 340 nm, which is a peak in the Huggins band absorption, is shown in figure 6.3 (c). At first sight the spectrum looks rather similar to those observed for O_2 ($a\ ^1\Delta_g$) (shown in figure 6.3 (a) and (b)). However, the position of the band does not fit at all well with the transitions calculated for O_2 ($a\ ^1\Delta_g$). The origin of the nearest O_2 ($a\ ^1\Delta_g$) band, involving the v = 2 level of the *d* state, is calculated to be some 600 cm^{-1} below the lowest energy feature in Figure 6.3 (c). This, together with other evidence cited below, allows us to eliminate O_2 ($a\ ^1\Delta_g$) as the carrier of this spectrum. The possibility that the spectrum might arise from vibrationally excited O_2 ($X\ ^3\Sigma_g^-$) has also been considered. The (2,9) band of the $d \leftarrow\leftarrow$ O_2 ($X\ ^3\Sigma_g^-$) transition is calculated to occur in this region. However, in the case of the O_2 ($X\ ^3\Sigma_g^-$) state, stronger spin-allowed transitions to the $C\ 3s\sigma\ ^3\Pi_g$ Rydberg state, which lie at an energy ~600 cm^{-1} below that of the *d* state should be prominent [8]. The lack of structure to lower energy of the features in figure 6.3 (c) indicates that this band is not due to the $d \leftarrow\leftarrow$ O_2 ($X\ ^3\Sigma_g^-$) transition.

The only remaining low lying meta-stable state of O_2 is the O_2 ($b\ ^1\Sigma_g^+$) state and the assignment of the features shown in figure 6.3 (c) to the (2,0) band of the $d \leftarrow\leftarrow b$ transition is confirmed by the following observations. First, visual inspection of the spectra illustrated in figure 6.3 (a), (b) and (c) shows that the rotational spacings are very similar. Since the upper level is the same in each of these bands the rotational constants of the vibrational levels of the O_2 ($a\ ^1\Delta_g$) state and the newly assigned state must be similar. This condition is satisfied by the O_2 ($b\ ^1\Sigma_g^+$), v = 0 level: B_v (O_2 ($a\ ^1\Delta_g$), v = 2) = 1.38365 cm^{-1}, B_v(O_2 ($a\ ^1\Delta_g$), v= 3) = 1.36655 cm^{-1} and B_v (O_2 ($b\ ^1\Sigma_g^+$), v = 0) = 1.39126 cm^{-1} [2]. This compares with B_v(O_2 ($X\ ^3\Sigma_g^-$), v= 9) = 1.29757 cm^{-1} [2], confirming that the lower state is not the ground state. Secondly, the depleted odd J levels observed in the bands of the $d\ 3s\sigma\ ^1\Pi_g \leftarrow\leftarrow O_2$ ($a\ ^1\Delta_g$) transition are now completely absent in the proposed $d\ 3s\sigma\ ^1\Pi_g \leftarrow\leftarrow O_2$ ($b\ ^1\Sigma_g^+$) band shown. Nuclear spin statistics in $^{16}O^{16}O$ ($b\ ^1\Sigma_g^+$) dictate that only even J levels are present. This is particularly convincing evidence that the lower state is indeed the O_2 ($b\ ^1\Sigma_g^+$) state. Thirdly, as we have shown, the rotational contours are very similar and therefore the energy spacing between equivalent rotational band heads (e.g. the O branch identified in figure 6.3) of each spectrum should reflect the known vibrational spacings of the lower levels. The observed energy differences are consistent with these calculated values (G_v (O_2 ($b\ ^1\Sigma_g^+$), v = 0) - G_v (O_2 ($a\ ^1\Delta_g$), v = 3) = 860.6 cm^{-1} and (G_v (O_2 ($b\ ^1\Sigma_g^+$), v = 0) - G_v (O_2 ($a\ ^1\Delta_g$), v = 2) = 2291.2 cm^{-1}) [2] to within the experimental limits (4 cm^{-1}).

Power Dependence

The possibility that two photons are absorbed by O_3 before fragmentation takes place was also considered. Indeed, the O_2 ($b\ ^1\Sigma_g^+$) state has been observed as a nascent product of photolysis of O_3 at 157.6 nm and 193 nm. The dependence of the O_2 ($b\ ^1\Sigma_g^+$) signal on pump power was therefore investi-

gated. Ozone was photolysed with the defocused pump laser with wavelength 340 nm and O_2 ($b\ ^1\Sigma_g^+$) was monitored *via* a ($2' + 1'$) detection scheme with a second laser set to the P branch of the (2,0) band of the $d \leftarrow\leftarrow b$ transition (shown in figure 6.3 (c)). The spectrum recorded by scanning the probe laser under these conditions is essentially the same as that of the (($1 + 1'$) + $1'$) spectrum shown in figure 6.3 (c). The observed linear power dependence of the pump power (power index of n = 0.95 ± 0.09) is consistent with a one-photon photolysis scheme. The difficulty with this experiment is that it does not exclude the possibility of a resonantly enhanced (1 + 1) absorption in ozone where the second absorption is step is completely saturated. Such a process would also exhibit the same power dependence as observed here. Therefore, another experiment is required involving the measurement of the velocity of the O_2 ($b\ ^1\Sigma_g^+$) fragments to confirm that they only possess the amount of translational energy of a one-photon process. The results of these experiments are described in the following section.

6.4.2 Detection of the O_2 ($b\ ^1\Sigma_g^+$, v = 0) Photofragments *via* v = 1 of the *d* State

Having conclusively confirmed the production of O_2 ($b\ ^1\Sigma_g^+$, v = 0) photofragments from the photolysis of ozone in the Huggins bands it is useful to attempt to evaluate the nascent rotational distribution of these fragments. Due to the perturbations of v = 2 of the *d* state the extraction of the rotational distribution of the lower state detected by a REMPI transition *via* this state is impossible.

As v = 1 of the *d* state is less perturbed by the Rydberg-valence interactions the spectra produced *via* two-photon transitions to this level should be easier to understand. The spectra shown in Figure 6.4 are due to the detection of O_2 ($b\ ^1\Sigma_g^+$, v = 0) photofragments from ozone photolysis 343.8 nm by a two-photon transition *via* v = 1 of the *d* state. The REMPI scheme used to

record this band is the same as that used to record the (2,0) band reported in the previous section, i.e. a ((1 + 1′) + 1) REMPI scheme.

The rotational contour of this band is quite similar to that of the (0,1) band of the $d \leftarrow\leftarrow O_2(a^1\Delta_g)$ transition shown in Figure 6.2. Therefore, the rotational distributions of the lower state fragments of these spectra are also probably quite similar. However, it was not possible to simulate all of the rotational features in this spectrum due to the perturbation effect experienced by the v = 1 level of the *d* state.

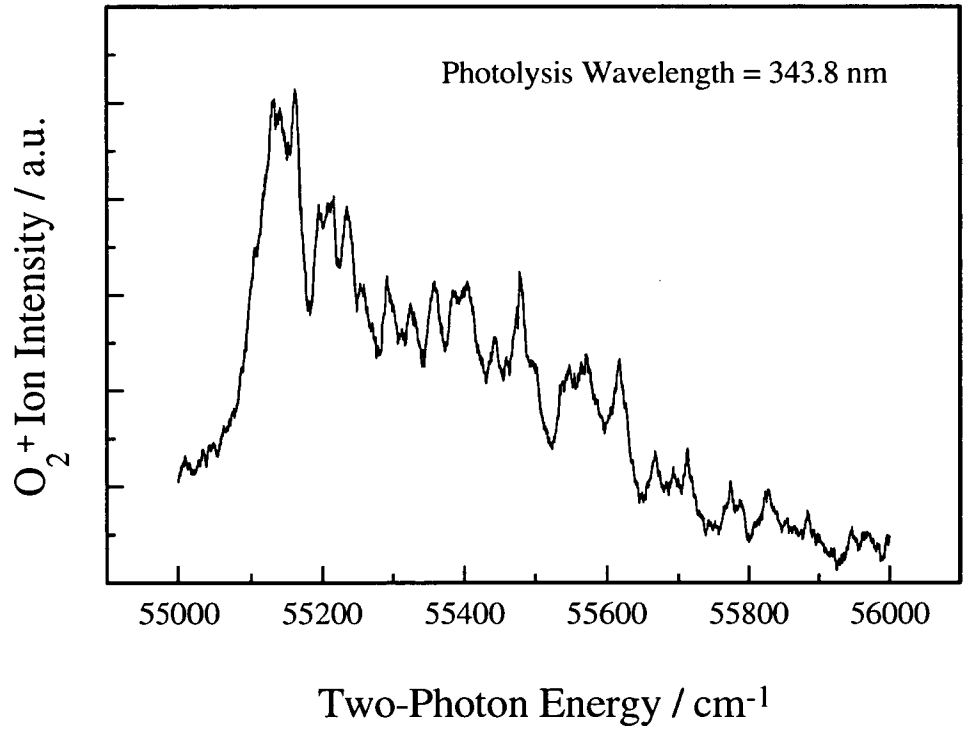

Figure 6.4.: The above spectrum is the (1,0) band of the $d\ 3s\sigma_g\ ^1\Pi_g \leftarrow\leftarrow O_2\ (b\ ^1\Sigma_g^+)$ produced following dissociation of ozone at 343.8 nm. The two-photon REMPI transition is accessed *via* a combination of ((1 + 1′) + 1) and ((1 + 1′) + 1′) processes.

6.5 Kinetic Energy Analysis of the O_2 ($b\ ^1\Sigma_g^+$) Fragments

Figure 6.5 shows the yield of O_2^+ as a single laser is scanned through the 349.5 - 352.0 nm region. The main feature observed involves the overlap of the O-branch rotational lines, O(20) and O(22), of the (2,0) band of the $O_2(d\ 3s\sigma\ ^1\Pi_g \leftarrow\leftarrow b\ ^1\Sigma_g^+)$ transition, with a Huggins band of ozone [13].

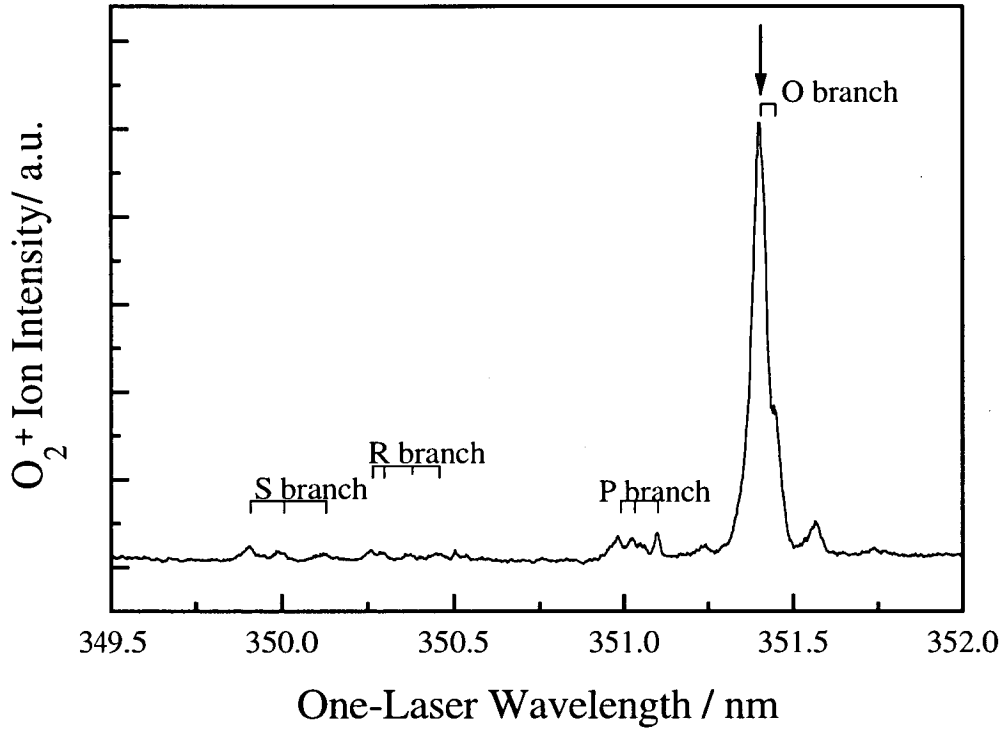

Figure 6.5.: The one-colour REMPI spectrum of O_3 between 349.5 and 352 nm recorded by collecting O_2^+ ions. The ions are formed as a result of a coincidence of a Huggins absorption band and the (2,0) band of the $d\ 3s\sigma_g\ ^1\Pi_g \leftarrow\leftarrow O_2\ (b\ ^1\Sigma_g^+)$ transition, the branches of which are shown on the spectrum.

The velocity release profiles shown in figure 6.6 were recorded at this wavelength, 351.4 nm, using linearly polarised light, with its electric field vector parallel to the TOF axis. The profiles were recorded by summing over 1000 laser shots and using a pulsed field delayed by 300 ns from the laser pulse. It is calculated from the core extracted velocity release profile (the closed circles

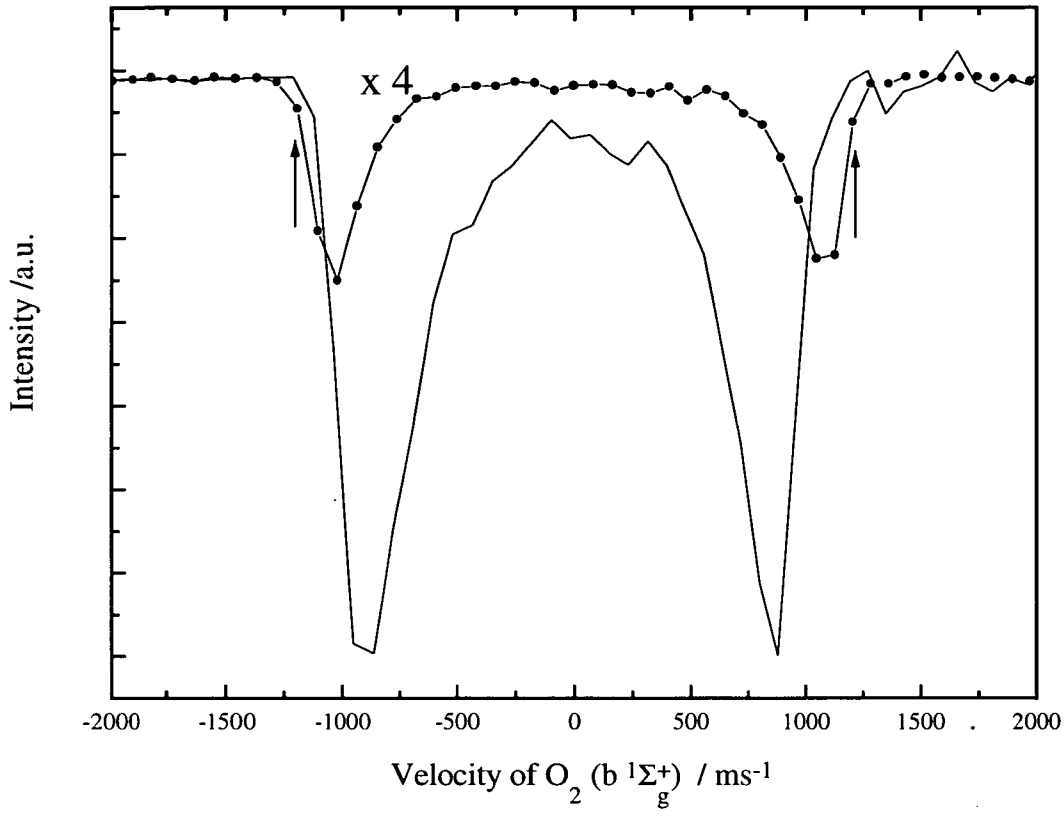

Figure 6.6.: The velocity profiles of the $O_2(b\ ^1\Sigma_g^+$, v = 0, J = 20 - 22) photofragments produced from 351.4 nm photolysis of ozone and detected by the O-branch of a (2 + 1) REMPI transition *via* the $d\ 3s\sigma\ ^1\Pi_g$, $v = 2$ intermediate state. The solid line is due to the full ion packet while closed circles show the core-extracted profile (x4). The arrows indicate the velocities used in the kinetic energy calculation reported in the text.

in figure 6.6) that the recoil velocity $v_z \sim v = 1200 \pm 100\ ms^{-1}$. The velocity release profile for the full ion packet (the solid line in figure 6.6) is included for comparison and shows the effect of the core-sampling technique on the intensity and width of the profile. Using this value of the centre of mass frame velocity release to the O_2 fragment, the translational energy release, $\langle E_{trans}(exp)\rangle$, from the dissociation process can be calculated as follows.

$$\begin{aligned}\langle E_{trans}(exp)\rangle &= \frac{1}{2}m_{O_2}v_{O_2}^2 + \frac{1}{2}m_O v_O^2 \\ &= \frac{3}{2}m_{O_2}v_{O_2}^2 \\ &= 5780 \pm 1000\ cm^{-1} \end{aligned} \quad (6.1)$$

This energy can be compared with the calculated translational energy, $\langle E_{trans}(calc)\rangle$, for photodissociation processes involving the $O_2(b\ ^1\Sigma_g^+, v'' = 0, J'' = 20 - 22)$ fragment, from the equation :

$$\begin{aligned}\langle E_{trans}(calc)\rangle &= nh\nu - \langle E_{diss}\rangle - \langle E_{elec}\rangle O_2 - \langle E_{vib}\rangle O_2 \\ &\quad -\langle E_{rot}\rangle O_2 - \langle E_{elec}\rangle O \end{aligned} \tag{6.2}$$

where n is the number of photons absorbed by O_3 prior to dissociation, $h\nu$ is the energy of the dissociative photon, $\langle E_{diss}\rangle$ is the energy threshold to forming the ground state fragments, $\langle E_{elec}\rangle O_2$, $\langle E_{vib}\rangle O_2$ and $\langle E_{rot}\rangle O_2$ are the electronic, vibrational and rotational energies of the O_2 ($b\ ^1\Sigma_g^+$, v = 0, J = 20 - 22) fragments and $\langle E_{elec}\rangle O$ is the electronic energy of the atomic fragment. The effect of the rotation of the parent molecule is negligible due to the low rotational temperature of the beam. The resulting $\langle E_{trans}(calc)\rangle$ for a one-photon photolysis producing the O_2 ($b\ ^1\Sigma_g^+$) fragment with $O(^3P_2)$ as the co-fragment is 6200 ± 80 cm^{-1} compared with values of 890 ± 80, 18800 ± 80 and 34770 ± 80 cm^{-1} for two-photon processes with the $O(^1S_0)$, $O(^1D_2)$ and $O(^3P_2)$ co-fragments, respectively. The quoted error in the $\langle E_{trans}(calc)\rangle$ values is due in part to the uncertainty of $\langle E_{diss}\rangle$ but mainly due to a separation of $\sim$ 120 cm^{-1} between $J = 20$ and $J = 22$ of O_2 ($b\ ^1\Sigma_g^+$) [2]. The true error will be slightly larger due to the approximations mentioned above. It is clear from these results that two-photon absorption can be eliminated from consideration and that the O_2 ($b\ ^1\Sigma_g^+$) fragments are produced solely via single-photon absorption followed by spin-forbidden dissociation of O_3. The experimentally measured translational energy of the channel, $\langle E_{trans}(exp)\rangle$, matches the calculated values for this channel, $\langle E_{trans}(calc)\rangle$, to well within experimental error.

6.6 Conclusions

The (0,1) band of the $d\ 3s\sigma_g\ ^1\Pi_g \leftarrow\leftarrow O_2\ (a\ ^1\Delta_g)$ transition was recorded following the photolysis of ozone at 275 nm. This band was accurately simulated using an unperturbed rotational constant for the upper level confirming that v = 0 of the d state is not perturbed even in the high J limit. Also, the (2,2) and (2,3) bands of this transition were recorded following photolysis at 254 nm revealing a strongly perturbed v = 2 level of the d state which exhibits a 'fingerprint' spectrum which is not dependent on the lower state J distribution.

Photolysis at 340 nm, a peak within the Huggins bands, was combined with ((1 + 1′) + 1) and ((1 + 1′) + 1′) REMPI techniques to record the (2,0) band of the $d\ 3s\sigma_g\ ^1\Pi_g \leftarrow\leftarrow O_2\ (b\ ^1\Sigma_g^+)$. The assignment initially suggested by the 'fingerprint' appearance of the band structure was confirmed by careful consideration of the transition energy, rotational constant of the lower state and the missing odd J levels consistent with the nuclear spin statistics of the $O_2\ (b\ ^1\Sigma_g^+)$. The (1,0) band of this transition was also presented and found to be similar in contour shape to the (0,1) band of the $d\ 3s\sigma_g\ ^1\Pi_g \leftarrow\leftarrow O_2\ (a\ ^1\Delta_g)$ transition. From this it was concluded that the $O_2\ (b\ ^1\Sigma_g^+,\ v = 0)$ fragments have a similar rotational distribution to the hot distribution of the $O_2\ (a\ ^1\Delta_g)$ fragments produced from Hartley photolysis.

Inconclusive power dependence measurements on the Huggins bands photolysis step producing the $O_2\ (b\ ^1\Sigma_g^+)$ fragments led to an experiment to measure the recoil velocity of these fragments. The measured velocity showed that the fragments were formed by a one-photon photolysis step in the Huggins bands.

All of the results entailing the $O_2\ (b\ ^1\Sigma_g^+)$ fragments produced from the Huggins bands confirm the conclusions made in the previous chapter about this dissociation channel.

References

[1] R. G. Tonkyn, J. W. Winniczek and M. G. White. *Chem. Phys. Lett.* **164** (1989) 137.

[2] T. G. Slanger and P. C. Crosby. *J. Phys. Chem.* **92** (1988) 267.

[3] A. Sur, C. V. Ramana and S. D. Colson. *J. Chem. Phys* **83** (1985) 904.

[4] A. Sur, C. V. Ramana, W. A. Chupka and S. D. Colson. *J. Chem. Phys.* **84** (1985) 69.

[5] A. Sur, R. S. Friedman and P. J. Miller. *J. Chem. Phys.* **94** (1991) 1705.

[6] A. Sur, L. Nguyen and N. Nikoi. *J. Chem. Phys.* **96** (1992) 6701.

[7] R. Ogorzalek-Loo, W. J. Marinelli, P. L. Houston, S. Arepalli, J. R. Wiesenfeld and R. W. Field. *J. Chem. Phys.* **91** (1989) 5185.

[8] R. D. Johnson III, G. R. Long and J. W. Hudgens. *J. Chem. Phys.* **87** (1987) 1977.

[9] C. E. Fairchild, E. J. Stone and G. M. Lawrence. *J. Chem. Phys.* **69** (1978) 3632.

[10] R. K. Sparks, L. R. Carlson, K. Shobatake, M. L. Kowalczyk and Y. T. Lee. *J. Chem. Phys.* **72** (1980) 1401.

[11] J. J. Valentini, D. P. Gerrity, D. L. Phillips, J. -C. Nieh and K. D. Tabor. *J. Chem. Phys.* **86** (1987) 6745.

[12] Two-Photon rotational band contour simulation program written by Z. Min, The University of Edinburgh.

[13] B. R. Lewis, M. L. Ginter and J. Morril, private communication.

Chapter 7

Re-analysis of the UV Absorption Spectrum of Ozone

7.1 Introduction

At this point it is necessary to depart slightly from the investigation of the photodissociation dynamics of ozone photolysis and to re-examine in greater detail the Huggins and Hartley band absorption systems. A brief review of the research performed to date on these absorption systems was given in chapter 2 where it was pointed out that the absorption is dominated by the bell-shaped Hartley continuum between 210 and 310 nm which is generally believed to be due to the electronically allowed transition from the X^1A_1 ground state to the lowest of the $^1B_2$ excited states (using C_{2v} symmetry nomenclature for the states). However, the key question that has not been answered with certainty is whether the band system to lower energy, called the Huggins bands, is due to a transition to the same upper electronic state or due to the other proposed upper electronic state, the 2^1A_1 state. This has a direct bearing on the vibrational assignment of the bands through vibronic symmetry arguments, but a broader

question that is somewhat decoupled from the symmetry arguments concerns the number of bound levels of the asymmetric stretch, ν_3, that are supported by the upper surface or surfaces. The coordinate q_3 associated with this mode is also that leading to dissociation of the triatomic and the number of bound levels provides information about the positions of curve or surface crossings that in turn influence the energy disposal among the various dissociation and predissociation channels.

This chapter contains a re-assignment of the vibrational structure of both the Huggins and Hartley band systems. These assignments are then related to a PES which could support both such vibrational progressions. The shape of this PES can then be compared with the topology of *ab initio* surfaces calculated for the $^1B_2$ state which is known to be responsible for the Hartley band absorption. Such a discussion can yield insight into the identity of the electronic upper state of the Huggins bands and hence on the vibrational assignment of the ν_3 mode for this state *via* the symmetry arguments mentioned above.

The earlier discussion of the excited electronic states in this region was confined to a simple one-dimensional description involving only the dissociative co-ordinate, ν_3. However, for the purposes of relating the vibrational information to the potential a more rigorous way of regarding these potentials is required. An example of this is given in Figure 7.1 where a generic potential energy surface which incorporates the features of all of the calculated $^1B_2$ surfaces is shown as a contour plot of the two co-ordinates of the O_3 molecule which correspond to the two bond lengths while the bond angle is kept constant. Also, shown in this diagram is the contour plot of the PES where the molecule is constrained to C_{2v}.

The diffuse structure of the Hartley bands has always been associated with quasi-periodic orbits executing motion in the q_1 and q_2 coordinates across the saddle point. That structure is resolvable at all must mean that there are several recurrences before the wavepacket created on the upper surface

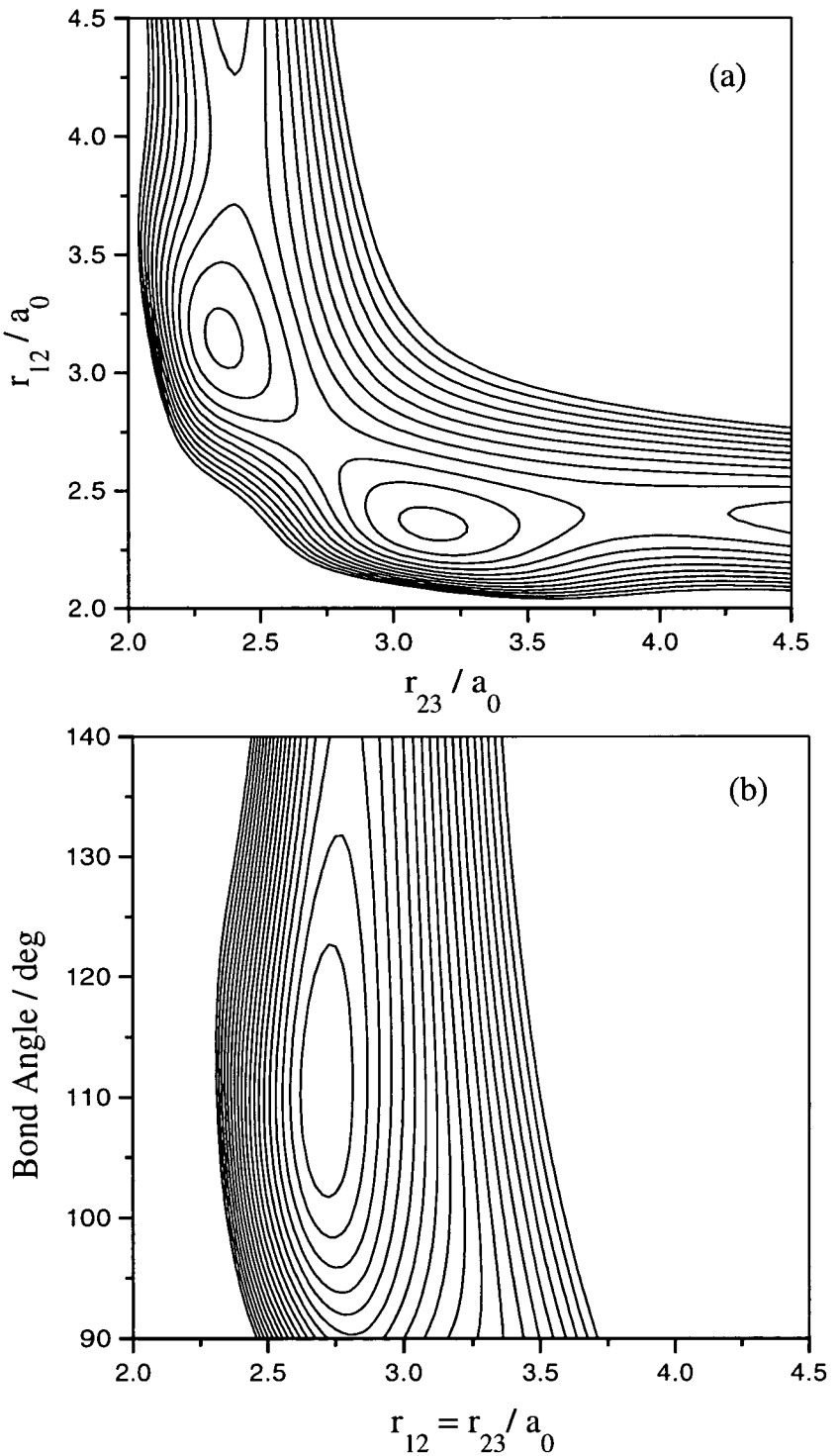

Figure 7.1.: A generic C_S representation of the 1^1B_2 (B) surface is shown in contour plot (a). Contour plot (b) shows the C_{2v} representation of the same surface for a fixed bond angle.

descends into the two valleys and the molecule dissociates. This structure is related to the generic PES as bound structure contained within the C_{2v} well shown in Figure 7.1 (b).

The crucial question, then, in assigning the Huggins bands is whether the shallow bound wells of the 1^1B_2 state (seen in the C_S representation of the PES in Figure 7.1 (a)) are accessible from the ground (000) state. If, in any of the three modes, the Franck-Condon factors associated with such a transition are negligible, then the structure must be assigned to the $2\ ^1A_1 \leftarrow$ X transition.

These questions are addressed in this chapter following the presentation of vibrational re-assignments of both the Huggins and Hartley band systems.

7.2 Re-assignment of the Huggins bands

7.2.1 Problems with Previous Assignments

The previous vibrational assignments of the Huggins bands are summarised in Chapter 3 of this thesis. The problems with these assignments which led to the re-assignment of this vibrational structure are given in this section. While the analyses of both Katayama [9] and Joens [10] explain most of the experimental observations, both authors recognise that there are two significant features which are not adequately accounted for. Firstly, in both overall assignments it was not possible to provide definite assignments for peaks appearing at higher energy, i.e. above 32000 cm^{-1}. It was suggested [10] that these bands were perturbed by a second electronic state. Secondly, all bands having one quantum of ν_2 excited are at least as intense as the equivalent bands with no ν_2 excitation but, surprisingly, no higher members of the progressions are observed. This phenomenon was explained [10] as being due to there being a barrier between v = 1 and v = 2 in ν_2 and that no bound levels were observed above this barrier. However, bound levels of some description

must exist above any such barrier since ν_2 is not a dissociative coordinate.

The following section outlines an alternative assignment which is intrinsically very simple but can still account for all of the spectroscopic features detailed in the previous studies. In this assignment, only ν_1 and ν_2 progressions are observed, as in the two earliest studies [5, 6], but in this assignment all hot bands originate in one quantum of ν_1 in the ground state rather than in one quantum of ν_3.

7.2.2 Re-assignment

There are three extensive experimental data sets of the positions of the vibrational bands of the Huggins system available in the literature; those given by Brand *et al.* [7] and Katayama [9] were obtained from their own experimental results, while that reported by Joens [10] was obtained from an analysis of the spectrum recorded by Freeman *et al.* [11]. The present analysis exclusively uses the data of Katayama [9] since it is the most extensive and also includes the equivalent data for the $^{18}O_3$; the band positions are presented in Table 7.1.

The current vibrational re-assignments of the cold bands, presented in Table 7.1, are essentially the same as those of Simons *et al.* [5] in that the spectrum only contains extended progressions in ν_1 and ν_2. All of the upper levels are assigned to the same number of quanta in ν_3, the value of which depends on the electronic assignment which is discussed later in the chapter. The other difference is in the numbering of the ν_1 progression which in the present analysis is taken from isotope studies [9] which predict an unseen origin around 27124 cm^{-1} and results in our numbering being two quanta higher than that given previously [5]. The intensities of the members of the ν_1 progression peak at v = 6, while the intensities of the members of each ν_2 progression built on these false origins show a smooth Franck-Condon envelope peaking between v = 2 and v = 3. The largest spacings in the ν_1 and ν_2 progressions are 696

$\nu_1\nu_2^a$	$^{16}O_3$ Cold Bands /cm^{-1}	Exp - Calc /cm^{-1}	$^{16}O_3$ Hot Bands /cm^{-1}	Exp - Calc /cm^{-1}	$^{18}O_3$ Cold Bands /cm^{-1}	Exp - Calc /cm^{-1}	$^{18}O_3$ Hot Bands /cm^{-1}	Exp - Calc /cm^{-1}
00	(27122)	32.9						
10	27818*	25.8			27799			
20	28465	8.8	27360	7.0	28405	4.6		
12	——		27415	-6.4	——			
21	28803	-5.3			28727	-1.9		
13	27765	-4.1						
30	29082	0.9	27974	-3.9	28992	-0.9		
22	29146	-2.1	28041	-4.0	29044	-3.2	28005	-0.7
14			28094	-10.4			28066	19.7
31	29412	-1.0	28305	-4.9	29301	-5.6	28257	-7.7
23			28367	-5.4			28313	-0.8
40	29660	-6.9	28555	-8.8	29546	-5.6	28500	-10.0
32	29724	-8.6	28620	-9.4	29607	-2.3	28563	-4.8
24			28678	-9.6			28625	13.2
41	29974	-4.6	28860	-15.5	29851	1.3	28804	-4.1
33	30036	-3.9	28935	-1.7	29901	-1.3	28860	-0.7
25			28995	4.6				
50	30209	-4.6			30076	-0.5		
42	30277	-1.0	29165	-9.8	30140	2.4	29088	-8.1
34	30329	-5.8	29231	-0.6	30186	0.9	29146	2.5
51	30509	3.9			30358	-1.4		
43	30570	5.0			30423	7.6		

Table 7.1.: cont. on next page

Assignment[a] /cm^{-1}	$^{16}O_3$ Cold Band Positions /cm^{-1}	$^{16}O_3$ Hot Band Positions	Exp-Calc /cm^{-1}	$^{18}O_3$ Cold Band Positions /cm^{-1}	$^{18}O_3$ Hot Band Positions	Exp-Calc /cm^{-1}
60	30724		2.7	30570		2.5
52	30790		5.7	30634		1.9
44	30850		10.2	30682		-0.9
61	30999		6.5	30836		0.8
53	31059		7.9	30894		-0.6
45	31104		1.8	30945		4.7
70	31193		3.2	31035		10.3
62	31248		-3.5	31090		-2.7
54	31309		3.4	31148		1.0
71	31435		-5.8	31272		-5.2
63	31486		-12.1	31325		-15.0
55	31538		-9.8	31377		-12.1
80	31616		-3.2	31439		-9.0
72	31686		6.4	31542		22.5
64	31756		23.6	31593		15.9
81	31898*		48.0	31686		0.7
73	31898*		-8.0	31736		-15.6
65	31898*		-56.4	31807		2.9

Table 7.1.: The re-assignment of the cold and hot bands in the Huggins absorption of $^{16}O_3$ and $^{18}O_3$. Also given are the differences between the transition energies observed [9] and those calculated using the constants given in Table 7.3. The values for the hot bands from $\nu_1'' = 1$ are calculated in the same way, with the additional information: ω_1'' ($^{16}O_3$) = 1103 cm^{-1} and ω_1'' ($^{18}O_3$) = 1042 cm^{-1}. [a] The assignments do not contain an assignment for the ν_3 mode, for reasons discussed in the text. * weak bands or very broad features not included in the fitting procedure.

ν_1 symmetric stretch	separation (ν-(ν-1))	ν_2 bend separation (ν-(ν-1))					
		1	2	3	4	5	6
0	0						
1	696	351					
2	647	338	343				
		1	1				
3	617	330	313	312	293		
	3	5	4	4	1		
4	562	314	303	293	280	254	
	10	17	18	17	12	6	
5	549	300	281	269	248	229	218
	24	38	44	46	38	25	10
6	515	271	249	238	200	212	
	28	48	50	46	50	45	
7	469	251	251	212	210		
	18	25	50	45	44		
8	423	—	210				
	11	—	42				
9		—					
		30					

Table 7.2.: Observed [10] intensity distributions in the Huggins bands.

and 351 cm^{-1}, respectively. These are much smaller than the ground state frequencies of 1103 and 701 cm^{-1} [12]. The spacings between the bands in the progressions of ν_1 and ν_2 are smoothly anharmonic, with the first quantum of ν_2' also smoothly decreasing as the quanta of ν_1 increase, as shown in Table 7.2. Both sets of observations are consistent with there being a large change in geometry between the ground and excited states, particularly in ν_1.

Brand *et al.* [7] have proposed that the hot band data of Eberhardt and Shand [13] was not consistent with the analysis of Simons *et al.* [5] with which the present analysis agrees in principle. The hot bands were assigned as being mainly due to a ground state vibration of 1043 cm^{-1} which is the observed value for ν_3 [12]. The positions of the hot bands in the spectra of $^{16}O_3$ and

$^{18}O_3$ recorded by Katayama [9], shown in Table 7.1, are effectively the same as those of the earlier study [13]. It can be seen from the present re-assignments that all of the observed hot bands can simply be interpreted as originating from ν_1 in the ground state which has a frequency of 1103 cm^{-1} (1042 cm^{-1} in $^{18}O_3$ [14]). No hot bands assignable to transitions from ν_2 were observed despite the vibrational frequency being only 701 cm^{-1}. This is consistent with there being a longer progression in ν_1 than in ν_2 in the cold band spectrum, both suggesting that, relatively, there is a larger change in the ν_1 coordinate than in ν_2.

The new assignments of the band positions given in Table 7.1 were fitted to equation 7.1 using a least squares fitting procedure and the resulting constants are presented in Table 7.3 along with the standard deviations for each constant.

$$\begin{aligned}\nu \quad = \quad & (\nu^*_{0e}) + \omega_1(\nu_1 + \tfrac{1}{2}) + \omega_2(\nu_2 + \tfrac{1}{2}) \\ & + x_{11}(\nu_1 + \tfrac{1}{2})^2 + x_{12}(\nu_1 + \tfrac{1}{2})(\nu_2 + \tfrac{1}{2}) + x_{22}(\nu_2 + \tfrac{1}{2})^2 \end{aligned} \tag{7.1}$$

where ν^*_{0e} is a false origin as no information is known about ν_3. Later in the chapter it will be seen to have the following value; $\nu^*_{eo} = \nu_{eo} + \frac{3}{2}\omega_3$. The fit generated from these constants is very good with most of the calculated band positions being within 10 cm^{-1} of the observed values. One of the reasons for the accuracy of the fit is that below 32000 cm^{-1} the individual vibronic bands do not overlap significantly, in marked contrast to the peaks in the Hartley band structure.

7.2.3 Simulation of the Huggins Bands

The region of the Huggins bands below 32000 cm^{-1} can be simulated by calculating the positions of the vibrational features using equation 7.1 and

	Huggins Bands		Hartley Bands	
	$^{16}O_3$	$^{18}O_3$	$^{16}O_3$	$^{18}O_3$
ω_1/cm^{-1}	752.3 ± 4.2	701.6 ± 4.8	927.7 ± 7.0	905.3 ± 7.8
ω_2/cm^{-1}	415.0 ± 5.1	376.7 ± 4.9	355.5 ± 15.1	321.5 ± 16.0
x_{11} /cm^{-1}	-19.5 ± 0.4	-16.9 ± 0.4	-23.2 ± 0.5	-23.6 ± 0.5
x_{12} /cm^{-1}	-20.2 ± 0.6	-15.2 ± 0.7	-8.3 ± 1.1	-7.9 ± 1.4
x_{22} /cm^{-1}	-6.2 ± 0.6	-5.1 ± 0.6	-4.0 ± 2.1	-1.6 ± 2.2
ν^*_{0e}	26516.9 ± 12.5	26583.9 ± 13.2	32290.5[a] ± 31.7	32358.4[a] ± 34.8
σ^b /cm^{-1}	7.4	7.6	28.6	39.1

Table 7.3.: Vibrational constants obtained by fitting the assignments presented in this chapter to equation 7.1 using a least squares method. For the Huggins bands $\nu^*_{0e} = \nu_{eo} + \frac{3}{2}\omega_3$ while ν^*_{0e} is the saddle point energy of the Hartley bands. [a] The C_{2v} equilibrium geometry. [b] Standard deviation of the calculated bands from experimental value.

the fitted vibrational constants given in Table 7.3. Each of these features was then convoluted with a Gaussian peak of FWHM = 40 cm^{-1} to provide a very approximate simulation of the rotational contour of each vibrational band. The intensity envelopes of the ν_1 and ν_2 progressions were also approximated by Gaussian profiles which peaked at $\sim$ 6 for the ν_1 progression and $\sim$ 3 for the ν_2 progression. Even such a very simple simulation provides a good fit of the absorption data as can be seen from Figure 7.2. It also provides a very good illustration of the assignment.

7.2.4 Extrapolation of the Fitted Features

There are several strong bands between 32000 and 33000 cm^{-1} which have not been fully assigned in previous studies [9, 10]. Extrapolations of the assigned progressions of ν_1 and ν_2 in the present analysis, presented in Table 7.4, show that these broad bands are due to overlaps of the members of several different progressions which have become coincident because of the

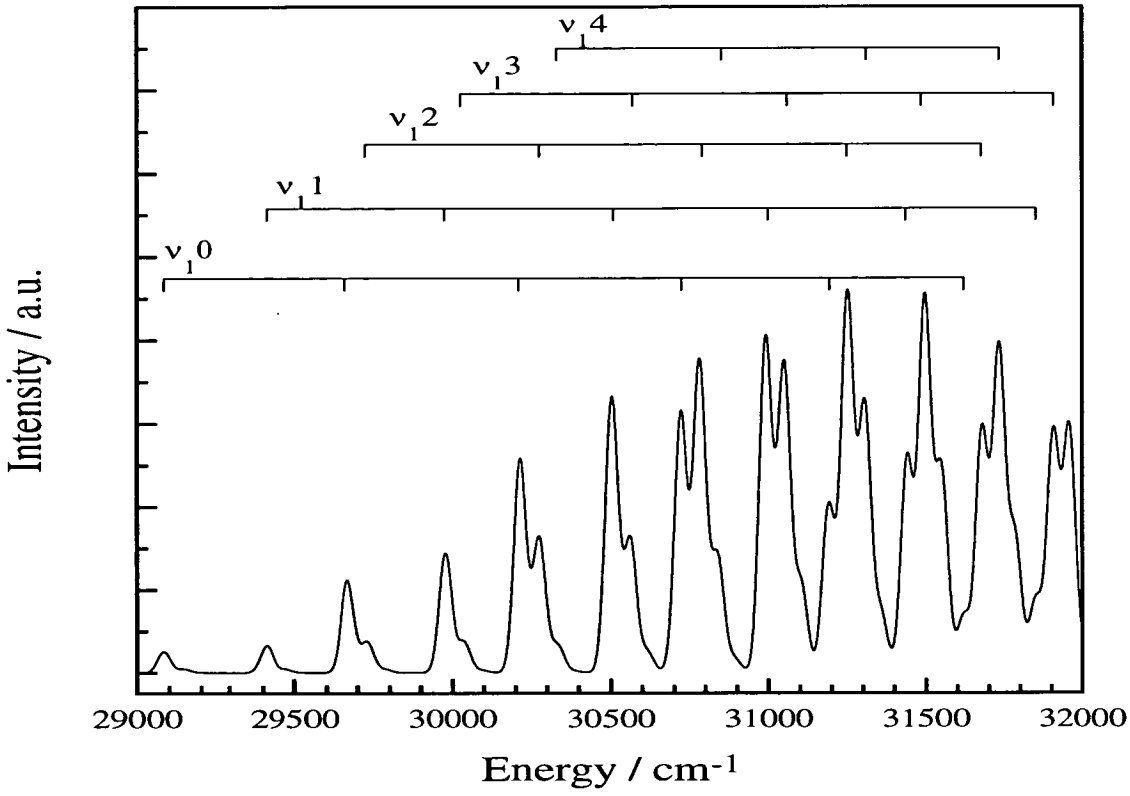

Figure 7.2.: A simulation of the Huggins bands of ozone using the fitted harmonic and anharmonic constants from Table 7.3 and smooth Gaussian intensity profiles, see text for details. The ladders indicate progressions of ν_1 with the first labelled feature in each progression involving $\nu_1 = 3$.

anharmonicities of the progressions and are not resolvable under the experimental temperature of 195 K [11]. Transitions involving low bending quanta appear to dominate the spectrum in this extrapolated region.

7.2.5 Implications of the New Assignment

As stated above, the principal difference between this assignment and the most recent assignments of the Huggins bands [9, 10] is the absence of a progression in ν_3. This is surprising since one would expect that there must also be a large change along this normal coordinate in the equilibrium geometry. To understand this all of the electronic states which are thought to be involved in the absorption of ozone in the UV region must be examined. Hay *et al.* [15] proposed that four surfaces, as illustrated schematically in figure 7.3,

	$^{16}O_3$		$^{18}O_3$	
	Calc.	Exp.	Calc.	Exp.
90	32010		31838	
82	32069		31912	
74	32120	32108	31974	31942
91	32220	32224	32060	
83	32275	32323	32129	32156
10 0	32361	32373	32193	
92	32419	32391	32272	32266
84	32469	32446	32336	32357
10 1	32551		32400	32409
93	32605	$\sim$ 32625	32473	
11 0	32673		32515	
10 3	32895	$\sim$ 32900	32783	
12 0	32946		32803	

Table 7.4.: Comparison of the extrapolated Huggins bands energies calculated using the constants reported in Table 7.3 with the observed Huggins absorption bands [9].

are involved. The two possible electronic transitions are illustrated by vertical arrows in this diagram. The reduced intensity of the Huggins bands with respect to that of the Hartley band can be explained either by the lowered transition intensity of the vibronically induced transition to the 2 $^1A_1$ state or due to lowered Franck-Condon overlap of the ground state wavefunction of the (000) state with those of the bound levels in the C_S wells of the electronically allowed 1 $^1B_2$ surface. In the two cases the explanation for only one bound level of ν_3 in the upper state is slightly different. If the excited state has $^1A_1$ symmetry then all of the observed transitions terminate on ν_3, v = 1 (due to the symmetry imposed $\Delta\nu_3$ = odd selection rule) with higher odd levels not being bound or having very short lifetimes due to tunnelling through a small barrier to dissociation. The alternative upper state symmetry of $^1B_2$ suggests that all levels terminate on ν_3, v = 0 with higher even levels being broadened by non-adiabatic coupling of this state with the lower 2 $^1A_1$ state. In the second case levels with ν_3, v > 0 could be broadened to such an extent that they are not observed as discrete structure as the non-adiabatic coupling increases with quanta of ν_3 of the upper state, however the levels could still exist.

The measurement of the angular distribution of O ($^3P_0$) fragments following the photolysis of ozone in the Huggins bands have shown that the transition moment is aligned along the axis joining the two terminal atoms [16]. This is supported by the measurements on the O_2 ($a\ ^1\Delta_g$) fragments in a similar experiment [17]. Therefore, the overall symmetry of the transition is b_2 which could either be due to transition to ν_3, v = even of the $^1B_2$ or ν_3, v = odd of the 2 $^1A_1$ state. Measurements of the anisotropy of the fragments cannot distinguish between the two possibilities. Other attempts to identify the upper state such as rotational band contour analysis of certain vibrational features have led to conflicting electronic assignments. Therefore, to date no experimental evidence exists which can categorically identify the electronic nature of the upper state.

In contrast, the accepted upper electronic state assignment of the Hartley

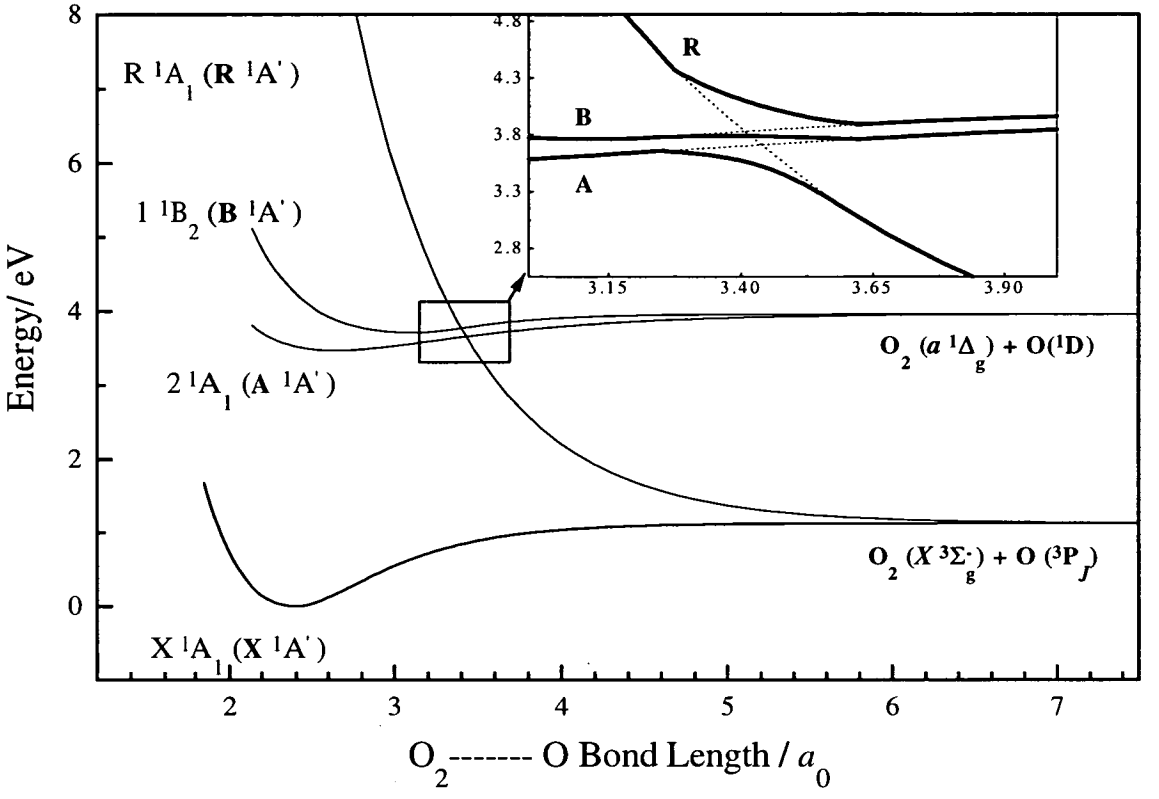

Figure 7.3.: The schematic diabatic potential energy curves of the four possible states involved in the UV dissociation of ozone. The inset shows the adiabatic representation of the curve crossing. This figure is adapted from the work of Hay *el al.* [15].

band is the 1^1B_2 state. Therefore, to aid the assignment of the Huggins bands it is useful to consider the vibrational assignments of both band systems at the same time. The topology of a single upper surface which could account for both absorption bands can then be sketched and compared with the *ab initio* calculations to determine if such a surface is feasible. However, some problems with the existing vibrational assignments of the Hartley band led to a reassignment which is described in the following section. The electronic assignment of the Huggins bands is therefore postponed until after the Hartley band assignment has been discussed.

7.3 Re-assignment of the Hartley bands

7.3.1 Previous assignments

As discussed in chapter 2 only two previous assignments of the vibrational structure in the Hartley band region have been presented in the literature, a brief summary of which is given here. In the first, Joens [21] carried out an analysis using previously recorded experimental data [1, 11, 22, 23]. In this analysis, the underlying Hartley continuum was first subtracted leaving only the structured portion. The assignment included long progressions in ν_1, v' = 0 - 8, and shorter progressions in ν_2, v' = 0 - 5, which were essentially harmonic with vibrational spacings of 1108 and 298 cm^{-1}, respectively. An attempt to resolve the uncertainty in the absolute numbering of both bending and symmetric stretching progressions reported in this study was made by Parisse *et al.* [24]. They recorded the absorption spectra of both $^{16}O_3$ and $^{18}O_3$ and analysed them using the same method as Joens [21]. The observed isotope shifts were used to confirm the vibrational numbering proposed in the earlier study.

Both studies contained several anomalous observations. Firstly, the fits of the experimental data gave deviations which were approximately three times larger than the estimated precision of the bands. Furthermore, the assignments were unable to explain the intensity alternation along the bending progressions built on certain quanta of symmetric stretch or the large variation in the observed bandwidths. Finally, the calculated anharmonicity parameter for the bending vibration had, unusually, a small but significant positive value.

7.3.2 Re-assignment

In this section the alternative assignment of the Hartley bands will be presented. While there are more uncertainties associated with this re-assignment than there are with that proposed for the Huggins bands, it can explain most

of the anomalies in the positions, widths and intensities of the bands which were identified in the previous assignment. Furthermore, it will be shown that the vibrational constants which are calculated are similar to those determined for the Huggins bands.

The band positions given by Parisse *et al.* [24] will be used exclusively as the experimental data set in the present study. The observed band positions of $^{16}O_3$ and $^{18}O_3$ are presented, together with their new assignments, in Table 7.5. The spectrum is believed to be made up of short ν_2 progressions of up to six members built on a long progression of around eleven quanta of ν_1.

Assignment	$^{16}O_3$ Band Positions /cm^{-1}	Exp-Calc /cm^{-1}	$^{18}O_3$ Band Positions /cm^{-1}	Exp-Calc /cm^{-1}
03	33908	-20.7	33833	-63.3
10	—	—	33833	15.4
04	34152	-95.7	34108	-92.7
11	34152	16.8	34108	-15.9
05	—	—	34446	-55.8
12	34440	-22.0	34446	19.0
20	34613	-17.9	34616	-8.4
13	34798	17.2	34749	22.2
21	34943	-14.4	34925	2.2
14	35096	4.6	35049	25.8
22	35273	-3.0	35198	-20.0
15	35409	15.0	35359	42.6
30	35409	-6.1	35359	25.0
23	35569	-17.4	35467	-42.9
31	35722	-11.4	35608	-66.5
24	35868	-20.7	35773	-25.4
32	36038	-5.5	35979	17.2
25	36187	4.0	—	—
40			36166	69.7
33	36375	29.4	36166	-79.8
41			36381	2.0
34	36669	29.4	—	—
42	36758	-6.7	36632	-26.3
50	36874	29.7	36789	27.6
43	37047	-11.4	36928	-6.4
51	37182	36.1	37073	36.8
44	37325	-19.1	37187	-20.2
52	37519	79.6	35348	40.3
60	37519	29.7	35348	-31.1
45	35624	2.3	—	—
53	37783	58.2	37615	39.2
61	37783	0.5	37615	31.1
46	—	—	37739	4.0

Table 7.5.: (a) See caption of Table 7.5 (b).

The current assignment differs from those in the earlier studies in two fundamental aspects: the symmetric stretching frequency is *ca.* 900 cm^{-1} rather than 1100 cm^{-1} and both ν_1 and ν_2 are very anharmonic. The most significant result of these two changes to the assignment is that almost all of the observed experimental peaks are comprised of at least two overlapping vibronic bands, hence neither the position nor the intensity of each individual vibronic band can be measured very accurately. In contrast, every peak observed in the Huggins bands up to that labelled (8,0) is a single vibronic band and the spacings and intensities of bands along any progression can be determined quite accurately. It should be noted that the spacing of 1100 cm^{-1} observed throughout the Hartley band spectrum and previously assigned [21, 24] to one quantum of ν_1 is approximately equal to one quantum of ν_1 plus one quantum of ν_2 in the present analysis.

The numbering of the vibrational progressions is very problematical. In the spectrum of the Huggins bands equivalent pairs of vibronic bands of $^{16}O_3$ and $^{18}O_3$ could be unambiguously identified and hence the vibrational numbering could be easily calculated. As a result of the large number of overlapping features in the Hartley band spectrum these pairs of bands cannot be uniquely identified with such certainty. The approach used here was to assume that, in the low energy region of the spectra of the two isotopic species, each peak in the $^{16}O_3$ spectrum was paired with that of the nearest in energy in the $^{18}O_3$ spectrum and given the same vibronic assignment, i.e. in agreement with the analysis of Parisse *et al.* [24]. If this assumption is correct, the relatively high frequency of ν_1 means that the proposed numbering of the ν_1 should be quite certain.

The numbering of the ν_2 progressions are much less certain because of the lower frequency of ν_2. The ν_2 numbering in Joens's [21] assignment is based on three bands which were assigned as (2,0), (3,0) and (4,0) as he could not identify any bands shifted to low energy of them by one quantum of bend. However, in the data presented by Parisse *et al.* [24] the positions of bands

Assignment	$^{16}O_3$ Band Positions /cm^{-1}	Exp-Calc /cm^{-1}	$^{18}O_3$ Band Positions /cm^{-1}	Exp-Calc /cm^{-1}
54	37975	-27.1	—	—
70	38091	3.2	37939	-10.8
62	38091	23.3	37939	29.3
63	38332	-12.8	38238	68.0
71	38332	-40.7	38238	29.2
80	38628	-12.0	38478	4.8
64	38628	14.3	38478	51.0
72	38628	-21.6	38478	13.5
65	—	—	38652	-28.8
81	38873	-43.5	38754	29.7
73	38873	-45.3	38754	37.0
82	39138	-47.0	38920	-52.0
90	39138	-7.7	38920	-29.3
74	39138	-41.0	38920	-46.0
83	39409	-36.4	39182	-34.6
91	39409	-4.9	39182	-10.5
92	39694	19.9	39422	-10.4
84	39694	-3.7	39422	-35.8
93	39989	62.9	39645	-24.0
10 2	40150	33.3	39860	14.5
94	40150	-20.1	39860	-42.3
10 3	40397	36.6	40169	94.8
11 2	—	—	40169	-42.3
11 3	40718	-30.3	40361	71.2
10 4	—	—	40361	61.3
11 4	41000	24.4	—	—
12 2	—	—	40562	32.1

Table 7.5.: (b) The re-assignment of the vibrational structure in the Hartley absorption of $^{16}O_3$ and $^{18}O_3$. Also given are the differences between the observed and calculated energies. The constants given in table 7.3 were used to calculate energies of the bands.

assignable to all three lower energy bands were tabulated. These data appear to contain only one band of medium intensity which does not have a band shifted by one quantum of ν_2 to low energy of it and this occurs at 36789 cm^{-1} in the spectrum of $^{18}O_3$. Since, in the present re-assignment, all bending quanta in the spectra of both isotopic species are numbered relative to this one band, the numbering must remain tentative.

The assignment of bands below 41000 cm^{-1}, given in Table 7.5, were fitted to equation 7.1, as before, and the resulting constants are presented in Table 7.3. When bands above 41000 cm^{-1} were included in the experimental data set, there was a distinct deterioration of the overall fit. The most likely cause of this observation is that it is not possible to fit such an anharmonic progression as that of ν_1 above v = 10 using only the anharmonicity constants of the first order Dunham expansion shown in equation 7.1. Including higher order anharmonicities [25, 26] in the fitting procedure improves the numerical fit and allowed all higher energy vibrational features tabulated in the experimental data of Parisse *et al.* [24] to be included. However, this method resulted in physically unrealistic fitted constants due to the number of overlapping bands combined with the greater number of fitting constants and hence the second order fitting is not presented here. This procedure also highlighted that, unlike the case of the Huggins bands, an extrapolation of the first order fit to higher energy than the fitted region is unrealistic. A further result of the large anharmonicity of ν_1, was that above 41000 cm^{-1} the values of ν_1 and ν_2 quanta are very similar introducing an extra degree of uncertainty in their assignments.

While recognising that there are many uncertainies in the assignment presented here the standard deviation of the overall fit of around 30 cm^{-1} is quite similar to that of the previous assignments. It does, however, have a major advantage over the alternatives reported previously [21, 24] as many of the observed peaks consisting of two or more overlapping bands can explain the relatively poor fit. The same phenomenon of overlapping bands also explains

why the intensities and widths of the bands belonging to what was originally assigned as single progressions vary so much and so irregularly.

The intensities of the observed bands of $^{16}O_3$ have been estimated by Joens [21]. As a result both of the blending of individual vibronic bands and the inevitable errors involved in subtracting a large continuum background of the observed spectrum, it is not possible to gain much quantitative intensity information on the Hartley bands as it is in the Huggins bands. However, qualitatively it appears that the ν_1 and ν_2 progressions peak around v = 8 and v = 3, respectively.

7.3.3 Relating the Assignment to the PES of the Upper State

The implications of this assignment are realised by relating the assigned Hartley absorption spectrum to the generic surface shown in figure 7.1. A Franck-Condon (FC) analysis of an absorption spectrum due to a transition to just such a surface with a saddle point at extended C_{2v} geometry relative to the lower state and two exit channels was first proposed for the two-dimensional case by Pack [27] and was later extended to three dimensions by Alder-Golden [28]. The important aspect of these analyses is the decoupling of the motion in the q_3 coordinate at the saddle point geometries (i.e. C_{2v}) which allows the FC analysis of this mode to be separated from that of the symmetric modes ν_1 and ν_2. The FC amplitude in the q_3 mode can be calculated by the consideration of the saddle point barrier between the C_S wells. When the energy available for this mode is below the energy difference between the ground state and the maximum of the barrier the overlap is low, this overlap then increases to a maximum when the barrier top is reached and decreases above this energy again. This effect is illustrated schematically in Figure 7.4. The shape of a peak formed in this way is controlled by the relative force constants

in the q_3 coordinate of the upper and lower states, k_3' and k_3'' [29]. The overall absorption can then be calculated by the convolution of this peak with each of the large number of peaks in the FC overlap of the remaining two co-ordinates, q_1 and q_2.

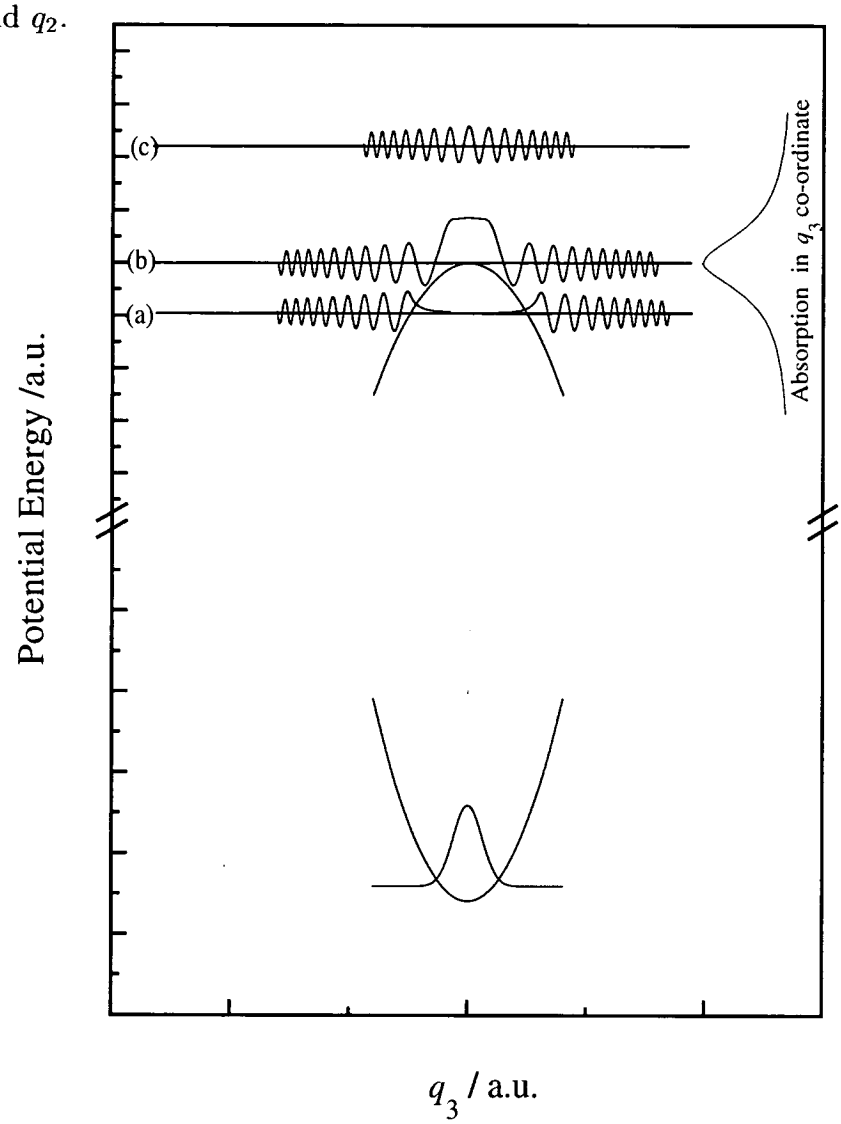

Figure 7.4.: An illustration of the absorption to a saddle point of a surface such as that depicted in Figure 7.1 (a). The saddle point is illustrated with simple parabolic function and the wavefunctions encountering such a barrier are illustrated.

Therefore, the two factors which govern the overall shape of the Hartley band absorption are the density of ν_1 and ν_2 levels of the upper state and the shape of the barrier between the two C_S minima. No information about the shape of the barrier between the two exit channels is obtained from our analysis. However, it can be concluded that, due to the anharmonicities of the

modes, the density of the ν_1 and ν_2 levels is much higher than the previous harmonic models suggest. Attempts to simulate the Hartley bands using this method [28, 29] assumed a harmonic progression of both ν_1 and ν_2 modes and hence the density of peaks used in these calculations were too low. To compensate for this the shape of the q_3 peak to be convoluted with each of these had to be broadened using unrealistic k_3' values in order to simulate the overall envelope of the Hartley bands. As a result of this process the calculation could not reproduce the small oscillations which appear to be superimposed on the top of the Hartley bands. The inclusion of anharmonicities in the ν_1 and ν_2 modes is an essential consideration in any successful attempt to analyse the Hartley band using the Franck-Condon model outlined above.

As an illustration of this, the Hartley band absorption can be simulated in a very approximate fashion by assuming that the q_3 peak convoluted with each of the $\nu_1\nu_2$ peaks can be approximated by a Lorentzian peak with a width of 430 cm^{-1}. This is a gross over-simplification of the problem but this 'simulation' is solely for the purpose of illustration of the above points. The positions of the $\nu_1\nu_2$ peaks are calculated from using the fitted constants of Table 7.3 and their intensities are given by simple Gaussian envelopes in each of these two modes. The results of this method are shown in Figure 7.5 where the simulation is compared with the 226 K absorption data of Molina and Molina in the assigned energy region.

The finer discrepancies between the simulated and experimental absorptions is due to the approximation of the intensities and the shape of the q_3 peak. However, the general trend shows that the apparently small peaks superimposed on the Hartley band can be reproduced in this way.

7.4 One upper state or two?

As there is no doubt that the absorption in the Hartley band continuum

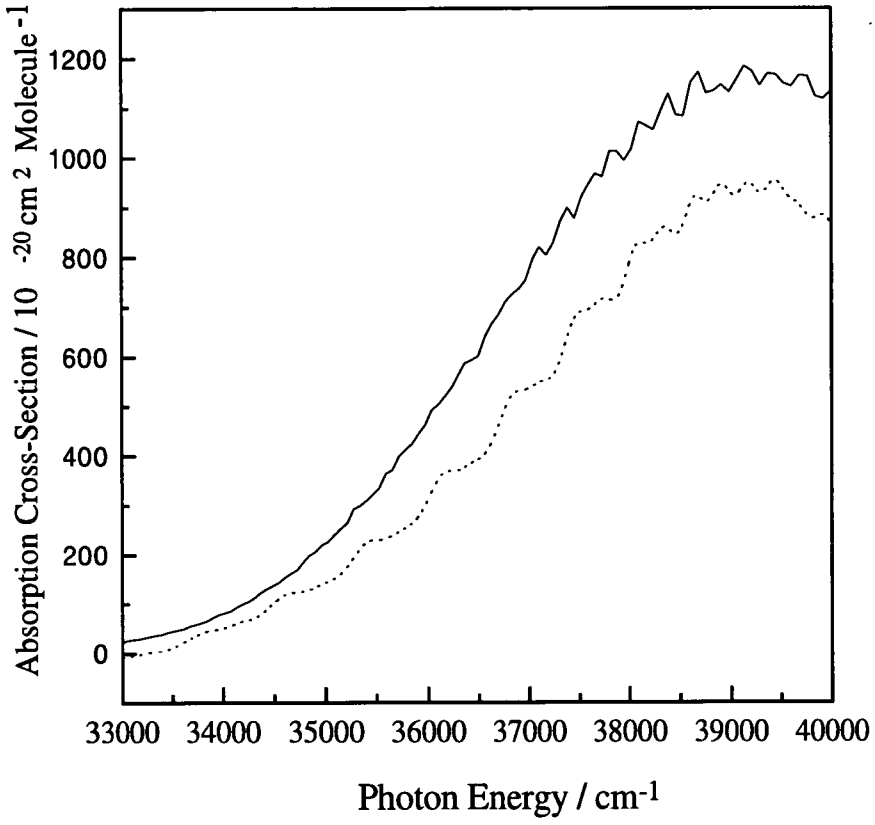

Figure 7.5.: The full line shows the 226 K absorption data of Molina while the dotted line is the approximate simulation outlined in the text.

terminates somewhat above the saddle point on the 1^1B_2 surface it is possible to evaluate the energy of this saddle point using the reassignment presented in the previous section. The new Hartley band assignments of the ν_1 and ν_2 progressions can be used to locate their origin and by subtracting the zero point energy of these two modes the energy of the saddle point is found. The origin of the Huggins bands can also be found in a similar manner. Combining this information with value for the thermodynamic threshold for the $O(^1D)$ + O_2 ($a\ ^1\Delta_g$) dissociation limit a reaction coordinate cut which links these three energies can be created. As illustrated in figure 7.6, this leads to the saddle point being almost exactly the same energy as the dissociation limit and consequently to the origin of the C_S wells (i.e. the extrapolated origin of the Huggins bands) being $\sim$ 5000 cm^{-1} below both of these. This represents the

reaction cut through a *single* upper surface which could account for both the Huggins and Hartley band absorption. The few limitations to the accuracy of this cut include the possibility that the saddle point barrier should be lowered due to unobserved low energy Hartley band features in the absorption. Also, it is possible that there is a barrier to dissociation in the exit channel, but due to the lack of a progression in ν_3 in the Huggins bands absorption we have no information about this barrier.

Key features of the two most recent *ab initio* 1^1B_2 surfaces are compared numerically with the single surface predicted from the assignments of both absorptions in table 7.6. The calculated vibrational modes in the C_S wells of these surfaces match those of the Huggins bands quite closely. However, the overall shape of the calculated surfaces is such that the saddle point is well above the dissociation limit along the q_3 coordinate and the C_S well minima are just a few hundred wavenumbers below the asymptote. These are both at variance with the experimental results of the detailed vibrational assignment. Although these simple energetic considerations of the experimental data which are largely independent of the details of the assignments have been noted previously [30] they were not made in conjunction with a discussion of the *ab initio* surfaces and hence no conclusions of the type made here were drawn.

It seems, therefore, that the single surface model breaks down under comparison with *ab initio* work. This points to the Huggins bands terminating on the 2^1A_1 surface rather the 1^1B_2 surface. It must be noted at this point that, even when the two surface model is adapted for the Huggins and Hartley band systems and that only the Hartley bands are due to the 1^1B_2 surface, some discrepancies between the *ab initio* surfaces and the energetic arguments presented here remain. The principal one of these is that this analysis, and indeed that of other authors [24], indicate that the saddle point of the 1^1B_2 surface should be close in energy to that of the $O(^1D) + O_2\ (a\,^1\Delta_g)$ dissociation limit while *ab initio* calculations show energy differences of 1370 cm^{-1} [2] and 3570 cm^{-1} [3] between these points. However, this discrepancy is relatively

	C_S Wells Huggins Bands			C_{2v} Hartley Bands		Barrier Height[a]	C_S Well Depth[b]
	ω_1 /cm^{-1}	ω_2 /cm^{-1}	ω_3 /cm^{-1}	ω_1 /cm^{-1}	ω_1 /cm^{-1}	/cm^{-1}	/cm^{-1}
Ref [18]	743.5[c]	440.6[c]	800.2[c]	—	—	2060[d]	690[d]
Ref [3, 4]	770	612	586	1235	574	3390[e]	-180[e]
Present Work	752.3	415.0	—	927.7	355.5	5200 ± 70	5230 ± 35

Table 7.6.: A comparison of parameters characterising the calculated *ab initio* 1^1B_2 surfaces of Leforestier *et al.* [18] and Banichevich *et al.* [3, 4] with the same parameters taken from the assignments presented in this chapter assuming a single upper surface. [a] The barrier height from the (000) level in the C_S wells to the top of the barrier between the C_S wells. [b] C_S well depth relative to the $O(^1D)$ + O_2 ($a\,^1\Delta_g$) dissociation limit. [c] Values taken from ref [19]. [d] Calculated from the published analytical fit of the surface the Murrel-Sorbie function [31] and the zero-point energy. [e] Values taken from ref [4].

minor in comparison to that which would be required for a single surface model for both absorption systems to be valid.

It is now necessary to return briefly to the vibrational assignment of the Huggins bands with the electronic assignment of the 2^1A_1 as the upper state. This leads to the conclusion that all of the cold bands involve one quantum of ν_3 in the excited state. The question which may now be asked is why no hot bands due to excitation of (001) levels of the ground state to those with $\nu_3' = 0$ in the upper state are observed. It is suggested that these bands may occur but have relatively very small intensities due to small FC factors. Support for this conclusion can be drawn from the fact that the (001) $\leftarrow$ (000) band is not observed which indicates a large change in equilibrium bond lengths. It is therefore also not surprising that none of the diagonal transitions, (ν_1', ν_2', 0) $\leftarrow$ (001), are observed with significant intensities because of the additional fact that the shallow bound nature of the upper state in the q_3 coordinate will cause a large decrease of the range between the turning points of this mode on going from $\nu_3' = 1$ to $\nu_3' = 0$. The smaller increase of the range of the ground state turning points on going from $\nu_3'' = 0$ to $\nu_3'' = 1$ in the more deeply bound

ground state results in the negligible FC factors.

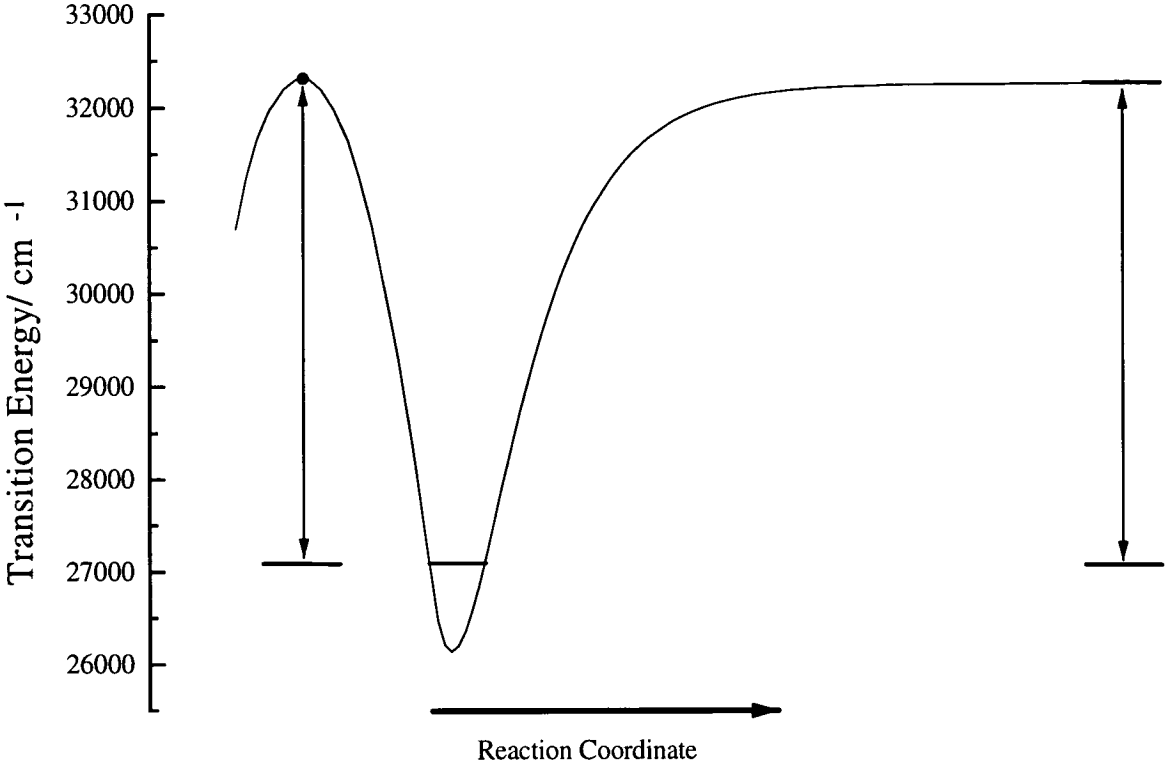

Figure 7.6.: The schematic reaction coordinate of a surface which could be responsible for both Huggins and Hartley band absorptions.

7.5 Conclusions

The discrete vibronic structure in both the Huggins and the Hartley bands has been re-assigned. The Huggins band structure has been re-assigned to progressions in the ν_1 and ν_2 modes with only a single active quantum of ν_3.

The discrete structure in the Hartley bands is also assigned solely to ν_1 and ν_2 with similar frequencies to those observed in the Huggins bands. The major changes from the previous assignments are the large anharmonicity of the ν_1 mode and the inclusion of double assignments of a number of features due to overlapping bands. The important implications of this anharmonicity

for Franck-Condon models of the Hartley bands was also demonstrated.

The question of whether the UV absorption of ozone must be assigned to one or two upper electronic states is addressed by a comparison of the shape of the single surface required to support both sets of vibrational data with the *ab initio* calculations of the 1^1B_2 which is known to be responsible for the Hartley band. Serious discrepancies between the shapes of the these potentials lead to the conclusion that the Huggins bands almost certainly terminate on the 2^1A_1 state rather than the 1^1B_2 of the Hartley bands.

References

[1] L. T. Molina and M. J. Molina, *J. Geophys. Res.* **91** (1986) 14501.

[2] F. Lequere, C. Leforestier, K. Yamashita and K. Morokuma. *J. Chem. Phys.* **101** (1994) 3806.

[3] A. Banichevich and S. D. Peyerimhoff. *Chem. Phys.* **173** (1993) 93.

[4] A. Banichevich, S. D. Peyerimhoff and F. Grein. *Chem. Phys.* **178** (1993) 155.

[5] J. W. Simons, R. J. Paur ,H. A. Wębster III and E. J. Blair, *J. Chem. Phys.* **59** (1973) 1203.

[6] A. Jakowlewa and V. Kondratjew, *Phys. Z. Sowjetunion* **9** (1936) 106.

[7] J. C. D. Brand, K. J. Cross and A. R. Hoy, *Can. J. Phys.* **56** (1978) 327.

[8] P. J. Hay and T. H. Dunning, Jr., *J. Phys. Chem.* **67** (1977) 2290.

[9] D. H. Katayama. *J. Chem. Phys.* **71** (1979) 815.

[10] J. A. Joens. *J. Chem. Phys.* **101** (1994) 5431.

[11] D. E. Freeman, K. Yoshino, J. R. Esmond and W. H. Parkinson. *Planet. Space Sci.* **32** (1984) 239.

[12] A. Barbe, C. Secroun and P. Jouve. *J. Mol. Spec.* **49** (1974) 171.

[13] W. H. Eberhardt and W. Shand, *J. Chem. Phys.* **14** (1946) 327.

[14] J. M. Flaud, C. Camy-Peyret, V. Malathy-Devi, C. R. Rinsland and M. A. H. Smith. *J. Mol. Spec.* **122** (1987) 221.

[15] P. J. Hay, R. T. Pack, R. B. Walker and E. J. Heller. *J. Phys. Chem.* **86** (1982) 862.

[16] P. O'Keeffe, T. Ridley, K. P. Lawley, R. R. J Maier and R. J. Donovan, *J. Chem. Phys.* **110** (1999) 10803.

[17] W. Denzer, G. Hancock, J. Pinot de Moira and P. L. Tyley, *Chem. Phys.* **231** (1998) 109.

[18] F. Lequere and C. Leforestier. *Chem. Phys. Lett.* **189** (1992) 537.

[19] O. Bludsky and P. Jensen. *Mol. Phys.* **91** (1997) 653.

[20] K. Yamashita and K. Morokuma. *Faraday Discuss. Chem. Soc.* **91** (1991) 47.

[21] J. A. Joens. *J. Chem. Phys.* **100** (1994) 3407.

[22] E. C. Y. Inn and Y. Tanaka. *Adv. Chem.* **21** (1959) 263.

[23] K. Yoshino, J. R. Esmond, D. E. Freeman and W. H. Parkinson. *J. Geophys. Res.* **91** (1986) 14501.

[24] C. Parisse, J. Brion and J. Malicet. *Chem. Phys. Lett.* **248** (1996) 31.

[25] J. D. Tobiason, J. R. Dunlop and E. A. Rohlfing. *Chem. Phys. Lett.* **235** (1995) 268.

[26] E. Leonardi and C. Petrongolo. *J. Chem. Phys.* **106** (1997) 10066.

[27] R. T. Pack. *J. Chem. Phys.* **65** (1976) 4765.

[28] S. M. Alder-Golden. *J. Quant. Spectrosc. Radiat. Transfer* **30** (1983) 175.

[29] O. Atabek, M. T. Bourgeois and M. Bacon. *J. Chem. Phys.* **84** (1986) 6699.

[30] R. Bacis, A. J. Bouvier and J.M. Flaud. *Spectrochim. Acta Part A* **54** (1998) 17.

[31] J. N. Murrell, S. Carter, S. C. Farantos, P. Huxley and A. J. C. Varandas. *Molecular potential energy functions*, (John Wiley & sons, U. K., 1984).

Chapter 8

Analysis of Huggins Bands Photofragments

8.1 Introduction

Previous chapters have outlined new vibrational re-analyses of the Huggins and Hartley band and experimental data on the photodissociation following absorption into these bands. In particular, Chapter 5 described in depth translational and angular measurements of the O ($^3P_0$) photofragments formed from Huggins band photolysis. The analysis of this information revealed complex photodissociation dynamics involving both spin-allowed dissociation *via* channel (A)[1] as well as *via* the less expected spin-forbidden channels (B) and (C). The participation of channel (C) was confirmed by REMPI detection and translational energy analysis of the O_2 ($b\ ^1\Sigma_g^+$) fragments in Chapter 6. However, no discussion was made relating the participation of these channels to the vibrational structure of the Huggins bands which was re-analysed in Chapter 7. Neither was a full characterisation of all of the multiplets of the O (^3P_j) fragments attempted. The results and discussions presented in this chapter

[1]The labelling of the dissociation channels of ozone in this chapter follow the notation outlined in the introduction of Chapter 5

endeavour to rectify both of these deficiencies and as a result it is hoped to develop a more complete model of the dissociation dynamics of ozone in this energy region than previously realised. The experimental and analysis techniques used to record and interpret the extensive results related in this chapter are the same as those described in the previous chapters and hence the reader will be referred to previous discussions where applicable.

8.2 Results

The PHOFEX spectrum in Figure 8.1 shows the $O(^3P_0)$ fragment yield produced by the photolysis of ozone in the range 312 - 345 nm. The $O(^3P_0)$ fragments were detected by (2 + 1) REMPI with a probe laser at 226.23 nm. This spectrum is a composite of a number of shorter scans using different dyes to access the required photolysis wavelengths as shown. Although the scans are not corrected for power variations within the region 310 - 335 nm the frequency doubled laser power was approximately constant. In this region, the intensities of the features correspond well with the intensities in the absorption spectrum (shown by the dotted line for comparison). The pump wavelengths between 335 and 345 nm were generated by the fundamental of the PTP dye. The output power changed significantly over this range, therefore the relative intensities of the bands in this region are much more uncertain. The vibrational assignments ($\nu_1\nu_2\nu_3$) are those made in Chapter 7 where ν_1 is the symmetric stretch, ν_2 is the bending motion and ν_3 is the asymmetric stretch.

The most notable difference between the absorption and PHOFEX spectra is at higher energies approaching the threshold of channel (E), 310 nm, where the relative intensities of the PHOFEX bands become much less than their counterparts in the absorption spectrum. This is due to a decrease in the quantum yield of the $O(^3P_0)$ fragment as dissociation *via* channel (E) becomes thermodynamically accessible. This trend was also observed in the PHOFEX

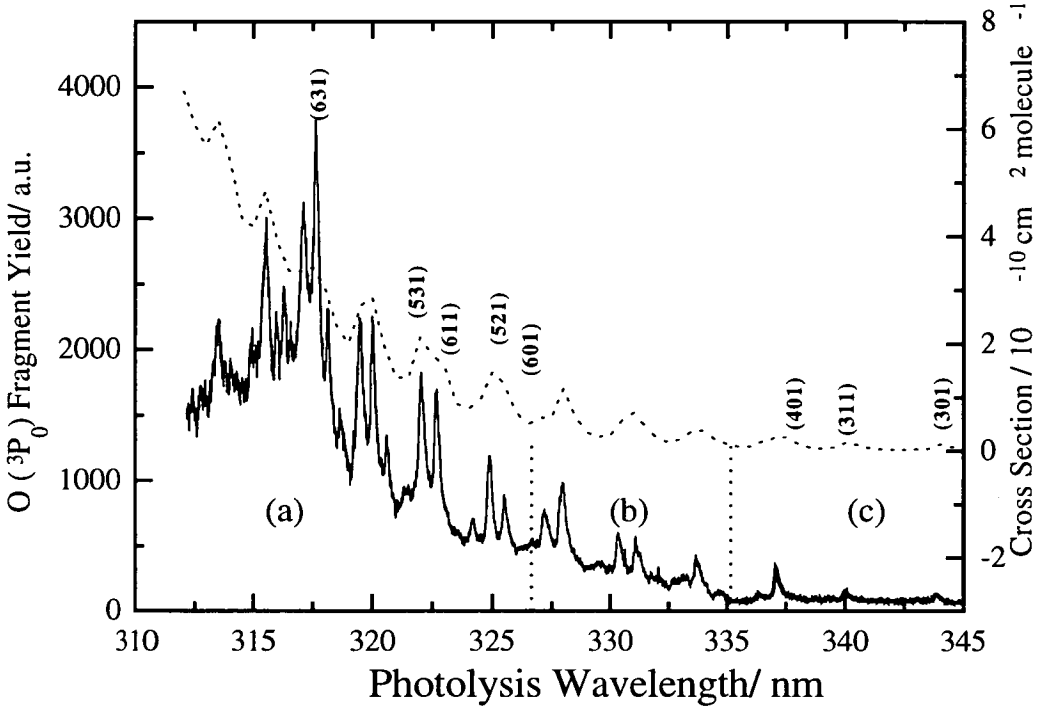

Figure 8.1.: The PHOFEX spectrum of $O(^3P_0)$ fragments produced in the 312 to 345 nm region recorded by detecting the $O(^3P_0)$ state *via* the (2 + 1) 3p $^3P \leftarrow\leftarrow$ 2p ^3P REMPI transition at 226.23 nm following the photolysis of ozone. Section (a), (b) and (c) were recorded with frequency doubled R101 and DCM and the fundamental of PTP respectively. The 226 K absorption spectrum of Molina [1] and vibrational assignments of the features investigated in this chapter are also shown.

spectrum of Takahashi *et al.* [2]. The narrower width of the vibrational features of the LIF PHOFEX spectrum is due to the lower rotational temperature of the parent molecules in the molecular beam ($\sim$ 15 K) compared with 226 K of the absorption spectrum. There are some subtle differences between the jet-cooled spectra recorded by detecting the multiplets, $O(^3P_2)$, $O(^3P_1)$ and $O(^3P_0)$, as illustrated by the spectra shown in Figures 8.2 and 8.3 which show two short scan regions of the Huggins bands.

Two prominent points that should be noted about these spectra are firstly that the best signal to noise ratio (S/N) is achieved in the spectra recorded on the $O(^3P_0)$ fragments. In each spectrum there is a small contribution to the total signal from the probe laser alone. This is due to the fact that the

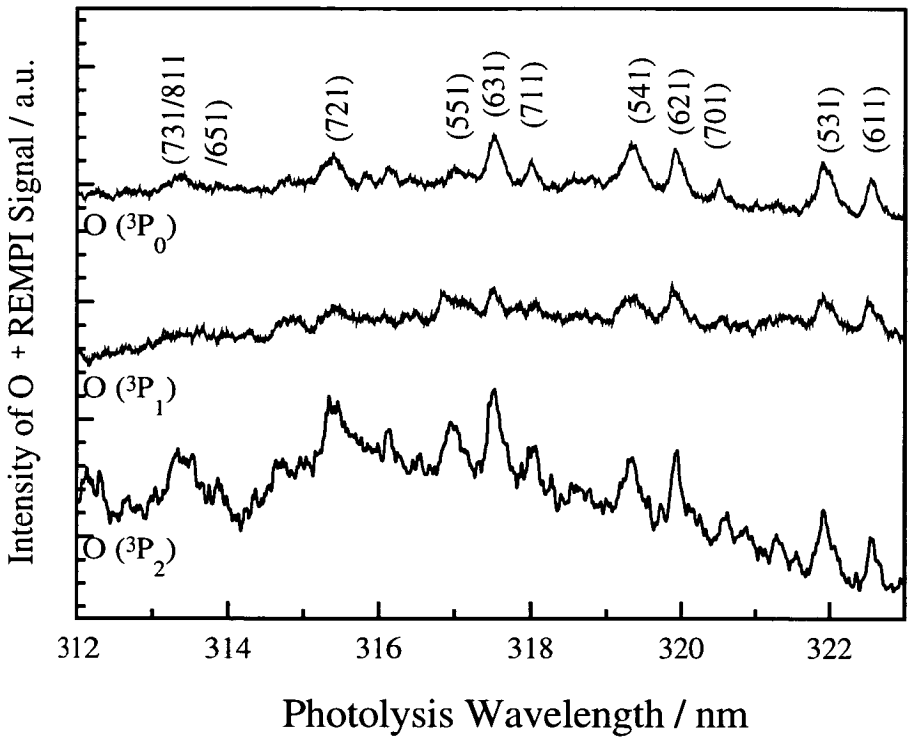

Figure 8.2.: The PHOFEX spectra recorded by detecting the $O(^3P_2)$, $O(^3P_1)$ and $O(^3P_0)$ fragments *via* the (2 + 1) 3p $^3P \leftarrow\leftarrow$ 2p ^3P REMPI transitions at 225.65, 226.05 and 226.23 nm following photolysis of ozone in the Huggins bands between 312 and 323 nm.

226 nm wavelength of the probe laser also photolyses ozone with a significant quantum yield of channel (E). The contribution of this channel to total ozone dissociation has been estimated for λ = 222 nm to be Φ(E) = 0.13 [3] and so plays an important role in the dissociation of ozone at these wavelengths. Since the absorption cross-section at 226 nm is $\sim$ 150 times that at 320 nm (for T = 226 K) and $\sim$ 2000 times that at 340 nm [1], the probe dissociation of the parent ozone is a difficult problem to overcome in these experiments. However, this probe 'contamination' is minimised by the use of optimum spatial overlap of the lasers, laser powers and focusing conditions.

The contribution of this 'contamination' signal for the $O(^3P_0)$ spectra is quite small and so the small variations in the shot to shot power of the probe laser have only a small detrimental effect on the S/N ratio of the signal. On the other hand, the $O(^3P_2)$ PHOFEX spectrum is produced by relatively small variations in the total ion signal due to the large one-colour signal of the

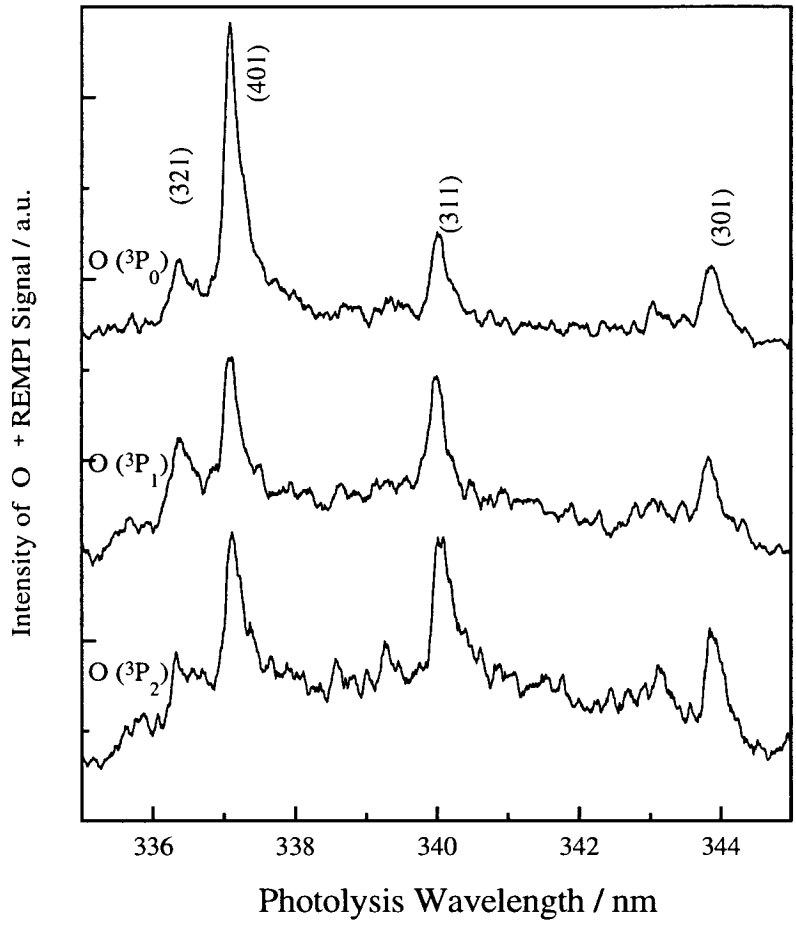

Figure 8.3.: The PHOFEX spectra recorded by detecting the $O(^3P_2)$, $O(^3P_1)$ and $O(^3P_0)$ fragments *via* the (2 + 1) 3p $^3P \leftarrow\leftarrow$ 2p ^3P REMPI transitions at 225.65, 226.05 and 226.23 nm following photolysis of ozone in the Huggins bands between 335 and 345 nm.

probe laser for this fragment. Hence, it was found that the PHOFEX spectra recorded by detecting the $O(^3P_0)$ fragments was the most suitable tool for the characterisation of the entire Huggins bands in spite of them having lowest signal intensities.

Secondly, there is also a two-colour continuum signal underlying each of the spectra. In the PHOFEX spectra recorded between 312 - 323 nm this continuum signal is particularly apparent in the $O(^3P_2)$ spectrum and is seen to increase with energy until the dissociation limit of channel (E) is approached when the total signal intensity decreases as the spin-allowed channel switches on. The 335 - 345 nm PHOFEX, shown in Figure 8.3 spectra also exhibit this 'continuum' signal and again is most obvious in the $O(^3P_2)$ spectrum where it

appears to fill in the energy regions between the peaks. In these spectra the signal decreases at both ends of the spectra due to the fall off in dye power in these regions. The source of this signal is discussed in subsequent sections of this chapter.

The next interesting step is to examine the velocity distributions of these three O (^3P_j) fragments produced by photolysis at a wavelength corresponding to one of the discrete structures. The wavelength chosen corresponds to the feature labelled (611) in Figures 8.1 and 8.2 and the velocity profiles recorded for each of the multiplets are shown in Figure 8.4. These profiles are the result of core-extraction of the ion packet with E_{photo} arranged both parallel and perpendicular to the TOF axis as described in Chapter 5. From this information the angular distribution of the fragments from one-photon photolysis processes can be reconstructed and so the internal energy distribution of the O_2 co-fragments can be calculated. These distributions are shown in Figure 8.5 along with the internal energy ladders of the O_2 fragments of channels (A), (B) and (C).

The $O(^3P_2)$ and $O(^3P_0)$ velocity distributions exhibit a trimodal behaviour, as reported for the $O(^3P_0)$ fragment in Chapter 5. The three velocity peaks at $\sim$ 2400 ms^{-1}, $\sim$ 3400 ms^{-1} and $\sim$ 4200 ms^{-1} were assigned to the formations of these fragments *via* channels (C), (B) and (A), respectively, with increasing amounts of translational energy given to the atomic fragment with decreasing electronic energy of the diatomic co-fragment. The fragments created by the probe laser dissociation arrive at $\sim$ 0 ms^{-1} and this signal has been subtracted from these profiles. The increasing noise level in the - 2000 ms^{-1} to + 2000 ms^{-1} region on going from $j = 0$ to 1 to 2 is due to the difficulty of subtracting the increasingly large probe signals. Slight distortions of the $O(^3P_2)$ profiles (and to a lesser extent the $O(^3P_1)$ profiles) may occur due to this subtraction routine and hence most of the velocity data presented in this chapter involved the $O(^3P_0)$ fragment. Interestingly, channel (C) is very weak for the velocity profile, and subsequent O_2 co-fragment energy distribution, of

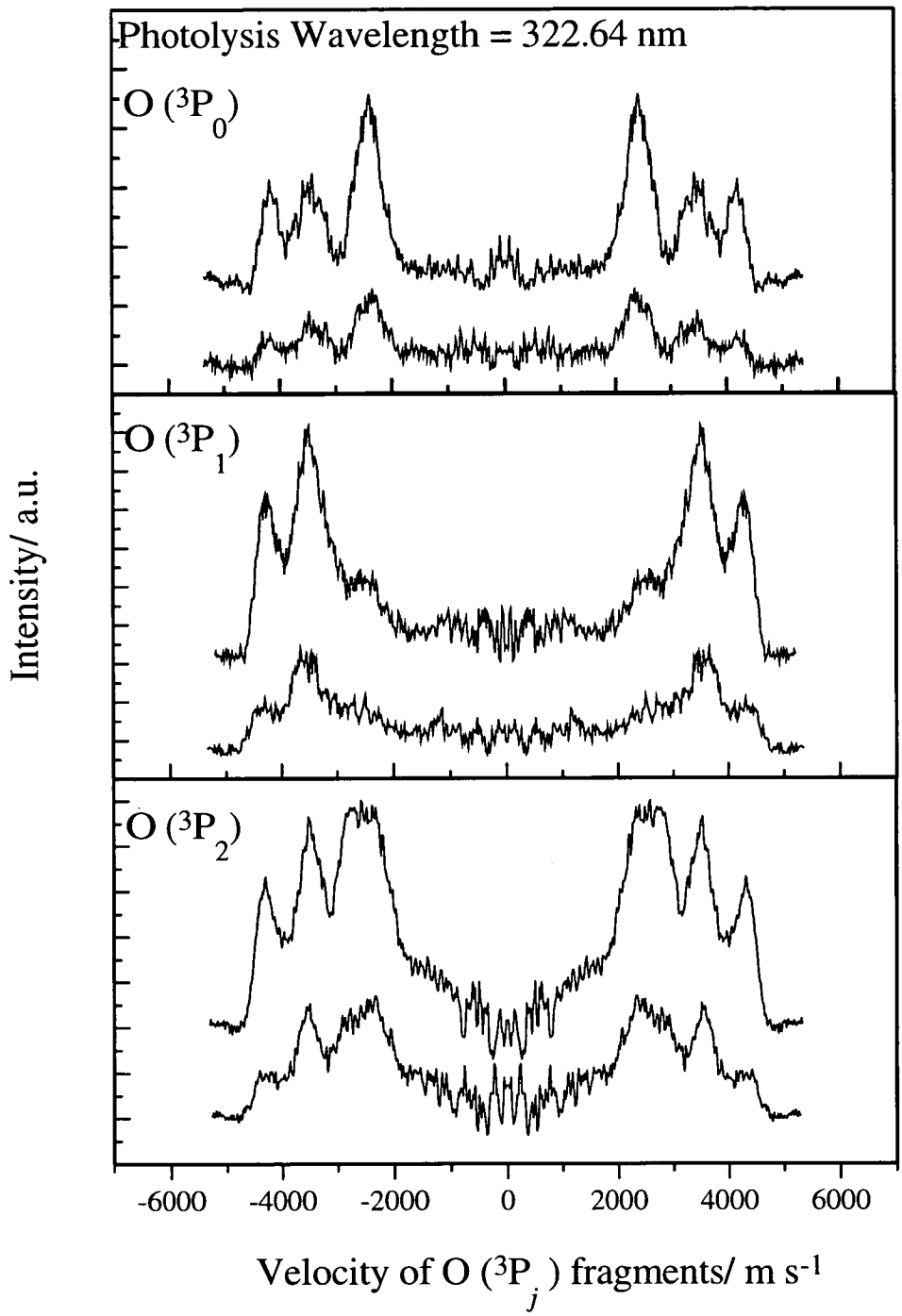

Figure 8.4.: The velocity profiles of the O($^3P_{2,1,0}$) fragments formed by the photolysis of O_3 *via* the (611) feature of the Huggins bands. The profiles recorded are all core-extracted and both E_{photo} || TOF axis (top) and E_{photo} ⊥ TOF axis (bottom) profiles are shown for each fragment. The signal due to the fragments formed by the probe laser only have been subtracted from all profiles.

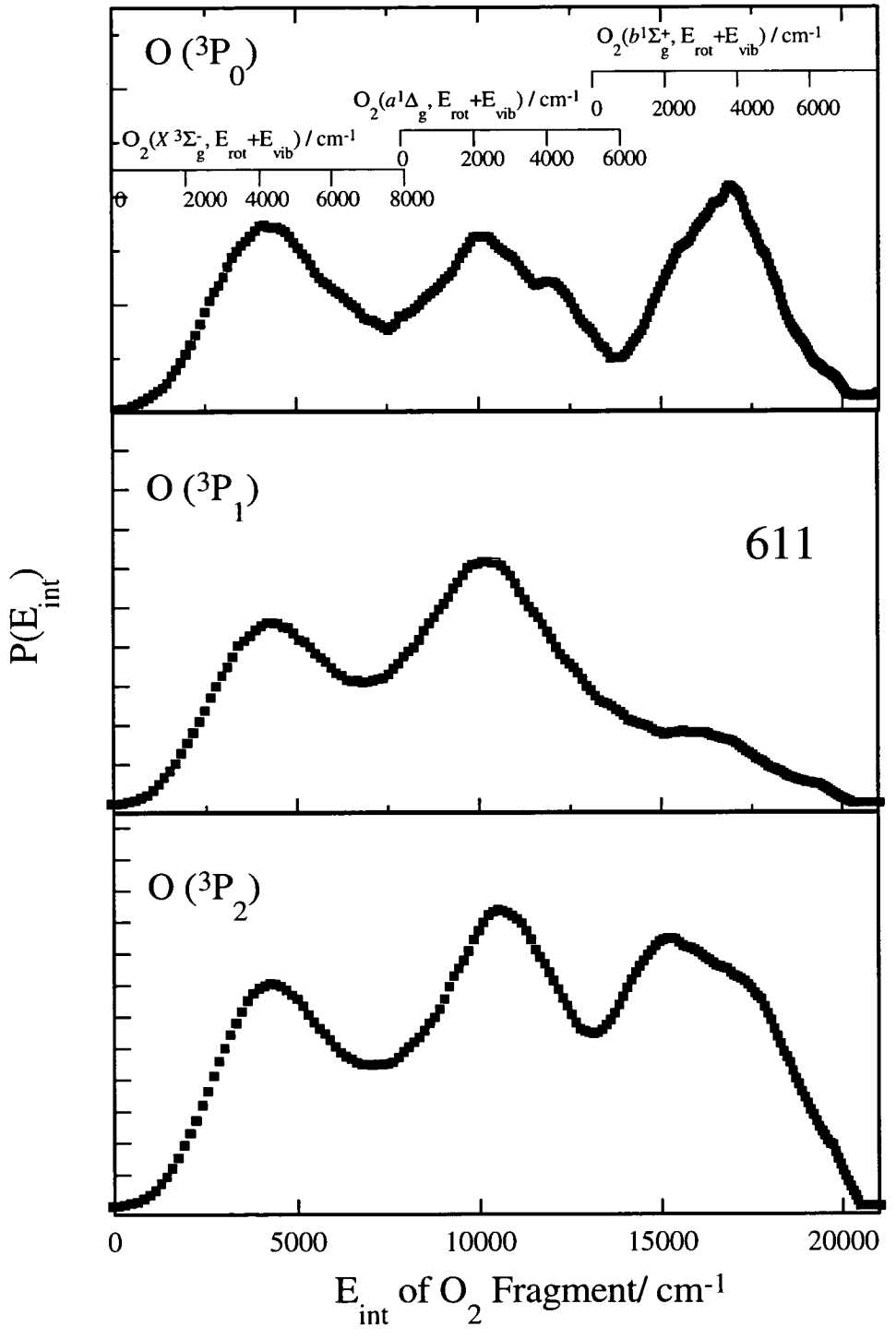

Figure 8.5.: The internal energy distributions of the O_2 co-fragments of the $O(^3P_{2,1,0})$ atomic fragments produced by photolysis of O_3 *via* the (611) feature of the Huggins bands. These distributions were calculated from the information presented in the velocity profiles of Figure 8.4.

the $O(^3P_1)$ fragments. The implications of this observation are discussed later in the text.

A demonstration of the mode specificity of these dissociation channels is portrayed in the TOF profiles of Figure 8.6 (a), (b) and (c), which were produced following photolysis of ozone *via* the absorption features labelled (401), (311) and (301) in Figure 8.1, respectively, and detecting the $O(^3P_0)$ fragments. Unlike the previous velocity profiles only the TOF profiles are shown here as the full core-extraction technique was not applied in these cases and hence the angular and translational components of the ion packet are not separated. The partial core-extraction conditions however do allow for an assignment of the peaks of the profile. The central peak is due to the probe laser which has not been subtracted from the profiles in this case. The peaks immediately on either side of the central peak are due to photolysis *via* channel (C) while the outer peaks are due to channels (A) and (B). The resolution of these profiles are not sufficient to separate the peaks due to these two channels.

Finally, as an example of the mode specificity of these processes the fragment velocity distributions from the three peaks in the PHOFEX spectrum labelled (611), (631) and (531), as in Figure 8.1, are examined. The $O(^3P_0)$ fragment was chosen for detection as there are fewer problems from the probe laser signal and hence a more reliable profile is obtained for the reasons explained above. The core extracted profiles were recorded with the photolysis laser electric field vector again E_{photo} arranged both parallel and perpendicular to the TOF axis. Therefore the angular distribution of the fragments and hence the internal energy distributions of the O_2 co-fragment could be calculated and are presented in Figure 8.7. A discussion of these distributions follows in the next section.

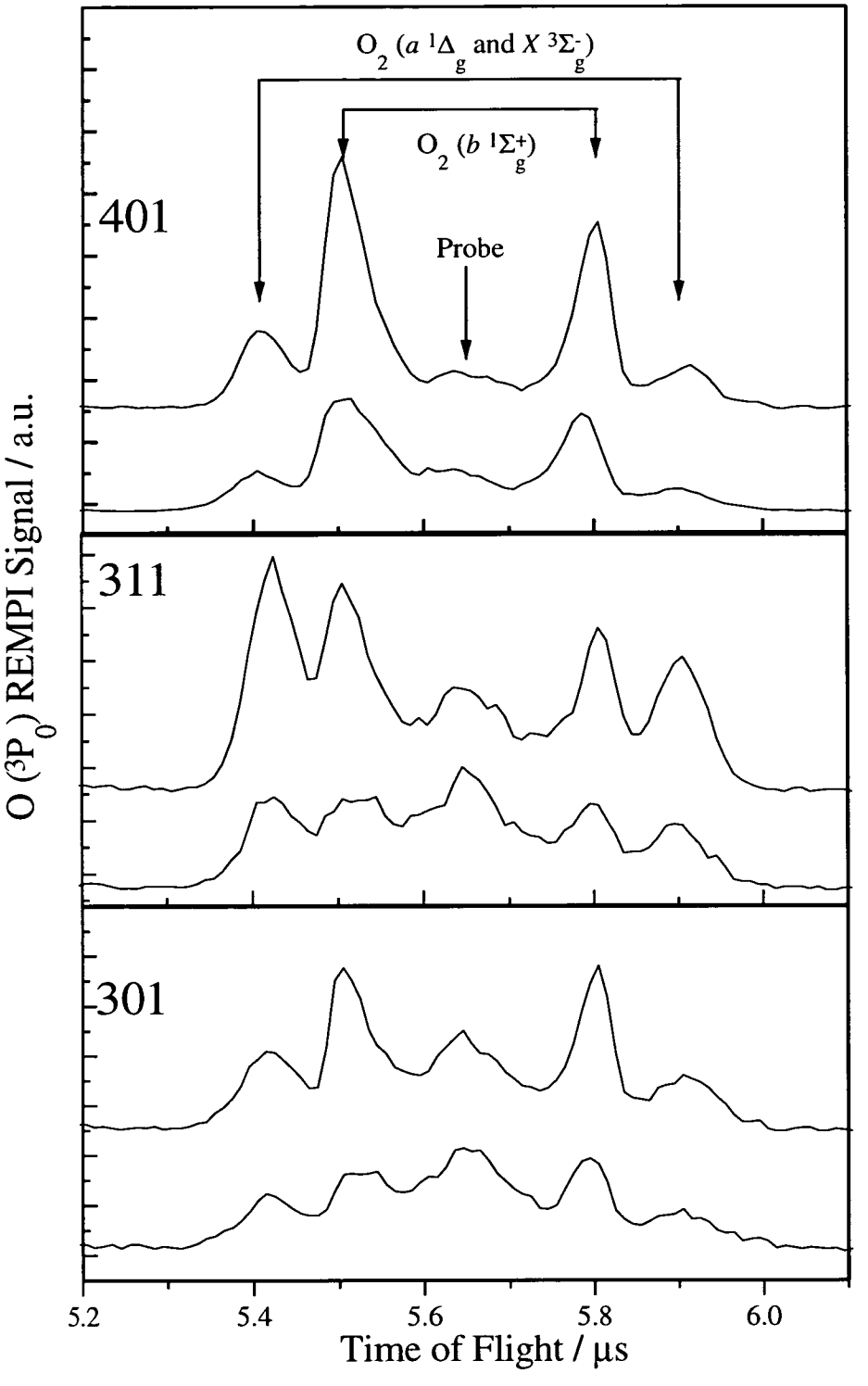

Figure 8.6.: The partially core-extracted TOF profiles of the $O(^3P_0)$ fragments formed by ozone photolysis *via* the (401), (311) and (301) vibrational levels of the Huggins bands. Profiles produced using laser geometries with E_{photo} || TOF axis (top) and E_{photo} ⊥ TOF axis (bottom) are shown. In these cases the probe only signal has not been subtracted from the profiles.

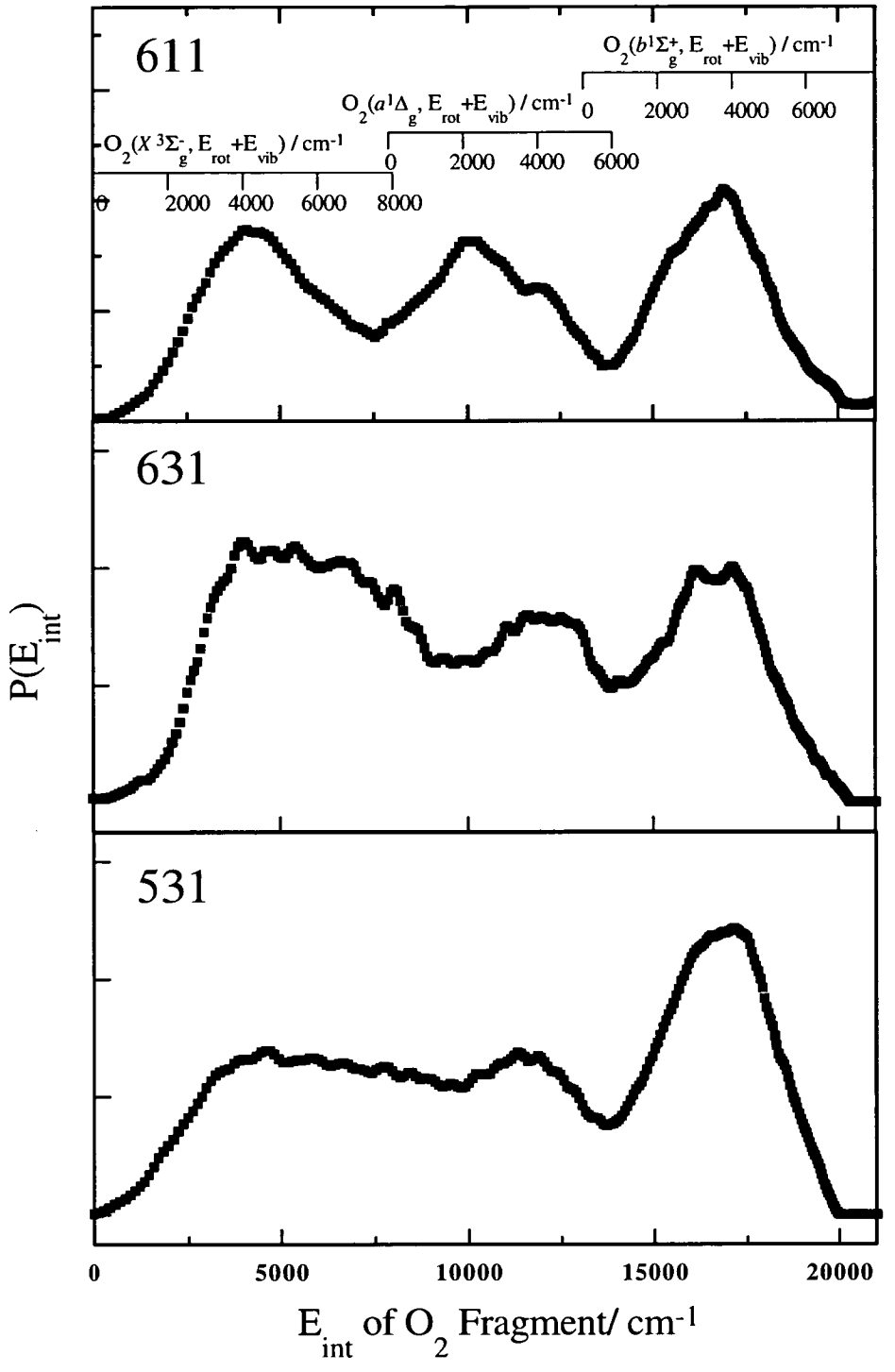

Figure 8.7.: The internal energy distributions of the O_2 co-fragments of the $O(^3P_0)$ atomic fragment produced by photolysis of O_3 *via* the (611), (631) and (531) features of the Huggins bands. These were calculated using the same method as used for the distributions in Figure 8.5 although the velocity profiles used are not presented for the sake of brevity.

8.3 Discussion

The results presented in the previous section contain a great deal of new information about the photodissociation dynamics of ozone following Huggins band absorption. To fully appreciate the value of this information it is useful to summarise the present understanding of the photodissociation dynamics in this region. In doing this it is convenient to distinguish between spin-allowed and spin-forbidden processes. The experimental data will be discussed in terms of these models and the new conclusions invoked by the results presented will be discussed.

8.3.1 Spin-Allowed Dissociation

The previous chapter which outlined the vibrational reassignment of the Huggins bands led to the conclusion that the initially excited upper state for this system is the 2 $^1A_1$ state. This excited state was calculated to have a C_{2v} global minimum with a geometry of R = 2.76 a_0 and bond angle, α = 87° but also a local secondary minimum at R = 2.56 a_0 and α = 131° [7]. The FC overlap of the ground state (equilibrium geometry: R = 2.41 a_0 and α = 116.8°) with the secondary minimum is significant and hence most likely to be responsible for the Huggins bands. A calculation, by the same group, was also performed on this state for a range of C_S geometries and revealed a small barrier of only 2000 cm^{-1} between the C_S minimum for α = 116.8° (g.s. equilibrium geometry) and the dissociation exit channel leading to the $O(^3P_j)$ + O_2 (X $^3\Sigma_g^-$) fragments [8]. These calculations are consistent with there being no more than two bound vibrational quanta of ν_3. The 2 $^1A_1$ $\leftarrow$ X $^1A_1$ transition is orbitally forbidden and only borrows intensity through mixing with the 'bright' $^1B_2$ state. As this coupling occurs in a symmetry specific manner *via* ν_3 only transitions involving $\Delta\nu_3$ = odd [11] are observed

in the transition. Therefore only the $\nu_3' = 1 \leftarrow \nu_3'' = 0$ transitions are observed as shown by the vibrational assignment in Chapter 7. The transition to higher energies in the ν_3 mode gives a continuum absorption which underlies the structured part of the Huggins bands. These points are illustrated in Figure 7.3 of the previous chapter which shows the schematic cuts of the relevant states in the q_3 coordinate.

8.3.2 Spin-Forbidden Photodissociation

Unlike the singlet states described above very few calculations on the the highly excited triplet states of ozone have been reported in the literature. Banichevich *et al.* [8] mention the possibility that mixing of the $1\ ^1B_2$ ($3\ ^1A'$) state with repulsive triplet states which correlate with the products of channels (B) to (D) could give rise to the spin-forbidden dissociation processes observed in this region. More recently, however, Minaev *et al.* [9] have performed a calculation evaluating the spin-orbit coupling ($H_{SO} = 29\ \mathrm{cm}^{-1}$) between the low-lying $1\ ^3A_2$ ($2\ ^3A''$ in C_S notation) state which correlates with the $O(^3P_j) + O_2\ (a\ ^1\Delta_g)$ products and the exit channel of the $2\ ^1A_1$ surface. This 'secondary' coupling may explain the source of the channel (B) spin-forbidden products in the Huggins band and is consistent with the conclusions of the previous chapter regarding the initially excited upper state. Takahashi *et al.* [2] proposed a similar mechanism for the production of the channel (D) spin-forbidden products but did not mention which triplet state correlating with these products was involved in the coupling.

From the limited results presented in Chapter 5 it was noted that channels (A) and (B) appeared to be accessed *via* different processes to that of channel (C). In fact, it was proposed that dissociation *via* this third channel occurs due to a 'primary' coupling of a repulsive triplet state of unknown identity with the initially excited $2\ ^1A_1$ ($2\ ^1A'$) surface. The results presented in the previous section contain a large amount of information regarding this channel

and so will help further characterisation of the dynamics involved during the subsequent subsections of this chapter.

8.3.3 PHOFEX Spectra and Velocity Profiles of $O(^3P_j)$ Fragments

It is necessary to consider the contribution of each channel involving the $O(^3P_j)$ fragments to the total photolysis to understand the PHOFEX spectra and so both the PHOFEX spectra and velocity profiles of the $O(^3P_j)$ fragments are discussed in this section.

On and Off Resonance Dissociation

The TOF profiles of the $O(^3P_0)$ fragments following off resonance absorption presented in Chapter 5 showed the presence of co-fragments from channels (A) and (B) only. From these observations and the above discussions of the spin-allowed and spin-forbidden dissociation processes it is proposed that the continuum of the Huggins band is the result of dissociation *via* the ν_3' continuum. This leads directly to the $O(^3P_j) + O_2\ (X\,^3\Sigma_g^-)$ exit channel (A) while a subsequent secondary interaction allows a crossing of some of the dissociating molecules to the $O(^3P_j) + O_2\ (a\,^1\Delta_g)$ spin-forbidden exit channel (B).

The structured part of the Huggins band, on the other hand, contains contributions from both channel (C) dissociation and the two channels described above. Therefore, it appears that there are two competitive primary dissociation pathways following on resonance dissociation, one of which leads to the $O(^3P_j) + O_2\ (b\,^1\Sigma_g^+)$ products. The lifetime of the bound states is determined by the tunnelling rate through the q_3 barrier to the $O(^3P_j) + O_2\ (X\,^3\Sigma_g^-)$ exit channel and also the strength of the predissociation interaction between the triplet state leading to the $O(^3P_j) + O_2\ (b\,^1\Sigma_g^+)$ products and

the bound levels of the 2 $^1A_1$ surface.

The increasing continuum contribution to the PHOFEX spectra with increasing energy is then simply associated with the increasing amount of dissociation *via* the ν_3 continuum at higher photolysis energies. This model of dissociation has the important advantage that both discrete and continuum contributions to the $O(^3P_j)$ yield can be accounted for by transitions to a single upper surface from the (000) level of the $X\ ^1A_1$ state of O_3. In other vibrational assignments [10, 11] all of the excited state modes are bound and therefore the continuum would have to be explained either by transition to a second surface or photodissociation of vibrationally excited molecules of the $X\ ^1A_1$ state.

Branching Ratios of $O(^3P_j)$ Fragments

Comparing the $O(^3P_2)$, $O(^3P_1)$ and $O(^3P_0)$ PHOFEX spectra of Figures 8.2 and 8.3 reveals a decreasing two-colour continuum signal on proceeding from $j = 2$ to $j = 1$ to $j = 0$ suggesting that most of the continuum dissociation described above proceeds to the $O(^3P_2)$ fragments. The structured part of the PHOFEX spectra exhibit slightly different behaviour which can be recognised by examining the $O(^3P_2)$, $O(^3P_1)$ and $O(^3P_0)$ fragment velocity profiles recorded following 322.64 nm, (611), photolysis which are shown in Figure 8.4. This figure and the resultant Figure 8.5, which shows the calculated O_2 co-fragment internal distributions, reveal that the O_2 ($b\ ^1\Sigma_g^+$) products are produced with a very different distribution of $O(^3P_2)$:$O(^3P_1)$:$O(^3P_0)$ fragments from those of the O_2 ($X\ ^3\Sigma_g^-$) and O_2 ($a\ ^1\Delta_g$) channels.

Takahashi *et al.* [2] measured the total branching ratio of the $O(^3P_j)$ fragments without velocity discrimination using a LIF technique. They found close to statistical (5:3:1) branching ratios for all photolysis wavelengths and temperatures investigated (T = 227 K : λ_{photo} = 305, 312 and 328 nm and also T = 295 K : λ_{photo} = 308, 316 and 324 nm). From these results it is

inferred that the branching ratio of the $O(^3P_j)$ multiplets averaged over all of the velocities can be said to be close to the statistical limit. Following this deduction, examination of Figure 8.5 immediately allows the subsequent conclusion that the branching ratio of $O(^3P_j)$ fragments formed in coincidence with the O $_2$ $(X\ ^3\Sigma_g^-)$ and O_2 $(a\ ^1\Delta_g)$ diatomic fragments is also close to the statistical limit but those formed with O_2 $(b\ ^1\Sigma_g^+)$ are strongly non-statistical.

This information can be combined with the conclusion from the on/off resonance profiles that the O_2 $(b\ ^1\Sigma_g^+)$ products are only produced following resonant absorption to provide an explanation for the fact that the structure in the PHOFEX spectra is most prominent in the $O(^3P_2)$ and $O(^3P_0)$ spectra while the continuum dissociation competes more successfully with the resonant dissociation in the $O(^3P_1)$ spectrum.

The reason why the O_2 $(b\ ^1\Sigma_g^+)$ channel in conjunction with the $O(^3P_1)$ fragments is so weak in comparison with the $O(^3P_2)$ and $O(^3P_0)$ fragments is not clear. The photolytically generated $O(^3P_j)$ distribution has been measured for a number of molecules including NO_2 [12, 13], SO_2 [14], O_2 [15, 6] and OClO [16]. The most common distribution for such photolytically generated fragments is a distribution close to the statistical degeneracy of the j states of the atom which can be derived from a simple count of the m_j states giving a 5:3:1 ratio for the $O(^3P_2)$:$O(^3P_1)$:$O(^3P_0)$ fragment population. In general this statistical distribution dominates in the cases of high energy fragment recoil while adiabatic dissociation which can lead to non-statistical populations is more likely at low recoil energy [14].

To help with the discussion of the mixing of the j states of the atom it is necessary to briefly present the relevant coupling schemes of the surfaces correlating with these states in the different regions of nuclear separation of the fragments. The three regions of dissociation which are considered are (a) the parent molecular region (FC region), (b) the intermediate separation and (c) finally the 'free' fragment region which occurs at large internuclear separation [4, 5, 6].

From the previous discussion it was found that the O_2 ($b\ ^1\Sigma_g^+$) channel is only produced when a bound level of the initially excited single state is accessed while dissociation *via* the ν_3 continuum (off-resonance) produced very few fragments from this channel. From this it appears that the interaction between the initially excited state and the triplet state correlating with the products O_2 ($b\ ^1\Sigma_g^+$) + $O(^3P_j)$ occurs in or very near to the parent molecular region. In a diabatic view of the dissociation where the effect of spin-orbit coupling on the different excited states of the molecule is not included in the calculation of the PESs a crossing may occur between such a triplet state and the initially excited singlet state in this region. If the spin-orbit coupling between the states is sufficient some molecules may cross onto the triplet state and subsequently dissociate to the O_2 ($b\ ^1\Sigma_g^+$) + $O(^3P)$ products. How such a states evolves into the different $O(^3P_j)$ multiplet states is difficult to visualise but may be viewed as a re-coupling of the angular momentum when the energy differences between the diabatic states becomes comparable to the spin-orbit splitting at extended nuclear geometries.

To gain some insight into how each $O(^3P_j)$ state is accessed in each channel it may be more instructive to consider the alternative, adiabatic, view of dissociation in which the spin-orbit coupling effects are taken into account when calculating the PESs. In this formalism the PESs of the different states which are effectively coupled do not cross but may instead have avoided crossings. These states may then only be coupled by the nuclear kinetic energy operator, the effect of which was ignored in the calculation of the PESs due to the Born-Oppenheimer approximation. In the limit of strong spin-orbit coupling states may have mixed singlet/triplet character and thus the conservation of spin selection rule may be weakened. Usually the light O atoms in ozone would be considered to exhibit weak spin-orbit coupling and therefore unlikely to undergo such effects. However, the experimental evidence surprisingly shows that spin-forbidden dissociation (and hence spin-orbit coupling) plays an extremely important role in the dissociation of this molecule.

To complete this rather speculative discussion it is interesting to examine the adiabatic view of dissociation a little more and to attempt to determine the amount of non-adiabatic coupling which can occur in the exit channels assuming that these channels have been accessed by some mechanism in the parent molecular region. A simple criterion for assessing the extent of non-adiabatic coupling in this region due to the radial kinetic energy coupling operator is to determine the ratio of nuclear recoil time to electronic precession time. This ratio which has been called the translational adiabaticity parameter [6] is determined by equation 8.1.

$$A = \frac{t_n}{t_e} = \frac{R\,\Delta E_{SO}}{\hbar v} \tag{8.1}$$

where $t_n = R/v$ and R is the characteristic radial width where the adiabatic functions are coupled by the kinetic operator and v is the relative nuclear velocity of the fragments. The relative nuclear velocity for the channel being examined can be calculated from the peak velocities taken from Figure 8.4. Also, $t_e = \Delta E_{SO}/\hbar$ where ΔE_{SO} is the spin-orbit splitting of the atomic states being coupled, i.e. $O(^3P_j)$.

The value of R requires a detailed knowledge of the PES curves involved and so is not explicitly known, however, the Massey criterion indicates that the sudden limit is reached when $A < 1$. In the sudden limit a statistical distribution of multiplet states is expected, whereas if $A > 1$ then adiabatic dissociation will dominate. As a guide to the possible value of A a comparison with theoretical calculations can be made where it was shown that the statistical limit of multiplet populations is reached at $A = 1.1$ for HCl [18] (with R = 2 Å) and at $A = 0.65$ for NaAr [19] (with $R = 3.7$ Å) whereas these ratios are double the statistical value for $A = 1.6$ and 1.4 respectively.

The value of A can be graphed against R to find the necessary values of R for which the sudden limit may apply. The relative nuclear velocity for the channel being examined can be calculated from the peak velocities taken from Figure 8.4. This is shown in Figure 8.8 where the values of A have been

calculated for coupling between the $O(^3P_2)$ and $O(^3P_0)$ surfaces of the O_2 ($b\ ^1\Sigma_g^+$) channel and also for coupling between the $O(^3P_2)$ and $O(^3P_1)$ surfaces of the O_2 ($X\ ^3\Sigma_g^-$) channel. It is reasonable to expect values of R in the 1 Å to 2 Å range [6] and so it is clear that kinetic coupling in the O_2 ($b\ ^1\Sigma_g^+$) channel is not likely to be important while it will be more important in the case of the higher energy fragments of the O_2 ($X\ ^3\Sigma_g^-$).

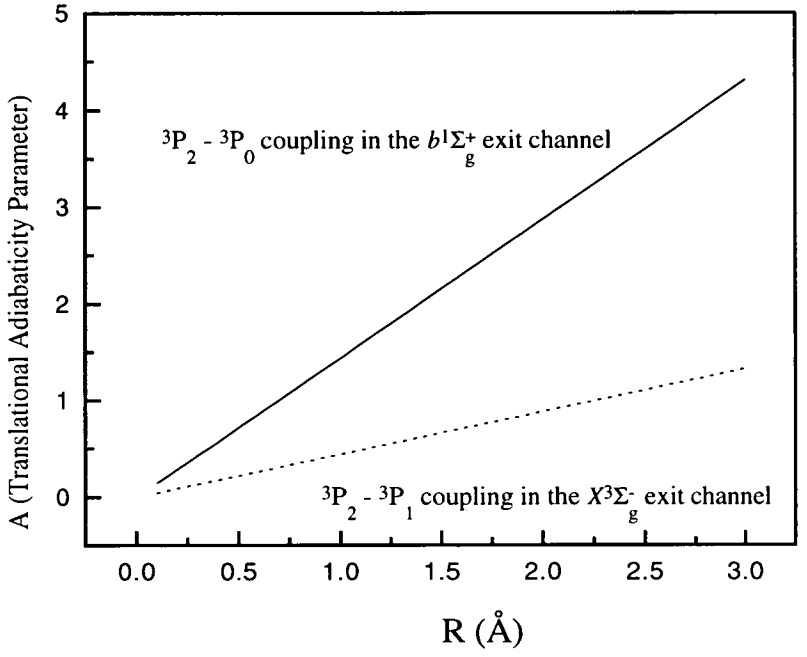

Figure 8.8.: A plot of A, the calculated translational adiabaticity parameter versus R, the characteristic radial width where the adiabatic functions are coupled by the kinetic operator. These provide an approximate measure of the non-adiabatic coupling of the indicated exit channels.

Therefore, from these very approximate calculations it seems likely that the non-statistical distribution of $O(^3P_j)$ states in the O_2 ($b\ ^1\Sigma_g^+$) channel is due to adiabatic dissociation whereas non-adiabatic effects may be more important in the O_2 ($X\ ^3\Sigma_g^-$) exit channel.

More rigorous conclusions would require a full theoretical treatment of the dissociation similar to that performed by Graff and Wagner [20] on the O + OH system or by Grinberg *et al.* [21] on the NOCl dissociation. Such an approach would require very accurate PESs of all of the states involved which are presently not available.

8.3.4 Mode Specificity of the Dissociation Processes

Strong mode specificity of the dissociation channels is observed in the TOF profiles of the $O(^3P_0)$ fragments produced following absorption into the (401), (311) and (301) Huggins bands as shown in Figure 8.6. Only partial core-extraction conditions were applied to these spectra and so the internal energy distribution of the O_2 co-fragments cannot be calculated in the same manner as for the core-extracted profiles. The resulting lower resolution does not allow the separation of the peaks due to the O_2 ($X\ ^3\Sigma_g^-$) and O_2 ($a\ ^1\Delta_g$) channels. However, a strong mode specific production of the O_2 ($b\ ^1\Sigma_g^+$) relative to these channels is seen for the (401) and (301) photolysis while a much weaker production is observed following (311) photolysis.

In terms of the model presented above the production of both of the O_2 ($X\ ^3\Sigma_g^-$) and O_2 ($a\ ^1\Delta_g$) channels is due to the same primary crossing while the O_2 ($b\ ^1\Sigma_g^+$) channel is due to a different primary predissociation route. Therefore, the relative rates of these two predissociative crossing will be reflected directly in the relative amounts of the O_2 ($b\ ^1\Sigma_g^+$) channel versus the combined yield of the O_2 ($X\ ^3\Sigma_g^-$) and O_2 ($a\ ^1\Delta_g$) channels. As the primary crossing producing the O_2 ($X\ ^3\Sigma_g^-$) and O_2 ($a\ ^1\Delta_g$) channels is proposed to occur in the q_3 co-ordinate the efficiency of this channel is unlikely to change significantly with small changes in the number of quanta of ν_1 and ν_2 excited. Conversely, the crossing producing the O_2 ($b\ ^1\Sigma_g^+$) fragments was proposed to occur in the FC molecular region and thus changes in the excited quanta of ν_1 and ν_2 could strongly effect the strength of predissociation. The TOF profiles shown in Figure 8.6 reveal that the modulation of the O_2 ($b\ ^1\Sigma_g^+$) production is controlled by the amount of the ν_2 excitation in the excited state.

Another effect of the mode specific photodissociation in this region can be observed by examining the REMPI spectra of the O_2 ($b\ ^1\Sigma_g^+$, v = 0) fragments produced by the photolysis *via* these vibrational levels. In Chapter 6 the (1,0) and (2,0) bands of the (2 + 1) $d\ 3s\sigma_g\ ^1\Pi_g \leftarrow\leftarrow O_2$ ($b\ ^1\Sigma_g^+$) REMPI transition

recorded following (301) and (311) photolysis respectively were presented. In that chapter it was revealed that due to the heavily perturbed nature of the v = 2 level of the *d* state that it was difficult to extract rotational distributions of the fragments by REMPI spectra recorded by exciting *via* this state. The (1,0) band is, however, less perturbed and by comparison of the (1,0) band of the $d\ 3s\sigma_g\ ^1\Pi_g \leftarrow\leftarrow (b\ ^1\Sigma_g^+)$ transition following photolysis at different wavelengths it is possible to make some assessment of the relative rotational distribution of the O_2 $(b\ ^1\Sigma_g^+)$ fragments detected. As an illustration of this the (1,0) band recorded following photolysis *via* the (401) and (301) upper state vibrational levels are show in Figure 8.9.

A brief comparison of the (1,0) band of the $d\ 3s\sigma_g\ ^1\Pi_g \leftarrow\leftarrow O_2\ (b\ ^1\Sigma_g^+)$ produced following (301) Huggins band dissociation with the (0,1) band of the $d\ 3s\sigma_g\ ^1\Pi_g \leftarrow\leftarrow O_2\ (a\ ^1\Delta_g)$ transition produced following Hartley band dissociation (shown in Figure 5.2 of Chapter 5) reveals quite a close similarity between these bands. The $d \leftarrow\leftarrow O_2\ (a\ ^1\Delta_g)$ band was unperturbed and line position were accurately simulated in Chapter 5. Unfortunately such a rotational analysis of the (1,0) band of the $d\ 3s\sigma_g\ ^1\Pi_g \leftarrow\leftarrow O_2\ (b\ ^1\Sigma_g^+)$ shown in Figure 8.9 (b) was not possible due to lower resolution of the spectrum and the presence of perturbations of the v = 1 level of the *d* state which are reflected in the dips indicated by the arrows on both parts (a) and (b) of this figure.

However, comparing figures (a) and (b) it is clear that the O_2 $(b\ ^1\Sigma_g^+$, v = 0) fragments formed from photolysis *via* the (401) level involve higher rotational excitation than those produced following (301) photolysis. Furthermore, initial attempts to simulate these spectra using an unperturbed rotational constant for the upper level suggested that the rotational distribution of O_2 $(b\ ^1\Sigma_g^+$, v = 0) fragments produced from (301) photolysis peaks at approximately J = 26 - 30 while those produced from (401) photolysis peak at approximately J = 36 - 40. Unfortunately the TOF profiles are not of high enough resolution to confirm these conclusions.

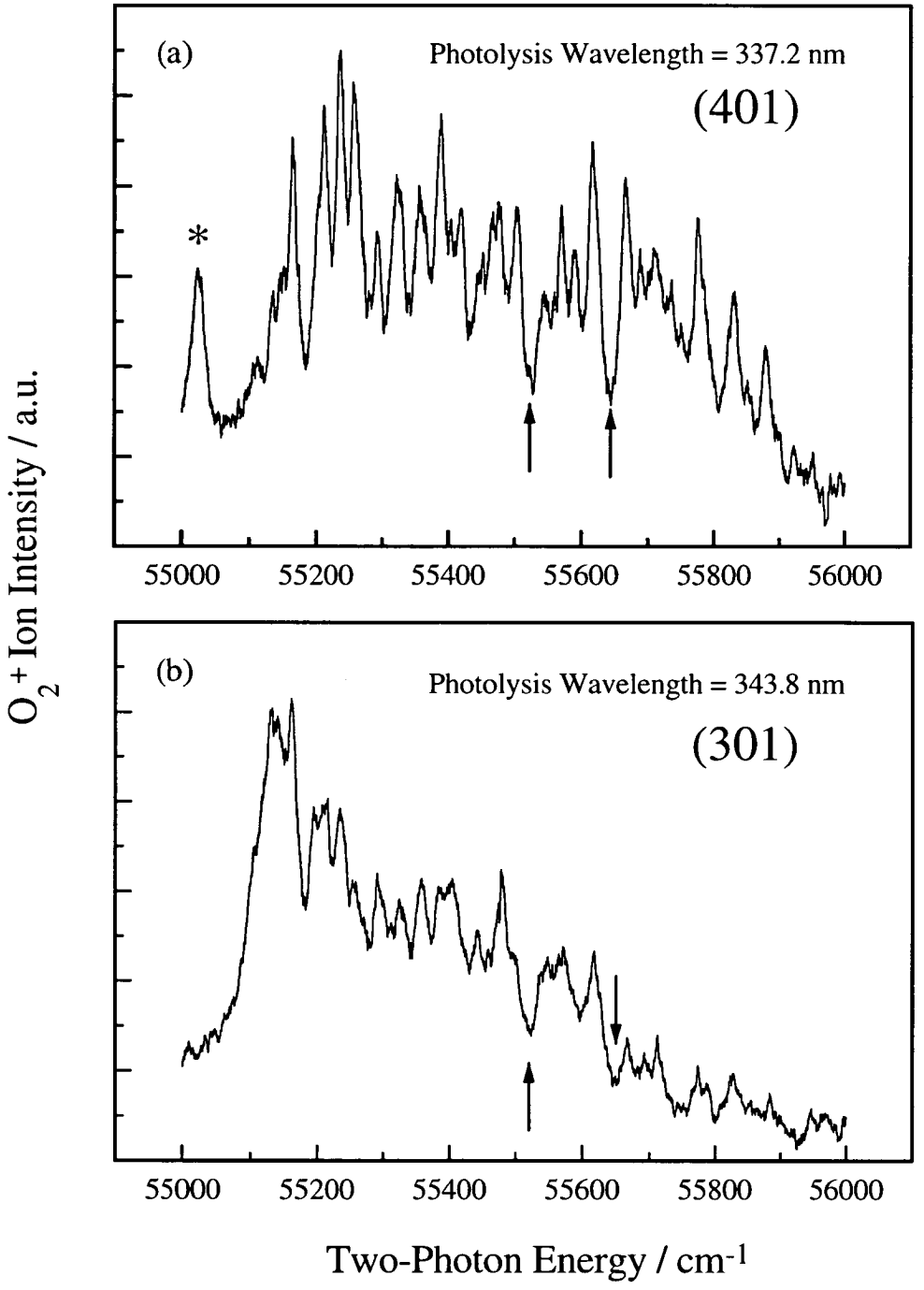

Figure 8.9.: The above spectra are the (1,0) bands of the of the $d\ 3s\sigma_g\ ^1\Pi_g \leftarrow\leftarrow O_2\ (b\ ^1\Sigma_g^+)$ produced following dissociation of ozone at 337.2 nm (401), (a), and 343.8 nm (301) (b). The two-photon REMPI transition is accessed *via* a combination of $((1 + 1') + 1)$ and $((1 + 1') + 1')$ processes. The feature marked with an asterisk is due to a $((2' + 1) + 1)$ REMPI transition from the ground state of O_2.

8.3.5 Further Mode Specificity of the Fragment Channels

A more complicated effect of the mode specificity was seen in the velocity distributions of the $O(^3P_0)$ fragments produced by the photolysis of the (611), (631) and (531) Huggins bands. The internal energy distributions of the O_2 fragments which are formed in coincidence with these fragments have been calculated using the procedure as described above and are shown in Figure 8.7. The wavelengths indicated were chosen as the quantum yield of the $O(^3P_0)$ fragments is greatest in this energy region. These wavelengths 322.64, 322.0 and 317.64 nm correspond to the features labelled as (611), (531) and (631) in the PHOFEX spectrum of Figure 8.1. As the velocity profile of the atomic fragments can only give information on the total internal energy of the O_2 fragment, no information about the relative amounts of rotational, vibrational and electronic energy of these fragments can be directly extracted. However, the three electronic state peaks O_2 $(X\ ^3\Sigma_g^-)$, O_2 $(a\ ^1\Delta_g)$ and O_2 $(b\ ^1\Sigma_g^+)$ are distinguishable in all three distributions and hence we retain the same electronic assignment of the peaks as in the (611) case.

The mode specificity of competition between the O_2 $(b\ ^1\Sigma_g^+)$ channel and the O_2 $(X\ ^3\Sigma_g^-)$ and O_2 $(a\ ^1\Delta_g)$ channels is not as clear in these distributions as for the TOF profile shown in the previous section. It appears that relatively more O_2 $(b\ ^1\Sigma_g^+)$ fragments are formed following (531) photolysis than photolysis *via* the other bands presented. However, a slightly misleading aspect of comparing the (631) distribution with the other two distributions is that there is a much larger two-colour continuum contribution to the dissociation at this wavelength than the lower energies (see Figure 8.1). As principally O_2 $(X\ ^3\Sigma_g^-)$ and O_2 $(a\ ^1\Delta_g)$ fragments are produced from continuum dissociation these parts of the distribution may be distorted by this effect. In order to compare only the distributions resulting from on-resonance dissociation it would

be necessary to subtract the continuum contribution from each distribution. This experiment however was not possible due to the lower intensity of the continuum.

However, the (611) and (531) bands photolysis wavelengths are only separated by 0.64 nm and hence the continuum contribution to both of these distributions is likely to be quite similar. The main difference between these distributions appears to be in the 0 - 13000 cm^{-1} internal energy region involving the O_2 ($X\ ^3\Sigma_g^-$) and O_2 ($a\ ^1\Delta_g$) fragments. It is clear that the O_2 ($X\ ^3\Sigma_g^-$) distribution is significantly broadened on going from (611) to (531) photolysis. Estimating the effect on the O_2 ($a\ ^1\Delta_g$) distribution is more difficult but it appears to be slightly shifted to higher energy and may or may not be broadened. The O_2 ($b\ ^1\Sigma_g^+$) distribution appears to be largely unchanged in all three profiles.

Understanding such a varying behaviour of the O_2 internal energy distributions is extremely difficult especially since it is not possible to discern whether it is the rotational or vibrational distribution of the fragments which are causing the changes in the overall internal energy distribution. A possible explanation for the broadening of the O_2 ($X\ ^3\Sigma_g^-$) internal energy distribution may be found in the excited modes accessed prior to dissociation. A particularly relevant observation was made by Levene and Valentini who noted that the bending mode of a triatomic is the only mode which can contribute significantly to the diatomic fragment rotation [22]. Thus the broader distributions would be associated with the excitation of the $\nu_2 = 3$ mode as this vibration 'washes into' the diatomic rotational distribution as the molecule dissociates. As the O_2 ($a\ ^1\Delta_g$) fragment is accessed *via* a crossing in the exit channel which produces the O_2 ($X\ ^3\Sigma_g^-$) channel the internal energy distribution of these fragments would be expected to broaden in a similar manner.

It is quite clear, however, that the O_2 ($b\ ^1\Sigma_g^+$) internal energy distribution is not broadened and this may be accounted for by the different type of predissociative crossing which yields these fragments. If the crossing is con-

sidered to take place in the bending coordinate the dissociating geometries leading to this channel and, hence, rotational distribution of this fragment is controlled by the overlap of the continuum wavefunction of the triplet state with that of the excited bound level of the 2 $^1A_1$ surface. Therefore the rotational distribution of the O_2 (b $^1\Sigma_g^+$) fragments will vary in a completely different way to that of the other fragments.

From the internal energy distribution of the O_2 (b $^1\Sigma_g^+$) fragments it would appear that changing the number of quanta of ν_2 in the excited state does not noticeably broaden the rotational distribution of these fragments in the same manner as the effect on the O_2 (X $^3\Sigma_g^-$) and O_2 (a $^1\Delta_g$) state. Therefore it seems that the crossing to the O_2 (b $^1\Sigma_g^+$) channel imposes a selection on the geometries of the molecules dissociating *via* this channel. This observation confirms again the conclusion that the O_2 (b $^1\Sigma_g^+$) channel is due to a different dissociation mechanism to that of the other channels. It may also explain the different deviations of these dissociation channels from the impulsive model described in Chapter 5 where is was shown that while the impulsive model predicted more rotational energy than observed in the O_2 (X $^3\Sigma_g^-$) and O_2 (a $^1\Sigma_g^+$) channels it predicted less rotational energy than observed in the O_2 (b $^1\Sigma_g^+$) channel. The differing dissociation geometries suggested above may explain this as the impulsive model assumed the same dissociating geometry for all channels.

To confirm these rather tentative proposals, information about the O_2 energy distributions from a larger range of excited state vibrational bands would be required. Also, REMPI of all of the diatomic fragments produced *via* the levels investigated would clarify whether the broadening of the internal energy distributions is truly due to a broadening of the rotational distribution of the fragments or a change in the vibrational distribution. Such an experiment would be extremely difficult due to the large energy range of the O_2 fragments involved.

8.3.6 Rotational Contours of the Vibrational Features of the Huggins bands

There have been two previous rotational band contour studies of the vibrational structure of ozone in the Huggins bands [23, 24]. Both of these studies concentrated on the two features at 324.9 and 325.5 nm corresponding to the features labelled (521) and (601) in Figure 8.1. However, these studies appear to give conflicting results from both the experimental point of view and their final conclusions. Sinha *et al.* [23] who used a dissociative resonance Raman/fluorescence technique observed rotational resolution in their spectra (linewidths of features = 1.4 cm^{-1}) whereas Takahashi *et al.* [24] observed no such structure in their O (^1D) PHOFEX spectra in spite of using a photolysis laser of narrower bandwidth (laser bandwidth of 0.2 cm^{-1}) than the features observed in the first study.

Sinha *et al.* [23] based their rotational analysis on the vibrational assignment of Katayama [10] who assigned the levels to (501) and (600) respectively. They concluded that the features which they analysed were due to the same type of rotational transition (a-type i.e. $\Delta K = 0$) and hence deduced that this would be consistent with excited state levels residing in a well of overall $^1B_2$ electronic symmetry with a double minimum along the q_3 coordinate. They estimated the excited state bond angle from rotational constants which were fit to the spectra to be $70° \leq \theta \leq 106°$.

In contrast, Takahashi *et al.* based their rotational analysis on the vibrational assignments of Joens [11] whose assignment for these bands are (303) and (501) respectively. As both of these features would be expected to have the same overall vibrational symmetry (ν_3 = odd in both upper levels) the conclusion that both features have the same rotational type is a trivial one and so Takahashi *et al.* again assumed a-type transitions for both features. The best fit of the upper state rotational constants to their spectra yielded an

expected upper state geometry of $\theta = 127° \pm 8°$ and $r_1 = r_2 = 2.75 \pm 0.16\ a_0$ and resulted in the conclusion that the upper state was electronic symmetry 2 $^1A_1$ (i.e. the first excited $^1A_1$ state which requires the $\Delta\nu_3$ = odd selection rule to facilitate electronic mixing with the nearby strongly allowed $^1B_2$ state).

Our recent reassignment of the vibrational levels requires a reassessment of these analyses. The primary difference between previous assignments and our present assignment is in the total number of stretching quanta ($\nu_1 + \nu_3$) versus the number of bending quanta, ν_2 for each level. The $\nu_1 + \nu_3$ remained constant between the previous assignments and also between the two features mentioned in the analyses above ($\nu_1 + \nu_3 = 6$). Therefore, a significant change of the equilibrium geometry between the upper states of these transitions would not be expected and hence use of the same rotational constants for their analysis is valid. The case of the new assignment is quite different however, as the number of quanta of both bend and total stretch change between these features ((521) $\rightarrow$ (601)). Thus, a change of the rotational constants will be required to accurately simulate these peaks using this assignment. In particular, it is necessary to consider the change of average bond angle with increasing ν_2.

With these points in mind a re-analysis of the rotational contours recorded by Takahashi *et al.* [24] was performed. As stated above the two bands simulated by Takahashi *et al.* were the features labelled (601) and (521) in Figure 8.1. The method used here to simulate the rotational contours of the Huggins bands is the same as that used by Takahashi. An *a*-type transition was assumed and the rotational energies of the lower and upper states were calculated using a rigid rotor description of a prolate symmetric top [25, 26]. The rotational temperature of the lower state molecules was given by a Boltzmann distribution while the natural linewidth of the upper state levels was assumed to be constant with K and J and represented by a Lorentzian profile.

The simulated spectra of Takahashi *et al.* are shown in Figure 8.10 (a) and (b) by the solid lines where the rotational constants used for both upper state levels are shown in Table 8.1. Also contained within this table are the

	This Work			ref [24]		
	Rotational constants A, $\bar{B}$ /cm^{-1}	Natural linewidth /cm^{-1}	Geometry γ, R /deg, /a_0	Rotational constants A, $\bar{B}$ /cm^{-1}	Natural linewidth /cm^{-1}	Geometry γ, R /deg, /a_0
(601)	4.0, 0.29	6.0	130, 2.8	4.0, 0.30	5.0	127, 2.75
(521)	6.65, 0.278	6.0	141, 2.75	4.0, 0.30	8.5	127, 2.75

Table 8.1.: The parameters used in the rotational contour simulations shown in Figure 8.10.

natural linewidths used and it is clear that the broadening of the observed rotational contour on going from the feature designated (601) to that given by (521) was assumed to be a lifetime broadening effect. In terms of Joens' assignment (501) and (303) this could be understood as a higher excitation of the dissociative ν_3 coordinate.

The reanalysis of the contours assuming a variable upper state equilibrium geometry but constant lifetime is presented as the dotted lines in Figure 8.10. The constants used in this simulation and resulting geometry of the upper state are again shown in Table 8.1. Small differences between the two simulations are within the S/N of the original experimental data reported by Takahashi *et al.* [24]. The new simulations revealed that the apparent broadening of the rotational contours may, in fact, be due to a change in the upper state equilibrium geometry. The geometry change of bond angle, $\gamma = 130°$ $\rightarrow 141°$ as a resulting of considering first the geometry due to $\nu_2 = 0$ then $\nu_2 = 2$ is large, indicating a very anharmonic potential. This geometry change, however, is an upper limit as it is quite possible that either of the primary pre-dissociation channels may be more efficient for the (521) bound level than for the (601) level and so lifetime broadening may contribute to the rotational contour broadening.

The new simulations indicate what a large effect a change of geometry of

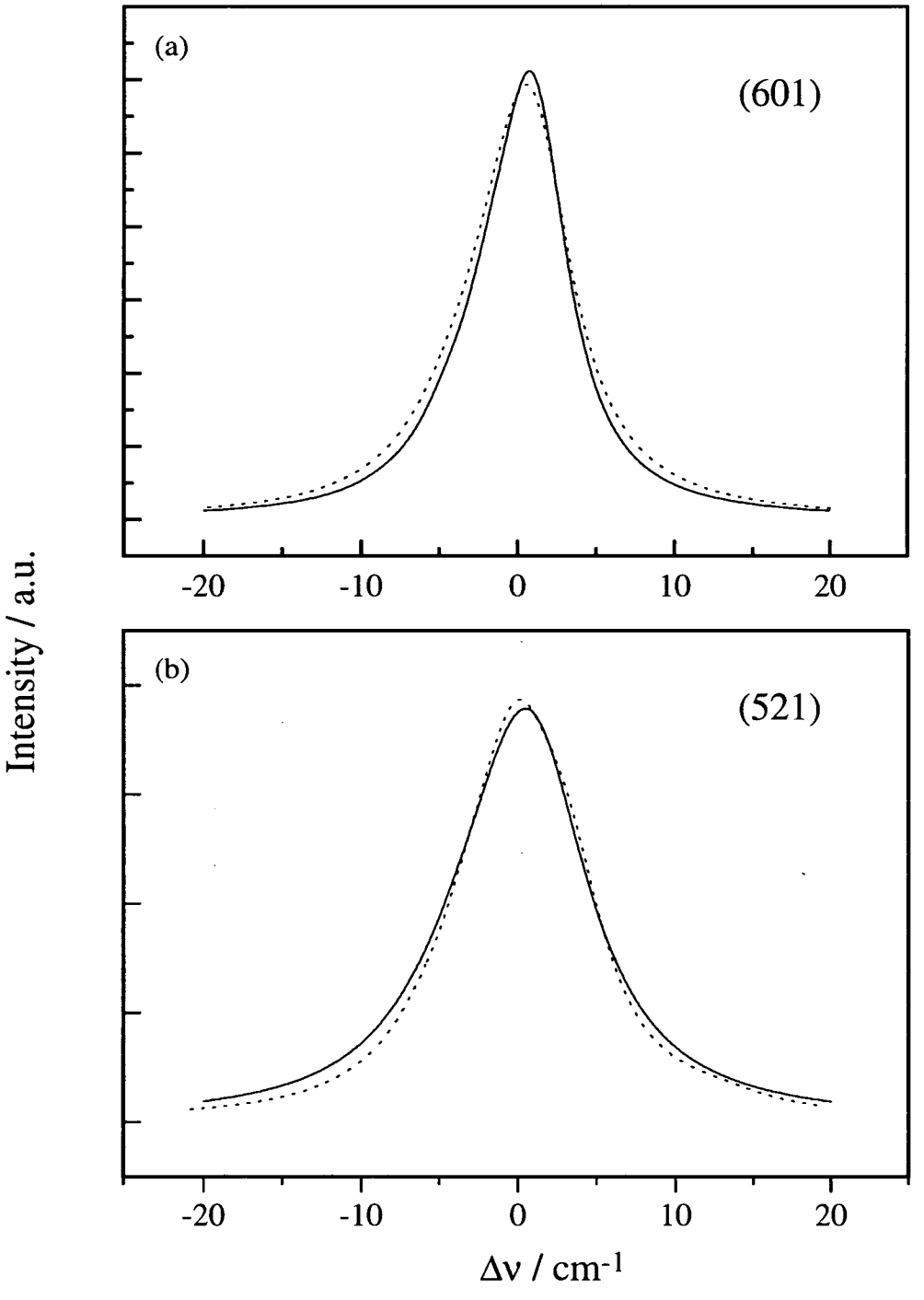

Figure 8.10.: The solid lines in both (a) and (b) are the optimised simulations performed by Takahashi *et al.* [24] to the experimental contours reported by these authors. The simulations were repeated using the same procedure outlined in this reference. The dotted lines are the simulations performed in this work taking into account the changes in the upper state equilibrium geometry with different quanta of vibrational excitation. The rotational constants, linewidths and geometries used in both sets of simulations are given in Table 8.1.

the upper state due to anharmonicity of the modes may have on the rotational contours.

8.4 Conclusions

8.4.1 Dissociation of Ozone following Huggins Bands Absorption

The results and subsequent discussion presented in this chapter provide a description of the dynamics of photodissociation following Huggins band absorption to yield channels (A), (B) and (C). The previous results chapters of the thesis involved discussions on individual aspects of ozone absorption and photodissociation. Chapter 5 entailed the analysis of the translational and angular properties of the O ($^3P_0$) photofragments from photolysis at a single wavelength within the Huggins bands and led to the conclusion that along with the expected spin-allowed dissociation *via* channel (A), the spin-forbidden channels (B) and (C) also play an important role in the dissociation in this region. The results of Chapter 6 provided confirmation of the production of the O_2 ($b\ ^1\Sigma_g^+$) fragments at a different wavelength also within the Huggins bands by analysis of the diatomic REMPI spectra. Although these chapters add important information about Huggins band dissociation the conclusions were limited by the small number of discrete photolysis wavelengths analysed. Prior to performing more general analysis on the Huggins band dissociation it was necessary to re-examine the entire UV absorption spectrum of O_3. The resulting analysis provided a new vibrational analysis of the discrete Huggins bands features as well as identifying the upper electronic state involved. It was shown that the Huggins band system is due to absorption into the $2\ ^1A_1$ electronic state.

The more complete set of experimental results presented in this chapter allows the limited conclusions of Chapters 5 and 6 to be expanded and linked with the new vibrational and electronic assignment of Chapter 7. This was achieved by examining the photodissociation products following photolysis at a number of discrete Huggins bands ranging over the entire region and relating the results to the vibrational structure of the upper state.

The discussion revealed that two 'primary' predissociation routes following the excitation into discrete vibrational levels of the Huggins bands accounts for the three channels which involve the O (^3P_j) fragments. The first of these is summarised in Figure 8.11 which shows the schematic q_3 potential energy diagram where the predissociation of the initially excited 2 $^1A_1$, ν_3 bound levels to the repulsive R $^1A_1$ state produces molecules in the O_2 ($X\ ^3\Sigma_g^-$) + O (^3P_j) exit channel. A subsequent 'secondary' crossing in this exit channel with the 2 $^3A'$ state accounts for the spin-forbidden production of the O_2 ($a\ ^1\Delta_g$) + O (^3P_j) fragments. The O_2 ($b\ ^1\Sigma_g^+$) channel on the other hand was concluded to be due to overlap of one or more repulsive triplet states with the bound wavefunctions of the 2 $^1A_1$ state in the parent molecular region. This 'primary' crossing is not represented on the q_3 schematic in Figure 8.11 as this crossing may occur largely in both the q_1 and q_2 coordinates and hence is impossible to represent in a single coordinate potential energy diagram. Switching to an adiabatic description of the dissociation to describe the exit channel region a simple comparison of the relative nuclear velocity of the fragments and spin-orbit splittings in the asymptotic region of dissociation revealed that non-adiabatic mixing in the exit channels leading to the O_2 ($b\ ^1\Sigma_g^+$) + O (^3P_j) fragments is not likely to dominate. Hence the non-statistical distribution of O (^3P_j) multiplets produced *via* this channel was concluded to be due to largely adiabatic dissociation along surfaces correlating with this limit. Due to the higher recoil velocities of the fragments in the O_2 ($X\ ^3\Sigma_g^-$) and O_2 ($a\ ^1\Delta_g$) exit channels non-adiabatic mixing may be more important. The above switching between diabatic and adiabatic descriptions of the dissociation in different regions is not completely valid but does illustrate some effects in the dissociation process.

The continuum dissociation within the Huggins bands was concluded to be due to a slightly different process involving the unbound $\nu_3 > 1$ coordinate. The production of only O_2 ($X\ ^3\Sigma_g^-$) and O_2 ($a\ ^1\Delta_g$) diatomic fragments following continuum dissociation is consistent with the above description of the

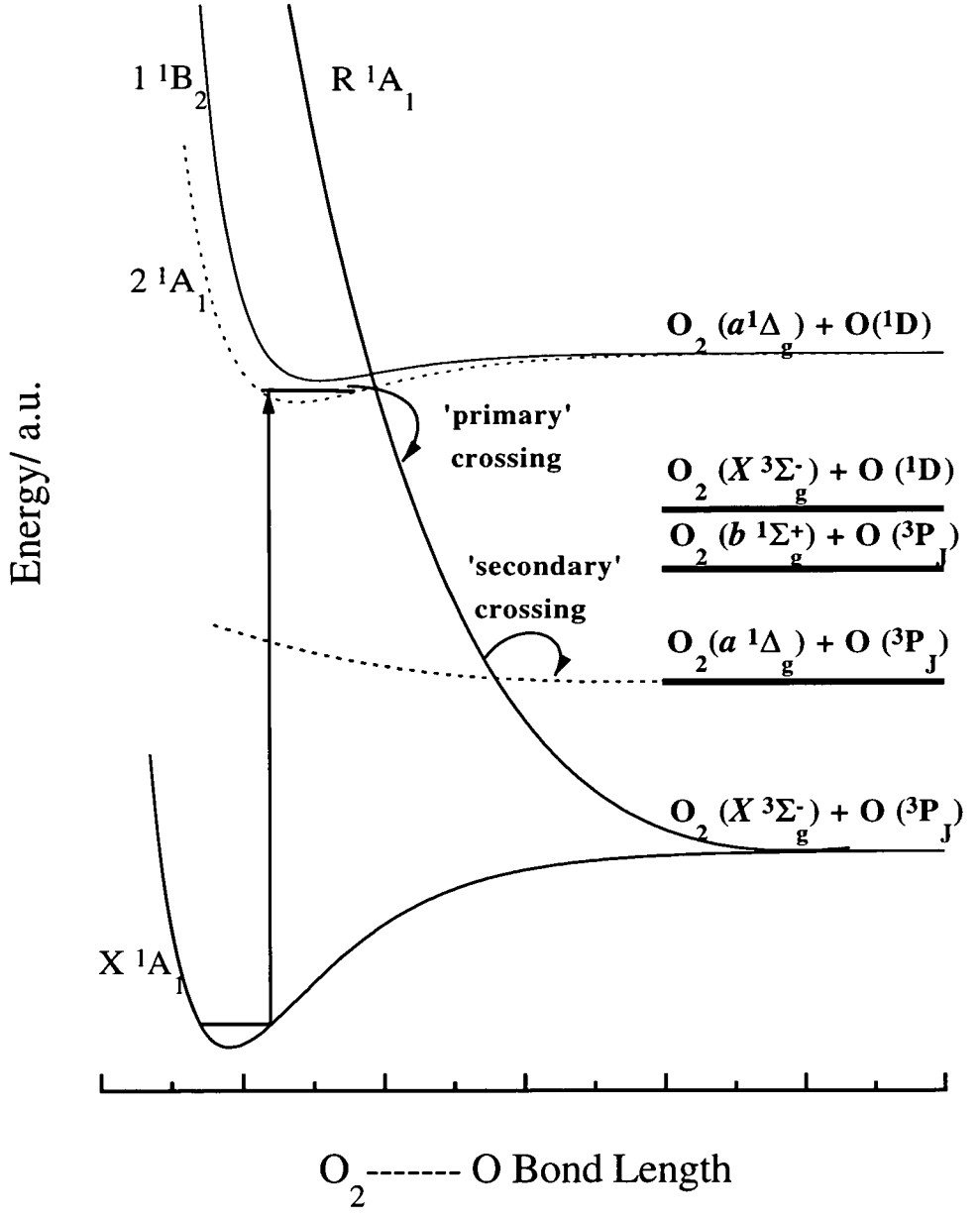

Figure 8.11.: The q_3 schematic potential energy curves involved in the Huggins band dissociation process to yield channel (A) and (B) fragments.

dissociation processes. All aspects of the $O(^3P_2)$, $O(^3P_1)$ and $O(^3P_0)$ PHOFEX spectra can be explained using these models of dissociation involving a single upper surface.

A strong effect of mode specificity was seen in the TOF profiles of the $O(^3P_0)$ fragments produced from (401), (311) and (301) photolysis. From these profiles it was seen that the production of the O_2 ($b\ ^1\Sigma_g^+$) channel was much stronger relative to the O_2 ($X\ ^3\Sigma_g^-$) and O_2 ($a\ ^1\Delta_g$) channels for the (401) and (301) photolysis than for the (311) photolysis. This was related to the mode specific efficiency of the primary crossing which produces the O_2 ($b\ ^1\Sigma_g^+$) state fragments. Also, a brief examination of the (1,0) band of the (2 + 1) $d\ 3s\sigma_g\ ^1\Pi_g \leftarrow\leftarrow O_2$ ($b\ ^1\Sigma_g^+$) REMPI transition following the production of O_2 ($b\ ^1\Sigma_g^+$) fragments by photolysis *via* the (401) and (301) bands revealed a difference in the peak of the rotational distribution of the O_2 ($b\ ^1\Sigma_g^+$, v = 0) fragments. The (401) photolysis produced a higher peak in the rotational distribution than the (301) photolysis and is due to more subtle effects of the crossing which produced these fragments. This smaller change in rotational distributions was not observed directly from the TOF profiles due to the limited translation energy resolution of the experiment.

A less apparent mode specificity was observed when the internal energy distributions of the O_2 co-fragments of $O(^3P_0)$ atoms produced from photolysis *via* the (611), (631) and (531) bands were measured. The varying continuum contribution to the distributions made it difficult to compare the relative amounts of O_2 ($b\ ^1\Sigma_g^+$) fragments produced in comparison to the O_2 ($X\ ^3\Sigma_g^-$) and O_2 ($a\ ^1\Delta_g$) fragments. However, by examination of the $O(^3P_0)$ co-fragment internal energy distributions following (611), (531) and (631) dissociation it was found that excitation of higher bending mode quanta produced broader internal energy distributions of the O_2 ($X\ ^3\Sigma_g^-$). The O_2 ($b\ ^1\Sigma_g^+$) state internal energy distribution was not noticeably broadened with the higher quanta of ν_2 in the bands investigated. A possible explanation for these general observations was proposed in terms of the models of predissociation developed.

However, further experiments would be required to prove such proposals.

Finally, the rotational contour analysis of two discrete vibrational features of the Huggins band system was re-examined. The literature reported analysis suggested that the broadening of the rotational band contour on going from the (601) to (521) upper states was due to a lifetime decreasing effect due to more rapid dissociation following excitation of the (521) band. This analysis was consistent with the vibrational assignment of Joens. The re-analysis presented here suggests that such an apparent broadening can equally be accounted for by a change in the upper state equilibrium geometry due to the anharmonicity of the ν_2 mode (as well as some contribution from ν_1 anharmonicity). And so both rotational contours were simulated with the same predissociation lifetime but different rotational constants of the upper state. This rotational contour analysis is consistent with the vibrational re-assignment of the Huggins bands presented in Chapter 7.

8.4.2 General Comments

From a more general viewpoint the discussion presented in this thesis provides a great deal of previously unreported information about O_3 photolysis. In particular the dissociation in the Huggins bands to yield O_2 ($b\ ^1\Sigma_g^+$) fragments had not previously been observed. The information disclosed in this chapter provides a great deal of information about this new channel. Also, the new vibrational analysis of the Huggins bands as well as the definitive assignment of the electronic upper state involved should provide for a greater understanding of the other processes occurring following Huggins band absorption. The implications of these assignments for photolysis yielding the $O(^3P_j)$ fragments have been outlined in this chapter however similar ramifications for the atmospherically important $O(^1D)$ product channel may also exist. The greater understanding of the photodissociation to yield $O(^3P_j)$ fragments may, therefore, have important consequences for the dynamics of the channel leading

to $O(^1D)$ products about which only rudimentary information is known.

A greater knowledge of the dissociation processes such as the identity of the predissociating curves producing the O_2 ($b\ ^1\Sigma_g^+$) fragments and a complete description of the selective coupling which leads to the strong mode specificity will require a full theoretical analysis including dynamical calculations on the full PESs of the states involved. However, further experiments may be required to provide a sufficient basis for such an approach.

References

[1] L. T. Molina and M. J. Molina, *J. Geophys. Res.* **91** (1986) 14501.

[2] K. Takahashi, N. Taniguchi, Y. Matsumi, M. Kawasaki and M. N. R. Ashfold. *J. Chem. Phys.* **108** (1998) 7161.

[3] A. A. Turnipseed, G. L. Vaghjiani, T. Gierczak, J. R. Thompson and A. R. Ravishankara. *J. Chem. Phys.* **95** (1991) 3244.

[4] G. M. Sweeney and K. G. McKendrick. *J. Chem. Phys.* **106** (1997) 9182.

[5] J. Cao, Y. Wang and C. X. W. Qian. *J. Chem. Phys.* **103** (1995) 9653.

[6] Y. L. Huang and R. J. Gordon, *J. Chem. Phys.* **94** (1991) 2640.

[7] A. Banichevich and S. D. Peyerimhoff, *Chem. Phys.* **174** (1993) 93.

[8] A. Banichevich, S. D. Peyerimhoff and F. Grein, *Chem. Phys.* **178** (1993) 155.

[9] B. P. Minaev and O. M. Kozlo, *Theoretical and Experimental Chemistry* **33** (1997) 219.

[10] D. H. Katayama. *J. Chem. Phys.* **71** (1979) 815.

[11] J. A. Joens. *J. Chem. Phys.* **101** (1994) 5431.

[12] J. Miyawaki, T. Tsuchizawa, K. Yamanouchi and S .Tsuchiya, *Chem. Phys. Lett.* **165** (1990) 168.

[13] H. G. Rubahn, W. J. van der Zande, R. Zhang, M. J. Bronikowski and R. N. Zare, *Chem. Phys. Lett.* **186** (1991) 154.

[14] Y. L. Huang and R. J. Gordon, *J. Chem. Phys.* **93** (1990) 868.

[15] Y. Matsumi and M. Kawasaki, *J. Chem. Phys.* **93** (1990) 2481.

[16] M. Roth, C. Maul and K. H. Gericke, *J. Chem. Phys.* **107** (1997) 10582.

[17] W. R. Gentry and C. F. Giese, *J. Chem. Phys.* **67** (1977) 2355.

[18] S. C. Givertz and G. G. Balint-Kurti. *J. Chem. Soc. Faraday Trans.* **82** (1986) 1231.

[19] L. L. Vahala, P. S. Julienne and M. D. Harvey. *Phys. Rev. A* **34** (1986) 1856.

[20] M. M. Graff and A. F. Wagner. *J. Chem. Phys.* **92** (1990) 2423.

[21] H. Grinberg, K. F. Freed and C. J. Williams. *J. Chem. Phys.* **107** (1997) 1849.

[22] H. B. Levene and J. J. Valentini *J. Chem. Phys.* **87** (1987) 2594.

[23] A. Sinha, D. Imre, J. H. Goble, Jr., and J. L. Kinsey *J. Chem. Phys.* **84** (1986) 6108.

[24] K. Takahashi, M. Kishigami, N. Taniguchi, Y. Matsumi, and M. Kawasaki, *J. Chem. Phys.* **106** (1997) 6390.

[25] R. N. Zare. *Angular Momentum, John Wiley & Sons* (1988).

[26] FORTRAN77 Program written by Z. Min, University of Edinburgh.

Chapter 9

REMPI of the Perturbed $d\ 3s\sigma_g\ ^1\Pi_g$ State of O_2

9.1 Introduction

The Rydberg state, $d\ 3s\sigma_g\ ^1\Pi_g$, used in the (2 + 1) REMPI detection of the O_2 ($b\ ^1\Sigma_g^+$) and O_2 ($a\ ^1\Delta_g$) photofragments from ozone photolysis in Chapter 6 is perturbed by a nearby valence state. In spite of the great wealth of research which has been performed in this area the perturbations observed in the REMPI spectra *via* this state are still not completely understood. Many of the difficulties arise from the lack of definitive experimental data on the transition energies and linewidths of the spectra [1]. A new method for probing this state is outlined in this chapter with the aim to resolve some of these issues.

This method involves the population of individual J levels of the O_2 ($b\ ^1\Sigma_g^+$, v = 0) state by direct optical pumping from the O_2 ($X\ ^3\Sigma_g^-$) ground state. Although the $b \leftarrow X$ transition is strictly forbidden under the electric dipole approximation due to multiplicity, parity and spin selection rules, the transition does have a very weak magnetic dipole oscillator strength. Interestingly, the $b \rightarrow X$ transition is observed to be 345 times more intense than the $a \rightarrow X$ transition which is of the same magnetic nature. This was found to be due to the comparatively large spin-orbit coupling between the $b\ ^1\Sigma_g^+$

and one of the spin sublevels of the $X\ ^3\Sigma_g^-$ ground state [2].

These individually pumped J levels of the $b\ ^1\Sigma_g^+$ state can then be probed *via* the perturbed v = 2 and 3, of the d Rydberg state. The limited number of J levels accessed in the d state is controlled by the two-photon selection rules and allows absolute assignment of the upper rotational levels. The probe laser is simultaneously calibrated to allow accurate determination of the transition energies.

This chapter outlines the experimental technique, a detailed background on the perturbations experienced by the vibrational levels of d state investigated, as well as the results obtained. These results are compared with the plethora of experimental data on this subject and discussed in terms of the theoretical models previously reported in the literature.

9.2 Experimental Details

Due to the difficulty of attaining a high enough laser power at the wavelengths required to pump the $b \leftarrow X$ magnetic dipole transition using an Excimer pumped dye laser system an alternative pump laser system was employed. The laser system chosen for this purpose was a Nd:YAG pumped Ti:Sapphire laser which generates a high power fundamental output in the required wavelength region.

9.2.1 The Ti:Sapphire Laser System

The Solar Laser Systems (LX 351) Ti:Sapphire laser employed utilises a Ti^{3+} doped Al_2O_3 crystal as the active laser medium [3]. The ground state of the Ti^{3+} ion is split by the crystalline field to provide the upper and lower states of the lasing system with peak absorption between 400 and 650 nm and hence the second harmonic of a Solar Laser System (LQ 514) Nd:YAG laser is a

suitable pump source for this material. The excited crystal fluoresces over the 600 to 1100 nm range from which a narrow spectral linewidth ($\sim 0.4\ cm^{-1}$) can be selected for amplification using prism dispersive components, a diffraction grating and a holographic selector. The n1 holographic selector used in the these experiments allowed the selection of laser output from 710 - 780 nm with a maximum output of $\sim$ 25 mJ at 755 nm with a pulse length of 12 ns. The Nd:YAG laser used to pump the Ti:Sapphire laser was operated in the Q-switched mode generating second harmonic radiation at 532 nm with a power output of 130 mJ/pulse [4]. The timing was controlled by external triggering of the Xenon flashlamp used for optical pumping of the laser medium and the electrooptic Q-switch which generates the short intense output pulse.

9.2.2 Incorporating the 'New' Laser System into the Experimental Set-up

While the Ti:Sapphire system provides the high power required to pump the initial $b \leftarrow X$ transition the excimer pumped dye laser system probes the resultant O_2 ($b\ ^1\Sigma_g^+$, v = 0, J) levels *via* a (2 + 1) REMPI transition in the 335 - 355 nm region. A major difficulty encountered was to temporally synchronise the laser outputs of the two laser systems.

The control over the temporal overlap was achieved using a 4-channel (DG 535) Stanford Research Digital Delay which produces trigger pulses capable of externally triggering the Nd:YAG laser's flashlamp and Q-switch and is incorporated into the system as illustrated in the schematic shown in Figure 9.1. A further feature of this set-up is the photodiode monitor of the relative timings of the lasers. Silica disks are used to steer 10% of each laser beam onto the same realtime photodiode, the signal from which is channelled to an oscilloscope so that the signals due to the two light pulses are observed on the same channel. In this way the temporal overlap of the lasers could be

observed while the experiments were proceeding so that any drift of the two lasers could be corrected for. A typical delay of 50 - 100 ns between the pump and probe lasers was employed for maximum ion signal.

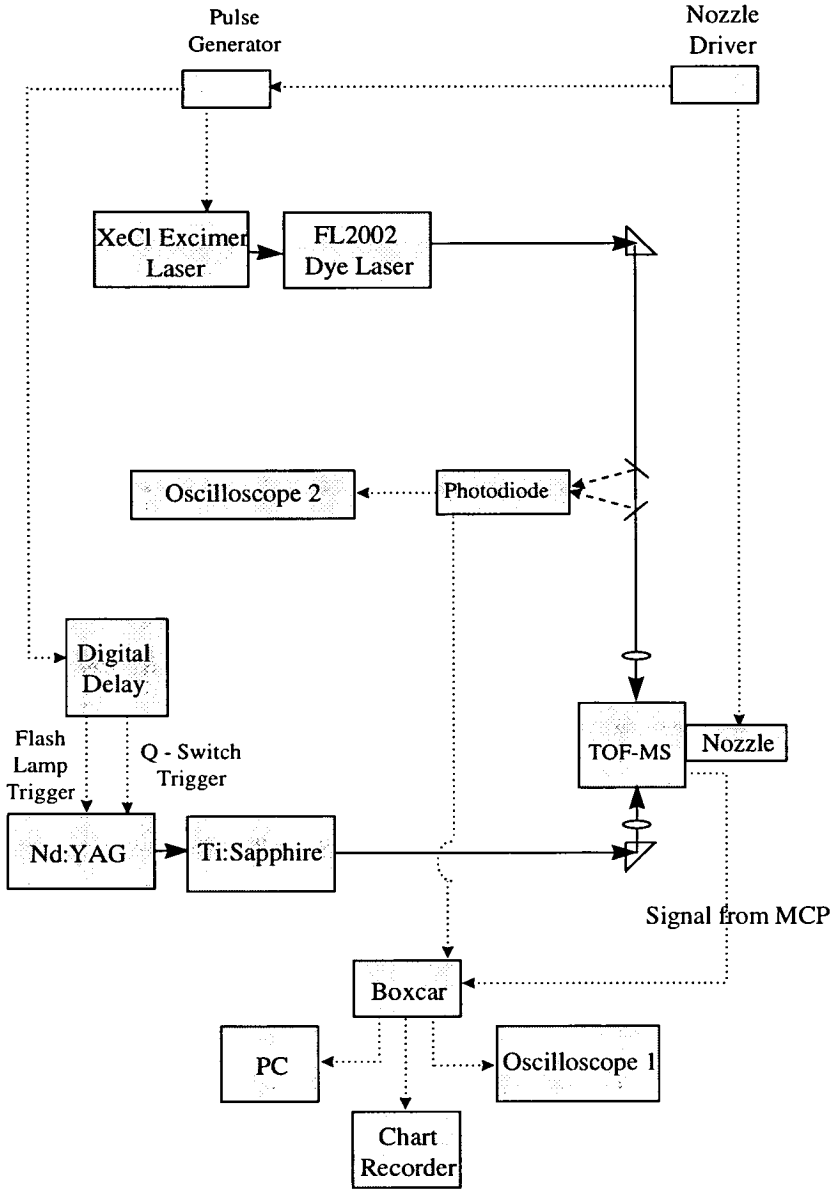

Figure 9.1.: A schematic diagram outlining the experimental set-up employed.

9.2.3 Spatial Alignment of the Lasers

Another difficulty encountered when setting up this experiment was spatially overlapping the foci of the counter propagating lasers. The principal problem was that no ion signal could be generated using the pump laser as $\geq$ 8 photons of this wavelength would be required to ionise the O_2 molecules in the beam. A novel alignment technique was adopted to circumvent this problem, which involved using molecular iodine seeded in a beam of helium. A known (2 + 1) REMPI signal generates I_2^+ ions at a wavelength of 341.25 nm. It was found that when the laser light from the pump laser (710 - 780 nm) was both temporally and spatially overlapped with the REMPI laser the signal intensity due to the two-photon transition in iodine was depleted by a one-photon transition from the ground state of iodine. This was interpreted as being due to the greater efficiency of the one-photon transition into the *A* state continuum which resulted in dissociation of the ground state I_2 molecules in the interaction region and hence a decrease in the less efficient two-photon ion signal. The continuum nature of the depletion was confirmed by scanning of the 'red' laser which produced a variation in the I_2^+ ion signal consistent with the power curve of the Ti:Sapphire laser. However, the effect proved to be very useful in the optimisation of the overlap of the lasers with complete depletion of the signal being achieved even for reduced powers of the 'red' laser.

The I_2/He bulb was then replaced with pure O_2 to proceed with the experimental aims outlined at the beginning of this chapter.

9.2.4 Calibration of the Laser Wavelength

The calibration method used involved directing $\sim$ 10 % of the FL 2002 dye laser radiation into a hollow cathode lamp filled with neon. In this way the laser induced atomic neon transitions [5] could be monitored as each scan

was performed. For each O_2^+ spectrum recorded a scan of the neon transitions in the wavelength region was simultaneously recorded *via* another channel of the boxcar. The wavelength offset of the laser could then be corrected for by comparison of the known atomic transition wavelengths with the laser grating reading for these transitions. The calibrated air wavelengths were then vacuum corrected [6] to achieve an absolute accuracy of $\pm$ 1 cm^{-1} for all spectra reported.

9.3 The Perturbations of the $d\ 3s\sigma_g\ ^1\Pi_g$, v = 2 and 3 Levels

9.3.1 Potential Energy Curves and Configurations of the Interacting States

The potential energy curves of the electronic states of O_2 [7] discussed in this chapter together with the experimental pumping scheme are shown in Figure 9.2.

The orbital occupancy of the perturbing valence and Rydberg states are very important in the determination of the strength of the interaction. In cases where the occupancy differs by a single orbital, a strong interaction can take place and when such an interaction takes place between states of the same symmetry their potential energy curves are best represented in the adiabatic formalism where these states are not allowed to cross. The vibrational spacings and rotational constants are then quite different from that of the unperturbed state [8]. However, in the case where the molecular configurations differ by the occupancy of two orbitals the interactions are much weaker and it is better to model the perturbation using the diabatic model where potentials of the same symmetry are allowed to cross. As can be seen from the orbital make-up of the states under investigation, shown below, the second scenario is most suitable

for the analysis of the perturbation experienced by the $d\ ^1\Pi_g$ state and hence all of the curves are given in their diabatic format [8].

$d\ ^1\Pi_g$	$(core)\ (3\sigma_g)^2(1\pi_u)^4(1\pi_g)^1(3s\sigma_g)^1$
$I\ ^1\Pi_g$	$(core)\ (3\sigma_g)^2(1\pi_u)^3(1\pi_g)^2(3\sigma_u)^1$
$II\ ^1\Pi_g$	$(core)\ (3\sigma_g)^1(1\pi_u)^4(1\pi_g)^3$

9.3.2 The Types of Interactions

Three types of interactions can occur between the states: Rydberg-Rydberg, Rydberg-valence and valence-valence interactions. The effects of all of these are reflected in the REMPI spectra of the $d\ ^1\Pi_g$ state. Of these the most important is the Rydberg-valence interaction which has been studied by a number of groups by solution of the Coupled Schroedinger Equations (CSE) of the mixed Rydberg-valence system [7, 8, 9] and using *ab initio* methods [10, 11, 12, 13, 14]. In this case the input to the coupled equations involve the unperturbed wavefunctions of the $d\ ^1\Pi_g$ Rydberg and $II\ ^1\Pi_g$ valence states, their diabatic potentials and the coupling strength between the two states. Generally, the mixing of a level of the Rydberg state with that of a valence level gives rise to coupled levels in the vicinity of the two uncoupled levels. The ratio of Rydberg to valence character of these mixed rovibrational levels is dependent on the energy difference between the uncoupled levels. As this energy difference is strongly J dependent due to the difference between the rotational constants of the unperturbed Rydberg state ($B_e = 1.69\ cm^{-1}$) and valence state ($B_e = 0.99\ cm^{-1}$) [7], a rotationally dependent interaction is observed.

There is a low ionisation efficiency from the $II\ ^1\Pi_g$ valence state due to the difference in equilibrium geometry between this state ($R_e = 1.49$ Å) and the ion ($R_e = 1.14$ Å) [7] (see Figure 9.2) and hence these levels are not ob-

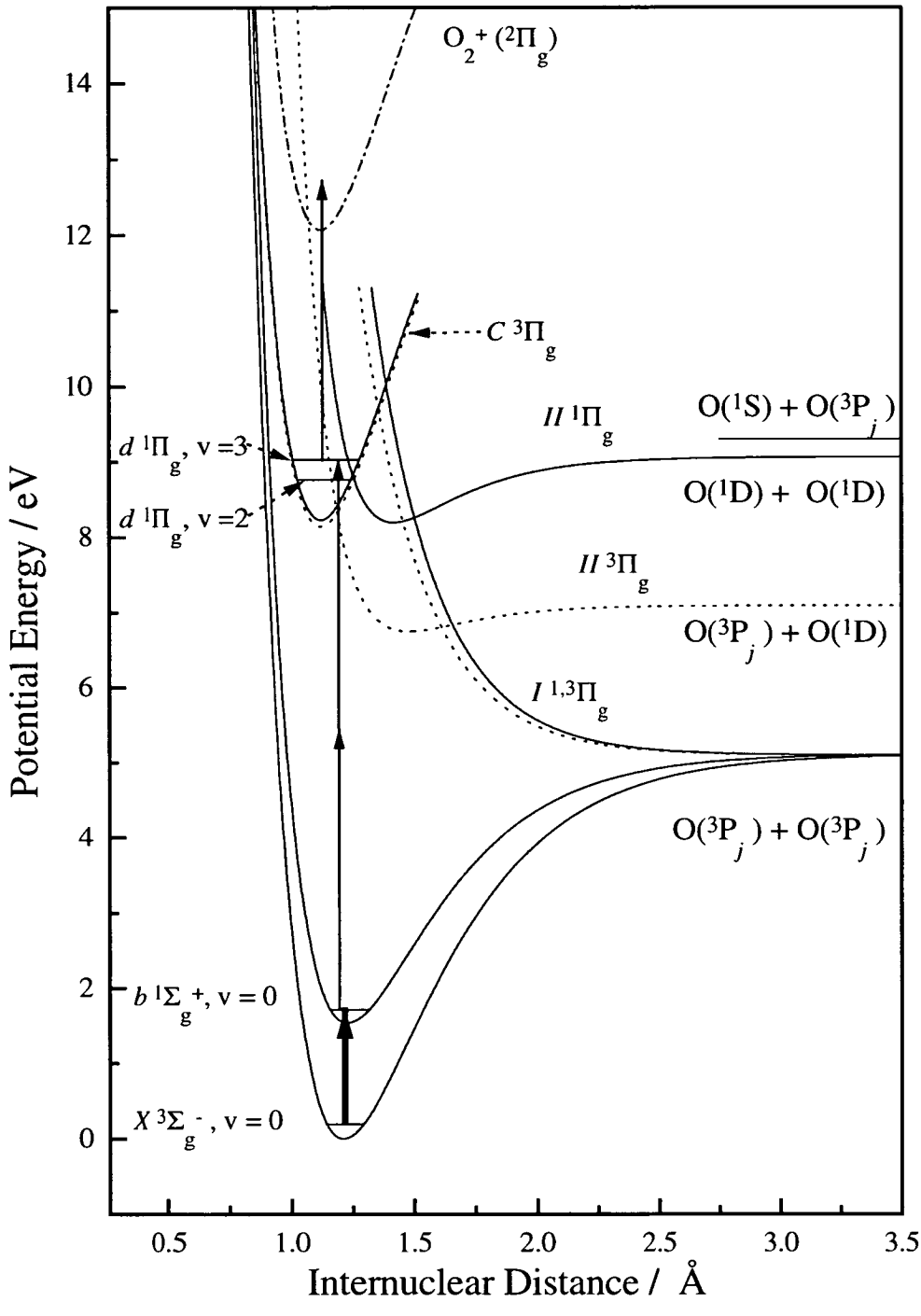

Figure 9.2.: Diabatic potential energy curves of all of the states involved in the REMPI spectra presented in this chapter. The experimental excitation scheme is also shown for the case of the $d\ ^1\Pi_g$ v = 3 $\leftarrow$ $b\ ^1\Sigma_g^+$, v = 0, J transition.

served directly in the spectra. As a result it is very difficult to determine the exact energy of the vibrational levels of this state. However, in a recent CSE analysis of all of the available experimental data, Lewis *et al.* have succeeded in determining the vibrational energies of the II $^1\Pi_g$ state from the perturbational effects of these levels on the REMPI spectra of the d $^1\Pi_g$ Rydberg state. The energy position of these levels relative to the Rydberg state v = 2 and 3 levels are shown in Figure 9.3 which has been adapted from Figure 8 of ref [7]. The effect of the II $^1\Delta_g$ state will be discussed later in the text.

According to the calculations of Lewis *et al.* [7] the observed spectral perturbations are predominantly due to valence levels which lie higher in energy than the Rydberg levels which they perturb. Thus they suggest that the v = 8 and 9 levels of the II $^1\Pi_g$ state perturb v = 2 of the d $^1\Pi_g$ state while v = 13 and 14 perturb the v = 3 level. When such a case is considered in detail using the coupled equation model approach it is found that a vibrational level of the valence state couples with a lower energy Rydberg level and two coupled levels are formed, the lower of which is predominantly Rydberg in character while the higher level is predominantly valence. In these experiments the Rydberg level is selectively detected due to the greater ionisation efficiency of this state and the larger predissociation rate of the valence state which is discussed in more detail below. However, as J increases the Rydberg rovibronic levels become close to being degenerate with those of the valence state in which case the two coupled states have almost equal contributions from both diabatic states, with both levels having a significant probability of existing with low internuclear separation and hence both levels will be detected. Further increase in J results in the Rydberg state rovibronic levels becoming higher in energy than those of the valence state and therefore the higher of the mixed levels will be mostly Rydberg character with the lower feature incorporating principally valence character and hence it is the higher energy feature which will be detected. A beautiful example of this trend is illustrated in the spectra to be presented in this chapter.

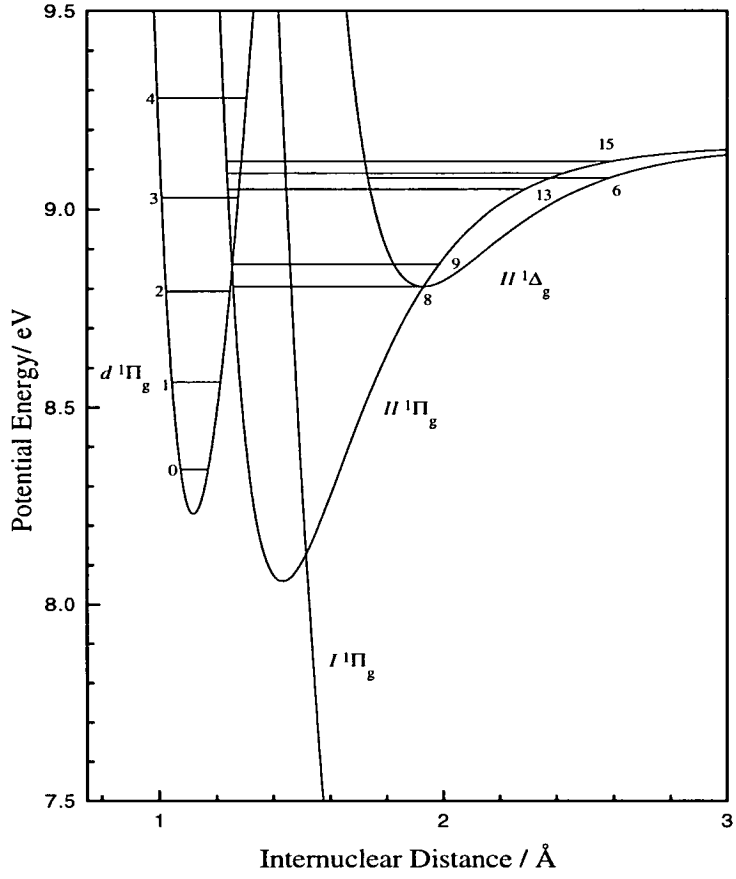

Figure 9.3.: An enlargement of the diabatic potential energy curves of the singlet states involved in the Rydberg-valence interactions investigated. The energies of the vibrational levels of interest are shown and are discussed in the text. This figure is adapted from Figure 8 of ref [7]

Both the valence-valence and Rydberg-Rydberg interactions influence the predissociative lifetimes of the coupled states. The two routes to predissociation of the excited Rydberg state are:

(i) Rydberg-Rydberg coupling of the $d\ ^1\Pi_g$ state with the $C\ ^3\Pi_g$ state which is due to spin-orbit mixing of these states. The resulting $C\ ^3\Pi_g$ state can then be predissociated by Rydberg-valence coupling with the repulsive limb of the $II\ ^3\Pi_g$ state leading to $O(^1D) + O(^3P_j)$ products.

(ii) Rydberg-valence coupling of the $d\ ^1\Pi_g$ state with the $II\ ^1\Pi_g$ state in the manner described above. The bound $II\ ^1\Pi_g$ levels are then strongly predissociated by valence-valence interactions with the $I\ ^1\Pi_g$ which yields the $O(^3P_j) + O(^3P_j)$ products.

As the Rydberg-Rydberg spin-orbit singlet-triplet interaction (coupling constant = 95 cm^{-1}) is much weaker than the Rydberg-valence (coupling constant = 630 cm^{-1}) and valence-valence (coupling constant = 500 cm^{-1}) interactions, the lifetime of the Rydberg states is longer than those of the valence state. Hence, the spectral features due to levels which are made up of mostly Rydberg character will have a narrower linewidth than the predominantly valence levels. Although, this rule holds true in general a slight complication must be considered due to the dependency of the predissociation rates of the II $^1\Pi_g$ and C $^3\Pi_g$ state on vibrational levels. Both of these states are predissociated by repulsive states and hence an oscillation of the predissociation rate with vibrational level of the bound state will be observed due to the overlap of the wavefunctions involved.

9.4 Results and Discussion

9.4.1 Optical Pumping of the O_2 (b $^1\Sigma_g^+$, v = 0) State

The transitions expected in the $b \leftarrow X$ transition are illustrated in Figure 9.4. It is seen that the $^1\Sigma$ state in which both spin and orbital angular momentum are zero is best modelled by Hund's case (a) as the angular momentum due to nuclear rotation, N, is identical to the total angular momentum, J [15]. Also, it may be noted that due to the nuclear spin of zero of the homonuclear O_2 only totally symmetric levels can exist which results in only even J levels of the b $^1\Sigma_g^+$ state. Conversely, the spin uncoupling due to the triplet nature of the ground state means that Hund's case (b) provides a more appropriate description of the rotational levels of this state. In this case, K ($\equiv$ N) is the total angular momentum excluding spin and each of these levels is split into three sublevels due to the effects of spin giving the total angular momentum designation $J = N + 1$ (F_1), N (F_2) and N - 1 (F_3).

The appearance of only odd N levels is again due to the nuclear spin statistics which result in only totally symmetric levels.

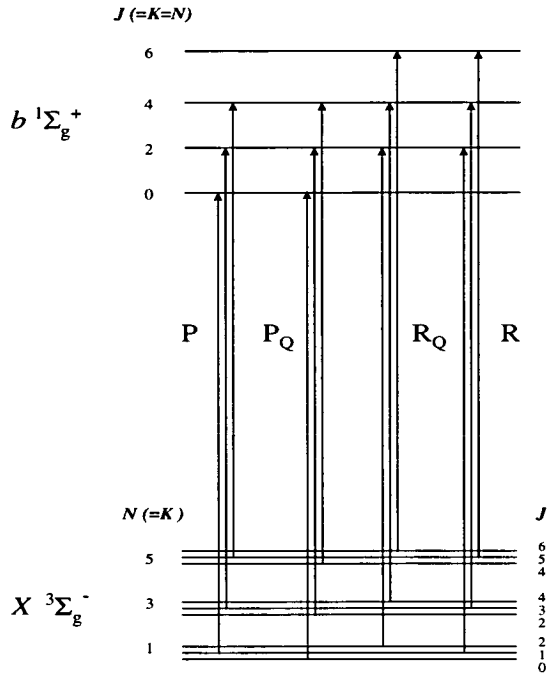

Figure 9.4.: The allowed rotational levels of the $X\,^3\Sigma_g^-$ and $b\,^1\Sigma_g^+$ states are illustrated above. The spectroscopic branches observed in the $b \leftarrow X$ transition are shown. The P branch was used exclusively in the population of the $b\,^1\Sigma_g^+$ J levels in these experiments.

All of these points are combined in Figure 9.4 where it is seen that there are four branches observed in the $b \leftarrow X$ transition. In the subsequent experiments the pumping of the P branch of this transition was employed where pumping the P1, P3, P5 etc. lines populate the J = 0, 2, 4 etc. levels respectively of the $b\,^1\Sigma_g^+$. An experimental difficulty encountered was that the holographic selector of the Ti:Sapphire was not controlled by a stepper motor and was only hand tunable by a micrometer screw.

However, because of the fingerprint nature of the $b \leftarrow X$ transition λ could be tuned such that the P branch features could be unambiguously selected. The shape of the (0,0) band of the $b \leftarrow X$ is illustrated in Figure 9.5. A simple procedure of setting the detection laser at the wavelength of a rotational band head of a band of the $d \leftarrow\leftarrow b$ allowed the identification of the

lines of the $b \leftarrow X$ transition by reference to the known rotation transition spacings illustrated in Figure 9.5.

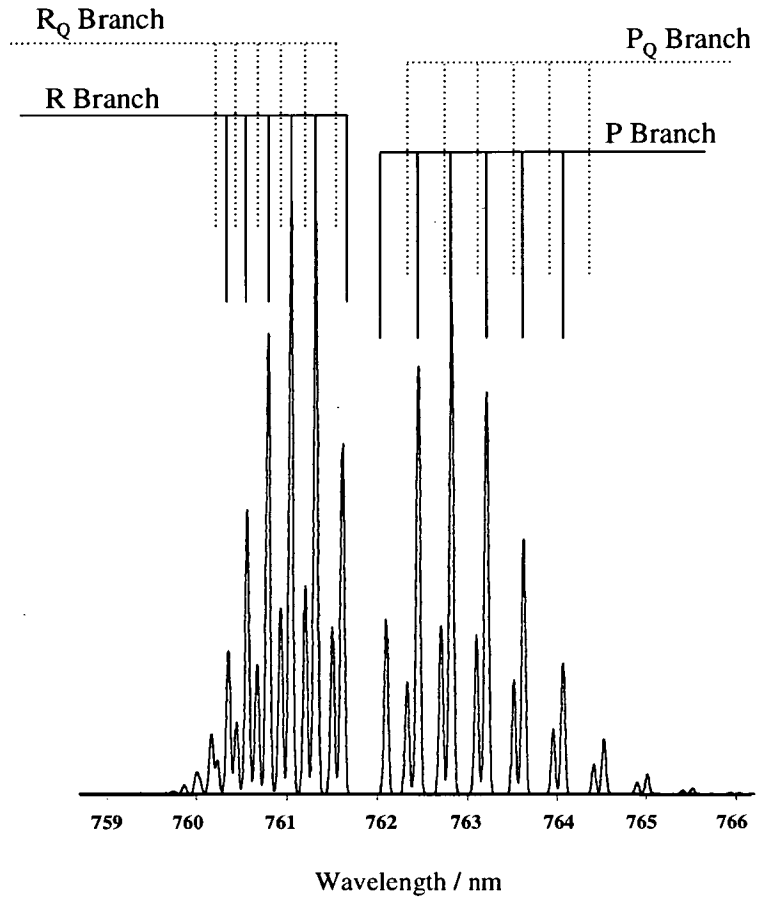

Figure 9.5.: The rotational structure of the (0,0) band of the $b \leftarrow X$. A Boltzmann distribution was used in the simulation [16].

9.4.2 Rotationally Selective Probing of the v = 3 level of the $d\ ^1\Pi_g$ State

Due to the two-photon selection rules which allow $\Delta J = 0, \pm 1$ and ± 2 a total of 5 rotational levels of the $d\ ^1\Pi_g$ state are accessible from a single J level of the $b\ ^1\Sigma_g^+$ state. The (2 + 1) REMPI scheme utilised in these experiments

	Origin			
v	Ref [9] cm^{-1}	Ref [8] cm^{-1}	CSE model of ref [7] cm^{-1}	This Work cm^{-1}
0	66380		66356	
1	68237		68226	
2^a		70108	70011	70022^b
			70142	70156^b
3	71956	71920	71950	71950^c

Table 9.1.: Origins, v_0, in cm^{-1}, are the transition energies from the effective origin, E_∞ [7], of the X state to the $J = 0$ of the $d\,^1\Pi_g$, v levels. [a] The higher energy corresponds to the origin of the $II\,^1\Pi_g$, $v = 8$ level. [b] Estimated from the most intense features in the ($d\,^1\Pi_g$, $v = 2$) $\leftarrow\leftarrow$ ($b\,^1\Sigma_g^+$, $v = 0$, $J = 0$) spectrum. [c] Taken from the origin used in the line position simulation of the low J of the ($d\,^1\Pi_g$, $v = 3$) $\leftarrow\leftarrow$ ($b\,^1\Sigma_g^+$, $v = 0$, $J = 4, 6, 8$) spectra

is illustrated in Figure 9.2. The spectra produced in this manner by probing the energy region of v = 3 of the $d\,^1\Pi_g$ state following pumping of the P1 to P17 lines of the $b \leftarrow X$ transition are shown in Figures 9.6 and 9.7.

The transition energies and linewidths of the rotational lines of these spectra are tabulated in Table 9.2. There is no significant variation of the linewidths which are around 3.5 $\pm$ 1 cm^{-1}. Also, it should be noted that the more subtle intensity variations in these spectra should be ignored due to significant variations in the pump power while the spectra were being recorded. However, a great deal of very useful information can be extracted from these spectra, not least of which is an accurate determination of the origin of the v = 3 of the $d\,^1\Pi_g$ state for which a number of conflicting values have been reported in the literature. The newly determined value is compared with those previously reported in Table 9.1.

Also, a very clear effect of the Rydberg-valence interaction between the v = 3 level of the $d\,^1\Pi_g$ and the v = 13 level of the $II\,^1\Pi_g$ is observed. The effects

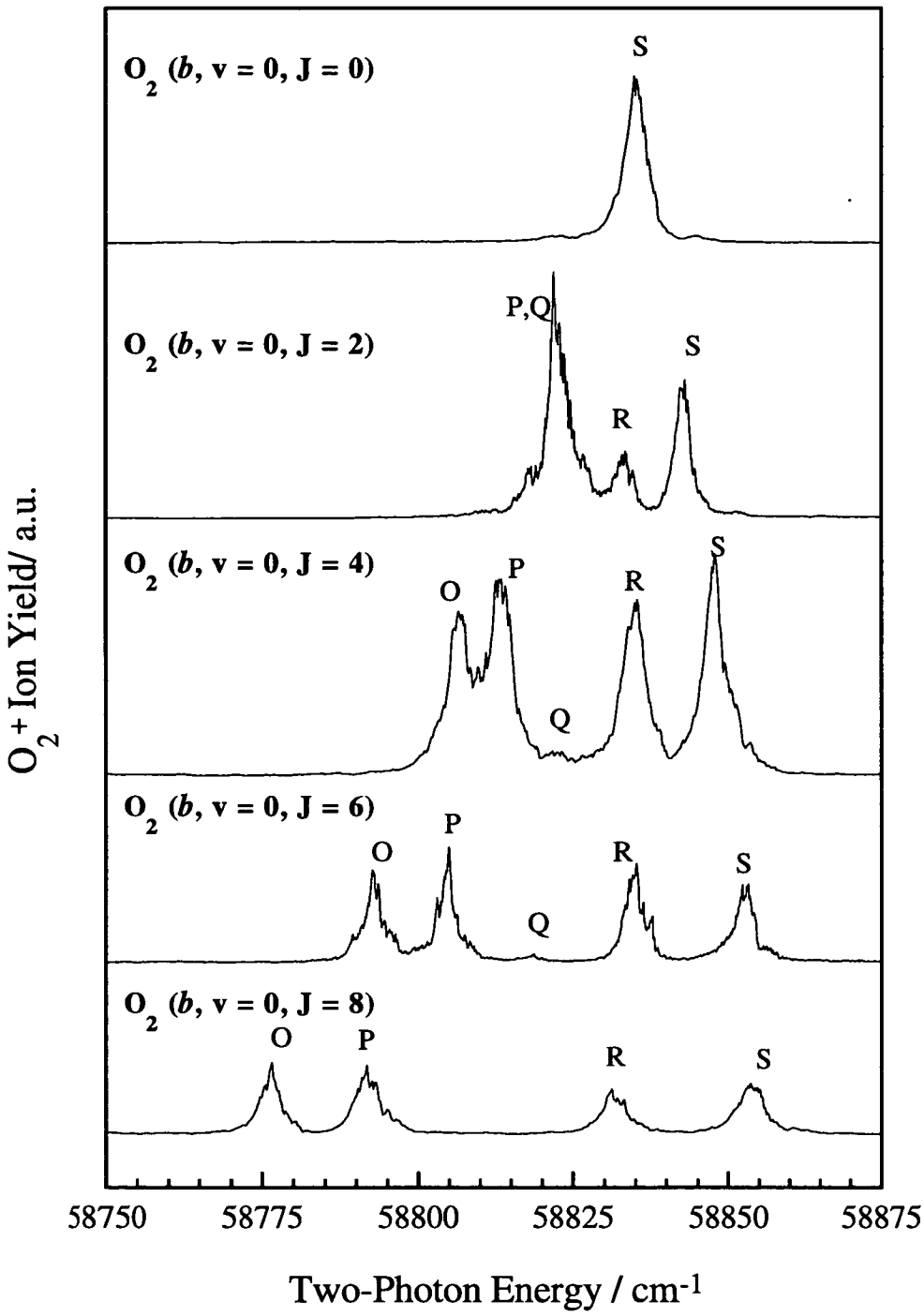

Figure 9.6.: The spectra shown here involve pumping of the P branch of the $b \leftarrow\leftarrow X$ transition to populate J levels of the $b\,^1\Sigma_g^+$, $v = 0$, J state shown on the left of the diagram. The resulting J levels are then ionised *via* the O (ΔJ = -2), P (ΔJ = -1), Q , R and S branches of the (2 + 1) REMPI ($d\,^1\Pi_g$, $v = 3$) $\leftarrow\leftarrow$ ($b\,^1\Sigma_g^+$, $v = 0$)

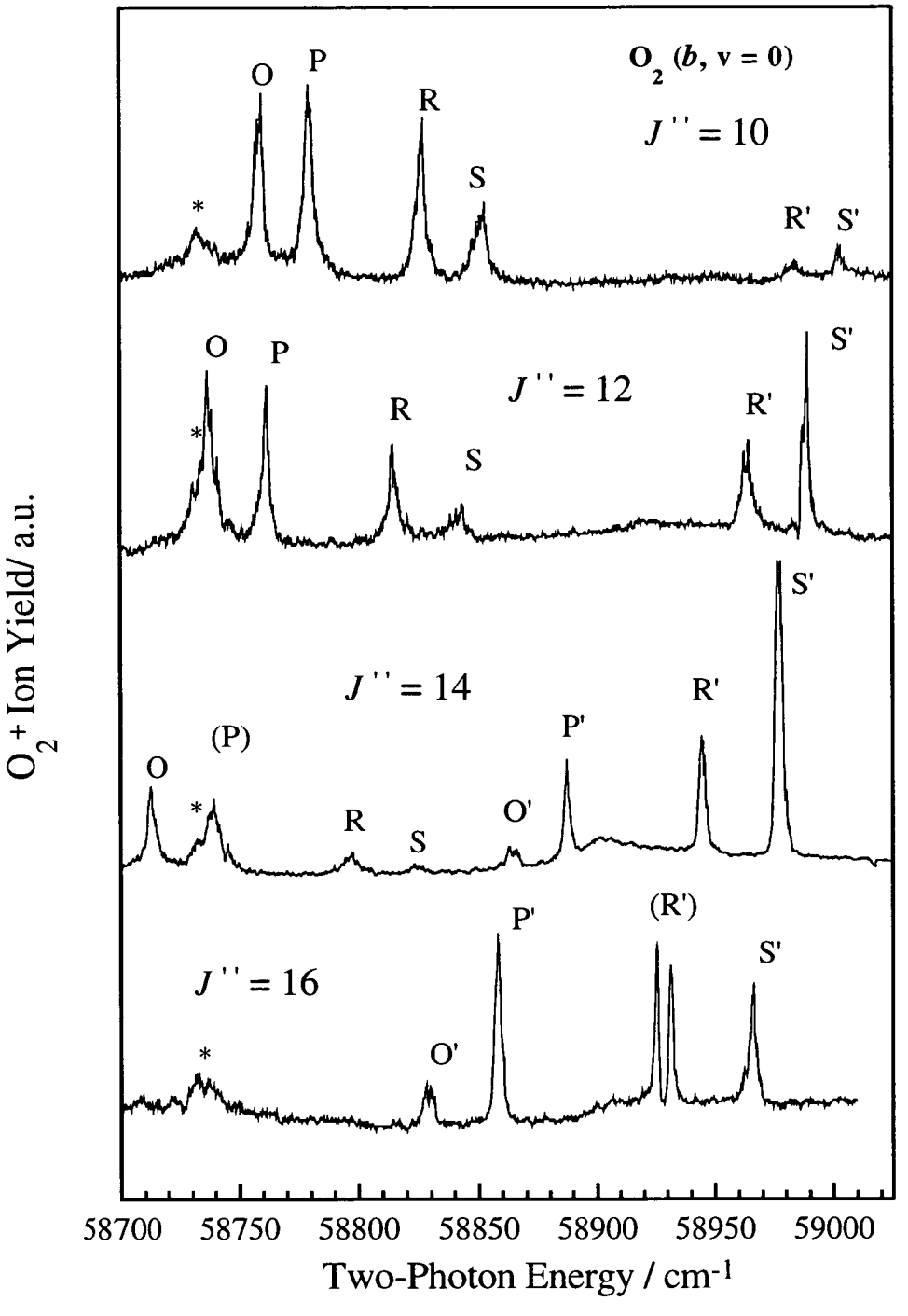

Figure 9.7.: These spectra are equivalent to those in Figure 9.6 except with the higher rotationally populated J levels of the b state indicated on the diagram. The primed features are due to transitions to the higher energy levels resulting from the coupling of the $d\ ^1\Pi_g$, $v = 3$ level of the Rydberg state with the $II\ ^1\Pi_g$, $v = 13$ level of the valence state. See text for details of these couplings. The features marked with an * are due to a (3 + 1) REMPI transition from g.s. O_2.

	Transition line of $d\,^1\Pi_g, v = 3 \leftarrow\leftarrow b\,^1\Sigma_g^+$				
$b\,^1\Sigma_g^+$ J	O /cm^{-1}	P /cm^{-1}	Q /cm^{-1}	R /cm^{-1}	S /cm^{-1}
0			58834.7 *4.0*	58834.7 *4.0*	58834.7 *4.0*
2	588821.9 *3.0*	588821.9 *3.0*	588821.9 *3.0*	58833.3 *3.9*	58842.9 *2.6*
4	58806.5 *3.5*	58813.5 *~ 4*	58821.7	58835.2 *~ 4*	58847.7 *3.3*
6	58792.6 *2.8*	58805.0 *2.5*	58818.7	58835.1 *3.4*	58853.3 *3.3*
8	58776.6 *3.6*	58791.7 *4.4*		58831.2 *4.2*	58853.7 *5.5*
10	58759.5 *~4.5*	58779.3 *~3.9*		58827.1 *4.4*	58852.7 *5.8*
12	58737.1	58762.5 *3.4*		58815.1 *4.1*	58844.2
14	58712.5 *4.1*	58739.4 *~7*		58797.4 *~7*	58823.1
	O′	P′	Q′	R′	S′
10				58983.9 *~6*	59003.1 *4.8*
12				58965.1 *4.4*	58989.9 *3.2*
14	58863.3	58887.3 *~3.0*		58944.5 *3.1*	58977.6 *3.8*
16	58828.0 *5.5*	58857.9 *3.5*		58925.2 58931.0 *1.6* *2.0*	58966.0 *3.2*

Table 9.2.: The transition energies of the features shown in Figure 9.6 and 9.7. The estimated FWHM of the features are shown in italics below the transition energies. The doubled feature, R′ (16) of Figure 9.7, due to the weak coupling discussed in the text involves two values of both transition energies and linewidths.

illustrated in these spectra have been well characterised by Lewis *et al.* [7] who determined that the low J levels of the v = 3 level experience a relatively small perturbation. As the Rydberg electron has only a small effect on the vibrational and rotational structure of the molecule the rotational structure of the unperturbed vibrational levels of the $d\ ^1\Pi_g$ state is equivalent to that of the O_2^+ ($^2\Pi_g$) ion on which the Rydberg series converges. For example, the rotational constant of the unperturbed v = 0 of the d state is the same as that of the same level of the ion, B_v = 1.68 cm^{-1}. As v = 3 of the ion has a rotational constant of B_v = 1.62 cm^{-1} this would be expected to be the unperturbed value for the same vibrational level of the $d\ ^1\Pi_g$ state. However, in previous work the rotational structure between 58700 and 58950 cm^{-1} has been successfully simulated using a rotational constant of 1.15 cm^{-1} for the upper state [17] which shows the effect of mixing of the Rydberg level with the vibrational level of the valence state which has a much lower rotational constant. The authors [17] who performed this simulation noted that there appeared to be a faster fall off of intensity in the high J transitions than could be accounted for by their model.

A similar calculation has been performed here using the known B_v = 1.39126 cm^{-1} for the lower level and a B_v = 1.14 cm^{-1} for the upper level. The simulation of the position and intensities of transition lines from individual lower J'' = 4, 6, 8, 10, 12 and 14 to the upper state are shown in Figure 9.8. It is clear from these calculations that while the lower J transitions are well simulated by these constants, the simulation begins to break down for $J' \geq 13$. The breakdown in the matching of the calculated line positions and intensities with the experimental spectrum coincides with the appearance of features to higher energy which appear to take intensity from the lower levels. The reason for both of these anomalies can be seen from the CSE analysis of the problem from Lewis *et al.'s* [7] work who suggest that at $J \simeq 11$ v = 13 of the $II\ ^1\Pi_g$ state and the rovibronic levels of $d\ ^1\Pi_g$ v = 3 become energetically very similar. In terms of the previous discussion on the nature of the Rydberg-

valence interaction there is a very clear explanation for the spectra in the region $J' = 11$ - 18.

At energies less than $J' = 11$, v = 3 of the $d\ ^1\Pi_g$ state lies lower in energy than the v = 13 level of the $II\ ^1\Pi_g$ state. In this case, the lower energy feature of the mixed eigenstates arising from the coupling of the diabatic levels is mostly Rydberg in character and these levels are detected for $J'' \leq 11$. In the $J'' = 11$ - 15 region the rovibronic levels of the $d\ ^1\Pi_g$ v = 3 are almost degenerate with those of $II\ ^1\Pi_g$ v = 13 and so both of the coupled states have significant contribution from the Rydberg state and so both the higher and the lower energy features are detected.

Finally, for levels with $J' \geq 15$ the diabatic Rydberg level lies higher in energy than that of the valence level and thus the lower energy of the two coupled features has mostly valence character and so is not detected while the upper feature now consisting mostly of Rydberg character is detected. Unfortunately, no higher levels were detected due to the difficulty of pumping the P19 line as there is a very low concentration of $N = 19$ rotational levels of the $X\ ^3\Sigma_g^-$ state in the molecular beam.

Weak perturbation of the $J' = 17$ level

Another interesting point to be made is the splitting of the R(16) feature which was also noted by Lewis *et al.* from the non-rotationally selective and less well resolved spectra of Ogorzalek-Loo *et al.* [18]. Lewis *et al.* [7] postulated that the much weaker perturbation experienced by this level was due to the weak rotational interaction of the $II\ ^1\Delta_g$ v = 6, $J = 17$ with the Rydberg level. The relevant potentials are shown in Figure 9.3 where it can be seen that the extended R_e of the $II\ ^1\Delta_g$ allows negligible vibrational overlap with the $d\ ^1\Pi_g$ state. Also, the MO configuration of the $II\ ^1\Delta_g$ state:

$$II\ ^1\Delta_g \qquad (core)\ (3\sigma_g)^1(1\pi_u)^3(1\pi_g)^3(3\sigma_u)^1 \qquad (9.1)$$

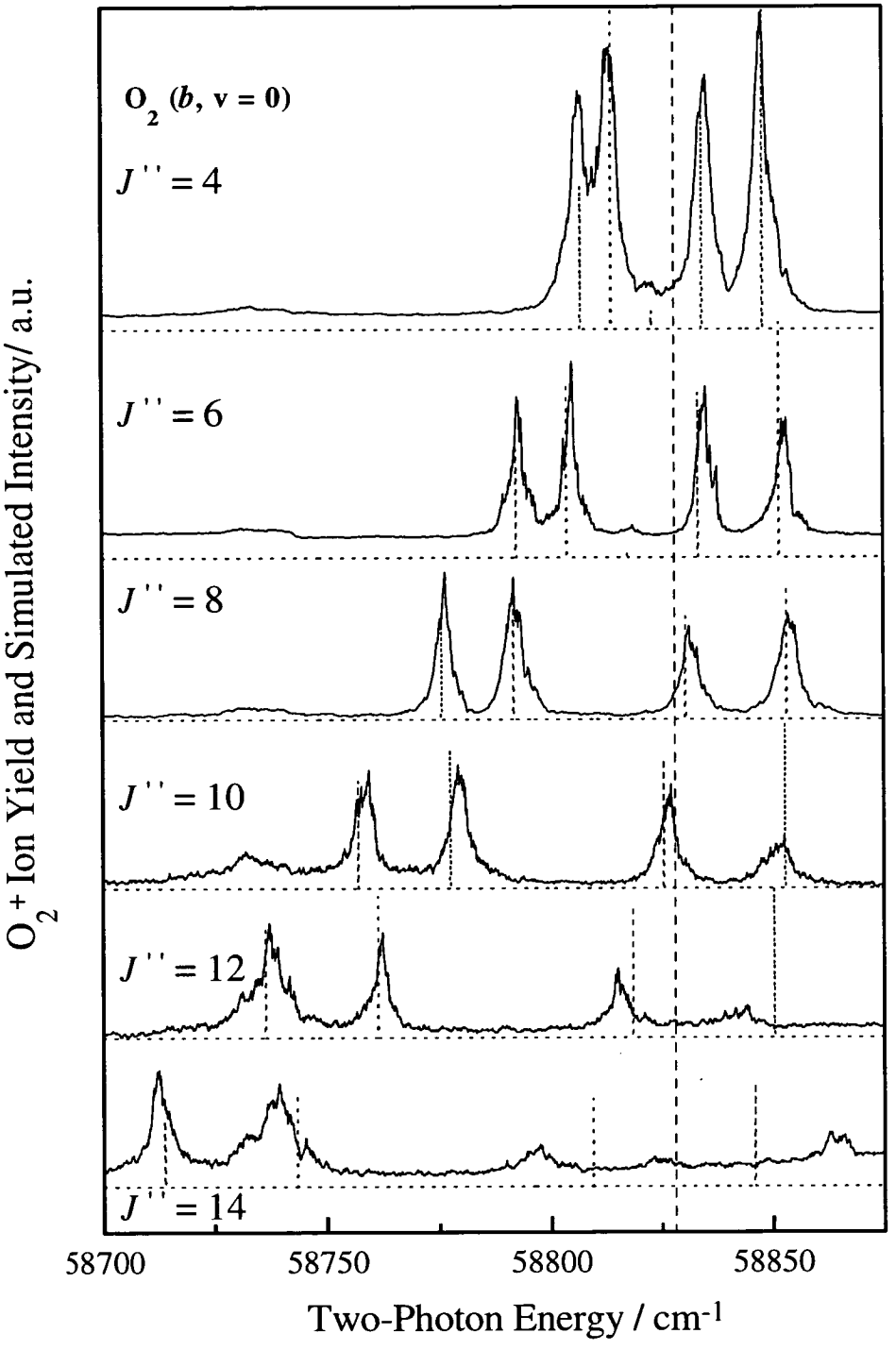

Figure 9.8.: The 2 + 1 ($d\ ^1\Pi_g$, v = 3) ←← ($b\ ^1\Sigma_g^+$, v = 0 REMPI spectra recorded following population of J = 4 - 14 of the b state are compared with the calculated line position and intensities. The line positions were calculated using a B_v = 1.39126 cm^{-1} for the lower level and a B_v = 1.14 cm^{-1} for the upper level with an origin of 58828 cm^{-1} (indicated by the vertical dashed line). Intensities were calculated using the Honl-London factors for a two-photon transition.

differs by the occupation of three orbitals from that of the $d\ ^1\Pi_g$ state. However, it was suggested that the interaction can occur in an indirect manner involving the $II\ ^1\Pi_g$ state as an intermediary. This state only differs in configuration from the $II\ ^1\Delta_g$ state by a single orbital ($\sigma_u \rightarrow \pi_u$) allowing a first-order **L** uncoupling interaction between the states. Therefore, it was concluded that the interaction only occurs due to the small contribution of the $II\ ^1\Pi_g$ state to the coupled level which is predominantly Rydberg in character.

The characteristics of our spectra are consistent with this conclusion and the splitting of the feature (5.9 cm^{-1}) is similar to that estimated from the spectra of Ogorzalek-Loo *et al.* (5.2 cm^{-1}). An interesting point which was not noted previously is the narrowing of these weakly perturbed features. While the FWHM of the features to higher and lower energy are 3.5 $\pm$ 1 cm^{-1} those of the two features arising from the weak perturbation are 1.6 and 2 cm^{-1} respectively. This is consistent with the mixing of the perturbing valence state, $II\ ^1\Pi_g$, with another valence state $II\ ^1\Delta_g$ which is not as strongly predissociated thus increasing the lifetime of the state.

9.4.3 Rotationally Selective Probing of the v = 2 level of the $d\ ^1\Pi_g$ State

Unlike the v = 3 level of the $d\ ^1\Pi_g$ state, perturbation of the v = 2 level is observed strongly for low J where this level interacts with v = 8 of the $II\ ^1\Pi_g$ state. The general characteristics of the spectra are outlined in Figure 9.9 which depicts fast scans of the v = 2 probe region following pumping of the P1 and P3 lines of the $b \leftarrow X$ transition which populate the J = 0 and 2 respectively of the $b\ ^1\Sigma_g^+$, v = 0 state. The trend in both of these spectra is an intense, low energy, structured feature and a weak higher energy feature. In terms of Lewis *et al.'s* [7] CSE model this is interpreted in a similar way to

the features observed for the J = 11 - 15 levels in the REMPI spectra of the v = 3 level of the $d\ ^1\Pi_g$ state. The lower energy feature is the predominantly Rydberg eigenstate resulting from the coupling of the lower v = 2 Rydberg diabatic level with the v = 8 valence level. The higher feature is conversely the predominantly valence level and therefore its detection efficiency is very low due to the low ionisation probability of the valence state.

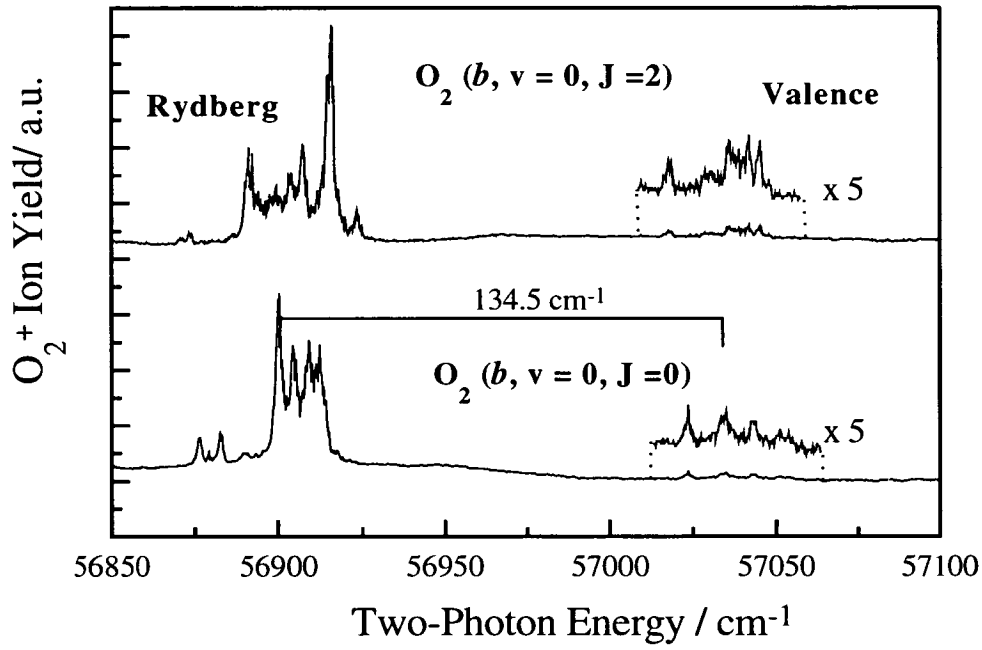

Figure 9.9.: The 2 + 1 ($d\ ^1\Pi_g$, v = 2) ←← ($b\ ^1\Sigma_g^+$, v = 0) REMPI spectra over the full energy region of the upper state. The features marked 'Rydberg' are those due to transitions to the predominantly Rydberg levels of the coupled states following the mixing of the ($d\ ^1\Pi_g$, v = 2) and ($II\ ^1\Pi_g$, v = 8) levels. The higher energy feature is, conversely, the mainly valence feature. The two features used to estimate the origins of the ($d\ ^1\Pi_g$, v = 2) and ($II\ ^1\Pi_g$, v = 8) levels and the energy difference between them are marked on the J = 0 spectrum.

However, on close inspection of the lower energy feature, as shown in the shorter and slower scans of the relevant energy region in Figure 9.10, it can be seen that the lower levels do not exhibit the expected simple rotational structure. For example, when the J'' = 0 level of the $b\ ^1\Sigma_g^+$, v = 0 state is populated only 1 rotational transition is allowed by the two-photon selection rules and yet six features are observed in the spectrum.

This perturbation of the low J of the $d\ ^1\Pi_g$ v = 2 level has not previously

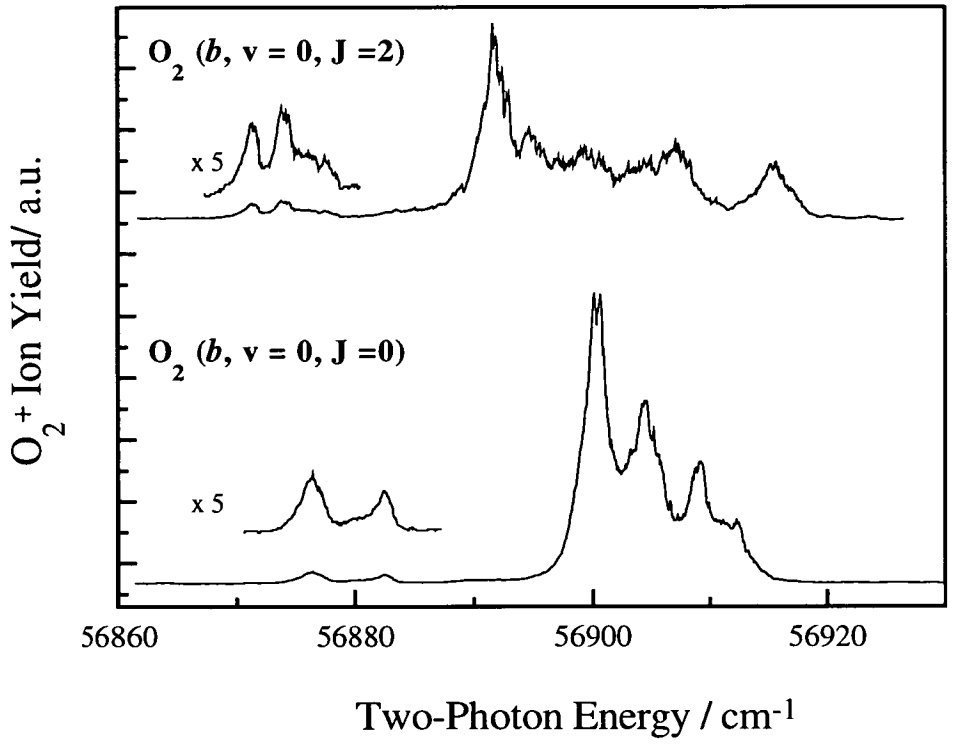

Figure 9.10.: A slow scan of the 2 + 1 ($d\,^1\Pi_g$, $v = 2$) $\leftarrow\leftarrow$ ($b\,^1\Sigma_g^+$, $v = 0$ REMPI spectra in the region of the Rydberg features. The lowest energy features are enlarged for clarity.

been observed principally due to the rotational congestion when transition from all of the lower J levels occur in the same spectrum. At present there is no clear explanation for the weak perturbation of the lower features. However, if the CSE model presented by Lewis *et al.* is correct then the source of the perturbation can be neither the $II\,^1\Pi_g$ valence state as the nearest vibrational level lies $\sim$ 150 cm^{-1} higher and is also observed in the spectra or the $C\,^3\Pi_g$ Rydberg state as the nearest vibrational level of this state is some $\sim$ 700 cm^{-1} lower in energy. A possible perturbing state may be the $II\,^1\Delta_g$ state which was proposed to be responsible for the rotational perturbation of the J = 17 level of v = 3 of the $d\,^1\Pi_g$ state. Due to the lower rotational spacing of the low J such a perturbation may range over a number of J unlike the single perturbed feature observed in the v = 3 spectra. It is possible to select pairs of features which are separated by 3 - 6 cm^{-1} consistent with the weak rotational perturbation observed in the v = 3 level. However, if this is the case the potential for this perturbing state, $II\,^1\Delta_g$, adapted by Lewis *et al.*

from the *ab initio* calculations of Partridge would need to be modified so that the low rotational levels of v = 0 of this level coincide with the low rotational levels of v = 2 of the $d\ ^1\Pi_g$ state.

9.5 Conclusions

The spectra presented in this chapter represent the first example of rotationally selective investigation of the lowest singlet Rydberg state of O_2. They are also the first well calibrated spectra to be presented. The perturbed features observed in the spectra involving $d\ ^1\Pi_g$, v = 3 are consistent with the CSE model reported recently by Lewis *et al.* where the effects of Rydberg-valence, valence-valance and Rydberg-valence interactions on the REMPI spectra were analysed.

However, the $d\ ^1\Pi_g$, v = 2 spectra contain some features which have not been observed previously due to rotational congestion of previous experimental methods. These features are not incorporated in the model of Lewis *et al.* and are presently not unequivocally understood. It is possible that the observed weak perturbation of the low J of the predominantly Rydberg levels may be rotationally, and hence, weakly perturbed by the $II\ ^1\Delta_g$ state in a similar manner proposed by Lewis *et al.* to account for the observed splitting of the $J = 17$ rotational level in the $d\ ^1\Pi_g$, v = 3 spectrum.

References

[1] J. S. Morrill, M. L. Ginter, B. R. Lewis and S. T. Gibson. *J. Chem. Phys.* **111** (1999) 173 ; and references therein.

[2] B. Minaev, O. Vahtras and H. Årgren *Chem. Phys.* **208** (1996) 299.

[3] *LX 351 Ti:Sapphire Laser User's Manual* (1996) Belarus.

[4] *LQ 514 Pulsed Nd:YAG Laser User's Manual* (1996) Belarus.

[5] S. H. Ashworth and J. M. Brown. *An Atlas of Optogalvanic Transitions in Neon* **CLRC Rutherford Appleton Laboratory** (1991).

[6] B. Edlen. *Vacuum Corrections to Three Decimal Places* **Lund** (1951).

[7] B. R. Lewis, S. T. Gibson, J. S. Morrill and M. L. Ginter. *J. Chem. Phys.* **111** (1999) 186.

[8] W. J. van der Zande, W. Koot, J. Los and J. R. Peterson. *J. Chem. Phys.* **89** (1988) 6758.

[9] A. Sur, R. S. Friedman and P. J. Miller. *J. Chem. Phys.* **94** (1991) 1705.

[10] Y. Li, D. Petsalakis, H. P. Liebermann, G. Hirsch and R. J. Buenker. *J. Chem. Phys.* **106** (1997) 1123.

[11] R. Klotz and S. D. Peyerimhoff. *Mol. Phys.* **57** (1986) 573.

[12] R. P. Saxon and B. Liu. *J. Chem. Phys.* **73** (1980) 870.

[13] R. P. Saxon and B. Liu. *J. Chem. Phys.* **73** (1980) 876.

[14] R. J. Buenker and S. D. Peyerimhoff. *Chem. Phys.* **8** (1975) 324.

[15] G. Herzberg. *Spectra of Diatomic Molecules* (Van Nostrand, Princeton, 1950).

[16] This simulation was performed by Helmut Telle, The University of Swansea.

[17] R. D. Johnson III, G. R. Long and J. W. Hudgens. *J. Chem. Phys.* **87** (1987) 1977.

[18] R. Ogorzalek-Loo. *PhD Thesis* **Cornell University** (1989).

Appendix A

University Regulations

A.1 Lecture Courses Attended

In accordance with the regulations of the University of Edinburgh, Department of Chemistry, the following lecture courses were attended during the last three years:

1. Excited States
2. Molecular Quantum Mechanics
3. Reaction Dynamics
4. Reactive and Inelastic Scattering
5. Physical Chemistry Section Colloquia during the Academic years 1996-1997, 1997-1998 and 1998-1999

A.2 Conferences and Meetings Attended

1. First Summer School on Trends in Molecular Physics: Crossing the borders between bound states and the continuum of molecules: dissociation, association, ionisation and recombination.
Les Houches, France, 22-27/6/1997;
Contribution: Poster.

2. Faraday Discussion 108. Dynamics of Electronically Excited States in Gaseous, Cluster, and Condensed Media.
University of Sussex, Brighton, U.K., 15-17/12/1997;
Contribution: Poster.

3. Second Summer School on Trends in Molecular Physics. Molecular Physics and chemical reaction dynamics: fundamental aspects and application to atmospheric and environmental sciences.
Jonkerbosch Conference Center, The Netherlands, 16-25/6/1998;
Contribution: Oral presentation and poster.

4. Gas Kinetics Meeting, 1999.
University of York, U.K., 6/1/1999.
Contribution: Oral presentation.

A.3 List of Publications

1. P. O'Keeffe, T. Ridley, S. Wang, K.P. Lawley, R.J. Donovan.
"Formation of O_2 ($b\ ^1\Sigma_g^+$) in the Ultraviolet Photolysis of O_3.", *Resonance Ionisation Meeting, Ninth International Symposium, Manchester, U.K.* AIP Conference Proceedings **454** (1998) 103.

2. P. O'Keeffe, T. Ridley, S. Wang, K.P. Lawley, R.J. Donovan.
"Photodissociation of ozone between 335 and 352 nm to give O_2 ($b\ ^1\Sigma_g^+$) and $O(^3P_J)$", *Chem. Phys. Lett.* **298** (1998) 368.

3. P. O'Keeffe, T. Ridley, R.R.J. Maier, K.P. Lawley, R.J. Donovan.
"Kinetic energy analysis of $O(^3P_0)$ and O_2 ($b\ ^1\Sigma_g^+$) fragments produced by photolysis of ozone in the Huggins bands.", *J. Chem. Phys.* **110** (1999) 10803.

4. P. O'Keeffe, T. Ridley, K.P. Lawley, R.J. Donovan.
"A Re-analysis of the UV spectrum of Ozone", in preparation.

5. P. O'Keeffe, T. Ridley, K.P. Lawley, R.J. Donovan.
"Insights into the spin-forbidden photodissociation channels in the Huggins bands of ozone", in preparation.